論文目録

1. 学位論文

題目：Electrochemical Crystal Growth and Physical Properties of Titanium Oxides and Oxyfluorides（チタン酸化物・酸フッ化物の電気化学的結晶育成と物性）

2. 論文リスト

(1) **Chiba, Y.**; Saito, M.; Hagiwara, T.; Takatsu, H.; Kageyama, H.; Motohashi, T. High-Temperature Electrochemical Crystal Growth of Hollandite-Type $Cs_xTi_8O_{16}$ with Controlled Electronic Properties. *Cryst. Growth Des.* **2017,** *17,* 5691–5696.

(2) **Chiba, Y.**; Koizumi, D.; Saito, M.; Motohashi, T. Structural Design of Alkali-Metal Titanates: Electrochemical Growth of $K_xTi_8O_{16}$, $Na_{2+x}Ti_6O_{13}$, and $Li_{2+x}Ti_3O_7$ Single Crystals with One-Dimensional Tunnel Structures. *CrystEngComm* **2019,** *21,* 3223–3231.

(3) **Chiba, Y.**; Shibata, K.; Takatsu, H.; Fujii, K.; Saito, M.; Kageyama, H.; Maeda, K.; Yashima, M.; Motohashi, T. Electrochemical Crystal Growth of Titanium Oxyfluorides—A Strategy for Development of Electron-Doped Materials. *Inorg. Chem.* **2021,** *60,* 14613–14621. **(Selected as Cover Art)**

千葉　裕介　㊞

2021年度　博士論文

チタン酸化物・酸フッ化物の電気化学的結晶育成と物性

千葉 裕介（工学研究科応用化学専攻）

論文の要旨：

本博士論文では，さまざまなチタン酸化物・酸フッ化物の単結晶試料を定電圧下における高温溶融塩電解により育成し，得られた結晶の結晶構造，電子特性，磁気特性，光学特性および水素生成光触媒活性を調査した．本手法によって得られた結晶は他の手法で育成することは困難であり，結晶にドープされたd電子が化合物の物性に大きく影響することを明らかにしている．本論文は6章構成をとり，第1章は総説，第2–5章は各論，第6章は全体総括となっている．以下，第2–5章の内容について簡潔に記す．なお，各項目に付されている数字は基になった発表論文の番号と対応している．

● **電子特性を制御したホーランダイト型 $Cs_xTi_8O_{16}$ 結晶の育成 [1]**

第2章では，TiO_2/Cs_2MoO_4 混合物の定電圧電解によりホーランダイト型 $Cs_xTi_8O_{16}$ の針状結晶（約2 mm）を育成した．結晶育成の際に印加する電圧を制御することにより，透明または金属光沢をもった結晶の作り分けに成功した．これらの結晶は全く異なる電子特性を示し，透明結晶はバルクの電子伝導性の低さから絶縁体であったのに対し，金属光沢結晶は半導体的な電気抵抗率の温度依存性を示した．本章では，高温溶融塩電解を用いたチタン酸化物の単結晶育成において，定電圧電解によって結晶のキャリア（d電子）濃度を制御できることを初めて示した．

● **一次元トンネル構造をもつ $K_xTi_8O_{16}$, $Na_{2+x}Ti_6O_{13}$ および $Li_{2+x}Ti_3O_7$ 結晶の育成 [2]**

第3章では，カリウム，ナトリウム，およびリチウムを含むチタン酸化物の単結晶を第2章と同様の手法で育成した．A_2MoO_4 (A = Li, Na, K) の溶融塩を用いることにより，$K_xTi_8O_{16}$（ホーランダイト型），$Na_{2+x}Ti_6O_{13}$，$Li_{2+x}Ti_3O_7$（ラムスデライト型）の針状結晶（約1–3 mm）の育成に成功した．これらの化合物は例外なく一次元のトンネル構造を有し，そのトンネル径はアルカリ金属イオンの大きさに依存することがわかった．電気化学的に育成したアルカリ金属過剰の $Na_{2+x}Ti_6O_{13}$ および $Li_{2+x}Ti_3O_7$ 結晶は，アルカリ金属定比の参照化合物（$Na_2Ti_6O_{13}$ および $Li_2Ti_3O_7$）には見られない明瞭な可視光吸収を示し，過剰なアルカリ金属の挿入と同時にd電子ドープされていることが示唆された．本章では，電気化学的手法がさまざまなアルカリ金属を含む電子ドープチタン酸化物の結晶育成に適用可能であることを示した．

● **高い光触媒活性を示すチタン酸フッ化物 $Li_2Ti(O,F)_3$ の結晶育成 [3]**

第 4 章では，第 2 章および第 3 章で培われたチタン酸化物の結晶育成ノウハウを酸フッ化物の単結晶育成に応用することを試みた．Li_2MoO_4–LiF 共晶溶融塩を用いて印加電圧を制御した場合に，立方晶岩塩型構造をもつチタン酸フッ化物 $Li_2Ti(O,F)_3$ の緑色八面体結晶（約 30 μm）の育成に成功した．得られた結晶は常磁性的な磁化率の温度依存性と明瞭な可視光吸収を示し，電子ドープされていることが確認された．紫外光の照射下においてメタノール水溶液からの水素生成光触媒活性を調査したところ，育成した結晶は電子非ドープの類似化合物 $Li_5Ti_2O_6F$ と比較して約 3 倍高い活性を示すことが明らかとなった．酸フッ化物の電気化学的結晶育成の報告は，チタン系以外の化合物を含めてもこれが初めてである．

● **Na/Mo/F 共ドープ $CaTiO_3$ 結晶の育成**

第 5 章では，$Li_2Ti(O,F)_3$ に次ぐチタン酸フッ化物の電気化学的結晶育成の 2 例目として，フッ素ドープ $CaTiO_3$ 結晶の育成を試みた．溶融塩に Na_2MoO_4–NaF–$CaMoO_4$ 混合物を用いることにより Na/Mo/F 共ドープ $CaTiO_3$ 結晶（約 0.2 mm）が得られた．ドーパント濃度は印加電圧を制御することによりコントロールできた．得られた結晶は褐色を呈しており，高光触媒活性の発現に有望な複数のドーパントイオン（Na, Mo および F イオン）も共存しているため，可視光下での光触媒活性評価の実施が期待される．本章は，さまざまなチタン酸フッ化物の単結晶が電気化学的手法によって育成できる可能性を示した．

【発表論文】

[1] **Chiba, Y.**; Saito, M.; Hagiwara, T.; Takatsu, H.; Kageyama, H.; Motohashi, T. High-Temperature Electrochemical Crystal Growth of Hollandite-Type $Cs_xTi_8O_{16}$ with Controlled Electronic Properties. *Cryst. Growth Des.* **2017**, *17*, 5691–5696.

[2] **Chiba, Y.**; Koizumi, D.; Saito, M.; Motohashi, T. Structural Design of Alkali-Metal Titanates: Electrochemical Growth of $K_xTi_8O_{16}$, $Na_{2+x}Ti_6O_{13}$, and $Li_{2+x}Ti_3O_7$ Single Crystals with One-Dimensional Tunnel Structures. *CrystEngComm* **2019**, *21*, 3223–3231.

[3] **Chiba, Y.**; Shibata, K.; Takatsu, H.; Fujii, K.; Saito, M.; Kageyama, H.; Maeda, K.; Yashima, M.; Motohashi, T. Electrochemical Crystal Growth of Titanium Oxyfluorides—A Strategy for Development of Electron-Doped Materials. *Inorg. Chem.* **2021**, *60*, 14613–14621. **(Selected as Cover Art)**

2021 Doctoral Dissertation

Electrochemical Crystal Growth and Physical Properties of Titanium Oxides and Oxyfluorides

Yusuke Chiba (Course of Applied Chemistry, Graduate School of Engineering)

Abstract:

In this dissertation, single crystals of various titanium oxides and oxyfluorides were grown employing high-temperature constant-voltage electrolysis of TiO_2 with A_2MoO_4 (A = Li, Na, K, Cs)-based melts. Structural, electronic, magnetic, and optical properties, and photocatalytic H_2 evolution activities of the resultant crystals were extensively investigated. The described method is highly effective in obtaining *electron-doped* titanium oxides and oxyfluorides with precisely controlled chemical compositions and crystal structures. Throughout the dissertation, the author emphasizes that crystals obtained herein are never obtained by any other techniques, and the doped d electrons significantly impact the properties of the materials.

Chapter 1 describes a brief overview of titanium oxides, mixed-anion compounds, and crystal growth techniques. The objectives of the dissertation are also mentioned in this chapter. In Chapter 2, needle-like crystals of hollandite-type $Cs_xTi_8O_{16}$ were successfully obtained by constant-voltage electrolysis of TiO_2 with the Cs_2MoO_4 melt. Depending on the applied voltages, the resultant crystals exhibit distinct properties, either electrical insulators with optical transparency or semiconductors with metallic luster. Chapter 3 deals with the crystal growth of titanium oxides containing lithium, sodium, and potassium by using the A_2MoO_4 (A = Li, Na, K) melt. Crystals of $K_xTi_8O_{16}$ (hollandite-type), $Na_{2+x}Ti_6O_{13}$, and $Li_{2+x}Ti_3O_7$ (ramsdellite-type) are successfully grown. These compounds unexceptionally crystallize in one-dimensional tunnel structures with various tunnel shapes depending on the alkali metals incorporated. In Chapter 4, the crystal growth of titanium oxyfluorides is attempted by using the eutectic Li_2MoO_4–LiF melt. Rocksalt-type $Li_2Ti(O,F)_3$ (F/Ti ~ 0.15) crystals are obtained by precisely tuning the applied voltage. The crystals were found to produce H_2 more efficiently from aqueous methanol under UV light than a nondoped oxyfluoride $Li_5Ti_2O_6F$ reference. Chapter 5 reports the successful growth of Na/Mo/F-codoped $CaTiO_3$ crystals by using the Na_2MoO_4–NaF–$CaMoO_4$ melt. The dopant concentration is controlled by the applied voltage values. Finally, the concluding remarks and suggestions for future works are given in Chapter 6.

2021 Doctoral Dissertation

Electrochemical Crystal Growth and Physical Properties of Titanium Oxides and Oxyfluorides

(チタン酸化物・酸フッ化物の電気化学的結晶育成と物性)

A Dissertation

Presented to

Graduate School of Engineering

Kanagawa University

In Partial Fulfillment of the Requirements for the Degree

Doctor of Engineering

by

Yusuke Chiba

January 2022

Acknowledgments

First and foremost, I would like to express my deepest gratitude to Professor Teruki Motohashi and Dr. Miwa Saito for their kind and persistent guidance over the last seven years toward the doctoral degree. Everything I have learned from them will be invaluable for the rest of my life. Also, this work would never be completed without the following: Dr. Hiroshi Takatsu and Professor Hiroshi Kageyama (Kyoto University), and Associate Professor Yoji Kobayashi (King Abdullah University of Science and Technology) for the electronic/magnetic and XPS measurements; Mr. Kengo Shibata and Associate Professor Kazuhiko Maeda (Tokyo Institute of Technology) for the optical and photocatalytic activity measurements; Dr. Takeshi Hagiwara and Dr. Keiko Orisaku (Kanagawa University), and Assistant Professor Kotaro Fujii and Professor Masatomo Yashima (Tokyo Institute of Technology) for the single-crystal X-ray diffraction study; Mr. Daisuke Koizumi (Kanagawa University) for the crystal growth of $Na_{2+x}Ti_6O_{13}$. Special thanks should go to all the people for their support.

This work was supported by JSPS Grant-in-Aid for Scientific Research on Innovative Areas "Mixed anion" (Grant Numbers JP16H6439, JP16H6440, JP16H6441, JP17H05490, and JP19H04707) and JSPS Core-to-Core Program (JPJSCCA20200004). I would also like to acknowledge financial support from Grant-in-Aid for JSPS Fellows from JSPS (Grant Number JP20J14378).

Last but certainly not least, I truly feel grateful for my parents' continuous support and affectionate encouragement that mean a lot to me in finishing the doctoral program.

January 2022

Yusuke Chiba

Table of Contents

Chapter 1

General Introduction

This chapter briefly overviews the research background (including some fundamental knowledge and historical context) that motivates the author to launch the study. Please note that the subsequent chapters (Chapters 2, 3, 4, and 5) also include the *Introduction* section, in which the detailed background for each chapter is described.

1.1. Titanium Oxides—Their Structures, Properties, and Applications

1.1.1. Titanium Dioxide

General. Titanium dioxide (TiO_2), discovered individually by W. Gregor in 1791 and M. H. Klaproth in 1795,[1] is the most popular and important material among the simple binary titanium oxides. TiO_2 generally features high chemical/thermal stability, abundance (0.44% of the Earth's crust as titanium),[2] low cost, and nontoxicity toward both human beings and the environment. Practical uses of TiO_2 cover every scene of our daily lives, including pigments, paints, coatings, printing inks, paper textiles, plastics, rubbers, antibacterial agents, cosmetics, food additives, and so on.[3,4]

Industrially, TiO_2 is manufactured starting from ore sources (typically rutile and ilmenite $FeTiO_3$) by two main routes:[5–8] (1) the chlorine method and (2) the sulfuric acid method. The chlorine method involves the formation of $TiCl_4$ by reacting rutile ore and chlorine gas under reductive conditions (eq

1), followed by high-temperature oxidation of purified $TiCl_4$ to obtain rutile-type TiO_2 (eq 2).

$$TiO_2 \text{ (rutile ore)} + C + 2Cl_2 \rightarrow TiCl_4 + CO_2 \quad (1)$$

$$TiCl_4 + O_2 \rightarrow TiO_2\downarrow + 2Cl_2\uparrow \quad (2)$$

The sulfuric acid method is the first commercialized process in the 1920s for the production of the TiO_2 pigment and includes the following three-step reactions (eqs 3–5). In the first step, ilmenite $FeTiO_3$ is dissolved in concentrated sulfuric acid (eq 3). Next, the resultant $TiOSO_4$ is separated, purified, and then hydrolyzed to form insoluble precipitates of $TiO(OH)_2$ (eq 4). Finally, anatase- and rutile-type TiO_2 is obtained after the heat treatment of $TiO(OH)_2$ (eq 5).

$$FeTiO_3 + 2H_2SO_4 \rightarrow FeSO_4 + TiOSO_4 + 2H_2O \quad (3)$$

$$TiOSO_4 + 2H_2O \rightarrow TiO(OH)_2\downarrow + H_2SO_4 \quad (4)$$

$$TiO(OH)_2 \rightarrow TiO_2 + H_2O \quad (5)$$

Regarding cost and waste managements, the chlorine method dominates the majority of the recent industry: ~60% for the chlorine method and ~40% for the sulfuric acid method.[6] The world total production of TiO_2 is approximated at 6.6 million tons per year, where Japan accounts for about 3% of the total.[7]

Structure. TiO_2 exists in many types of crystal structures. This feature is called polymorphism, which describes the same crystalline compound showing different atomic arrangements. The most widely known polymorphs of TiO_2 must be anatase, rutile, and brookite. At the present day, anatase and rutile are predominant in the industrially manufactured TiO_2. As far as the author knows, however, at least five polymorphs—TiO_2(B), α-PbO_2, ramsdellite, hollandite, and baddeleyite—have been

reported other than the aforementioned three. Figure 1.1 shows a polyhedral representation of crystal structures for the eight known polymorphs (the VESTA software[9] for visualization), and Table 1.1 provides the crystallographic data.[10–17] These polymorphs include both the naturally-occurring phases (anatase, rutile, brookite, and TiO_2(B)) and synthetic phases (α-PbO_2, ramsdellite, hollandite, and baddeleyite), exhibiting a wide variety of structural motifs. Rutile is the most stable form at ambient conditions, and other polymorphs irreversibly transform to rutile upon heating.[18–20] Both of α-PbO_2- and baddeleyite-type TiO_2 are high-pressure polymorphs: while α-PbO_2-type TiO_2 is stable at ambient conditions, baddeleyite-type TiO_2 is not.[21] The syntheses of TiO_2(B), α-PbO_2, ramsdellite, hollandite, and baddeleyite are relatively difficult, limiting physical research on these polymorphs with highly crystalline samples.

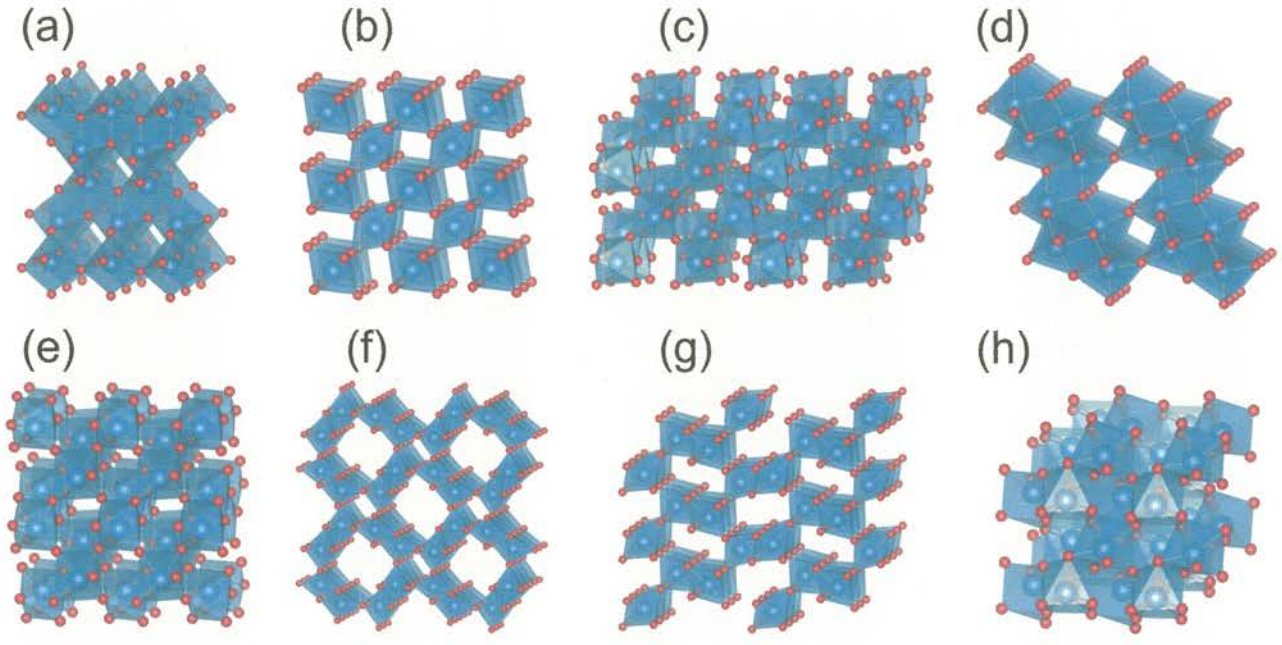

Figure 1.1. Polyhedral representation of the crystal structures of the eight TiO_2 polymorphs: (a) anatase, (b) rutile, (c) brookite, (d) TiO_2(B), (e) α-PbO_2, (f) hollandite, (g) ramsdellite, and (h) baddeleyite. Blue and red spheres represent Ti and O ions, respectively. Ti ions are six coordinated in (a)–(g) but are seven coordinated in (h).

Table 1.1. Crystallographic data for eight TiO_2 polymorphs.

phase	anatase	rutile	brookite	TiO_2(B)	α-PbO_2	ramsdellite	hollandite	baddeleyite
system	tetragonal	tetragonal	orthorhombic	monoclinic	orthorhombic	orthorhombic	tetragonal	monoclinic
space group	$I4_1/amd$	$P4/mnm$	$Pbca$	$C2/m$	$Pbcn$	$Pbnm$	$I4/m$	$P2_1/c$
a / Å	3.785	4.594	9.184	12.1787	4.5271	4.9022	10.161	4.525
b / Å	(= a)	(= a)	5.447	3.7412	5.4972	9.459	(= a)	4.767
c / Å	9.514	2.959	5.145	6.5249	4.9001	2.9585	2.97	4.718
α/°	90	90	90	90	90	90	90	90
β/°	(= α)	(= α)	(= α)	107.054	(= α)	(= α)	(= α)	98.7
γ/°	(= α)	(= α)	(= α)	(= α)	(= α)	(= α)	(= α)	(= α)
CN[a] (Ti)	6	6	6	6	6	6	6	7
notes	—	—	—	—	synthetic (high-P[b])	synthetic	synthetic	synthetic (high-P[b])
ref	10	11	12	13	14	15	16	17

[a] Coordination numbers. [b] High-pressure phases.

Buckeridge and co-workers revealed in their theoretical calculations that the band structures of TiO_2 can be tuned largely by varying the local coordination environments of Ti and O,[22] which may suggest broadened applications in each polymorph. The calculated band structures and density of states (DOS) of the eight TiO_2 polymorphs are shown in Figures 1.2 and 1.3. For all the polymorphs, the valence band maximum (VBM) and conduction band minimum (CBM) are mainly composed of the O 2p and Ti 3d orbitals, respectively. Clearly, the conduction band of baddeleyite-type TiO_2 is highly dispersive; it ranges approximately from −8 to 0 eV relative to VBM. Baddeleyite-type TiO_2 also features the narrowest band-gap energy of 2.20 eV originating from the significantly raised VBM. On the other hand, the largest band-gap energy of 4.11 eV is obtained in TiO_2(B).

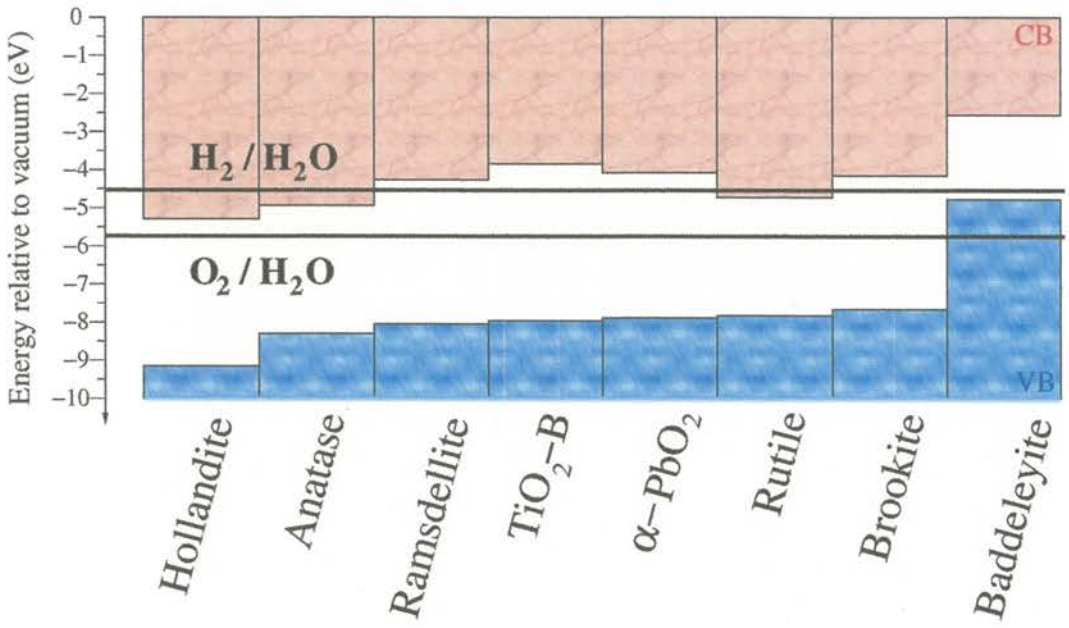

Figure 1.2. Calculated valence band (VB) and conduction band (CB) positions relative to the vacuum level for the eight TiO_2 polymorphs. The H_2 and O_2 redox potentials are also shown for comparison. Reprinted (adapted) with permission from ref 22. Copyright 2015 American Chemical Society.

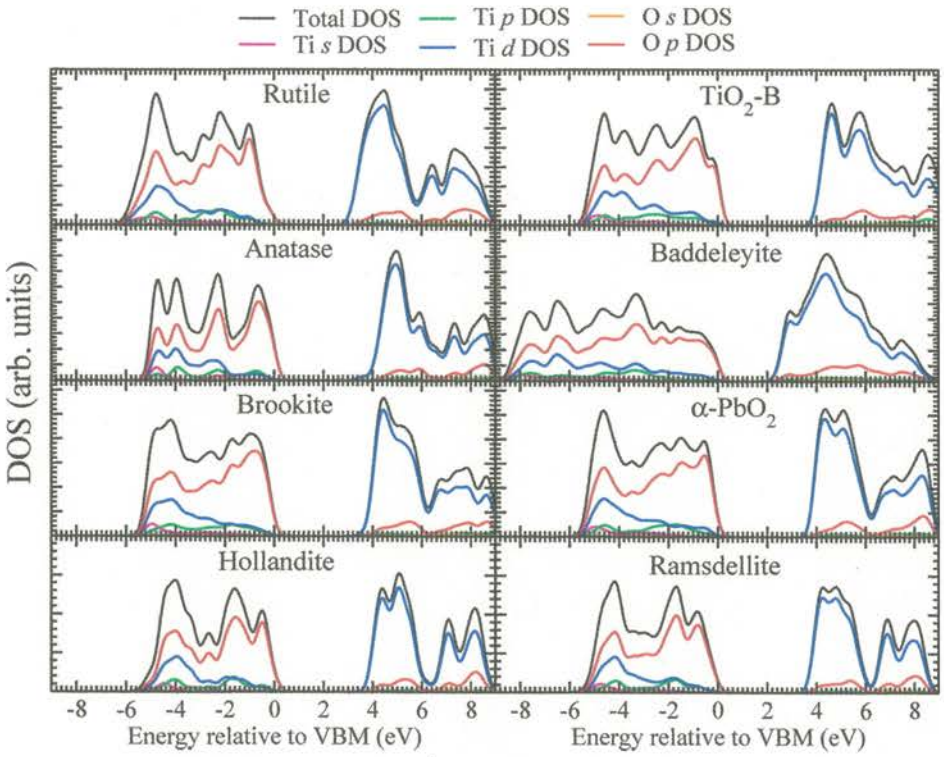

Figure 1.3. Calculated density of states (DOS) and partial DOS of the eight TiO_2 polymorphs as a function of energy relative to the valence band maximum (VBM). Reprinted (adapted) with permission from ref 22. Copyright 2015 American Chemical Society.

Photocatalyst. The historic breakthrough in the research on TiO_2 is willing to bet the discovery of catalytic effects induced by light, viz., photocatalysis. As one of the early works, Kato and Mashio reported in 1964 the liquid-phase oxidation of tetralin (1,2,3,4-tetrahydronaphthalene) promoted by anatase- and rutile-type TiO_2 photocatalysts under UV-light irradiation.[23] In 1972, Honda and Fujishima discovered the renowned "Honda–Fujishima effect" involving the electrolysis of water into hydrogen and oxygen by using a rutile-type TiO_2 single crystal as a photoanode and a Pt cathode.[24] With the irradiation of UV light onto the TiO_2 photoanode, the oxidation/reduction reactions of water take place at a much lower anodic bias voltage than the electrolysis without irradiating UV light. Ever since the pioneering study by Honda and Fujishima, attempts have been made to apply the principle

to heterogeneous catalysts.[25] In 1976, Bulatov and Khidekel achieved water splitting over rutile-type TiO_2 powder modified by Pt particles under UV light.[26] The Pt particles deposited on the surface of TiO_2 grains work as electron scavengers, inhibiting electron–hole recombination to improve the photocatalytic performance.[27] It should be noted that anatase and rutile are both commonly-used polymorphs in photocatalysis. They are mainly photosensitive in the UV range because of their wide bandgaps (~3.2 eV and ~3.0 eV for anatase and rutile, respectively).[28] Anatase generally exhibits higher photocatalytic activities than rutile because of, e.g., its electronic structure[29] and surface properties.[30]

Other Applications. The open-circuit voltage (OCV) for TiO_2(B)-used batteries is higher than those of anatase- and rutile-used ones (1.6 V for TiO_2(B),[31] 1.55 V for anatase,[32] and 1.4 V for rutile[33]), allowing this polymorph a potential anode material for lithium-ion secondary batteries (LIBs). Ramsdellite- and hollandite-type TiO_2, both of which adopt large tunnel structures, are widely investigated for anode materials for LIBs as well.[34–37] Keeping an eye on the high work function and the large band gap (3.86 eV) of hollandite-type TiO_2, this polymorph may be applicable to transparent conducting oxides (TCOs), which possess both electrical conductivity and visible-range optical transparency, for photovoltaic devices as well as short-wavelength light-emitting diodes.[22] Noteworthy applications have not been reported for brookite-, α-PbO_2- and baddeleyite-type TiO_2.

1.1.2. Ternary and Higher-Order Titanium Oxides

The diversity of crystal structures of titanium oxides tremendously increases with a combination of additional elements, so more unique properties can arise in ternary and higher-order titanium oxides, as outlined below.

Three-Dimensional (3D) Structures. Barium titanate $BaTiO_3$, being ferroelectric at room temperature, adopts a perovskite-type structure with a slight tetragonal distortion (tetragonality c/a ~

1.01).[38–40] Owing to the high dielectric constant, $BaTiO_3$ has been utilized as, e.g., a component of multilayer ceramic capacitors (MLCCs).[41] Lead zirconate titanate perovskite $Pb(Zr,Ti)O_3$ (PZT) shows an exceptional piezoelectric effect and finds application in piezoelectric elements embedded in various types of machinery.[42] Spinel-type $Li_4Ti_5O_{12}$ is a promising anode material for LIBs, showing negligible volume change during charge/discharge cycles and a theoretical capacity of 175 mA h g^{-1}.[43] An *A*-site deficient $(La,Li)TiO_3$ perovskite is a fast lithium-ion conductor (10^{-3} S cm^{-1} at room temperature) and intensively studied as a candidate of solid electrolytes for all-solid LIBs.[44] Furthermore, pyrochlore-type $Ln_2Ti_2O_7$ (*Ln* = Dy, Ho) exhibits a geometrical frustration associated with ferromagnetic and dipolar interactions, called "spin ice."[45,46] Crystal structures of these compounds are depicted in Figure 1.4.

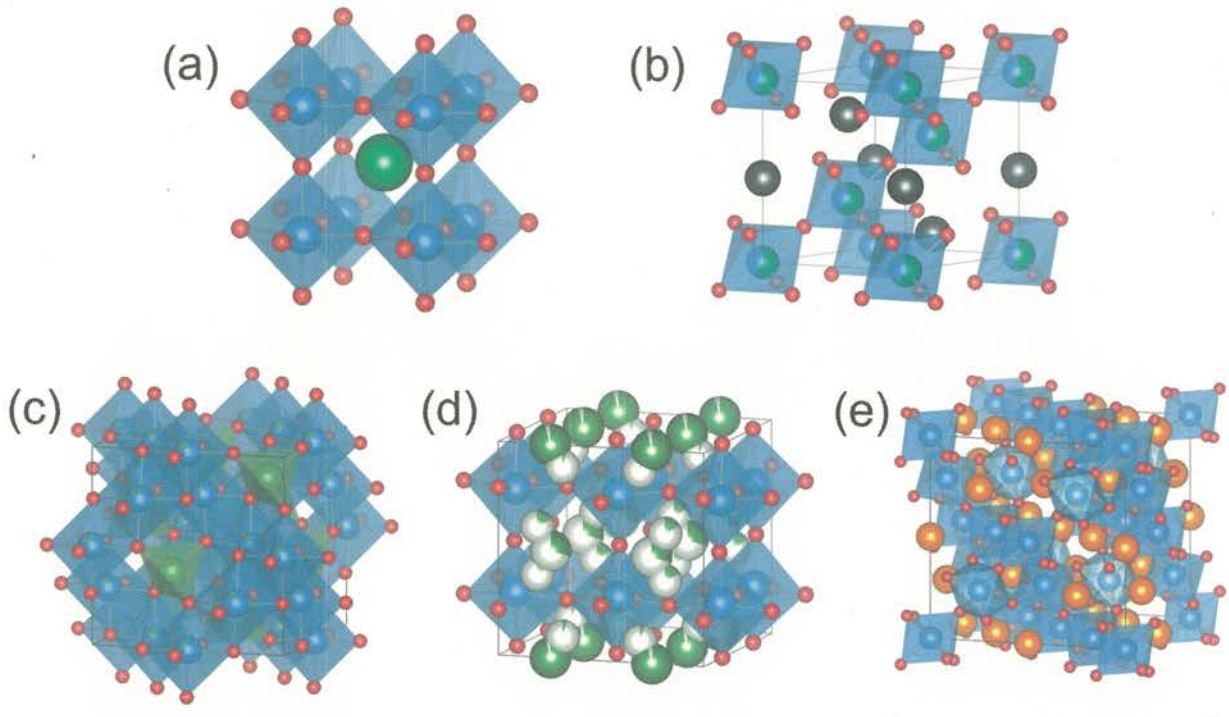

Figure 1.4. Crystal structures of various titanium oxides with 3D structures: (a) $BaTiO_3$, (b) $Pb(Zr,Ti)O_3$, (c) $Li_4Ti_5O_{12}$, (d) $(La,Li)TiO_3$, and (e) $Ln_2Ti_2O_7$ (*Ln* = Dy, Ho). For all the structures, blue and red spheres represent Ti and O ions, respectively.

Two-Dimensional (2D) Structures. $A_2La_2Ti_3O_{10}$ (A = K, Rb, Cs) with a Ruddlesden–Popper-type n = 3 structure exhibits a high photocatalytic activity for overall water splitting,[47] as well as photoluminescence[48] and upconversion luminescence.[49] Layered perovskite titanates that belong to the Ruddlesden–Popper (RP) phases,[50–52] $A'_2[A_{n-1}B_nO_{3n+1}]$, the Dion–Jacobson (DJ) phases,[53,54] $A'[A_{n-1}B_nO_{3n+1}]$, and the Aurivillius (AV) phases,[55–57] $[Bi_2O_2][A_{n-1}B_nO_{3n+1}]$ (A and A' are typically alkali, alkali-earth, or rare-earth metals; B is a transition metal; and n denotes the number of perovskite-like slabs $[A_{n-1}B_nO_{3n+1}]$) are quite attractive regarding host–guest chemistry (Figure 1.5). Numerous RP, DJ, and AV derivatives have been synthesized via insertion/extraction and ion-exchange reactions in an aqueous solution and a molten salt, or using solid reagents.[58–77]

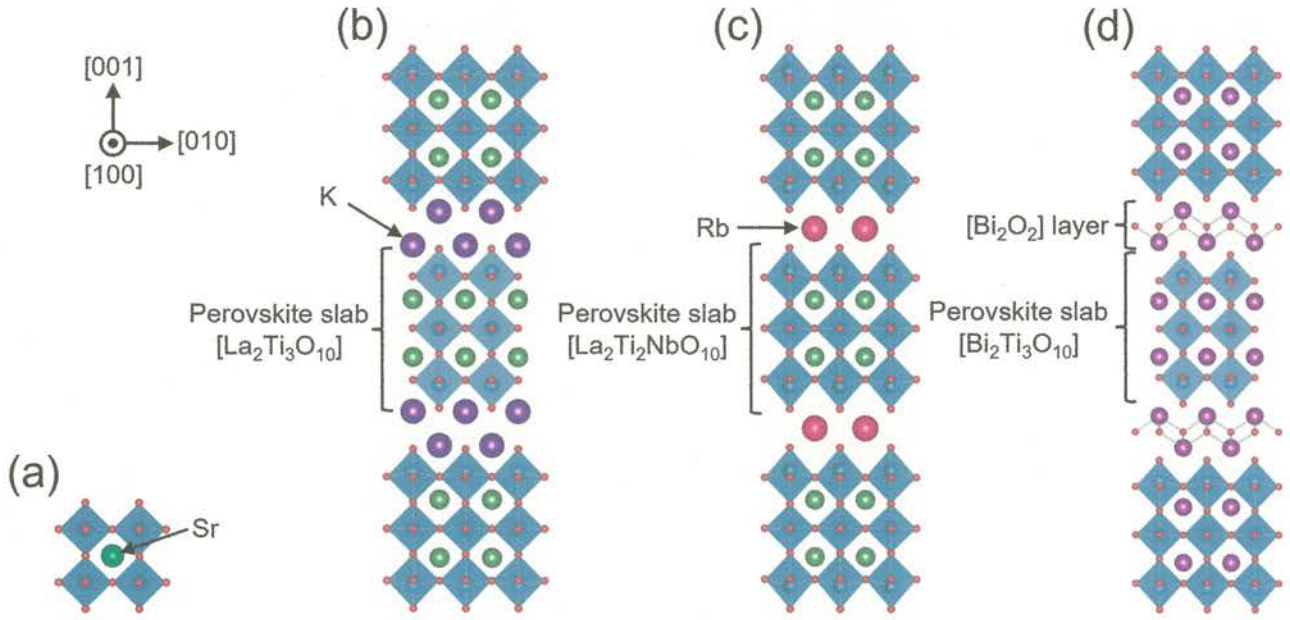

Figure 1.5. [100] view of selected perovskites and layered perovskites: (a) perovskite $SrTiO_3$, (b) Ruddlesden–Popper $K_2[La_2Ti_3O_{10}]$, (c) Dion–Jacobson $Rb[La_2Ti_2NbO_{10}]$, and (d) Aurivillius $[Bi_2O_2][Bi_2Ti_3O_{10}]$. For all the structures, blue and red spheres represent Ti and O ions, respectively.

One-Dimensional (1D) Structures. Some titanium oxides with 1D tunnel structures are found in the series of the so-called Wadsley–Andersson compounds, $A_2Ti_nO_{2n+1}$ (n = 3, 4, 6, 7, 9), where A is usually sodium (Figure 1.6).[78–83] The compounds with n = 6, 7, and 9 adopt 1D tunnel structures, albeit layered structures for n = 3 and 4. Sodium cations that reside in the interlayer galleries and tunnels built from edge- and corner-shared TiO_6 octahedra are readily replaced by Li^+ and H^+.[84–89] The $A_2Ti_nO_{2n+1}$ analog has been investigated as potential electrode materials[90–92] and photocatalysts.[93] Another large family with 1D tunnel structures meets hollandite-type compounds having the general formula $A_x(Ti,M)_8O_{16}$, where A is a large non-framework mono- or di-valent cation residing in tunnels and M is a di- or tri-valent cation substituting for Ti^{4+} (Figure 1.7).[94–96] To neutralize the negative charge of the framework, the x value in $A_x(Ti,M)_8O_{16}$ increases up to 2. Hollandite titanates have received attention mainly because of potential applications as, e.g., immobilizers of radioactive elements,[97,98] solid-state electrolytes,[99] and electrode materials.[100,101]

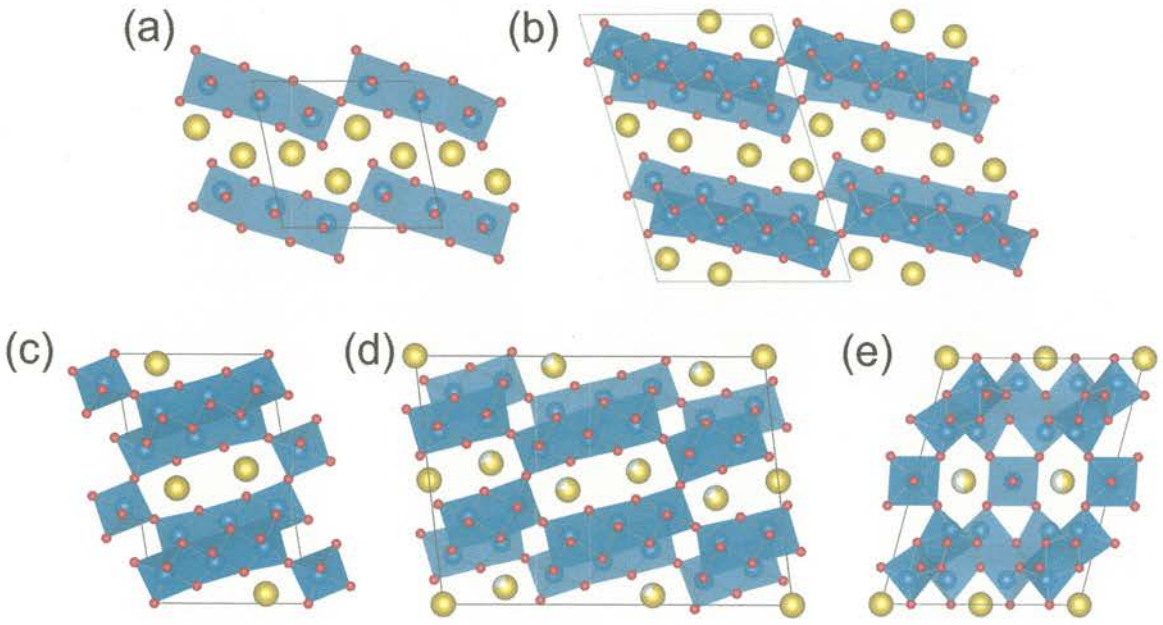

Figure 1.6. Wadsley–Andersson compounds $A_2Ti_nO_{2n+1}$ with n = 3, 4, 6, 7, and 9, viewed along layers and tunnels: (a) $Na_2Ti_3O_7$, (b) $Na_2Ti_4O_9$, (c) $Na_2Ti_6O_{13}$, (d) $Na_2Ti_7O_{15}$, and (e) $Na_2Ti_9O_{19}$. Sodium, yellow; titanium, blue; and oxygen; red.

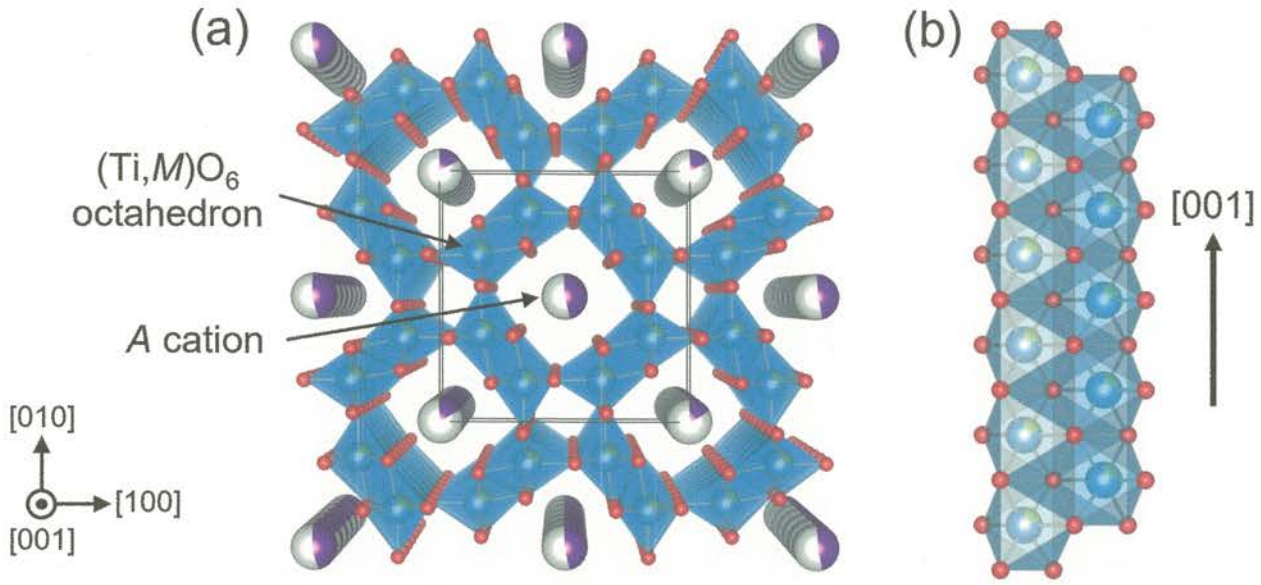

Figure 1.7. (a) Perspective view of hollandite-type A_x(Ti,M)$_8$O$_{16}$ from the [001] direction and (b) a double chain made up of edge-shared (Ti,M)O$_6$ octahedra.

1.1.3. Electron-Doped Titanium Oxides

Titanium ions in oxides usually show the +4 valence state (d^0 electronic configuration). However, compounds synthesized under strong reductive conditions (typically involving H_2 gas, graphite, and reduced oxygen partial pressure) contain low-valent Ti^{3+} (d^1) and Ti^{2+} (d^2) ions, often resulting in mixed-valent states. Such "reduced" titanium oxides exhibit various fascinating properties derived from the doped d electrons. For example, rocksalt-type TiO (ref 102), perovskite-type $SrTiO_{3-\delta}$ (refs 103 and 104), and spinel-type $LiTi_2O_4$ (refs 105 and 106) show superconducting transitions at ~1.0, ~0.5, and ~13.7 K, respectively. $SrTiO_{3-\delta}$ is the firstly discovered oxide superconductor. $LiTi_2O_4$ had been a transition metal superconductor with the highest T_c value until the discovery of high-temperature superconductivity in layered copper oxides.[107] A series of reduced binary titanium oxides, the so-called Magnéli phases, Ti_nO_{2n-1} ($n = 2–10$),[108–111] and TiO_2(B)-type Na_xTiO_2 (ref 112) undergo Peierls-like metal–insulator transitions induced by temperature, light, and pressure. The appearance of weak ferromagnetism at room temperature is suggested in hollandite-type $K_xTi_8O_{16}$.[113] Furthermore, $SrTiO_{3-\delta}$ exhibits much higher H_2/O_2 evolution activities under UV light than the oxygen-stoichiometric $SrTiO_3$ (i.e., negligible contents of Ti^{3+}), which are responsible for the prolonged lifetime of photogenerated electrons and the reinforced driving force for water oxidation.[114] Electron doping into titanium oxides is thus capable of not only providing unique electronic/magnetic properties but also improving some kind of catalytic activities.

1.2. Mixed-Anion Compounds

1.2.1. Interest in Mixed-Anion Compounds

Recent accelerating advances in mixed-anion compounds, which contain two or more anionic species in the solid state, arise from their expanding degrees of freedom in chemical compositions, local symmetry around cations, and related properties.[115–117] Such compounds are manifested as a new materials platform beyond the single anion for next-generation technologies. Figures 1.8 and 1.9 showcase basic concepts of mixed-anion compounds.[115]

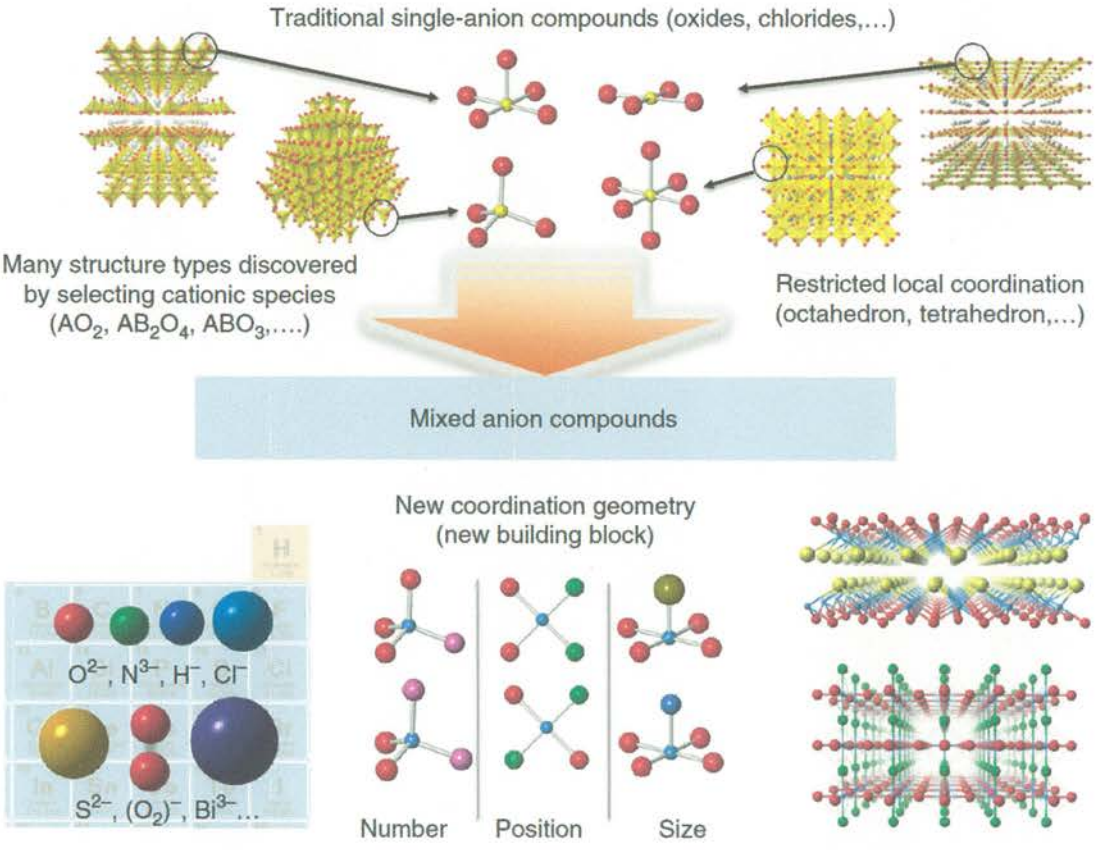

Figure 1.8. From oxides to mixed-anion compounds. Anion coordination and crystal structures of oxides (upper half) and mixed-anion compounds (lower half). Reprinted from ref 115 (open access).

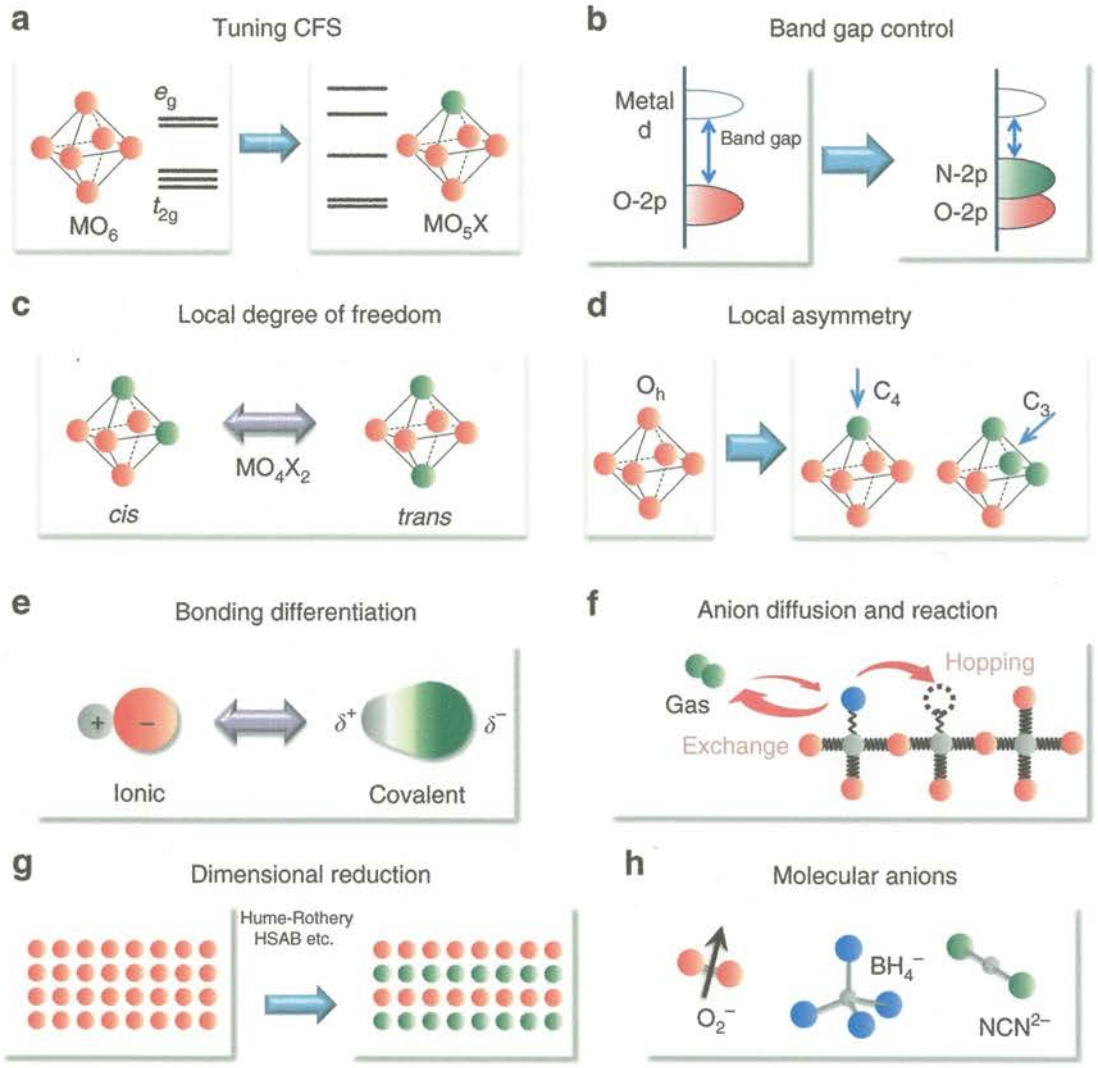

Figure 1.9. What mixed-anion compounds can do. (a) Tuning of crystal field splitting (CFS). (b) Band gap control. (c) Local degree of freedom. (d) Local asymmetry. (e) Bonding differentiation. (f) Anion diffusion and reaction. (g) Dimensional reduction. (h) Molecular anions. Reprinted from ref 115 (open access).

The perhaps most well-known mixed-anion compounds are oxide-anion-containing ones, including oxyhydrides (O^{2-}/H^-), oxynitrides (O^{2-}/N^{3-}), oxyhalides (O^{2-}/X; X = F^-, Cl^-, Br^-, or I^-), oxychalcogenides (O^{2-}/Ch; Ch = S^{2-}, Se^{2-}, or Te^{2-}), and oxypnictides (O^{2-}/Pn; Pn = P^{3-}, As^{3-}, Bi^{3-} or Sb^{3-}). Apart from the O^{2-} anion, however, compounds such as nitride-halides,[118,119] hydride-halides,[120,121] halide-chalcogenides,[122–124] hydride-chalcogenides,[125] phosphide-nitrides,[126] phosphide-tellurides,[127] and MXene-related materials (e.g., Y_2CF_2)[128,129] as well as containing molecular anions (e.g., OH^-, CO_3^{2-}, HCO_3^-, NO_3^-, SO_4^{2-}, PO_4^{3-}, HPO_3^{2-}, IO_3^-, SCN^-, BH_4^-, $(O_2)^{2-}$, and $(S_2)^{2-}$)[130–141] can also be recognized as the members of mixed-anion compounds.

The number of mixed-anion compounds containing the O^{2-} anion recorded in Inorganic Crystal Structure Database (ICSD)[142] is limited compared with common oxides: >50,000 for oxides and <3,000 for the sum of oxy-hydrides, -fluorides, -nitrides, -chalcogenides, and -pnictides (as of October 2017).[115,143] This fact clearly evidences that exploration and synthesis methods of mixed-anion compounds have not been established yet. The majority of the global atmosphere consists of oxygen (oxidative) and nitrogen (inert)—this is why many stable compounds exist in oxides on the earth. The difficulty in the synthesis of mixed-anion compounds is mainly caused by the different nature of anionic species. The most traditional synthesis method of ceramics is a simple "heat & beat" or "shake & bake" route, in which high-temperature firing (usually >1000 °C) of a mixture of metal oxide reagents in air atmosphere is included.[144] In this method, mixed-anion compounds are *not often* available even if reagents containing non-oxide anions are used, because of the loss of anions as gaseous products (e.g., H_2 and Cl_2) during the heating, as well as the formation of single-anion compounds with high stability (e.g., metal nitrides).[144]

1.2.2. Topochemical Reactions

Low-temperature topochemical reactions are an alternative approach to synthesizing mixed-anion compounds. Topochemical reactions lead to thermodynamically metastable phases, which are never obtained by standard high-temperature solid-state reactions, as a result of insertion/extraction and ion-exchange reactions with the crystal structure of parent phases maintained.[145] In particular, the following three examples are worthwhile to be noted. Al-Mamouri and co-workers demonstrated the synthesis of an oxyfluoride superconductor $Sr_2CuO_2F_{2+\delta}$ with $T_c = 46$ K via topochemical fluorination of Sr_2CuO_3 at 210 °C in flowing F_2/N_2 gas.[146] Kodenkandath and co-workers synthesized layered oxyhalides (CuX)$LaNb_2O_7$ (X = Cl and Br) by ion-exchange reactions between $RbLaNb_2O_7$ and CuX_2 at 325 °C.[147] Kobayashi and co-workers obtained perovskite oxyhydrides $BaTiO_{3-x}H_x$ by reacting $BaTiO_3$ and CaH_2 at 500–580 °C.[148] Crystal structures of compounds before and after topochemical reactions are compared in Figure 1.10. Besides the above, a number of mixed-anion compounds have been synthesized by low-temperature topochemical reactions.

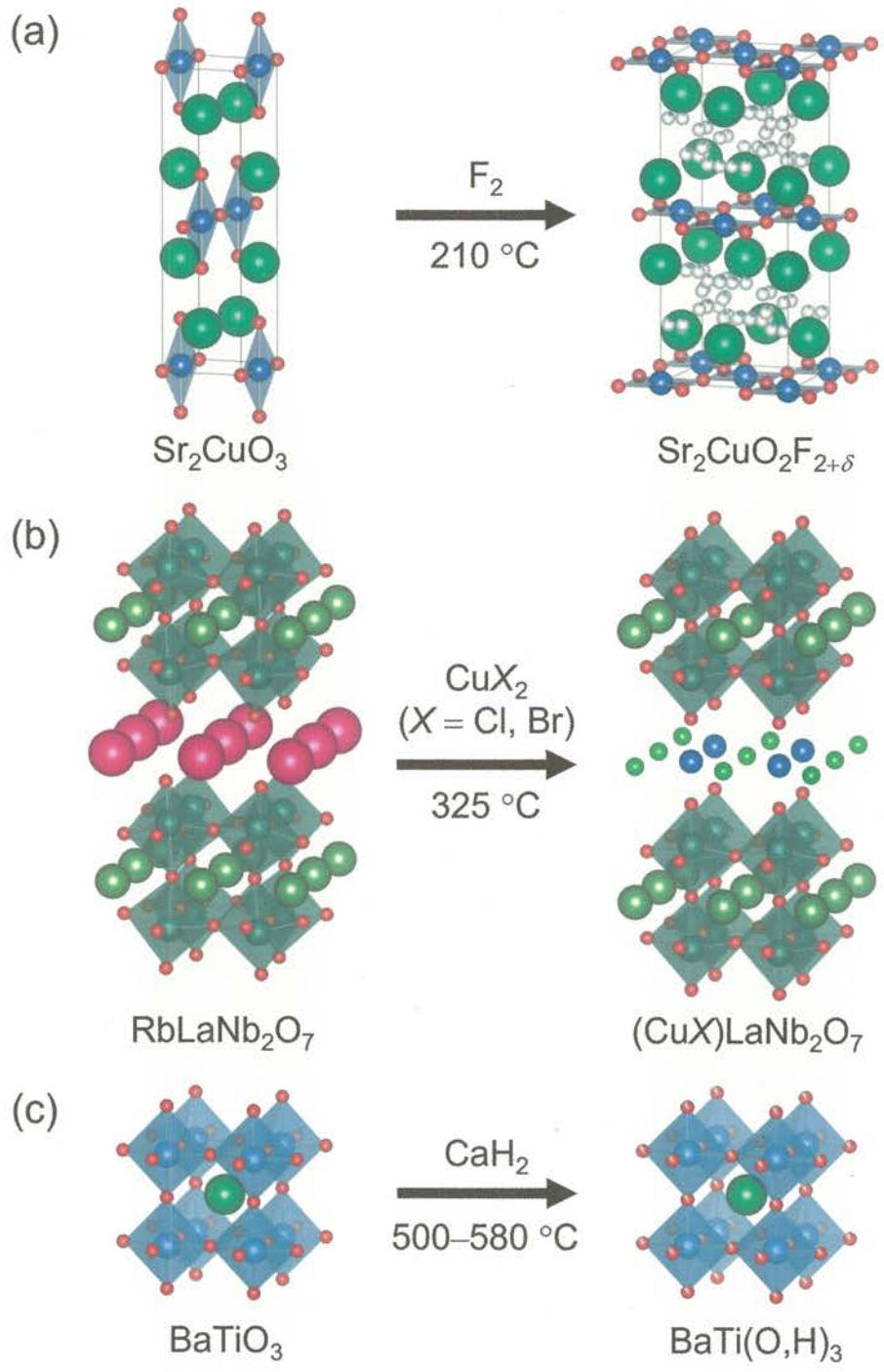

Figure 1.10. Three examples of topochemical reactions to obtain metastable mixed-anion compounds starting from stable oxide precursors: (a) from Sr_2CuO_3 to $Sr_2CuO_2F_{2+\delta}$, (b) from $RbLaNb_2O_7$ to $(CuX)LaNb_2O_7$ (X = Cl, Br), and (c) from $BaTiO_3$ to $BaTi(O,H)_3$.

1.2.3. Titanium-Based Mixed-Anion Compounds

Titanium-based compounds have been arduously pursued because of their appealing properties. Several examples are outlined below, underlining their respective properties.

Oxyhydrides. $BaTiO_{3-x}H_x$ catalyzes the formation of NH_3 in flowing H_2/N_2 gas at elevated temperatures (400 °C, 5 MPa).[149] $EuTiO_{3-x}H_x$ is a ferromagnetic metal below $T_c = 12$ K, at which an antiferromagnetic-to-ferromagnetic transition is observed.[150] $La_2Ti_2O_{7-x}H_x$ efficiently works as a photoanode for water splitting hydrogen evolution.[151]

Oxynitrides. $LaTiO_2N$ is capable of producing H_2 and O_2 from aqueous solutions containing sacrificial reagents under visible light.[152,153]

Oxysulfides. $Ln_2Ti_2S_2O_5$ (*Ln* = lanthanoids) is a visible-light-driven photocatalyst showing high activities for both water reduction and oxidation in the presence of sacrificial reagents.[154,155]

Oxyfluorides. Rb_2KTiOF_5 is a nonlinear optical material with a wide bandgap of 3.87 eV.[156] Mn^{4+}-doped $BaTiOF_4$ is a red-emitting phosphor and may find application in LED backlighting.[157] $Pb_2Ti_2O_{5.4}F_{1.2}$ shows a temperature-independent large dielectric constant,[158] and excellent visible-light-responsive photocatalytic activities for water splitting and CO_2 reduction.[159,160]

Clearly, anion mixing appears favorable for the formation of visible-light absorbing materials that have promise as photocatalysts. Incorporation of anions with lower electronegativity than that of O^{2-} (e.g., N^{3-} and S^{2-}) considerably raises the VBM position and thus reduces the bandgap energy without affecting the CBM position, as shown in Figure 1.11.[161,162] The visible-light response in the oxyfluoride $Pb_2Ti_2O_{5.4}F_{1.2}$ is an exceptional case, which is associated with strong interaction between the Pb 6s and O 2p orbitals arising from fluorine incorporation into the crystal lattice.[159,160]

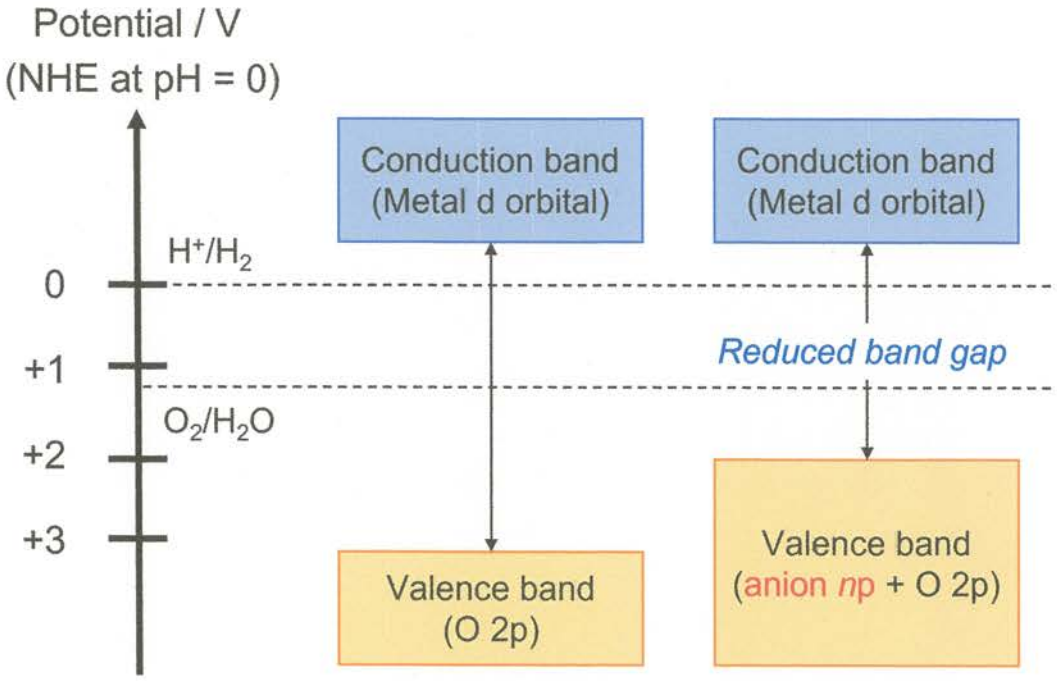

Figure 1.11. Schematic illustration of band gap narrowing via the incorporation of non-oxide anions. The broken lines represent the redox potentials for hydrogen and oxygen evolution reactions.

1.2.4. Oxyfluorides

Oxyfluorides, in which a metal center is coordinated by both O^{2-} and F^- anions, are considered as the most extensively studied class of mixed-anion compounds. Fluorine has the highest electronegativity among all elements, and the F^- anion in oxyfluorides is featured with (1) a lower ionic charge and (2) a similar ionic radius (1.33 Å for F^- vs 1.40 Å for O^{2-} in six-fold coordination[163]), with respect to the O^{2-} anion. These features often lead to interesting structural and physical properties unique to oxyfluorides.

Synthesis. Regarding the synthesis of oxyfluorides, a wide variety of methods have been developed—the details will be described in Chapter 4. Here, let the author deal with low-temperature fluorination reactions of oxide precursors using fluorinating agents that are one of the promising

approaches toward synthesizing novel oxyfluorides. Once a parent oxide is heated along with a fluorinating agent, reactions proceed in the different charge compensation manners as below:[164,165]

(1) one O^{2-} anion is replaced by one F^- anion with a *reduction* in the oxidation state of transition metals [e.g., $4RbLaNb^{5+}{}_2O_7 + C_2F_4 \rightarrow 4RbLaNb^{4.5+}{}_2O_6F + 2CO_2$ (ref 166), where C_2F_4 represents the monomer unit of polytetrafluoroethylene (PTFE)];

(2) one O^{2-} anion is replaced by two F^- anions with *no change* in the oxidation state of transition metals [e.g., $Sr_2Ti^{4+}O_4 + CuF_2 \rightarrow Sr_2Ti^{4+}O_3F_2 + CuO$ (ref 167)]; and

(3) insertion of F^- anions into vacant or interstitial sites with an *increase* in the oxidation state of transition metals [e.g., $LaSrMn^{3+}O_4 + 0.85F_2 \rightarrow LaSrMn^{4.7+}O_4F_{1.7}$ (ref 168)].

Despite being extensively used, the reaction mechanism of these reactions is poorly understood because the oxidation state of transition metals is sometimes maintained and sometimes altered upon fluorination, even if similar parent phases are employed: RP-type ruthenium oxides $Sr_2Ru^{4+}O_4$ and $Sr_3Ru^{4+}{}_2O_7$ yield $Sr_2Ru^{4+}O_3F_2$ (ref 169) and $Sr_3Ru^{5+}{}_2O_7F_2$ (ref 170), respectively.

Fluorine Occupation Patterns. Arrangements of O^{2-} and F^- anions in oxyfluorides range from order (site-selective occupation) to disorder (random distribution), arising from their comparable ionic sizes. This is in sharp contrast to oxyhalides containing larger halogens (X = Cl, Br, I), in which O^{2-}/X^--ordered low-dimensional structures are usually formed.[171–175] Most of the O^{2-}/F^--disordered structures are found in compounds with simple structures such as rocksalt-,[176,177] perovskite-,[178,179] and ReO_3-type,[180,181] all of which have only one anion site. On the other hand, more complex oxyfluorides with multiple anion sites can adopt the O^{2-}/F^--ordered structure. To give an example, RP-type layered oxyfluorides, such as K_2NbO_3F (ref 182), Sr_2MO_3F (M = Sc, Mn, Fe, Co, Ni),[183–187] and Ba_2MO_3F (M = Sc, In),[188] show the preferential occupation of the F^- anions at the apical sites.

Meanwhile, it has been reported that the degree of O^{2-}/F^{-} anion order in Sr_2FeO_3F (ref 185) and *RE*OF (*RE* = Y, La, Pr, Sm–Er)[189–191] is tuned by external stimuli such as pressure and temperature. Taking into account these facts, the O^{2-}/F^{-} arrangement in oxyfluorides seems to depend heavily on counter cation species (and the character of crystal structures).

In principle, it is practically impossible to distinguish between O^{2-} and F^{-} anions by diffraction experiments because of their similar scattering powers for both X-ray and neutron. For this reason, the structure analysis of oxyfluorides is often performed with constraints relevant to the crystallographic positions and occupancy factors of O^{2-} and F^{-} anions.[192–194] Recently, the presence of O^{2-}/F^{-} anion order in $Pb_2Ti_4O_9F_2$ was confirmed by considering bond valence sums (BVSs) and charge density distribution visualized by the maximum entropy method (MEM), taking into account the different bonding nature between metal–oxygen (*M*–O) and metal–fluorine (*M*–F) bonds.[195,196]

1.3. Crystal Growth Techniques

1.3.1. Preface[197]

For researchers working on solid-state chemistry and physics, high-quality single crystals of target materials are highly desirable to gain deeper insight into their crystal structures and physical properties. In a single crystal without any imperfections, constituent atoms arrange in an orderly and repetitive fashion, so that single crystals bring out the best performance in materials. Various physical property measurements such as electrical resistivity are performed on single crystals with more accuracy than polycrystalline samples composed of a huge number of crystals. This is because the latter has randomly orientated crystallites and grain boundaries, both of which are harmful to studies on intrinsic properties. In addition, high-quality single crystals enable us to perform structure analysis by single-crystal X-ray diffraction, which is the most conclusive way for the structure determination of crystalline compounds. Although many compounds can be obtained as single crystals, the best growth method strongly depends on properties of each compound (melting point, congruent or incongruent melting, solubility, and volatility, just to name a few). Hence, the choice of growth methods is of capital importance.

Crystal growth techniques of materials are classified into the following three categories: solid-, liquid-, and gas-phase reactions. From the viewpoint of growing sizable and well-developed crystals, the liquid-phase reaction is more suitable than the others because of the ease of atomic reconstructions. Now, several commonly-used growth methods will be briefly reviewed in the subsequent subsections.

1.3.2. Melt Growth and Solution Growth Methods[197–199]

Crystal growth techniques through liquid phases fall into two classifications: (1) melt growth and (2) solution growth methods (Figure 1.12). For the former (1), crystals are obtained by cooling their

own melt, employing supercooling as a driving force of crystal growth. The Bridgman, Czochralski, Vemeuil, and optical floating zone (OFZ) methods are typical examples of this class. These methods can grow large-sized crystals in a short period, but cannot be applied to crystal growth of compounds that show incongruent melting (i.e., decomposition into another solid and a liquid), phase transformation before melting, and high volatility.

For the latter (2), crystal growth is driven by supersaturation triggered by slow cooling and/or evaporation of solvents. The solution growth method is further divided into three categories based on the kinds of solvents: (i) the aqueous solution method–water; (ii) the hydrothermal method–high-temperature/pressure water; and (iii) the flux method–molten inorganic compounds (e.g., oxides and halides). In all cases, solvents are required to adequately dissolve solutes under specific experimental conditions. These methods can be employed with simpler apparatus and much lower operating temperatures than those of the melt growth methods. However, the crystal growths generally result in relatively small crystals despite a fairly long period.

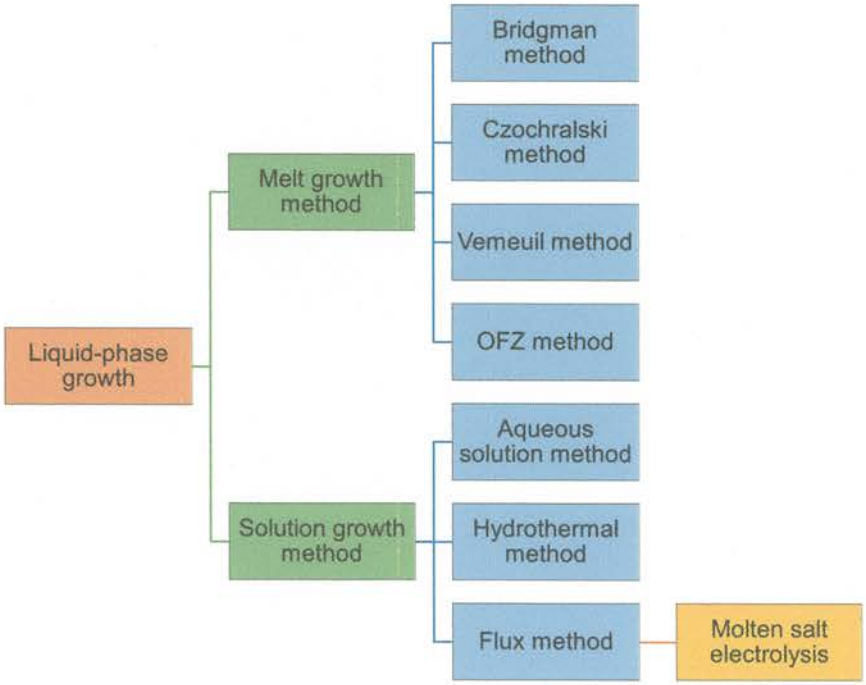

Figure 1.12. Overview of crystal growth techniques through liquid phases.

1.3.3. Molten Salt Electrolysis

Molten salt electrolysis is another technique to grow single crystals, which belongs to the class of the solution growth method. This technique bears relation to the flux method to some extent—but includes redox-driven electrocrystallization by applying an electric current or voltage to the system.[197,200,201] In modern society, the significant industrial importance of molten salt electrolysis meets the productions of aluminum and sodium metals. The metallic aluminum is obtained via electrolysis of a molten mixture consisting of Al_2O_3 and cryolite Na_3AlF_6 (the so-called Hall–Héroult process), where Na_3AlF_6 works as a flux to lower the melting point of Al_2O_3 from ~2000 °C to ~1000 °C.[202] The metallic sodium is produced by electrolyzing molten NaCl to which $CaCl_2$ is added (the so-called Downs process), where the electrolysis is performed at about 600 °C.[203]

Regarding the growth of oxide crystals by molten salt electrolysis, early works trace back over 160 years. In 1860, Scheibler obtained single crystals of tungsten bronzes Na_xWO_3 by electrolytic reduction of polytungstate melts.[204] Afterward, numerous compounds with wide varieties of constituent elements and structural types have been synthesized by this technique.[205–235] The thus-obtained crystals sometimes exhibit new, unexpected structures as well as intriguing properties, such as superconductivity. For titanium oxides, examples include spinel-type $LiTi_2O_4$ (ref 236), pseudo-brookite-type $CaTi_2O_4$ (ref 237), and hollandite-type $Cs_xTi_8O_{16}$ (ref 238).

It is worth noting that, in most of the previous studies, crystal growth was performed under constant-current conditions. One can assume that the constant-voltage mode may be advantageous than the constant-current mode because the former leads to a more stable driving force of crystal growth. A few researchers performed constant-voltage growth; however, little mention was made of how applied voltage values affect the resulting phases and their chemical compositions, opening up opportunities for further detailed investigations (see also: Chapter 2, Introduction). In addition, the author emphasizes here that the crystal growth of oxyfluorides by molten salt electrolysis had not

been reported, irrespective of constant-current and -voltage conditions (see also: Chapter 4, Introduction).

In a typical experiment, starting materials containing both solute and flux components are packed into a crucible as a reaction vessel. The reactants are heated above the melting point of the flux in an electric furnace, and two or three inert electrodes (typically platinum wires) are inserted into the molten mixture. The number of electrodes is based on whether the electrolysis is performed employing two- or three-electrode configurations. Crystals will grow on the surface(s) of the cathode and/or anode as a result of the electrolysis of the molten mixture. The duration time of the electrolysis greatly depends on the literature; it ranges from ~30 min to several tens of hours. Compared with other crystal growth techniques, molten salt electrolysis possesses the following advantages:[197,200]

(1) the technique involves oxidation or reduction of metal ions, often giving rise to compounds with unusual valency (i.e., hole or electron doping);
(2) it is an isothermal process—temperature gradients are not needed for crystal growth;
(3) sizeable crystals sometimes grow within a relatively short period; and
(4) the crystal growth can be controlled by tuning electrochemical parameters.

Besides the advantages mentioned above, there is a possible disadvantage; crystals are obtained with a low yield and occasionally in an aggregated form because of a limited number of nucleation sites (i.e., electrode surfaces). Sometimes this feature hinders functional/physical research that needs a large number of samples or well-developed crystals. Nevertheless, molten salt electrolysis is still very useful for growing single crystals.

1.4. Objectives of This Dissertation

As overviewed in **1.1** and **1.2**, properties of both titanium oxides and oxyfluorides are largely composition- and structure-dependent, which means, in turn, the precise manipulation of target materials is important. Unlike tetravalent titanium oxides that we usually encounter, electron-doped (reduced) titanium oxides are attractive because of their interesting electronic/magnetic properties and catalytic activities arising from the d electrons doped into the crystal lattice, see **1.1.3**. Meanwhile, electron-doped titanium oxyfluorides have never been exploited well. Sizable single crystals of these compounds are highly craved because various characterizations are feasible on single crystals with more accuracy than polycrystalline samples, see **1.3.1**. However, a possible problem emerges in achieving the crystal growth, mainly originating from the difficulty in the reduction of stable tetravalent titanium ions. To overcome this problem, the author had his eyes on molten salt electrolysis in which crystal growth involving electrochemical redox reactions is included. This technique is indeed one of the effective methods in yielding sizable single crystals of electron-doped compounds, see **1.3.3**. Additionally, crystals with finely tuned compositions and structures may be obtained by altering both adding metal species and electrochemical parameters.

Electrochemical reactions represent the basic principle of batteries so that studies aimed at energy applications have been arduously performed. On the other hand, it bears mentioning that this study features a positive utilization of electrochemical reactions toward material synthesis and crystal growth. This dissertation is therefore of significance in presenting the utility of the electrochemical technique for the research on solid-state chemistry and physics. Such a study is relatively rare—so the author is convinced that this dissertation will have a major impact on the community of inorganic materials chemistry.

Of specific concerns in this dissertation are the following three points.

(1) To grow sizable single crystals of electron-doped titanium oxides employing high-temperature molten salt electrolysis with constantly applied voltages.

(2) To apply this technique to crystal growth of multiple-anion-containing compounds, in particular titanium oxyfluorides.

(3) To investigate structural, electronic, magnetic, and optical properties, and photocatalytic activities.

1.5. Outline

This dissertation consists of the following chapters. Chapter 1 describes a brief overview of titanium oxides, mixed-anion compounds, and crystal growth techniques to build bridges between the subsequent chapters. The objectives of the dissertation are also mentioned in this chapter.

Chapter 2 demonstrates the crystal growth of hollandite-type $Cs_xTi_8O_{16}$ employing high-temperature molten salt electrolysis with constantly applied voltages. The structural and electronic properties of the resultant crystals are investigated.

Chapter 3 deals with the crystal growth of titanium oxides containing lithium, sodium, and potassium. Crystals of $K_xTi_8O_{16}$ (hollandite-type), $Na_{2+x}Ti_6O_{13}$, and $Li_{2+x}Ti_3O_7$ (ramsdellite-type) are successfully grown. The crystal structure–alkali species relationships are systematically discussed.

In Chapter 4, the crystal growth of titanium oxyfluorides is attempted. Rocksalt-type $Li_2Ti(O,F)_3$ (F/Ti ~ 0.15) crystals are obtained by precisely tuning the applied voltage. The structural, magnetic, and optical properties, and photocatalytic H_2 evolution activities of the resultant crystals are studied.

In Chapter 5, attempts to grow crystals of F-doped $CaTiO_3$ lead to Na/Mo/F-codoped $CaTiO_3$ crystals. The crystals are obtained only with a narrow range of applied voltages.

Finally, the works are concluded in Chapter 6, and suggestions for future works are given.

With some modifications, Chapters 2, 3, and 4 are written on the basis of the author's own publications—see the section on "Peer-Reviewed Original Papers." According to the policy on theses and dissertations of American Chemical Society (ACS) and Royal Society of Chemistry (RSC), authors may reuse all or part of the submitted, accepted, or published work in a thesis or dissertation that the author writes and is required to submit to satisfy the criteria of degree-granting institutions.[239,240] Statements of the proper permission are described on the last page of each chapter. Chapter 5 is an unpublished material, but will be submitted to be considered for publication in the future.

References

(1) Oil and Colour Chemists' Association, Australia, Titanium Dioxide Pigments. *Surface Coatings*, 1st ed.; Springer: Dordrecht, 1983; Vol. 1, pp 305–312.

(2) Daghrir, R.; Drogui, P.; Robert, D. Modified TiO_2 For Environmental Photocatalytic Applications: A Review. *Ind. Eng. Chem. Res.* **2013**, *52*, 3581–3599.

(3) Rahimi, N.; Pax, R. A.; Gray, E. M. Review of Functional Titanium Oxides. I: TiO_2 and Its Modifications. *Prog. Solid State Chem.* **2016**, *44*, 86–105.

(4) Haider, A. J.; Jameel, Z. N.; Al-Hussaini, I. H. M. Review on: Titanium Dioxide Applications. *Energy Procedia* **2019**, *157*, 17–29.

(5) Middlemas, S.; Fang, Z. Z.; Fan, P. A New Method for Production of Titanium Dioxide Pigment. *Hydrometallurgy* **2013**, *131–132*, 107–113.

(6) Jesús Gázquez, M.; Bolívar, J. P.; Garcia-Tenorio, R.; Vaca, F. A Review of the Production Cycle of Titanium Dioxide Pigment. *Mater. Sci. Appl.* **2014**, *5*, 441–458.

(7) Katayama, M. Surface Treatment of TiO_2 and Its Function. *J. Surf. Finish. Soc. Jpn.* **2019**, *70*, 494–499.

(8) Free, M. L. A Brief Introduction to Production of Titanium Dioxide and Titanium Tetrachloride. In *Extractive Metallurgy of Titanium*, 1st ed.; Fang, Z. Z., Froes, F. H., Zhang, Y., Eds.; Elsevier: Amsterdam, 2020; pp 13–18.

(9) Momma, K.; Izumi, F. *VESTA 3* for Three-Dimensional Visualization of Crystal, Volumetric and Morphology Data. *J. Appl. Crystallogr.* **2011**, *44*, 1272–1276.

(10) Cromer, D. T.; Herrington, K. The Structures of Anatase and Rutile. *J. Am. Chem. Soc.* **1955**, *77*, 4708–4709.

(11) Baur, W. H. Über die Verfeinerung der Kristallstrukturbestimmung einiger Vertreter des Rutiltyps: TiO_2, SnO_2, GeO_2 und MgF_2. *Acta Crystallogr.* **1956**, *9*, 515–520.

(12) Baur, W. H. Atomabstände und Bindungswinkel im Brookit, TiO_2. *Acta Crystallogr.* **1961**, *14*, 214–216.

(13) Feist, T. P.; Davies, P. K. The Soft Chemical Synthesis of TiO_2(B) from Layered Titanates. *J.*

Solid State Chem. **1992,** *101,* 275–295.

(14)Filatov, S.; Bendeliani, N.; Albert, B.; Kopf, J.; Dyuzheva, T.; Lityagina, L. Crystalline Structure of the TiO_2 II High-Pressure Phase at 293 223, and 133 K According to Single-Crystal X-ray Diffraction Data. *Dokl. Phys.* **2007,** *52,* 195–199.

(15)Latroche, M.; Brohan, L.; Marchand, R.; Tournoux, M. New Hollandite Oxides: TiO_2(H) and $K_{0.06}TiO_2$. *J. Solid State Chem.* **1989,** *81,* 78–82.

(16)Akimoto, J.; Gotoh, Y.; Oosawa, Y.; Nonose, N.; Kumagai, T.; Aoki, K.; Takei, H. Topotactic Oxidation of Ramsdellite-Type $Li_{0.5}TiO_2$, a New Polymorph of Titanium Dioxide: TiO_2(R). *J. Solid State Chem.* **1994,** *113,* 27–36.

(17)Swamy, V.; Dubrovinsky, L. S.; Dubrovinskaia, N. A.; Langenhorst, F.; Simionovici, A. S.; Drakopoulos, M.; Dmitriev, V.; Weber, H.-P. Size Effects on the Structure and Phase Transition Behavior of Baddeleyite TiO_2. *Solid State Commun.* **2005,** *134,* 541–546.

(18)Sang, L.; Zhao, Y.; Burda, C. TiO_2 Nanoparticles as Functional Building Blocks. *Chem. Rev.* **2014,** *114,* 9283–9318.

(19)Lee, S.-S.; Byeon, S.-H. Structural and Morphological Behavior of TiO_2 Rutile Obtained by Hydrolysis Reaction of $Na_2Ti_3O_7$. *Bull. Korean Chem. Soc.* **2004,** *25,* 1051–1054.

(20)Takahashi, Y.; Kijima, N.; Akimoto, J. Synthesis, Structural Change upon Heating, and Electronic Structure of Ramsdellite-Type TiO_2. *Chem. Mater.* **2006,** *18,* 748–752.

(21)Murata, H.; Taniguchi, T.; Tanaka, I. First-Principles Calculations of High-Pressure Phase Transition of TiO_2 during Decompression: From Baddeleyite-Type TiO_2 to α-PbO_2-Type TiO_2. *J. Appl. Phys.* **2016,** *120,* 142108.

(22)Buckeridge, J.; Butler, K. T.; Catlow, C. R. A.; Logsdail, A. J.; Scanlon, D. O.; Shevlin, S. A.; Woodley, S. M.; Sokol, A. A.; Walsh, A. Polymorph Engineering of TiO_2: Demonstrating How Absolute Reference Potentials Are Determined by Local Coordination. *Chem. Mater.* **2015,** *27,* 3844–3851.

(23)Kato, S.; Mashio, F. Titanium Dioxide-Photocatalyzed Liquid Phase Oxidation of Tetralin. *J. Soc. Chem. Ind. Jpn.* **1964,** *67,* 1136–1140.

(24)Fujishima, A.; Honda, K. Electrochemical Photolysis of Water at a Semiconductor Electrode. *Nature* **1972,** *238,* 37–38.

(25) Yamaguti, K.; Sato, S. Photolysis of Water over Pt/TiO_2 Catalysts. *Nippon Kagaku Kaishi* **1984,** *2,* 258–263.

(26) Bulatov, A. V.; Khidekel, M. L. Decomposition of Water under the Effect of UV Irradiation in the Presence of Platinized Titanium Dioxide. *Izv. Akad. Nauk SSSR, Ser. Khim.* **1976,** *8,* 1902–1903.

(27) Chen, X.; Shen, S. Guo, L.; Mao, S. S. Semiconductor-based Photocatalytic Hydrogen Generation. *Chem. Rev.* **2010,** *110,* 6503–6570.

(28) Scanlon, D. O.; Dunnill, C. W.; Buckeridge, J.; Shevlin, S. A.; Logsdail, A. J.; Woodley, S. M.; Catlow, C. R. A.; Powell, M. J.; Palgrave, R. G.; Parkin, I. P.; Watson, G. W.; Keal, T. W.; Sherwood, P.; Walsh, A.; Sokol, A. A. Band Alignment of Rutile and Anatase TiO_2. *Nat. Mater.* **2013,** *12,* 798–801.

(29) Zhang, J.; Zhou, P.; Liu, J.; Yu, J. New Understanding of the Difference of Photocatalytic Activity among Anatase, Rutile and Brookite TiO_2. *Phys. Chem. Chem. Phys.* **2014,** *16,* 20382–20386.

(30) Luttrell, T.; Halpegamage, S.; Tao, J.; Kramer, A.; Sutter, E.; Batzill, M. Why is Anatase a Better Photocatalyst than Rutile? - Model Studies on Epitaxial TiO_2 Films. *Sci. Rep.* **2014,** *4,* 4043.

(31) Armstrong, A.; Armstrong, G.; Canales, J.; García, R.; Bruce, P. Lithium-Ion Intercalation into TiO_2-B Nanowires. *Adv. Mater.* **2005,** *17,* 862–865.

(32) Subramanian, V.; Karki, A.; Gnanasekar, K.; Eddy, F. P.; Rambabu, B. Nanocrystalline TiO_2 (Anatase) for Li-Ion Batteries. *J. Power Sources* **2006,** *159,* 186–192.

(33) Pfanzelt, M.; Kubiak, P.; Fleischhammer, M.; Wohlfahrt-Mehrens, M. TiO_2 Rutile—An Alternative Anode Material for Safe Lithium-Ion Batteries. *J. Power Sources* **2011,** *196,* 6815–6821.

(34) Gover, R. K. B.; Tolchard, J. R.; Tukamoto, H.; Murai, T.; Irvine, J. T. S. Investigation of Ramsdellite Titanates as Possible New Negative Electrode Materials for Li Batteries. *J. Electrochem. Soc.* **1999,** *146,* 4348–4353.

(35) Kuhn, A.; Amandi, R.; García-Alvarado, F. Electrochemical Lithium Insertion in TiO_2 with the Ramsdellite Structure. *J. Power Sources* **2001,** *92,* 221–227.

(36) Sakao, M.; Kijima, N.; Akimoto, J.; Okutani, T. Synthesis, Crystal Structure, and Electrochemical Properties of Hollandite-Type $K_{0.008}TiO_2$. *Solid State Ionics* **2012,** *225,* 502–505.

(37) Sakao, M.; Kijima, N.; Akimoto, J.; Okutani, T. Lithium Insertion and Extraction Properties of Hollandite-Type K_xTiO_2 with Different K Content in the Tunnel Space. *Solid State Ionics* **2013**, *243*, 22–29.

(38) Su, C. Y.; Otsuka, Y.; Huang, C. Y.; Hennings, D. F.; Pithan, C.; Shiao, F. T.; Waser, R. Grain Growth and Crystallinity of Ultrafine Barium Titanate Particles Prepared by Various Routes. *Ceram. Int.* **2013**, *39*, 6673–6680.

(39) Jiang, B.; Iocozzia, J.; Zhao, L.; Zhang, H.; Harn, Y.-W.; Chena, Y.; Lin, Z. Barium Titanate at the Nanoscale: Controlled Synthesis and Dielectric and Ferroelectric Properties. *Chem. Soc. Rev.* **2019**, *48*, 1194–1228.

(40) Charoonsuk, T.; Sriphan, S.; Nawanil, C.; Chanlek, N.; Vittayakorn, W.; Vittayakorn, N. Tetragonal $BaTiO_3$ Nanowires: A Template-Free Salt-Flux-Assisted Synthesis and Its Piezoelectric Response Based on Mechanical Energy Harvesting. *J. Mater. Chem. C* **2019**, *7*, 8277–8286.

(41) Sakabe, Y.; Minai, K.; Wakino, K. High-Dielectric Constant Ceramics for Base Metal Monolithic Capacitors. *Jpn. J. Appl. Phys.* **1981**, *20*, 147–150.

(42) Tiwari, B.; Babu, T.; Choudhary, R. N. P. Piezoelectric Lead Zirconate Titanate as an Energy Material: A Review Study. *Mater. Today: Proc.* **2021**, *43*, 407–412.

(43) Sun, X.; Radovanovic, P. V.; Cui, B. Advances in Spinel $Li_4Ti_5O_{12}$ Anode Materials for Lithium-Ion Batteries. *New J. Chem.* **2015**, *39*, 38–63.

(44) Inaguma, Y. A Review of Recent Research on Perovskite-Type Lithium Ion-Conducting Oxides. *Nihon Kessho Gakkaishi* **2016**, *58*, 62–72.

(45) Bramwell, S. T.; Gingras, M. J. P. Spin Ice State in Frustrated Magnetic Pyrochlore Materials. *Science* **2001**, *294*, 1495–1501.

(46) Snyder, J.; Slusky, J. S.; Cava, R. J.; Schiffer, P. Dirty Spin Ice: The Effect of Dilution on Spin Freezing in $Dy_2Ti_2O_7$. *Phys. Rev. B: Condens. Matter Mater. Phys.* **2002**, *66*, 064432.

(47) Takata, T.; Furumi, Y.; Shinohara, K.; Tanaka, A.; Hara, M.; Kondo, J. N.; Domen, K. Photocatalytic Decomposition of Water on Spontaneously Hydrated Layered Perovskites. *Chem. Mater.* **1997**, *9*, 1063–1064.

(48) Kudo, A.; Sakata, T. Luminescent Properties of Nondoped and Rare Earth Metal Ion-Doped

$K_2La_2Ti_3O_{10}$ with Layered Perovskite Structures: Importance of the Hole Trap Process. *J. Phys. Chem.* **1995**, *99*, 15963–15967.

(49) Taniguchi, T.; Murakami, T.; Funatsu, A.; Hatakeyama, K.; Koinuma, M.; Matsumoto, Y. Reversibly Tunable Upconversion Luminescence by Host–Guest Chemistry. *Inorg. Chem.* **2014**, *53*, 9151–9155.

(50) Ruddlesden, S. N.; Popper, P. New Compounds of the K_2NiF_4 Type. *Acta Crystallogr.* **1957**, *10*, 538–539.

(51) Ruddlesden, S. N.; Popper, P. The Compound $Sr_3Ti_2O_7$ and Its Structure. *Acta Crystallogr.* **1958**, *11*, 54–55.

(52) Uma, S.; Raju, A. R.; Gopalakrishnan, J. Bridging the Ruddlesden–Popper and the Dion–Jacobson Series of Layered Perovskites: Synthesis of Layered Oxides, $A_{2-x}La_2Ti_{3-x}Nb_xO_{10}$ (A = K, Rb), Exhibiting Ion Exchange. *J. Mater. Chem.* **1993**, *3*, 709–713.

(53) Dion, M.; Ganne, M.; Tournoux M. Nouvelles familles de phases $M^IM^{II}_2Nb_3O_{10}$ a feuillets "perovskites." *Mater. Res. Bull.* **1981**, *16*, 1429–1435.

(54) Jacobson, A. J.; Johnson, J. W.; Lewandowski, J. T. Interlayer Chemistry between Thick Transition-Metal Oxide Layers: Synthesis and Intercalation Reactions of $K[Ca_2Na_{n-3}Nb_nO_{3n+1}]$ ($3 \le n \le 7$). *Inorg. Chem.* **1985**, *24*, 3727–3729.

(55) Aurivillius, B. Mixed Bismuth Oxides with Layer Lattices. I. The Structure Type of $CaNb_2Bi_2O_9$. *Ark. Kemi* **1949**, *1*, 463–480.

(56) Aurivillius, B. Mixed Bismuth Oxides with Layer Lattices. II. Structure of $Bi_4Ti_3O_{12}$. *Ark. Kemi* **1949**, *1*, 499–512.

(57) Aurivillius, B. Mixed Oxides with Layer Lattices. III. Structure of $BaBi_4Ti_4O_{15}$. *Ark. Kemi* **1950**, *2*, 519–527.

(58) Gopalakrishnan, J.; Bhat, V. $A_2Ln_2Ti_3O_{10}$ (A = K or Rb; Ln = La or Rare Earth): A New Series of Layered Perovskites Exhibiting Ion Exchange. *Inorg. Chem.* **1987**, *26*, 4299–4301.

(59) Toda, K.; Watanabe, J.; Sato, M. Crystal Structure Determination of Ion-Exchangeable Layered Perovskite Compounds, $K_2La_2Ti_3O_{10}$ and $Li_2La_2Ti_3O_{10}$. *Mater. Res. Bull.* **1996**, *31*, 1427–1435.

(60) Toda, K.; Kurita, S.; Sato, M.; New Layered Perovskite Compounds, $LiLaTiO_4$ and $LiEuTiO_4$. *J. Ceram. Soc. Jpn.* **1996**, *104*, 140–142.

(61) Hyeon, K.-A.; Byeon, S.-H. Synthesis and Structure of New Layered Oxides, $M^{II}La_2Ti_3O_{10}$ (M = Co, Cu, and Zn). *Chem. Mater.* **1999**, *11*, 352–357.

(62) Schaak, R. E.; Mallouk, T. E. K*Ln*TiO_4 (*Ln* = La, Nd, Sm, Eu, Gd, Dy): A New Series of Ruddlesden–Popper Phases Synthesized by Ion-Exchange of H*Ln*TiO_4. *J. Solid State Chem.* **2001**, *161*, 225–232.

(63) Schaak, R. E.; Mallouk, T. E. Perovskites by Design: A Toolbox of Solid-State Reactions. *Chem. Mater.* **2002**, *14*, 1455–1471.

(64) Nishimoto, S.; Matsuda, M.; Miyake, M. Novel Protonated and Hydrated n = 1 Ruddlesden–Popper Phases, $H_xNa_{1-x}LaTiO_4 \cdot yH_2O$, Formed by Ion-Exchange/Intercalation Reaction. *J. Solid State Chem.* **2005**, *178*, 811–818.

(65) Gönen, Z. S.; Paluchowski, D.; Zavalij, P.; Eichhorn, B. W.; Gopalakrishnan, J. Reversible Cation/Anion Extraction from $K_2La_2Ti_3O_{10}$: Formation of New Layered Titanates, $KLa_2Ti_3O_{9.5}$ and $La_2Ti_3O_9$. *Inorg. Chem.* **2006**, *45*, 8736–8742.

(66) Neiner, D.; Spinu, L.; Golub, V.; Wiley, J. B. Ferromagnetism in Topochemically Prepared Layered Perovskite $Li_{0.3}Ni_{0.85}La_2Ti_3O_{10}$. *Chem. Mater.* **2006**, *18*, 518–524.

(67) Yip, T. W. S.; Cussen, E. J.; MacLaren, D. A. Synthesis of $H_xLi_{1-x}LaTiO_4$ from Quantitative Solid-State Reactions at Room Temperature. *Chem. Commun.* **2010**, *46*, 698–700.

(68) Sanjaya Ranmohotti, K. G.; Josepha, E.; Choi, J.; Zhang, J.; Wiley, J. B. Topochemical Manipulation of Perovskites: Low-Temperature Reaction Strategies for Directing Structure and Properties. *Adv. Mater.* **2011**, *23*, 442–460.

(69) Gupta, A. S.; Akamatsu, H.; Strayer, M. E.; Lei, S.; Kuge, T.; Fujita, K.; Cruz, C. d.; Togo, A.; Tanaka, I.; Tanaka, K.; Mallouk, T. E.; Gopalan, V. Improper Inversion Symmetry Breaking and Piezoelectricity through Oxygen Octahedral Rotations in Layered Perovskite Family, Li*R*TiO_4 (*R* = Rare Earths). *Adv. Electron. Mater.* **2016**, *2*, 1500196.

(70) Gustin, L.; Hosaka, Y.; Tassel, C.; Aharen, T.; Shimakawa, Y.; Kageyama, H.; Wiley, J. B. From Tetrahedral to Octahedral Iron Coordination: Layer Compression in Topochemically Prepared $FeLa_2Ti_3O_{10}$. *Inorg. Chem.* **2016**, *55*, 11529–11537.

(71) Uppuluri, R.; Sen Gupta, A.; Rosas, A. S.; Mallouk, T. E. Soft Chemistry of Ion-Exchangeable Layered Metal Oxides. *Chem. Soc. Rev.* **2018**, *47*, 2401–2430.

(72) Schaak, R. E.; Mallouk, T. E. Topochemical Synthesis of Three-Dimensional Perovskites from Lamellar Precursors. *J. Am. Chem. Soc.* **2000**, *122*, 2798–2803.

(73) Hong, Y.-S.; Kim, K. New n = 3 Dion-Jacobson Phases $NaLn_2Ti_2NbO_{10}\cdot xH_2O$ (Ln = La, Pr, Nd, Sm). *Mater. Res. Bull.* **2001**, *36*, 1325–1334.

(74) Hong, Y.-S.; Han, C.-H.; Kim, K. Structural Characterization of New Layered Perovskites $MLa_2Ti_2TaO_{10}$ (M = Cs, Rb) and $NaLa_2Ti_2TaO_{10}\cdot xH_2O$ (x = 2, 0.9, 0). *J. Solid State Chem.* **2001**, *158*, 290–298.

(75) Wang, T.; Henderson, C. N.; Draskovic, T. I. Mallouk, T. E. Synthesis, Exfoliation, and Electronic/Protonic Conductivity of the Dion–Jacobson Phase Layer Perovskite $HLa_2Ti_2TaO_{10}$. *Chem. Mater.* **2014**, *26*, 898–906.

(76) Gopalakrishnan, J.; Sivakumar, T.; Ramesha, K.; Thangadurai, V.; Subbanna, G. N. Transformations of Ruddlesden–Popper Oxides to New Layered Perovskite Oxides by Metathesis Reactions. *J. Am. Chem. Soc.* **2000**, *122*, 6237–6241.

(77) Sivakumar, T.; Seshadri, R.; Gopalakrishnan, J. Bridging the Ruddlesden–Popper and the Aurivillius Phases: Synthesis and Structure of a Novel Series of Layered Perovskite Oxides, $(BiO)LnTiO_4$ (Ln = La, Nd, Sm). *J. Am. Chem. Soc.* **2001**, *123*, 11496–11497.

(78) Akimoto, J. Syntheses and Crystal Structures of the Compounds in the Na–Ti–O System. *Nihon Kessho Gakkaishi* **1991**, *33*, 67–72.

(79) Andersson, S.; Wadsley, A. D. The Crystal Structure of $Na_2Ti_3O_7$. *Acta Crystallogr.* **1961**, *14*, 1245–1249.

(80) Dion, M.; Piffard, Y.; Tournoux, M. The Tetratitanates $M_2Ti_4O_9$ (M = Li, Na, K, Rb, Cs, Tl, Ag). *J. Inorg. Nucl. Chem.* **1978**, *40*, 917–918.

(81) Andersson, S.; Wadsley, A. D. The Structures of $Na_2Ti_6O_{13}$ and $Rb_2Ti_6O_{13}$ and the Alkali Metal Titanates. *Acta Crystallogr.* **1962**, *15*, 194–201.

(82) Wadsley, A. D.; Mumme, W. G. The Crystal Structure of $Na_2Ti_7O_{15}$, an Ordered Intergrowth of $Na_2Ti_6O_{13}$ and '$Na_2Ti_8O_{17}$'. *Acta Crystallogr., Sect. B: Struct. Crystallogr. Cryst. Chem.* **1968**, *24*, 392–396.

(83) Watanabe, M.; Bando, Y.; Tsutsumi, M. A New Member of Sodium Titanates, $Na_2Ti_9O_{19}$. *J. Solid State Chem.* **1979**, *28*, 397–399.

(84) Chiba, K.; Kijima, N.; Takahashi, Y.; Idemoto, Y.; Akimoto, J. Synthesis, Structure, and Electrochemical Li-Ion Intercalation Properties of $Li_2Ti_3O_7$ with $Na_2Ti_3O_7$-Type Layered Structure. *Solid State Ionics* **2008,** *178,* 1725–1730.

(85) Kataoka, K.; Kijima, N.; Akimoto, J. Ion-Exchange Synthesis, Crystal Structure, and Physical Properties of Hydrogen Titanium Oxide $H_2Ti_3O_7$. *Inorg. Chem.* **2013,** *52,* 13861–13864.

(86) Kataoka, K.; Awaka, J.; Kijima, N.; Hayakawa, H.; Ohshima, K.; Akimoto, J. Ion-Exchange Synthesis, Crystal Structure, and Electrochemical Properties of $Li_2Ti_6O_{13}$. *Chem. Mater.* **2011,** *23,* 2344–2352.

(87) Pérez-Flores, J. C.; Baehtz, C.; Hoelzel, M.; Kuhn, A.; García-Alvarado, F. $H_2Ti_6O_{13}$, a New Protonated Titanate Prepared by Li^+/H^+ Ion Exchange: Synthesis, Crystal Structure and Electrochemical Li Insertion Properties. *RSC Adv.* **2012,** *2,* 3530–3540.

(88) Kataoka, K.; Kijima, N.; Akimoto, J. Structural and Electrochemical Properties of Hydrogen Titanium Oxides. *Solid State Ionics* **2013,** *252,* 109–115.

(89) Rousse, G.; Arroyo-de Dompablo, M. E.; Senguttuvan, P.; Ponrouch, A.; Tarascon, J.-M.; Palacín, M. R., Rationalization of Intercalation Potential and Redox Mechanism for $A_2Ti_3O_7$ (A = Li, Na). *Chem. Mater.* **2013,** *25,* 4946–4956.

(90) Shen, K.; Wagemaker, M. $Na_{2+x}Ti_6O_{13}$ as Potential Negative Electrode Material for Na-Ion Batteries. *Inorg. Chem.* **2014,** *53,* 8250–8256.

(91) Li, H.; Fei, H.; Liu, X.; Yang, J.; Wei, M. *In Situ* Synthesis of $Na_2Ti_7O_{15}$ Nanotubes on a Ti Net Substrate as a High Performance Anode for Na-Ion Batteries. *Chem. Commun.* **2015,** *51,* 9298–9300.

(92) Bhat, S. S. M.; Babu, B.; Feygenson, M.; Neuefeind, J. C.; Shaijumon, M. M. Nanostructured $Na_2Ti_9O_{19}$ for Hybrid Sodium-Ion Capacitors with Excellent Rate Capability. *ACS Appl. Mater. Interfaces* **2018,** *10,* 437–447.

(93) Xu, C.-Y.; Wu, J.; Zhang, P.; Hu, S.-P.; Cui, J.-X.; Wang, Z.-Q.; Huang, Y.-D.; Zhen, L. Molten Salt Synthesis of $Na_2Ti_3O_7$ and $Na_2Ti_6O_{13}$ One-Dimensional Nanostructures and Their Photocatalytic and Humidity Sensing Properties. *CrystEngComm* **2013,** *15,* 3448–3454.

(94) Moetakef, P.; Larson, A. M.; Hodges, B. C.; Zavalij, P.; Gaskell, K. J.; Piccoli, P. M.; Rodriguez, E. E. Synthesis and Crystal Chemistry of Microporous Titanates $K_x(Ti,M)_8O_{16}$ where M = Sc–Ni.

J. Solid State Chem. **2014**, *220*, 45–53.

(95) Carter, M. L.; Withers, R. L. A Universally Applicable Composite Modulated Structure Approach to Ordered $Ba_xM_yTi_{8-y}O_{16}$ Hollandite-Type Solid Solutions. *J. Solid State Chem.* **2005**, *178*, 1903–1914.

(96) Knyazev, A. V.; Mączka, M.; Ladenkov, I. V.; Bulanov, E. N.; Ptak, M. Crystal Structure, Spectroscopy, and Thermal Expansion of Compounds in M^I_2O–Al_2O_3–TiO_2 System. *J. Solid State Chem.* **2012**, *196*, 110–118.

(97) Ringwood, A. E.; Kesson, S. E.; Ware, N. G.; Hibberson, W.; Major, A. Immobilisation of High Level Nuclear Reactor Wastes in SYNROC. *Nature* **1979**, *278*, 219–223.

(98) Clark, B. M.; Tumurugoti, P.; Sundaram, S. K.; Amoroso, J. W.; Marra, J. C. Preparation and Characterization of Multiphase Ceramic Designer Waste Forms. *Sci. Rep.* **2021**, *11*, 4512.

(99) Yoshikado, S.; Taniguchi, I.; Watanabe, M.; Onoda, Y.; Fujiki, Y. Frequency Dependence of Ionic Conductivity in One-Dimensional Ionic Conductors $K_{1.6}Mg_{0.8}Ti_{7.2}O_{16}$ and $K_{1.6}Al_{1.6}Ti_{6.4}O_{16}$. *Solid State Ionics* **1995**, *79*, 34–39.

(100) Pérez-Flores, J. C.; Baehtz, C.; Kuhn, A.; García-Alvarado, F. Hollandite-Type TiO_2: A New Negative Electrode Material for Sodium-Ion Batteries. *J. Mater. Chem. A* **2014**, *2*, 1825–1833.

(101) Zhang, Q.; Wei, Y.; Yang, H.; Su, D.; Ma, Y.; Li, H.; Zhai, T. Tunnel-Structured K_xTiO_2 Nanorods by in Situ Carbothermal Reduction as a Long Cycle and High Rate Anode for Sodium-Ion Batteries. *ACS Appl. Mater. Interfaces* **2017**, *9*, 7009–7016.

(102) Hulm, J. K.; Jones, C. K.; Hein, R. A.; Gibson, J. W. Superconductivity in the TiO and NbO Systems. *J. Low Temp. Phys.* **1972**, *7*, 291–307.

(103) Schooley, J. F.; Hosler, W. R.; Cohen, M. L. Superconductivity in Semiconducting $SrTiO_3$. *Phys. Rev. Lett.* **1964**, *12*, 474–475.

(104) Schooley, J. F.; Hosler, W. R.; Ambler, E.; Becker, J. H.; Cohen, M. L.; Koonce, C. S. Dependence of the Superconducting Transition Temperature on Carrier Concentration in Semiconducting $SrTiO_3$. *Phys. Rev. Lett.* **1965**, *14*, 305–307.

(105) Johnston, D. C.; Prakash, H.; Zachariasen, W. H.; Viswanathan, R. High Temperature Superconductivity in the Li–Ti–O Ternary System. *Mater. Res. Bull.* **1973**, *8*, 777–784.

(106) Johnston, D. C. Superconducting and Normal State Properties of $Li_{1+x}Ti_{2-x}O_4$ Spinel Compounds.

I. Preparation, Crystallography, Superconducting Properties, Electrical Resistivity, Dielectric Behavior, and Magnetic Susceptibility. *J. Low Temp. Phys.* **1976**, *25*, 145–175.

(107) Bednorz, J. G.; Müller, K. A.; Possible High T_c Superconductivity in the Ba–La–Cu–O System. *Z. Phys. B* **1986**, *64*, 189–193.

(108) Ohkoshi, S.; Tsunobuchi, Y.; Matsuda, T.; Hashimoto, K.; Namai, A.; Hakoe, F.; Tokoro, H. Synthesis of a Metal Oxide with a Room-Temperature Photoreversible Phase Transition. *Nat. Chem.* **2010**, *2*, 539–545.

(109) Ueda, H.; Kitazawa, K.; Takagi, H.; Matsumoto, T. Strong Carrier Concentration Dependence of Pressure Effect on Bipolaronic Transitions in Magnéli Phase Ti_nO_{2n-1} (n = 4, 5, 6). *J. Phys. Soc. Jpn.* **2002**, *71*, 1506–1510.

(110) Watanabe, M.; Miyahara, M.; Tanaka, K. Photo-Induced Changes in Charge-Ordered State of Ti_4O_7. *J. Phys.: Conf. Ser.* **2009**, *148*, 012017.

(111) Kitada, A.; Hasegawa, G.; Kobayashi, Y.; Kanamori, K.; Nakanishi, K.; Kageyama, H. Selective Preparation of Macroporous Monoliths of Conductive Titanium Oxides Ti_nO_{2n-1} (n = 2, 3, 4, 6). *J. Am. Chem. Soc.* **2012**, *134*, 10894–10898.

(112) Sakurai, H.; Kato, M.; Yoshimura, K.; Tsujii, N.; Kosuge, K. Metal-Insulator Transition in Na_xTiO_2 (x = 0.20–0.25). *Phys. Rev. B: Condens. Matter Mater. Phys.* **2007**, *75*, 115128.

(113) Muraoka, Y.; Noami, K.; Wakita, T.; Hirai, M.; Yokoya, T.; Kayo, Y.; Muro, T; Tamenori, Y. Synthesis and Physical Properties of the Hollandite-Type Titanium Oxide $K_xTi_8O_{16}$. *Phys. Status Solidi C* **2011**, *8*, 555–557.

(114) Nishioka, S.; Hyodo, J.; Vequizo, J. J. M.; Yamashita, S.; Kumagai, H.; Kimoto, K.; Yamakata, A.; Yamazaki, Y.; Maeda, K. Homogeneous Electron Doping into Nonstoichiometric Strontium Titanate Improves Its Photocatalytic Activity for Hydrogen and Oxygen Evolution. *ACS Catal.* **2018**, *8*, 7190–7200.

(115) Kageyama, H.; Hayashi, K.; Maeda, K.; Attfield, J. P.; Hiroi, Z.; Rondinelli, J. M.; Poeppelmeier, K. R. Expanding Frontiers in Materials Chemistry and Physics with Multiple Anions. *Nat. Commun.* **2018**, *9*, 772.

(116) Liu, Y.; Wang, W.; Xu, X.; Marcel Veder, J.-P.; Shao, Z. Recent Advances in Anion-Doped Metal Oxides for Catalytic Applications. *J. Mater. Chem. A* **2019**, *7*, 7280–7300.

(117) Maeda, K.; Takeiri, F.; Kobayashi, G.; Matsuishi, S.; Ogino, H.; Ida, S.; Mori, T.; Uchimoto, Y.; Tanabe, S.; Hasegawa, T.; Imanaka, N.; Kageyama, H. Recent Progress on Mixed-Anion Materials for Energy Applications. *Bull. Chem. Soc. Jpn.* **2021**, in press.

(118) Headspith, D. A.; Sullivan, E.; Greaves, C.; Francesconi, M. G. Synthesis and Characterisation of the Quaternary Nitride-Fluoride $Ce_2MnN_3F_{2-\delta}$. *Dalton Trans.* **2009**, 9273–9279.

(119) Yamanaka, S. Intercalation and Superconductivity in Ternary Layer Structured Metal Nitride Halides (*MNX*: *M* = Ti, Zr, Hf; *X* = Cl, Br, I). *J. Mater. Chem.* **2010**, *20*, 2922–2933.

(120) Tsuchiya, Y.; Wei, Z.; Broux, T.; Tassel, C.; Ubukata, H.; Kitagawa, Y.; Ueda, J.; Tanabe, S.; Kageyama, H. Formation of $PbCl_2$-Type AHF (A = Ca, Sr, Ba) with Partial Anion Order at High Pressure. *Dalton Trans.* **2021**, *50*, 8385–8391.

(121) Ubukata, H.; Takeiri, F.; Shitara, K.; Tassel, C.; Saito, T.; Kamiyama, T.; Broux, T.; Kuwabara, A.; Kobayashi, G.; Kageyama, H. Anion Ordering Enables Fast H^- Conduction at Low Temperatures. *Sci. Adv.* **2021**, *7*, eabf7883.

(122) Shevelkov, A. V.; Dikarev, E. V.; Shpanchenko, R. V.; Popovkin, B. A. Crystal Structures of Bismuth Tellurohalides BiTe*X* (*X* = Cl, Br, I) from X-Ray Powder Diffraction Data. *J. Solid State Chem.* **1995**, *114*, 379–384.

(123) Deiseroth, H.-J.; Kong, S.-T.; Eckert, H.; Vannahme, J.; Reiner, C.; Zaiß, T.; Schlosser, M. Li_6PS_5X: A Class of Crystalline Li-Rich Solids with an Unusually High Li^+ Mobility. *Angew. Chem., Int. Ed.* **2008**, *47*, 755–758.

(124) Fujii, S.; Gao, S.; Tassel, C.; Zhu, T.; Broux, T.; Okada, K.; Miyahara, Y.; Kuwabara, A.; Kageyama, H. Alkali-Rich Antiperovskite M_3FCh (M = Li, Na; Ch = S, Se, Te): The Role of Anions in Phase Stability and Ionic Transport. *J. Am. Chem. Soc.* **2021**, *143*, 10668–10675.

(125) Gao, S.; Broux, T.; Fujii, S.; Tassel, C.; Yamamoto, K.; Xiao, Y.; Oikawa, I.; Takamura, H.; Ubukata, H.; Watanabe, Y.; Fujii, K.; Yashima, M.; Kuwabara, A.; Uchimoto, Y.; Kageyama, H. Hydride-Based Antiperovskites with Soft Anionic Sublattices as Fast Alkali Ionic Conductors. *Nat. Commun.* **2021**, *12*, 201.

(126) Li, B.-Z.; Wu, S.-Q.; Wang, Z.-C.; Wang, C.; Cao, G.-H. Synthesis, Structure and Properties of Layered Phosphide Nitrides *Ak*$Th_2Mn_4P_4N_2$ (*Ak* = Rb, Cs). *Chin. J. Chem.* **2021**, *39*, 2873–2880.

(127) Yajima, T.; Koshiko, M.; Zhang, Y.; Oguchi, T.; Yu, W.; Kato, D.; Kobayashi, Y.; Orikasa, Y.;

Yamamoto, T.; Uchimoto, Y.; Green, M. A.; Kageyama, H. Selective and Low Temperature Transition Metal Intercalation in Layered Tellurides. *Nat. Commun.* **2016**, *7*, 13809.

(128) Anasori, B.; Lukatskaya, M. R.; Gogotsi, Y. 2D Metal Carbides and Nitrides (MXenes) for Energy Storage. *Nat. Rev. Mater.* **2017**, *2*, 16098.

(129) Maeda, K.; Wakayama, H.; Washio, Y.; Ishikawa, A.; Okazaki, M.; Nakata, H.; Matsuishi, S. Visible-Light-Induced Photocatalytic Activity of Stacked MXene Sheets of Y_2CF_2. *J. Phys. Chem. C* **2020**, *124*, 14640–14645.

(130) Sanjeewa, L. D.; Fulle, K.; McMillen, C. D.; Kolis, J. W. Hydrothermal Synthesis and Structural Characterization of Several Complex Rare Earth Tantalates: $Ln_2TaO_5(OH)$ (Ln = La, Pr) and $Ln_3Ta_2O_9(OH)$ (Ln = Pr, Nd). *Dalton Trans.* **2019**, *48*, 7704–7713.

(131) Smith Pellizzeri, T. M.; Sanjeewa, L. D.; Pellizzeri, S.; McMillen, C. D.; Garlea, V. O.; Ye, F.; Sefat, A. S.; Kolis, J. W. Single Crystal Neutron and Magnetic Measurements of $Rb_2Mn_3(VO_4)_2CO_3$ and $K_2Co_3(VO_4)_2CO_3$ with Mixed Honeycomb and Triangular Magnetic Lattices. *Dalton Trans.* **2020**, *49*, 4323–4335.

(132) Ding, F.; Zhang, W.; Nisbet, M. L.; Zhang, W. Halasyamani, P. S.; Yang, Z.; Pan, S.; Poeppelmeier, K. R. $NaRb_3B_6O_9(OH)_3(HCO_3)$: A Borate-Bicarbonate Nonlinear Optical Material. *Inorg. Chem.* **2020**, *59*, 759–766.

(133) Smirnova, O.; Azuma, M.; Kumada, N.; Kusano, Y.; Matsuda, M.; Shimakawa, Y.; Takei, T.; Yonesaki, Y.; Kinomura, N. Synthesis, Crystal Structure, and Magnetic Properties of $Bi_3Mn_4O_{12}(NO_3)$ Oxynitrate Comprising S = 3/2 Honeycomb Lattice. *J. Am. Chem. Soc.* **2009**, *131*, 8313–8317.

(134) Fujihala, M.; Morita, K.; Mole, R.; Mitsuda, S.; Tohyama, T.; Yano, S.-i.; Yu, D.; Sota, S.; Kuwai, T.; Koda, A.; Okabe, H.; Lee, H.; Itoh, S.; Hawai, T.; Masuda, T.; Sagayama, H.; Matsuo, A.; Kindo, K.; Ohira-Kawamura, S.; Nakajima, K. Gapless Spin Liquid in a Square-Kagome Lattice Antiferromagnet. *Nat. Commun.* **2020**, *11*, 3429.

(135) Yakubovich, O. V.; Shvanskaya, L. V.; Kiriukhina, G. V.; Volkov, A. S.; Dimitrova, O. V.; Vasiliev, A. N. Hydrothermal Synthesis and a Composite Crystal Structure of $Na_6Cu_7BiO_4(PO_4)_4[Cl,(OH)]_3$ as a Candidate for Quantum Spin Liquid. *Inorg. Chem.* **2021**, *60*, 11450–11457.

(136) Asl, H. Y.; Ghosh, K.; Vidal Meza, M. P.; Choudhury, A. $Li_3Fe_2(HPO_3)_3Cl$: An Electroactive Iron Phosphite as a New Polyanionic Cathode Material for Li-Ion Battery. *J. Mater. Chem. A* **2015**, *3*, 7488–7497.

(137) Sun, C.-F.; Hu, C.-L.; Xu, X.; Ling, J.-B.; Hu, T.; Kong, F.; Long, X.-F.; Mao, J.-G. $BaNbO(IO_3)_5$: A New Polar Material with a Very Large SHG Response. *J. Am. Chem. Soc.* **2009**, *131*, 9486–9487.

(138) Yamamoto, T.; Oswald, I. W. H.; Savory, C. N.; Ohmi, T.; Koegel, A. A.; Scanlon, D. O.; Kageyama, H.; Neilson, J. R. Structure and Optical Properties of Layered Perovskite $(MA)_2PbI_{2-x}Br_x(SCN)_2$ ($0 \leq x < 1.6$). *Inorg. Chem.* **2020**, *59*, 17379–17384.

(139) Ley, M. B.; Ravnsbæk, D. B.; Filinchuk, Y.; Lee, Y.-S.; Janot, R.; Cho, Y. W.; Skibsted, J.; Jensen, T. R. $LiCe(BH_4)_3Cl$, a New Lithium-Ion Conductor and Hydrogen Storage Material with Isolated Tetranuclear Anionic Clusters. *Chem. Mater.* **2012**, *24*, 1654–1663.

(140) Grimaud, A.; Iadecola, A.; Batuk, D.; Saubanère, M.; Abakumov, A. M.; Freeland, J. W.; Cabana, J.; Li, H.; Doublet, M.-L.; Rousse, G.; Tarascon, J.-M. Chemical Activity of the Peroxide/Oxide Redox Couple: Case Study of $Ba_5Ru_2O_{11}$ in Aqueous and Organic Solvents. *Chem. Mater.* **2018**, *30*, 3882–3893.

(141) Sasaki, S.; Caldes, M. T.; Guillot-Deudon, C.; Braems, I.; Steciuk, G.; Palatinus, L.; Gautron, E.; Frapper, G.; Janod, E.; Corraze, B.; Jobic, S.; Cario, L. Design of Metastable Oxychalcogenide Phases by Topochemical (De)intercalation of Sulfur in $La_2O_2S_2$. *Nat. Commun.* **2021**, *12*, 3605.

(142) Inorganic Crystal Structure Database. https://icsd.fiz-karlsruhe.de (accessed Dec 12, 2021).

(143) Ogino, H. Development of New Mixed Anion Compounds. *Nihon Kessho Gakkaishi* **2018**, *60*, 246–253.

(144) Takeiri, F.; Kageyama, H. Mixed-Anion Compounds: A New Trend in Solid State Chemistry. *Nihon Kessho Gakkaishi* **2018**, *60*, 240–245.

(145) Kageyama, H.; Yajima, T.; Tsujimoto, Y.; Yamamoto, T.; Tassel, C.; Kobayashi, Y. Exploring Structures and Properties through Anion Chemistry. *Bull. Chem. Soc. Jpn.* **2019**, *92*, 1349–1357.

(146) Al-Mamouri, M.; Edwards, P. P.; Greaves, C.; Slaski, M. Synthesis and Superconducting Properties of the Strontium Copper Oxy-Fluoride $Sr_2CuO_2F_{2+\delta}$. *Nature* **1994**, *369*, 382–384.

(147) Kodenkandath, T. A.; Lalena, J. N.; Zhou, W. L.; Carpenter, E. E.; Sangregorio, C.; Falster, A.

U.; Simmons, W. B.; O'connor, C. J.; Wiley, J. B. Assembly of Metal-Anion Arrays within a Perovskite Host. Low-Temperature Synthesis of New Layered Copper-Oxyhalides, (CuX)$LaNb_2O_7$, X = Cl, Br. *J. Am. Chem. Soc.* **1999**, *121*, 10743–10746.

(148) Kobayashi, Y.; Hernandez, O. J.; Sakaguchi, T.; Yajima, T.; Roisnel, T.; Tsujimoto, Y.; Morita, M.; Noda, Y.; Mogami, Y.; Kitada, A.; Ohkura, M.; Hosokawa, S.; Li, Z.; Hayashi, K.; Kusano, Y.; Kim, J. E.; Tsuji, N.; Fujiwara, A.; Matsushita, Y.; Yoshimura, K.; Takegoshi, K.; Inoue, M.; Takano, M.; Kageyama, H. An Oxyhydride of $BaTiO_3$ Exhibiting Hydride Exchange and Electronic Conductivity. *Nat. Mater.* **2012**, *11*, 507–511.

(149) Kobayashi, Y.; Tang, Y.; Kageyama, T.; Yamashita, H.; Masuda, N.; Hosokawa, S.; Kageyama, H. Titanium-Based Hydrides as Heterogeneous Catalysts for Ammonia Synthesis. *J. Am. Chem. Soc.* **2017**, *139*, 18240–18246.

(150) Yamamoto, T.; Yoshii, R.; Bouilly, G.; Kobayashi, Y.; Fujita, K.; Kususe, Y.; Matsushita, Y.; Tanaka, K.; Kageyama, H. An Antiferro-to-Ferromagnetic Transition in $EuTiO_{3-x}H_x$ Induced by Hydride Substitution. *Inorg. Chem.* **2015**, *54*, 1501–1507.

(151) Pussacq, T.; Kabbour, H.; Colis, S.; Vezin, H.; Saitzek, S.; Gardoll, O.; Tassel, C.; Kageyama, H.; Laberty Robert, C.; Mentré, O. Reduction of $Ln_2Ti_2O_7$ Layered Perovskites: A Survey of the Anionic Lattice, Electronic Features, and Potentials. *Chem. Mater.* **2017**, *29*, 1047–1057.

(152) Kasahara, A.; Nukumizu, K.; Hitoki, G.; Takata, T.; Kondo, J. N.; Hara, M.; Kobayashi, H.; Domen, K. Photoreactions on $LaTiO_2N$ under Visible Light Irradiation. *J. Phys. Chem. A* **2002**, *106*, 6750–6753.

(153) Kasahara, A.; Nukumizu, K.; Takata, T.; Kondo, J. N.; Hara, M.; Kobayashi, H.; Domen, K. $LaTiO_2N$ as a Visible-Light (≤600 nm)-Driven Photocatalyst (2). *J. Phys. Chem. B* **2003**, *107*, 791–797.

(154) Ishikawa, A.; Takata, T.; Kondo, J. N.; Hara, M.; Kobayashi, H.; Domen, K. Oxysulfide $Sm_2Ti_2S_2O_5$ as a Stable Photocatalyst for Water Oxidation and Reduction under Visible Light Irradiation ($\lambda \leq 650$ nm). *J. Am. Chem. Soc.* **2002**, *124*, 13547–13553.

(155) Ishikawa, A.; Takata, T.; Matsumura, T.; Kondo, J. N.; Hara, M.; Kobayashi, H.; Domen, K. Oxysulfides $Ln_2Ti_2S_2O_5$ as Stable Photocatalysts for Water Oxidation and Reduction under Visible-Light Irradiation. *J. Phys. Chem. B* **2004**, *108*, 2637–2642.

(156) Atuchin, V. V.; Isaenko, L. I.; Kesler, V. G.; Kang, L.; Lin, Z.; Molokeev, M. S.; Yelisseyev, A. P.; Zhurkov, S. A. Structural, Spectroscopic, and Electronic Properties of Cubic G0-Rb_2KTiOF_5 Oxyfluoride. *J. Phys. Chem. C* **2013**, *117*, 7269–7278.

(157) Liang, Z.; Yang, Z.; Tang, H.; Guo, J.; Yang, Z.; Zhou, Q.; Tang, S.; Wang, Z. Synthesis, Luminescence Properties of a Novel Oxyfluoride Red Phosphor $BaTiOF_4:Mn^{4+}$ for LED Backlighting. *Opt. Mater.* **2019**, *90*, 89–94.

(158) Oka, K.; Hojo, H.; Azuma, M.; Oh-ishi, K. Temperature-Independent, Large Dielectric Constant Induced by Vacancy and Partial Anion Order in the Oxyfluoride Pyrochlore $Pb_2Ti_2O_{6-\delta}F_{2\delta}$. *Chem. Mater.* **2016**, *28*, 5554–5559.

(159) Kuriki, R.; Ichibha, T.; Hongo, K.; Lu, D.; Maezono, R.; Kageyama, H.; Ishitani, O.; Oka, K.; Maeda, K. A Stable, Narrow-Gap Oxyfluoride Photocatalyst for Visible-Light Hydrogen Evolution and Carbon Dioxide Reduction. *J. Am. Chem. Soc.* **2018**, *140*, 6648–6655.

(160) Wakayama, H.; Utimula, K.; Ichibha, T.; Kuriki, R.; Hongo, K.; Maezono, R.; Oka, K.; Maeda, K. Light Absorption Properties and Electronic Band Structures of Lead Titanium Oxyfluoride Photocatalysts $Pb_2Ti_4O_9F_2$ and $Pb_2Ti_2O_{5.4}F_{1.2}$. *J. Phys. Chem. C* **2018**, *122*, 26506–26511.

(161) Maeda, K.; Domen, K. New Non-Oxide Photocatalysts Designed for Overall Water Splitting under Visible Light. *J. Phys. Chem. C* **2007**, *111*, 7851–7861.

(162) Maeda, K. Photocatalytic Property of Mixed Anion Compounds. *Nihon Kessho Gakkaishi* **2018**, *60*, 260–267.

(163) Shannon, R. D. Revised Effective Ionic Radii and Systematic Studies of Interatomic Distances in Halides and Chalcogenides. *Acta Crystallogr., Sect. A: Cryst. Phys., Diffr., Theor. Gen. Crystallogr.* **1976**, *32*, 751–767.

(164) Clemens, O.; Slater, P. R. Topochemical Modifications of Mixed Metal Oxide Compounds by Low-Temperature Fluorination Routes. *Rev. Inorg. Chem.* **2013**, *33*, 105–117.

(165) Slater, P.; Driscoll, L. Modification of Magnetic and Electronic Properties, in Particular Superconductivity, by Low Temperature Insertion of Fluorine into Oxides. In *Photonic and Electronic Properties of Fluoride Materials*, 1st ed.; Tressaud, A., Poppelmeier, K., Eds.; Progress in Fluorine Science Series 1; Elsevier: Amsterdam, 2016; pp 401–421.

(166) Kobayashi, Y.; Tian, M.; Eguchi, M.; Mallouk, T. E. Ion-Exchangeable, Electronically

Conducting Layered Perovskite Oxyfluorides. *J. Am. Chem. Soc.* **2009**, *131*, 9849–9855.

(167) Slater, P. R.; Gover, R. K. B. Synthesis and Structure of the New Oxide Fluoride $Sr_2TiO_3F_2$ from the Low Temperature Fluorination of Sr_2TiO_4: An Example of a Staged Fluorine Substitution/Insertion Reaction. *J. Mater. Chem.* **2002**, *12*, 291–294.

(168) Aikens, L. D.; Li, R. K.; Greaves, C. The Synthesis and Structure of a New Oxide Fluoride, $LaSrMnO_4F$, with Staged Fluorine Insertion. *Chem. Commun.* **2000**, 2129–2130.

(169) Kawahara, K.; Chikamatsu, A.; Katayama, T.; Onozuka, T.; Ogawa, D.; Morikawa, K.; Ikenaga, E.; Hirose, Y.; Harayama, I.; Sekiba, D.; Fukumura, T.; Hasegawa, T. Topotactic Fluorination of Perovskite Strontium Ruthenate Thin Films using Polyvinylidene Fluoride. *CrystEngComm* **2017**, *19*, 313–317.

(170) Li, R. K.; Greaves, C. Double-Layered Ruthenate $Sr_3Ru_2O_7F_2$ Formed by Fluorine Insertion into $Sr_3Ru_2O_7$. *Phys. Rev. B: Condens. Matter Mater. Phys.* **2000**, *62*, 3811–3815.

(171) Batuk, M.; Batuk, D.; Tsirlin, A. A.; Filimonov, D. S.; Sheptyakov, D. V.; Frontzek, M.; Hadermann, J.; Abakumov, A. M. Layered Oxychlorides $[PbBiO_2]A_{n+1}B_nO_{3n-1}Cl_2$ (A = Pb/Bi, B = Fe/Ti): Intergrowth of the Hematophanite and Sillen Phases. *Chem. Mater.* **2015**, *27*, 2946–2956.

(172) Su, Y.; Tsujimoto, Y.; Fujii, K.; Tatsuta, M.; Oka, K.; Yashima, M.; Ogino, H.; Yamaura, K. Synthesis, Crystal Structure, and Optical Properties of Layered Perovskite Scandium Oxychlorides: Sr_2ScO_3Cl, $Sr_3Sc_2O_5Cl_2$, and $Ba_3Sc_2O_5Cl_2$. *Inorg. Chem.* **2018**, *57*, 5615–5623.

(173) Kodenkandath, T. A.; Kumbhar, A. S.; Zhou, W. L.; Wiley, J. B. Construction of Copper Halide Networks within Layered Perovskites. Syntheses and Characterization of New Low-Temperature Copper Oxyhalides. *Inorg. Chem.* **2001**, *40*, 710–714.

(174) Fujito, H.; Kunioku, H.; Kato, D.; Suzuki, H.; Higashi, M.; Kageyama, H.; Abe, R. Layered Perovskite Oxychloride Bi_4NbO_8Cl: A Stable Visible Light Responsive Photocatalyst for Water Splitting. *J. Am. Chem. Soc.* **2016**, *138*, 2082–2085.

(175) Ogawa, K.; Suzuki, H.; Zhong, C.; Sakamoto, R.; Tomita, O.; Saeki, A.; Kageyama, H.; Abe, R. Layered Perovskite Oxyiodide with Narrow Band Gap and Long Lifetime Carriers for Water Splitting Photocatalysis. *J. Am. Chem. Soc.* **2021**, *143*, 8446–8453.

(176) Clément, R. J.; Lun, Z.; Ceder, G. Cation-Disordered Rocksalt Transition Metal Oxides and

Oxyfluorides for High Energy Lithium-Ion Cathodes. *Energy Environ. Sci.* **2020**, *13*, 345–373.

(177) Chen, D.; Ahn, J.; Chen, G. An Overview of Cation-Disordered Lithium-Excess Rocksalt Cathodes. *ACS Energy Lett.* **2021**, *6*, 1358–1376.

(178) Rüdorff, W.; Krug, D. Alkaliniob(IV)-dioxidfluoride. *Z. Anorg. Allg. Chem.* **1964**, *329*, 211–217.

(179) Takeiri, F.; Yamamoto, T.; Hayashi, N.; Hosokawa, S.; Arai, K.; Kikkawa, J.; Ikeda, K.; Honda, T.; Otomo, T.; Tassel, C.; Kimoto, K.; Kageyama, H. $AgFeOF_2$: A Fluorine-Rich Perovskite Oxyfluoride. *Inorg. Chem.* **2018**, *57*, 6686–6691.

(180) Nakhal, S.; Bredow, T.; Lerch, M. Syntheses and Crystal Structures of New ReO_3-Type-Derived Transition Metal Oxide Fluorides. *Z. Anorg. Allg. Chem.* **2015**, *641*, 1036–1042.

(181) Nakhal, S.; Lerch, M. New Transition Metal Oxide Fluorides with ReO_3-Type Structure. *Z. Naturforsch. B* **2016**, *71*, 457–461.

(182) Galasso, F.; Darby, W. Preparation, Structure, and Properties of K_2NbO_3F. *J. Phys. Chem.* **1962**, *66*, 1318–1320.

(183) Wang, Y.; Tang, K.; Zhu, B.; Wang, D.; Hao, Q.; Wang, Y. Synthesis and Structure of a New Layered Oxyfluoride Sr_2ScO_3F with Photocatalytic Property. *Mater. Res. Bull.* **2015**, *65*, 42–46.

(184) Su, Y.; Tsujimoto, Y.; Matsushita, Y.; Yuan, Y.; He, J.; Yamaura, K. High-Pressure Synthesis, Crystal Structure, and Magnetic Properties of Sr_2MnO_3F: A New Member of Layered Perovskite Oxyfluorides. *Inorg. Chem.* **2016**, *55*, 2627–2633.

(185) Tsujimoto, Y.; Matsushita, Y.; Hayashi, N.; Yamaura, K.; Uchikoshi, T. Anion Order-to-Disorder Transition in Layered Iron Oxyfluoride Sr_2FeO_3F Single Crystals. *Cryst. Growth Des.* **2014**, *14*, 4278–4284.

(186) Tsujimoto, Y.; Li, J. J.; Yamaura, K.; Matsushita, Y.; Katsuya, Y.; Tanaka, M.; Shirako, Y.; Akaogi, M.; Takayama-Muromachi, E. New Layered Cobalt Oxyfluoride, Sr_2CoO_3F. *Chem. Commun.* **2011**, *47*, 3263–3265.

(187) Tsujimoto, Y.; Yamaura, K.; Uchikoshi, T. Extended Ni(III) Oxyhalide Perovskite Derivatives: Sr_2NiO_3X (X = F, Cl). *Inorg. Chem.* **2013**, *52*, 10211–10216.

(188) Needs, R. L.; Weller, M. T.; Scheler, U.; Harris, R. K. Synthesis and Structure of Ba_2InO_3X (X = F, Cl, Br) and Ba_2ScO_3F; Oxide/Halide Ordering in K_2NiF_4-Type Structures. *J. Mater. Chem.* **1996**, *6*, 1219–1224.

(189) Pistorius, C. W. F. T. Effect of Pressure on the Rhombohedral/Cubic Transitions of Some Lanthanide Oxide Fluorides. *J. Less-Common Met.* **1973**, *31*, 119–124.

(190) Petzel, T.; Marx, V.; Hormann, B. Thermodynamics of the Rhombohedral–Cubic Phase Transition of ROF with R = Y, La, Pr, Nd, Sm–Er. *J. Alloys Compd.* **1993**, *200*, 27–31.

(191) Müller, J.-H.; Petzel, T. High-Temperature X-Ray Diffraction Study of the Rhombohedral–Cubic Phase Transition of ROF with R = Y, La, Pr, Nd, Sm–Er. *J. Alloys Compd.* **1995**, *224*, 18–21.

(192) Hirai, D.; Climent-Pascual, E.; Cava, R. J. Superconductivity in $WO_{2.6}F_{0.4}$ Synthesized by Reaction of WO_3 with Teflon. *Phys. Rev. B: Condens. Matter Mater. Phys.* **2011**, *84*, 174519.

(193) Ogata, T.; Oka, K.; Azuma, M. Negative Thermal Expansion in Electron Doped $PbVO_{3-x}F_x$. *Appl. Phys. Express* **2019**, *12*, 023005.

(194) Inaguma, Y.; Sugimoto, K.; Ueda, K. Synthesis of the Perovskite-Type Oxyfluoride $AgTiO_2F$: An Approach Adopting the HSAB Principle. *Dalton Trans.* **2020**, *49*, 6957–6963.

(195) Oka, K.; Oh-ishi, K. Observation of Anion Order in $Pb_2Ti_4O_9F_2$. *Inorg. Chem.* **2015**, *54*, 10239–10242.

(196) Oka, K. Exploring Novel Functional Properties Arose from Anion Order in Mixed Anion Compounds. *J. Ceram. Soc. Jpn.* **2021**, *129*, 555–560.

(197) Tachibana, M. *Beginner's Guide to Flux Crystal Growth*, 1st ed.; Ohashi, N., Ed.; NIMS Monographs Series; Springer: Tokyo, 2016.

(198) Elwell, D.; Scheel, H. J. *Crystal Growth from High-Temperature Solutions;* Academic Press: London, 1975.

(199) Sunagawa, I. *Crystals: Growth, Morphology, & Perfection;* Cambridge University Press: Cambridge, 2005.

(200) Feigelson, R. S. Crystal Growth by the Electrolysis of Molten Salts. In *Solid State Chemistry: A Contemporary Overview;* Holt, S. L., Milstein, J. B., Robbins, M., Eds.; Advances in Chemistry Series; American Chemical Society: Washington, DC, 1980; pp 243–275.

(201) Wold, A.; Bellavance, D. Preparation of Transition Metal Compounds by Electrolytic Reduction of Fused Salts. In *Preparative Methods in Solid State Chemistry;* Hagenmuller, R., Ed.; Academic Press: New York, 1972; pp 279–308.

(202) Tabereaux, A. T.; Peterson, R. D. Aluminum Production. In *Treatise on Process Metallurgy*, 1st

ed.; Seetharaman, S., Ed.; Elsevier: Boston, 2014; Vol. 3, pp 839–917.

(203) Takeda, O.; Uda, T.; Okabe, T. H. Rare Earth, Titanium Group Metals, and Reactive Metals Production. In *Treatise on Process Metallurgy,* 1st ed.; Seetharaman, S., Ed.; Elsevier: Boston, 2014; Vol. 3, pp 995–1069.

(204) Scheibler, C. Ueber wolframsaure Salze. *J. Prakt. Chem.* **1860,** *80,* 204–213.

(205) Andrieux, J.-L.; Bozon, H. Sur la préparation électrolytique et les propriétés de quelques spinelles de vanadium. *C. R. Acad. Sci. Paris* **1949,** *228,* 565–566.

(206) Andrieux, J.-L.; Bozon, H. Sur la préparation électrolytique de deux composés oxygénés du vanadium. *C. R. Acad. Sci. Paris* **1950,** *230,* 953–954.

(207) de Roy, M. E.; Besse, J. P.; Chevalier, R. Structure of a Potassium Vanadium Hollandite Type Phase Result of an Intergrowth? *Mater. Res. Bull.* **1986,** *21,* 567–574.

(208) de Roy, M. E.; Besse, J. P.; Chevalier, R.; Gasperin, M. Synthèse et structure cristalline de NaV_6O_{11}. *J. Solid State Chem.* **1987,** *67,* 185–189.

(209) Abe, H.; Nishida, K.; Imai, M.; Kitazawa, H. Electrochemical Preparation of Single-Crystalline Cr_2O_3 from Molten Salts. *J. Cryst. Growth* **2004,** *267,* 42–46.

(210) Strobel, P.; Vicat, J.; Qui, D. T.; Thermal and Physical Properties of Hollandite-Type $K_{1.3}Mn_8O_{16}$ and $(K,H_3O)_xMn_8O_{16}$. *J. Solid State Chem.* **1984,** *55,* 67–73.

(211) McCarroll, W. H.; Ramanujachary, K. V.; Greenblatt, M. Synthesis of Doped Rare Earth Manganate Perovskite Crystals Using Fused Salt Electrolysis. *J. Solid State Chem.* **1997,** *130,* 327–329.

(212) McCarroll, W. H.; Ramanujachary, K. V.; Fawcett, I. D.; Greenblatt, M. Electrical and Magnetic Properties of Strontium Substituted Lanthanum Manganate Perovskite Crystals Prepared Using Fused Salt Electrolysis. *J. Solid State Chem.* **1999,** *145,* 88–96.

(213) Dodero, M.; Déportes, C. Sur la préparation de ferrites, nickelites et cobaltites alcalins par électrolyse ignée. *C. R. Acad. Sci. Paris* **1956,** *242,* 2939–2941.

(214) Wang, H.; Chen, Z.; Jin, Q. Crystal Growth and Transport Properties of α- and β-Phase Na_xCoO_2. *Mater. Lett.* **2005,** *59,* 3917–3920.

(215) Tang, H.-Y.; Lin, H.-Y.; Wang, M.-J.; Liao, M.-Y.; Liu, J.-L.; Hsu, F.-C.; Wu, M.-K. Crystallization and Anisotropic Properties of Water-Stabilized Potassium Cobalt Oxides. *Chem.*

Mater. **2005**, *17*, 2162–2164.

(216) Nguyen, T. N.; zur Loye, H.-C. Electrosynthesis in Hydroxide Melts. *J. Cryst. Growth* **1997**, *172*, 183–189.

(217) Tang, H. Y.; Lee, C. S.; Wu, M. K. Crystallization of $La_{2-x}Na_xCuO_4$ Superconductor by Low-Temperature Electrochemical Deposition. *Physica C* **1994**, *231*, 325–329.

(218) Tang, H. Y.; Hshu, H. Y.; Lee, C. S.; Yang, J. L.; Wu, M. K. Electrochemical Synthesis of Superconducting $EuBa_2Cu_3O_{7-x}$ from Low-Temperature Molten Salt. *J. Electrochem. Soc.* **1997**, *144*, 16–20.

(219) Ksenofontov, D. A.; Dem'yanets, L. N.; Ivanov-Schitz, A. K. Electric-Field Effect on Crystal Growth in the Li_3PO_4–Li_4GeO_4–Li_2MoO_4–LiF System. *Inorg. Mater.* **2008**, *44*, 1115–1120.

(220) Moshopoulou, E. G.; Bordet, P.; Capponi, J. J. Superstructure and Superconductivity in $Li_{1-x}NbO_2$ ($x \approx 0.7$) Single Crystals. *Phys. Rev. B: Condens. Matter Mater. Phys.* **1999**, *59*, 9590–9599.

(221) Greenblatt, M. Molybdenum Oxide Bronzes with Quasi-Low-Dimensional Properties. *Chem. Rev.* **1988**, *88*, 31–53.

(222) Tortelier, J.; McCarroll, W. H.; Gougeon, P. Synthesis, Crystal Structure, and Characterization of the New Ordered Hollandite-Type $NdMo_6O_{12}$. *J. Solid State Chem.* **1998**, *136*, 87–92.

(223) Abe, H.; Sato, A.; Tsujii, N.; Furubayashi, T.; Shimoda, M. Structural Refinement of $T_2Mo_3O_8$ (T = Mg, Co, Zn and Mn) and Anomalous Valence of Trinuclear Molybdenum Clusters in $Mn_2Mo_3O_8$. *J. Solid State Chem.* **2010**, *183*, 379–384.

(224) Samata, H.; Kai, M.; Uchida, T.; Ohtsuka, M.; Tanaka, G.; Sawada, S.; Taniguchi, T.; Nagata, Y. Synthesis and Properties of $Ba_3NaRu_2O_{9-\delta}$ and $Ba_3(Na,R)Ru_2O_{9-\delta}$ (R = Rare Earth) Crystals. *J. Alloys Compd.* **2003**, *350*, 77–85.

(225) Samata, H.; Saeki, Y.; Mizusaki, S.; Nagata, Y.; Ozawa, T. C.; Sato, A. Electrochemical Crystal Growth of Perovskite Ruthenates. *J. Cryst. Growth* **2009**, *311*, 623–626.

(226) Samata, H.; Tanaka, S.; Mizusaki, S.; Nagata, Y.; Ozawa, T. C.; Sato, A.; Kosuda, K. Synthesis and Characterization of $CaPd_3O_4$ Crystals. *J. Cryst. Process Technol.* **2012**, *2*, 16–20.

(227) Banks, E.; Fleischmann, C. W.; Meites, L. On the Nature of the Species Reduced During the Electrochemical Synthesis of Tungsten Bronzes. *J. Solid State Chem.* **1970**, *1*, 372–375.

(228) Shanks, H. R. Growth of Tungsten Bronze Crystals by Fused Salt Electrolysis. *J. Cryst. Growth* **1972**, *13–14*, 433–437.

(229) Nguyen, T. N.; Giaquinta, D. M.; zur Loye, H.-C. Synthesis of the New One-Dimensional Compound Sr_3NiPtO_6: Structure and Magnetic Properties. *Chem. Mater.* **1994**, *6*, 1642–1646.

(230) Zhao, L. Z.; Yin, B.; Zhang, J. B.; Li, J. W.; Xu, C. Y. Preparation and Magnetic Measurements of Ba-K-Pb-O and Ba-K-M-Pb-O (M = Tl, Sb) Crystals. *Physica C* **1997**, *282–287*, 1311–1312.

(231) Chong, N. S.; Suen, N. T.; Chou, T. L.; Tang, H. Y. Electrocrystallization and Characterization of Polymorphic Forms of Barium Metaplumbate. *Cryst. Growth Des.* **2008**, *8*, 1779–1782.

(232) Norton, M. L. Electrodeposition of $Ba_{0.6}K_{0.4}BiO_3$. *Mater. Res. Bull.* **1989**, *24*, 1391–1397.

(233) Norton, M. L.; Tang, H. Y. Superconductivity at 32 K in electrocrystallized barium potassium bismuth oxide. *Chem. Mater.* **1991**, *3*, 431–434.

(234) Nguyen, T. N.; Giaquinta, D. M.; Davis, W. M.; zur Loye, H.-C. Electrosynthesis of $KBiO_3$: A Potassium Ion Conductor with the $KSbO_3$ Tunnel Structure. *Chem. Mater.* **1993**, *5*, 1273–1676.

(235) Schlechter, M.; Kooi, J.; Billiau, R.; Charlier, R. A.; Dumont, G. L. The Preparation of UO_2 by Fused Salt Electrolysis Using UO_2 or UF_4 as Starting Material. *J. Nucl. Mater.* **1965**, *15*, 189–200.

(236) Chen, C.; Spears, M.; Wondre, F.; Ryan, J. Crystal Growth and Superconductivity of $LiTi_2O_4$ and $Li_{1+1/3}Ti_{2-1/3}O_4$. *J. Cryst. Growth* **2003**, *250*, 139–145.

(237) Bright, N. F. H.; Rowland, J. F.; Wurm, J. G. The Compound $CaO.Ti_2O_3$. *Can. J. Chem.* **1958**, *36*, 492–495.

(238) Abe, H.; Satoh, A.; Nishida, K.; Abe, E.; Naka, T.; Imai, M.; Kitazawa, H. Electrochemical Immobilization of Cs in Single-Crystalline SYNROC. *J. Solid State Chem.* **2006**, *179*, 1521–1524.

(239) ACS Publications. Use of Materials from ACS Journals (other than ACS AuthorChoice Open Access content). https://pubs.acs.org/page/copyright/permissions_journals.html (accessed Oct 3, 2021).

(240) RSC Publishing. Licences, Copyright & Permissions. https://www.rsc.org/journals-books-databases/author-and-reviewer-hub/authors-information/licences-copyright-permissions/#acknowledgements (accessed Oct 3, 2021).

Chapter 2

High-Temperature Electrochemical Crystal Growth of Hollandite-Type $Cs_xTi_8O_{16}$ with Controlled Electronic Properties

2.1. Abstract

Electrochemical crystal growth of hollandite-type $Cs_xTi_8O_{16}$ was examined employing high-temperature electrolysis of a molten mixture consisting of TiO_2 and Cs_2MoO_4 with constantly applied voltages. The resultant needle-like crystals showed obviously distinct appearances, either optical transparency or metallic luster, depending on the applied voltage. While the transparent crystals were electrical insulators, the metallic luster crystals were moderately conductive, with ρ–T curves being fitted with the one-dimensional (1D) VRH model, suggesting that the compound is a 1D metal involving carrier localization.

2.2. Introduction

Mixed-valent transition-metal compounds have attracted a great deal of attention because of their remarkable properties and functionalities. Such compounds have been studied extensively, including high-temperature superconducting copper oxides[1] and colossal magnetoresistance (CMR) manganese oxides.[2] A family of alkali-metal titanium oxides, the so-called titanium bronze, is another example displaying various interesting electronic and magnetic properties originating from mixed-valent Ti^{3+}/Ti^{4+}. For instance, the spinel-type $LiTi_2O_4$ exhibits superconductivity with critical temperatures as high as T_c = 13.7 K.[3] The TiO_2(B)-type $Na_{0.25}TiO_2$ shows a magnetic transition at T_c = 430 K, followed by a metal–insulator transition at T_p = 630 K.[4] Furthermore, magnetization measurements of hollandite-type $K_{1.46}Ti_8O_{16}$ revealed a small spontaneous magnetization at room temperature that suggests the appearance of weak ferromagnetism.[5] These oxides generally show a great deal of alkali-metal nonstoichiometry, leading to diversity in electronic/magnetic properties as a function of the alkali-metal content. For instance, the $Li_{1+x}Ti_{2-x}O_4$ (x = 0–1/3) solid solution shows distinct electric behaviors at the terminal compositions: $LiTi_2O_4$ (x = 0) is a superconductor, while $Li_4Ti_5O_{12}$ (x = 1/3) is an electrical insulator.[3] The control of chemical composition is thus essential for exploring novel electronic and magnetic properties.

Titanium oxides with a hollandite-type structure are members of titanium bronze phases, with a general formula of $A_xTi_8O_{16}$ ($x \leq 2$) where A = alkali metals.[5–10] The crystal structure consists of double-chains of edge-shared TiO_6 octahedra that are connected by sharing the corners, forming a one-dimensional (1D) tunnel structure along the c-axis, as illustrated in Figure 2.1. The A ions partially occupy the crystallographic sites inside the 1D tunnels, and the oxidation state of titanium varies with the A ion content (x). The unique crystal structure of hollandite-type titanium oxides gives rise to various ionic functionalities such as alkali-ion conductors,[6] electrode materials for lithium-ion

secondary batteries (LIBs),[7,8] and solid matrices for immobilization of radioactive cesium.[9] Taking into account possible nonstoichiometry, it is also of significance to study electronic properties of $A_xTi_8O_{16}$ with varying alkali-metal contents (x).

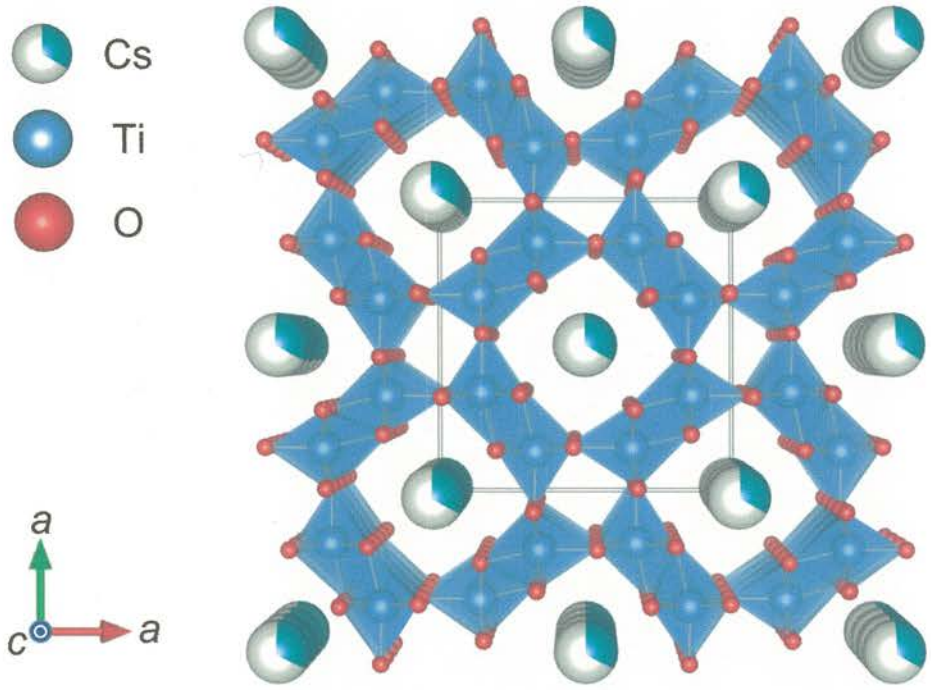

Figure 2.1. Polyhedral representation of the crystal structure of hollandite-type $Cs_xTi_8O_{16}$ viewed along the c-axis. Color scheme: Cs in turquoise, Ti in blue, and O in red. Connectivity of Cs ions is not shown for clarity. The black box outlines the unit cell. The illustration was generated by the VESTA software[11] based on the structural model in ref 9.

Mixed-valent titanium oxides are usually synthesized involving a reduction of TiO_2 under an H_2-containing atmosphere,[4,5,7,10] but they can also be obtained by means of high-temperature electrochemical reduction.[9,12] Reid and Watts reported the crystal growth of hollandite-type $Cs_xTi_8O_{16}$ (originally represented as $Cs_xTi_4O_8$ with $x \leq 1$) by constant-current electrolysis of a molten mixture

of TiO_2 and $Cs_2Ti_2O_5$ at 925 °C.[12] They showed that the grown crystals were bronze-colored prisms with an anisotropic semiconductive behavior. Later Abe et al. successfully obtained needle-like $Cs_xTi_8O_{16}$ crystals (x = 1.35) by constant-current electrolysis of a molten mixture of TiO_2 and Cs_2MoO_4 at 900 °C.[9] Alkali-metal molybdenum oxides, A_2MoO_4, were used as efficient flux materials also for the electrochemical crystal growth of manganese oxide perovskites[13,14] and Cr_2O_3.[15] It should be noted that the electrochemically grown $Cs_xTi_8O_{16}$ crystals are favorable for transport measurements owing to their highly anisotropic morphology.

Although the earlier work only employed the crystal growth of $Cs_xTi_8O_{16}$ with constant-current conditions,[9,12] a constant-voltage mode may be more advantageous than the constant-current mode to precisely control the Cs content, because the former will lead to a more stable driving force of reduction. Nevertheless, such studies have never been reported. In this chapter, the electrochemical crystal growth of $Cs_xTi_8O_{16}$ with constant-voltage conditions has been examined. The resultant crystals showed obviously distinct appearances when varying the applied voltage, either optical transparency or metallic luster, suggesting different Cs contents for the two crystals. These results demonstrate that the constant-voltage electrolysis is highly effective to grow crystals with controlled chemical compositions. To the best of the author's knowledge, there were no experimental reports on the growth of transparent crystals of hollandite-type mixed-valent titanium oxides, which could be noteworthy in the research field of optoelectronics.

2.3. Experimental Section

2.3.1. Materials

TiO_2 (anatase, 99%, Kojundo Chemical Laboratory), Cs_2CO_3 (99.9%, Sigma-Aldrich), and MoO_3 (99.98%, Kojundo Chemical Laboratory) were used as received without further purification. Cs_2MoO_4 was prepared by a conventional solid-state reaction technique. A powder mixture of Cs_2CO_3 and MoO_3 with the same molar ratio was put into an alumina crucible and calcined at 600 °C for 12 h in air. Because of its heavily hygroscopic nature, the product was kept in a desiccator as soon as possible.

2.3.2. Electrochemical Crystal Growth

Single crystalline samples of $Cs_xTi_8O_{16}$ were grown by high-temperature constant-voltage (i.e., potentiometric) electrolysis of the molten mixture of TiO_2 and Cs_2MoO_4. An alumina crucible (30 cm^3 in volume) was used as a reaction vessel and filled with 4.0 g of the Cs_2MoO_4 powder. Three Pt wires (0.5 mm in diameter) connected to an external potentiostat (Hokuto Denko: HZ-5000) were introduced into the crucible in a box furnace as the working, counter, and pseudoreference electrodes (WE, CE, and PRE, respectively). A 0.10 g powder of TiO_2 was put in the vicinity of CE to prevent undissolved TiO_2 from being incorporated into grown crystals on WE; PRE and WE were placed near one another. Schematic illustrations of crystal growth equipment are shown in Figure 2.2.

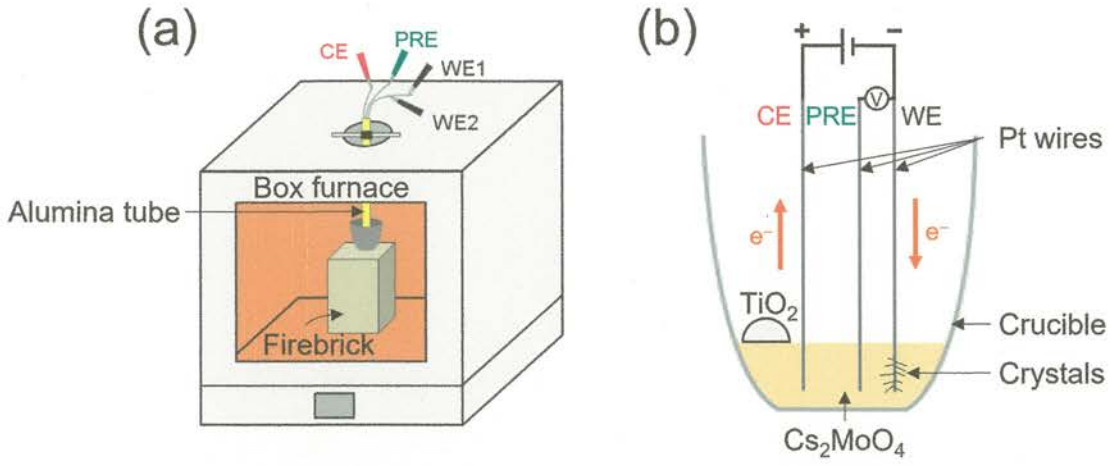

Figure 2.2. Schematic illustrations of equipment for high-temperature molten salt electrolysis, where (a) shows the overall view of the experimental setup and (b) indicates the arrangements of the electrodes and reactants in the crucible.

Cyclic voltammetry (CV) was performed to determine applied voltages for the subsequent constant-voltage electrolysis. Voltage scan range and scan rate were $-2.0\ \text{V} \le V \le 0\ \text{V}$ (vs Pt PRE) and 100 mV s^{-1}, respectively. Electrochemical reduction of TiO_2 at 1050 °C for 5 h was carried out in air with different applied voltages. Based on the result of CV, applied voltage values were set at V = −0.6, −1.0, −1.4, and −1.8 V. At the end of each run, the Pt electrodes were taken out from the furnace to be rapidly cooled to room temperature. Electrolysis for 5 h resulted in deposition of needle-like crystals on WE. The tip part of WE was immersed in distilled water for overnight to dissolve the Cs_2MoO_4 residue and thereby remove the crystals from WE.

2.3.3. Characterization

The resultant crystals were observed by a digital microscope (Keyence: VHX-5000) and field-emission scanning electron microscope (FE-SEM; Hitachi: SU-8010). The chemical composition of the crystals was analyzed by means of energy dispersive X-ray spectroscopy (EDX; Horiba: EMAX-2770) using ground crystals. The Cs/Ti cationic ratios were determined for the crystals grown with V = −0.6 V and −1.0 V by inductively coupled plasma-mass spectroscopy (ICP-MS; PerkinElmer: ELAN DRC II). The valence state of titanium was investigated by means of X-ray photoelectron spectroscopy (XPS; Ulvac-Phi: Model 5500; Mg Kα radiation). Phase identification of the grown crystals was conducted using a powder X-ray diffractometer (Rigaku: Ultima IV Protectus; Cu Kα radiation). The grown crystals were evenly spread on a "non-reflection" sample holder made of an obliquely cut silicon crystal, and analyzed in a 2θ range of 10°–90° with a step size of 0.02° (operating condition: 40 kV, 40 mA).

Single-crystal X-ray diffraction (SCXRD) was carried out utilizing a four-circle diffractometer (Rigaku: Saturn70; Mo Kα radiation). A cylindrical crystal of approximate dimensions 0.03 × 0.03 × 0.13 mm^3 was selected for data collection. The intensity data were collected by the ω scan method at 113 K (operating condition: 50 kV, 60 mA). The crystal structure was solved by direct methods (SHELXS97) and refined by full-matrix least-squares calculations on F^2 using SHELXL97 program.[16] All the atoms in the crystal lattice were refined anisotropically. Electrical resistivity (ρ) measurements were performed employing a four-probe technique (PPMS; Quantum Design) in a temperature range of 2–300 K.

2.4. Results and Discussion

2.4.1. Crystal Growth

Figure 2.3 shows a cyclic voltammogram of the molten mixture of TiO_2 and Cs_2MoO_4 at 1050 °C. When the applied voltage reaches approximately $V = -0.6$ V in the forward (cathodic) sweep, a small current with negative sign arises, indicating that a reduction reaction of TiO_2 takes place below −0.6 V. Then, the negative current starts to increase rapidly below −1.0 V and reaches −50 mA at −2.0 V. In the backward (anodic) sweep, the negative current steadily decreases and converges to 0 mA when the applied negative voltage is decreased. Clear oxidation peaks are not observed, presumably because of high electrochemical stability of the deposited crystals. The redox reactions at WE and CE can be described with the following formulas:

$$\text{WE: } 8TiO_2 + xCs^+ + xe^- \rightarrow Cs_xTi_8O_{16} \quad (1)$$

$$\text{CE: } x/2MoO_4^{2-} \rightarrow xe^- + x/2MoO_3 + x/4O_2 \quad (2)$$

Therefore, the overall reaction for the $Cs_xTi_8O_{16}$ formation is represented as

$$\text{Overall: } 8TiO_2 + x/2Cs_2MoO_4 \rightarrow Cs_xTi_8O_{16} + x/2MoO_3 + x/4O_2 \quad (3)$$

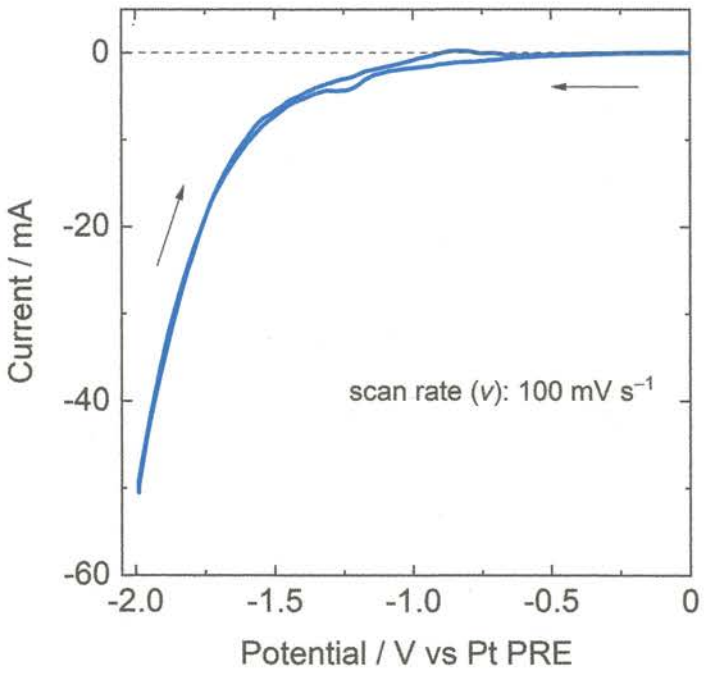

Figure 2.3. Cyclic voltammogram of the molten mixture of TiO_2 and Cs_2MoO_4 at 1050 °C in air. This plot was recorded at v = 100 mV s^{-1} with 0.5 mm-diameter Pt wire working, counter, and pseudoreference electrodes. Arrows mark the potential-scan direction. The horizontal broken line is a guide of 0 mA.

Electrochemical reduction reactions with constant-voltage conditions were conducted. Taking into account the result of CV, the applied voltages were set at onset (−0.6 V), moderate (−1.0 V), and high (−1.4 and −1.8 V) values. The shape of the resultant crystals is highly anisotropic, with the maximum length of ~2 mm (Figure 2.4). Noticeably, the appearance of the crystals depends on the applied voltage: the crystals are brownish with optical transparency for V = −0.6 V, while they show metallic luster for V = −1.0, −1.4, and −1.8 V. It should be noted that attempts with the constant-current mode always resulted in the growth of metallic luster crystals (Figure S2.1 of the Supporting Information), and optically transparent crystals were never obtained, consistent with the previous reports.[9,12]

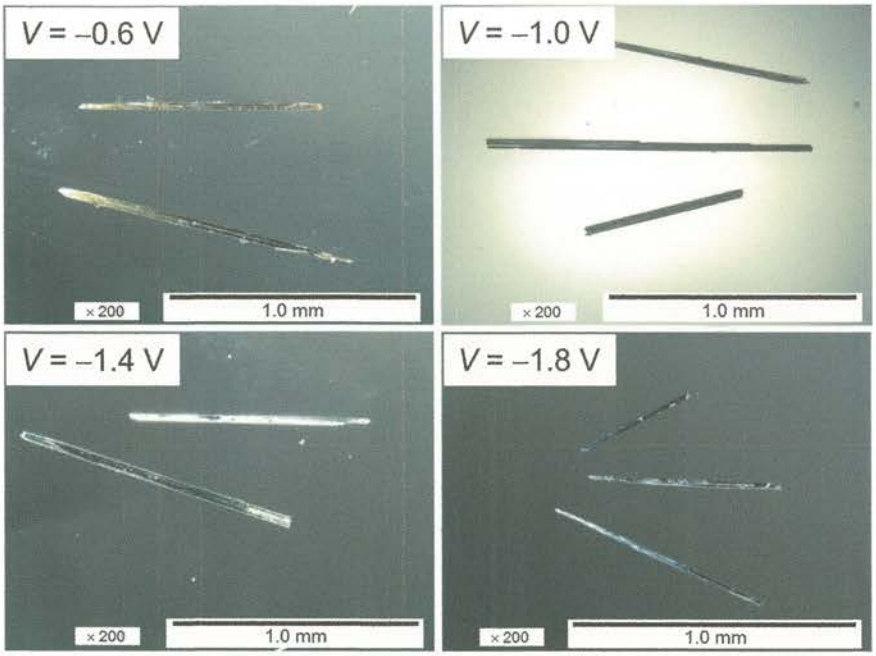

Figure 2.4. Optical micrographs of the crystals grown with the different applied voltages $V = -0.6$, -1.0, -1.4, and -1.8 V.

The distinct appearances most likely originate from different electronic properties. In fact, electron irradiation during SEM observations led to a severe charging effect only for the crystals grown with $V = -0.6$ V, as shown in Figure S2.2. This feature implies that the transparent crystals are electrically insulating, and hence the Cs content (x) would be lower than that in the metallic luster crystals. The x values estimated from EDX data were 1.4 ± 0.2 for both of the transparent and metallic luster crystals (Figure S2.3): the Cs/Ti ratio seems to be similar and cannot be distinguished. The Cs/Ti ratios of the crystals grown with $V = -0.6$ V and -1.0 V were also analyzed by ICP-MS (see Supporting Information for experimental details). The x values are 1.3–1.4 for both of the $V = -0.6$ V and -1.0 V crystals (Table S2.1): again, the Cs content cannot be distinguished within the accuracy of the chemical analyses.

The fact that the Cs/Ti ratios are close to each other between the optically transparent and metallic

luster crystals is worthy of attention. This feature is not surprising, as it is widely known that electronic properties of strongly correlated electron systems are often very sensitive to the carrier concentration. To investigate the valence state of titanium in the grown crystals, XPS measurements were performed. Experimental details are given in the Supporting Information. Ti 2p core-level spectra of the $Cs_xTi_8O_{16}$ crystals evidenced a negative chemical shift with respect to the TiO_2 reference (Figure S2.4). In addition, spectral deconvolution analysis indicated that each of the Ti $2p_{3/2}$ and $2p_{1/2}$ peaks can be fitted with two peaks, and the component at lower binding energies (E_B) gets enhanced as the negative voltage during the electrolysis is increased. Although the negative chemical shifts as well as the low-E_B component is consistent with the existence of reduced Ti species,[17] the author notes that this XPS result is preliminary, and further studies will be necessary to quantitatively discuss the valence state of titanium in the $Cs_xTi_8O_{16}$ crystals.

Powder X-ray diffraction (PXRD) patterns for the as-grown (i.e., nonpulverized) crystals are presented in Figure 2.5. While all the patterns exhibit common features typically seen for hollandite-type oxides, diffraction peaks with *hk*0 are only seen, reflecting highly anisotropic morphology with the longitudinal direction along the *c*-axis. These peaks are readily indexed based on a tetragonal unit cell, resulting in lattice parameters close to the literature values (a = 10.2866 Å and c = 2.9669 Å (ref 9)). Systematic changes in the lattice parameters expected for the sample series are not observed, probably because of poor accuracy of the diffraction data caused by misalignment of crystals mounted on the sample holder. For the $Cs_xTi_8O_{16}$ crystals, powder patterns were hardly obtained because the crystals were subject to mechanical fragility and easily amorphized when ground intensely.

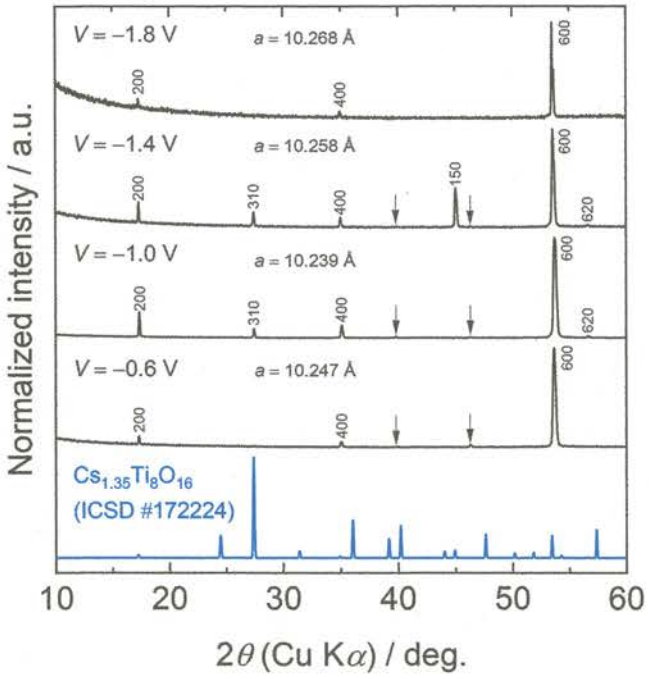

Figure 2.5. PXRD patterns for the nonpulverized crystals grown with $V = -0.6$, -1.0, -1.4, and -1.8 V. The simulated pattern for $Cs_{1.35}Ti_8O_{16}$ (ICSD #172224) was taken from the ICSD database. Arrows indicate unidentified reflections.

Some peaks are still unknown (marked with arrows), assignable to neither the hollandite-related structures nor the starting materials. Carter and Withers reported the appearance of extra reflections originating from an incommensurate sublattice in barium titanium oxide hollandites $Ba_xM_yTi_{8-y}O_{16}$ (M = Mg, Mn, Fe, Co, Ni, and Zn).[18,19] While the possibility that the extra reflections come from the Cs sublattice cannot be ruled out, the author tentatively concludes that this possibility is rather unlikely. The reasons are as follows: (1) There are no satellite reflections in the SCXRD pattern for the $V = -1.0$ V crystal. (2) The $Cs_xTi_8O_{16}$ crystals were relatively rapidly cooled to room temperature at the last process of the crystal growth. It has been recognized that the long-range order of the tunnel-site ions is smeared or disrupted in rapidly cooled samples, resulting in satellite reflections becoming weaker and broader.[19]

2.4.2. Structure Refinements and Description

Structural refinements for the grown crystals were attempted based on the SCXRD data. The crystallographic data, refinement details, and atomic coordinates for the metallic luster crystal grown with $V = -1.0$ V are listed in Tables 2.1–2.3. Meanwhile, refinements of the transparent crystals ($V = -0.6$ V) were unsuccessful, due to the inferior quality of the grown crystals (it should be noted that the analysis is severely hindered even with tiny crystalline defects). The diffraction pattern for the $V = -1.0$ V crystal is indexed based on a tetragonal unit cell with $I4/m$ space group, and the lattice parameters are determined to be $a = 10.2323(14)$ Å and $c = 2.9514(6)$ Å. These values are somewhat smaller than those of polycrystalline $Cs_{1.36(3)}Ti_8O_{16}$ refined with neutron diffraction data at 100 K:[21] $a = 10.2705(2)$ Å and $c = 2.96469(5)$ Å.

Table 2.1. Crystallographic data and refinement details for $Cs_{1.22}Ti_8O_{16}$.

Crystallographic data:	
formula	$Cs_{1.22}Ti_8O_{16}$
formula weight	801.35
crystal system	tetragonal
space group	$I4/m$ (no. 87)
a / Å	10.2323(14)
c / Å	2.9514(6)
V / Å^3	309.01(9)
Z	1
D_{calc} / g cm^{-3}	4.306
d_{Ti-O1} / Å	(2×) 1.947(3)
	2.017(5)
d_{Ti-O2} / Å	(2×) 1.974(3)
	1.938(5)

Table 2.1. continued.

[a]BVS for Ti	+3.998
Data collection:	
temperature / K	113
crystal dimensions / mm^3	$0.03 \times 0.03 \times 0.13$
μ(Mo Kα) / mm^{-1}	8.529
scan mode	ω
maximum 2θ/ deg.	60.8
index ranges	$-12 \le h \le 14$, $-14 \le k \le 14$, $-4 \le l \le 3$
no. of measured reflections	1293
no. of independent reflections	256
no. of observed reflections with $I > 2\sigma(I)$	207
R_{int}	0.1043
Refinement:	
calculated weights	$w = 1/[\sigma^2(F_o^2) + (0.0469P)^2]$ where $P = (F_o^2 + 2F_c^2)/3$
final R indices $[I > 2\sigma(I)]$[b]	$R_1 = 0.0499$, $wR_2 = 0.1024$
R indices (all data)[b]	$R_1 = 0.0641$, $wR_2 = 0.1120$
goodness-of-fit (GOF)	1.091
no. of refined parameters	24
largest difference peak and hole / e $Å^{-3}$	1.26, −1.26

[a]The BVS parameters used as follows: Ti^{4+}–O^{2-} ($l_0 = 1.815$)[20]

[b]$R_1 = \Sigma||F_o|-|F_c||/\Sigma|F_o|$, $wR_2 = [\Sigma w(F_o^2-F_c^2)^2/\Sigma w(F_o^2)^2]^{1/2}$

Table 2.2. Atomic coordinates, equivalent isotropic displacement parameters (U_{eq}) and occupancy factors (g) for $Cs_{1.22}Ti_8O_{16}$.

atom	site	g	x	y	z	U_{eq} / Å^2 [a]
Cs1	2*a*	0.11	1.0000	0	0	0.01(4)
Cs2	4*e*	0.25	1.0000	0	–0.10(2)	0.008(5)
Ti	8*h*	1.0	1.33382(12)	0.15034(12)	0	0.0075(4)
O1	8*h*	1.0	1.2099(4)	0.1574(4)	–0.5000	0.0034(9)
O2	8*h*	1.0	1.3337(4)	–0.0391(4)	0	0.0046(10)

[a] U_{eq} is defined as one-third of the trace of the orthogonalized U_{ij} tensor.

Table 2.3. Atomic anisotropic displacement parameters for $Cs_{1.22}Ti_8O_{16}$.

atom	U_{11}	U_{22}	U_{33}	U_{12}	U_{13}	U_{23}
Cs1	0.008(10)	0.008(10)	0.01(11)	0	0	0
Cs2	0.005(2)	0.005(2)	0.014(18)	0	0	0
Ti	0.0080(7)	0.0068(7)	0.0077(8)	0.0014(4)	0	0
O1	0.005(2)	0.003(2)	0.003(2)	0.0011(16)	0	0
O2	0.003(2)	0.006(2)	0.004(2)	–0.0009(16)	0	0

The local coordination environments around the Ti and Cs atoms are shown in Figure 2.6. The Ti atom is coordinated by six O atoms to form a distorted octahedron (Figure 2.6a). The Cs position was refined assuming a split-site model, because a preliminary analysis locating Cs atoms only on the symmetrical 2*a* position at (1, 0, 0) led to large residual electron density around this site. This can be interpreted as the presence of static displacement of Cs atoms, and it may be reasonable to refine the data setting a less-symmetrical site (assigned as "4*e*") at (1, 0, *z*) in addition to the 2*a* site (Figure 2.6b). The refinement with this split-site model indeed improved the goodness-of-fit factor. The occupancy factors (*g*) of Cs atoms were converged to 0.11 and 0.25 for the Cs1 (2*a*)- and Cs2 (4*e*)-sites, respectively. From the refined occupancy factors of the constituent elements, the chemical composition can be written as $Cs_{1.22}Ti_8O_{16}$. This implies that Cs atoms are present at a 30% probability within the 1D cavity randomly occupying either symmetrical or less-symmetrical site. As shown in Table 2.3, the atomic displacement parameters for the Cs sites are highly anisotropic along the *c*-axis, that is, larger value for U_{33} than U_{11} and U_{22}. Similar features were reported for other hollandite-type oxides, including $K_2Ru_8O_{16}$ (ref 22), $K_2V_8O_{16}$ (ref 23), $K_2Ir_8O_{16}$ (ref 24), and $Cs_{1.1}Ti_8O_{16}$ (ref 25), in which unusual *A*-site occupancies[23] or competitions between atomic size and bond valence were taken into account.[24]

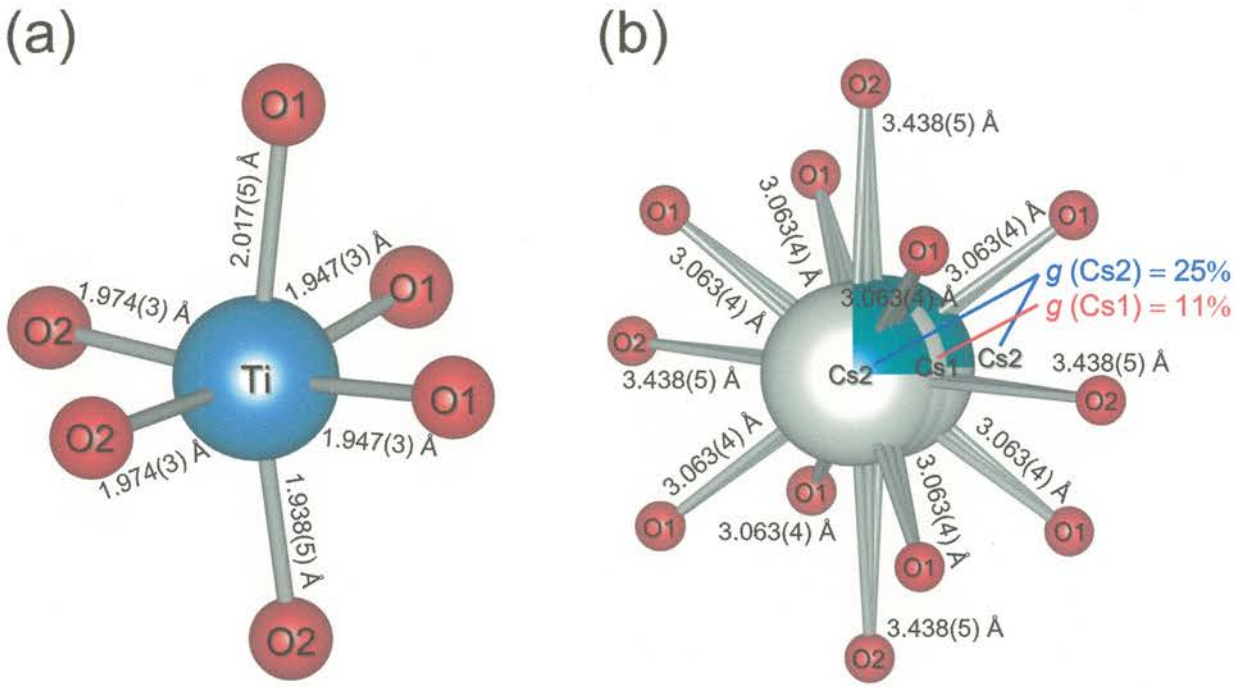

Figure 2.6. Local coordination environments around the (a) Ti and (b) Cs cations in the $Cs_{1.22}Ti_8O_{16}$ hollandite structure. The color scheme is the same as Figure 2.1. The Ti and Cs cations are coordinated by six and twelve O anions, respectively, forming a distorted octahedron and an octadecahedron. The Cs cation is disordered over two positions, Cs1 (2*a*) and Cs2 (4*e*), along the *c*-axis. For the image (b), the interatomic distances of the Cs1–O1 and Cs1–O2 bonds are shown and those of the Cs2–O1 and Cs2–O2 bonds are omitted. The occupancy factors (*g*) of the Cs1 and Cs2 sites are shown in red and blue, respectively.

2.4.3. Electronic Properties

In Figure 2.7, electrical resistivity (ρ) along the *c*-axis is plotted as a function of temperature for the crystals grown with $V = -1.0$ V and -1.8 V. The resistivity data for the $V = -0.6$ V and -1.4 V crystals were less reliable and hence excluded from the figure, because of quite low bulk conductivity for the former, and non-ohmic contacts of gold electrodes attached on a too small crystal for the latter. As the temperature is lowered, the resistivity values for the $V = -1.0$ V and -1.8 V crystals are enhanced and eventually unable to be measured at approximately 100 and 75 K, respectively. Both crystals show a semiconducting behavior with relatively small resistivity values of 10^2–10^3 Ω m at room temperature. The magnitude of resistivity is lower for the $V = -1.8$ V crystal than the $V = -1.0$ V crystal, strongly suggesting that the former is more electron-doped than the latter.

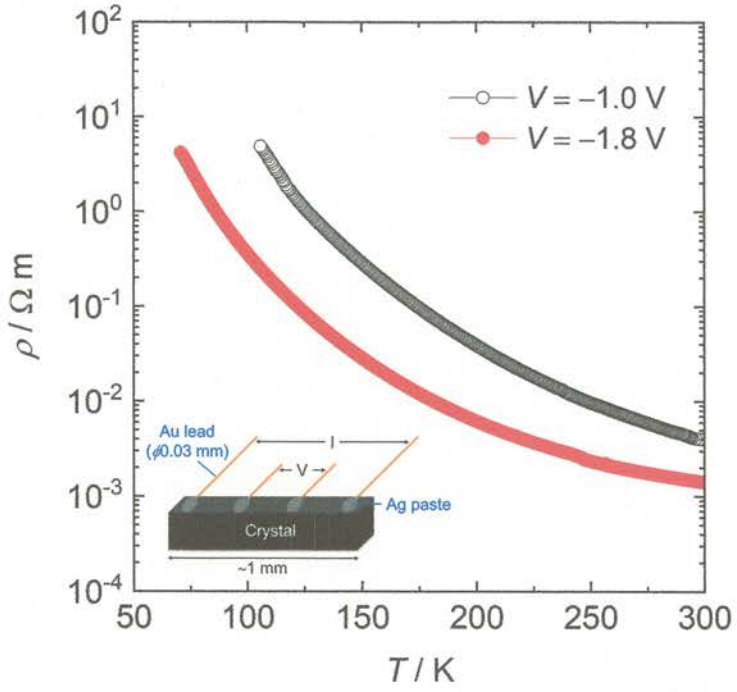

Figure 2.7. Temperature dependence of electrical resistivity (ρ) for the crystals grown with $V = -1.0$ V (empty black circles) and -1.8 V (filled red circles). Inset shows a schematic illustration of the electrical resistivity measurements with a four-probe configuration.

The ρ–T curves do not follow the Arrhenius law (Figure 2.8a), but they are nicely fitted with the variable range hopping (VRH) model (Figure 2.8b–d). The VRH model describes electrical conduction mechanisms where the periodicity of the crystal lattice is disturbed by randomness and/or defects, and electron conduction takes place via tunneling effects, which leads to the following equation:[26,27]

$$\rho \propto \exp[(T_0/T)^{1/(n+1)}] \qquad (4)$$

where T_0 and n denote a characteristic temperature and the dimensionality, respectively. Least-squares calculations of the ρ–T curves were carried out for $n = 1$, 2, and 3, and the calculation with $n = 1$ gave the best fit for the both crystals (Figure 2.8b). This result indicates that the crystals are likely to be so-called "disordered metals" containing 1D-tunnel structures occupied by Cs atoms. Moetakef et al. recently reported crystal growth and density functional theory (DFT) study of a related hollandite, $K_xTi_8O_{16}$ ($x = 1.4$).[10,28] Their calculations indicated that a finite density of states (DOS) exists at the Fermi level, consistent with the metallic character of the $V = -1.0$ V and -1.8 V crystals. The random Cs distribution as revealed by the structural analysis is the possible source of the disturbed periodic potential. The T_0 values are 13.4 and 11.6 K for the $V = -1.0$ V and -1.8 V crystals, respectively. Because the T_0 value is related to a degree of localization, the smaller T_0 value for the crystal with $V = -1.8$ V is consistent with the fact that the crystals grown with larger negative voltages tend to be more carrier-doped because of stronger reductive conditions.

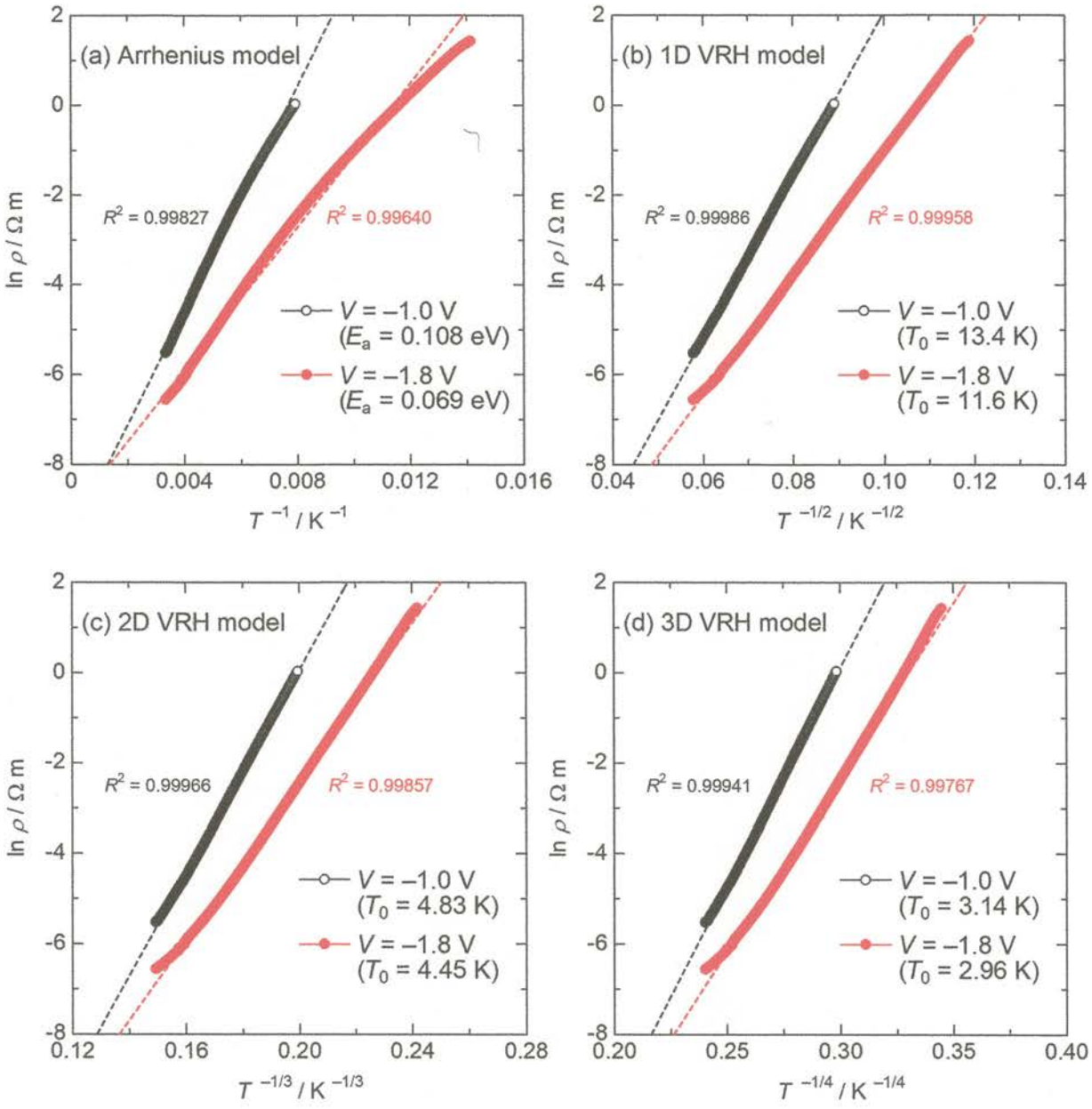

Figure 2.8. Ln ρ vs $T^{-1/n+1}$ (n = 0, 1, 2, 3) curves for the crystals grown with V = –1.0 V (empty black circles) and –1.8 V (filled red circles) plotted based on the (a) Arrhenius (n = 0), (b) 1D VRH (n = 1), (c) 2D VRH (n = 2), and (d) 3D VRH (n = 3) models. The best fit is obtained in (b).

Finally, the author comments on the optical property of hollandite-type $Cs_xTi_8O_{16}$ and its possible applications to optoelectronics. A recent theoretical work by Buckeridge et al. revealed that the band structures of TiO_2 can be tuned largely by varying the local coordination environments of Ti and O.[29] Among eight known polymorphs, hollandite TiO_2 may be noteworthy because the hollandite has the largest work function together with the large band gap. Such a characteristic feature makes this polymorph a potential transparent conducting oxide (TCO) used for photovoltaic devices as well as short-wavelength light emitting diodes.[29] The transparent $Cs_xTi_8O_{16}$ crystals obtained herein are too resistive at this moment, but optimally doped $Cs_xTi_8O_{16}$ crystals may be noteworthy as promising TCOs, if further electron doping is possible while retaining their transparency.

2.5. Concluding Remarks

This chapter demonstrated the electrochemical crystal growth of hollandite-type $Cs_xTi_8O_{16}$ employing high-temperature electrolysis of the molten mixture of TiO_2 and Cs_2MoO_4 with constant-voltage conditions. Needle-like single crystals were successfully grown with different applied voltages of $V = -0.6$, -1.0, -1.4, and -1.8 V. Importantly, the resultant crystals showed obviously distinct appearances and electronic properties: while the crystals grown with $V = -0.6$ V were electrically insulating with optical transparency, the crystals with $V = -1.0$, -1.4, and -1.8 V were moderately conductive with metallic luster. As far as the author knows, there are no experimental reports on the growth of transparent crystals of hollandite-type mixed-valent titanium oxides, which could be noteworthy in the research field of optoelectronics.

The author emphasizes that the $Cs_xTi_8O_{16}$ crystals grown with constant-voltage conditions are chemically well-controlled and sufficiently large in size for physical property measurements. This technique may be applicable to crystal growth of various transition metal oxide systems, and the

resultant crystals are valuable for systematic studies on their optical/electronic properties in relation to the chemical composition.

Accession Codes

CCDC 1545319 contains the supplementary crystallographic data for this chapter. These data can be obtained free of charge via www.ccdc.cam.ac.uk/data_request/cif, or by emailing data_request@ccdc.cam.ac.uk, or by contacting The Cambridge Crystallographic Data Centre, 12 Union Road, Cambridge CB2 1EZ, UK; fax: +44 1223 336033.

Rights and Permission

References

(1) See, for example, Kishio, K. Anisotropy in HTSC Oxides: Its Chemical Control and Flux Pinning. In *Coherence in High Temperature Superconductors,* Deutscher, G.; Revcolevschi, A., Eds.; World Scientific: Singapore, 1996; pp 212–225.

(2) See, for example, Tokura, Y.; Tomioka, Y. Colossal Magnetoresistive Manganites. *J. Magn. Magn. Mater.* **1999,** *200,* 1–23.

(3) Johnston, D. C. Superconducting and Normal State Properties of $Li_{1+x}Ti_{2-x}O_4$ Spinel Compounds. I. Preparation, Crystallography, Superconducting Properties, Electrical Resistivity, Dielectric Behavior, and Magnetic Susceptibility. *J. Low Temp. Phys.* **1976,** *25,* 145–175.

(4) Sakurai, H.; Kato, M.; Yoshimura, K.; Tsujii, N.; Kosuge, K. Metal-Insulator Transition in Na_xTiO_2 (x = 0.20–0.25). *Phys. Rev. B: Condens. Matter Mater. Phys.* **2007,** *75,* 115128.

(5) Muraoka, Y.; Noami, K.; Wakita, T.; Hirai, M.; Yokoya, T.; Kayo, Y.; Muro, T; Tamenori, Y. Synthesis and Physical Properties of the Hollandite-Type Titanium Oxide $K_xTi_8O_{16}$. *Phys. Status Solidi C* **2011,** *8,* 555–557.

(6) Yoshikado, S.; Taniguchi, I.; Watanabe, M.; Onoda, Y.; Fujiki, Y. Frequency Dependence of Ionic Conductivity in One-Dimensional Ionic Conductors $K_{1.6}Mg_{0.8}Ti_{7.2}O_{16}$ and $K_{1.6}Al_{1.6}Ti_{6.4}O_{16}$. *Solid State Ionics* **1995,** *79,* 34–39.

(7) Sakao, M.; Kijima, N.; Akimoto, J.; Okutani, T. Lithium Insertion and Extraction Properties of Hollandite-Type K_xTiO_2 with Different K Content in the Tunnel Space. *Solid State Ionics* **2013,** *243,* 22–29.

(8) Kijima, N.; Sakao, M.; Tanuma, Y.; Kataoka, K.; Igarashi, K.; Akimoto, J. Synthesis, Crystal Structure, and Electrochemical Properties of Hollandite-Type $K_xTi_{1-y}Mn_yO_2$. *Solid State Ionics* **2014,** *262,* 14–17.

(9) Abe, H.; Satoh, A.; Nishida, K.; Abe, E.; Naka, T.; Imai, M.; Kitazawa, H. Electrochemical Immobilization of Cs in Single-Crystalline SYNROC. *J. Solid State Chem.* **2006,** *179,* 1521–1524.

(10) Moetakef, P.; Larson, A. M.; Hodges, B. C.; Zavalij, P.; Gaskell, K. J.; Piccoli, P. M.; Rodriguez,

E. E. Synthesis and Crystal Chemistry of Microporous Titanates $K_x(Ti,M)_8O_{16}$ where M = Sc–Ni. *J. Solid State Chem.* **2014**, *220*, 45–53.

(11) Momma, K.; Izumi, F. *VESTA 3* for Three-Dimensional Visualization of Crystal, Volumetric and Morphology Data. *J. Appl. Crystallogr.* **2011**, *44*, 1272–1276.

(12) Reid, A. F.; Watts, J. A. Single Crystal Syntheses by the Electrolyses of Molten Titanates, Molybdates and Vanadates. *J. Solid State Chem.* **1970**, *1*, 310–318.

(13) McCarroll, W. H.; Ramanujachary, K. V.; Greenblatt, M. Synthesis of Doped Rare Earth Manganate Perovskite Crystals Using Fused Salt Electrolysis. *J. Solid State Chem.* **1997**, *130*, 327–329.

(14) McCarroll, W. H.; Ramanujachary, K. V.; Fawcett, I. D.; Greenblatt, M. Electrical and Magnetic Properties of Strontium Substituted Lanthanum Manganate Perovskite Crystals Prepared Using Fused Salt Electrolysis. *J. Solid State Chem.* **1999**, *145*, 88–96.

(15) Abe, H.; Nishida, K.; Imai, M.; Kitazawa, H. Electrochemical Preparation of Single-Crystalline Cr_2O_3 from Molten Salts. *J. Cryst. Growth* **2004**, *267*, 42–46.

(16) Sheldrick, G. M. A Short History of *SHELX*. *Acta Crystallogr., Sect. A: Found. Crystallogr.* **2008**, *64*, 112–122.

(17) González-Elipe, A. R.; Munuera, G.; Espinos, J. P.; Sanz, J. M. Compositional Changes Induced by 3.5 keV Ar^+ Ion Bombardment in Ni-Ti Oxide Systems: A Comparative Study. *Surf. Sci.* **1989**, *220*, 368–380.

(18) Carter, M. L.; Withers, R. L. An Electron and X-ray Diffraction Study of the Compositely Modulated Barium Nickel Hollandite $Ba_x(Ni_xTi_{8-x})O_{16}$, $1.16 < x < 1.32$, Solid Solution. *Z. Kristallogr.—Cryst. Mater.* **2004**, *219*, 763–767.

(19) Carter, M. L.; Withers, R. L. A Universally Applicable Composite Modulated Structure Approach to Ordered $Ba_xM_yTi_{8-y}O_{16}$ Hollandite-Type Solid Solutions. *J. Solid State Chem.* **2005**, *178*, 1903–1914.

(20) Brese, N. E.; O'Keeffe, M. Bond-Valence Parameters for Solids. *Acta Crystallogr., Sect. B: Struct. Sci.* **1991**, *47*, 192–197.

(21) Cheary, R. W. Caesium Substitution in the Titanate Hollandites $Ba_xCs_y(Ti^{3+}_{y+2x}Ti^{4+}_{8-2x-y})O_{16}$ from 5 to 400 K. *Acta Crystallogr., Sect. B: Struct. Sci.* **1991**, *47*, 325–333.

(22) Djafri, F.; Canonne, J.; Abraham, F.; Thomas, D. Insertion du lithium dans la phase de structure hollandite: $K_xRu_8O_{16}$ ($x \approx 1,5$). *J. Less-Common Met.* **1985**, *109*, 323–329.

(23) Abriel, W.; Rau, F.; Range, K.-J. New Compounds $A_{2-x}V_8O_{16}$ (A = K, Tl) with Hollandite Type Structure. *Mater. Res. Bull.* **1979**, *14*, 1463–1468.

(24) Talanov, A.; Phelan, W. A.; Kelly, Z. A.; Siegler, M. A.; McQueen, T. M. Control of the Iridium Oxidation State in the Hollandite Iridate Solid Solution $K_{1-x}Ir_4O_8$. *Inorg. Chem.* **2014**, *53*, 4500–4507.

(25) Fanchon, E.; Hodeau, J. L.; Vicat, J.; Watts, J. A. Three-Dimensional/One-Dimensional Transition in the Cs^+ Sublattice of the Mixed Valence $CsTi_8O_{16}$ Hollandite: Structures at 297 and 673 K. *J. Solid State Chem.* **1991**, *92*, 88–100.

(26) Shante, V. K. S.; Varma, C. M. Hopping Conductivity in "One-Dimensional" Disordered Compounds. *Phys. Rev. B: Condens. Matter Mater. Phys.* **1973**, *8*, 4885–4889.

(27) Corraze, B.; Ribault, M. One-Dimensional Variable Range Hopping Conduction in a Single Crystal of La_2CuO_{4+y}. *Phys. Lett. A* **1993**, *173*, 479–483.

(28) Moetakef, P.; Wang, L.; Maughan, A. E.; Gaskell, K. J.; Larson, A. M.; Hodges, B. C.; Rodriguez, E. E. Tuning the Electronic Band Structure of Microporous Titanates with the Hollandite Structure. *J. Mater. Chem. A* **2015**, *3*, 20330–20337.

(29) Buckeridge, J.; Butler, K. T.; Catlow, C. R. A.; Logsdail, A. J.; Scanlon, D. O.; Shevlin, S. A.; Woodley, S. M.; Sokol, A. A.; Walsh, A. Polymorph Engineering of TiO_2: Demonstrating How Absolute Reference Potentials Are Determined by Local Coordination. *Chem. Mater.* **2015**, *27*, 3844–3851.

Chapter 3

Structural Design of Alkali-Metal Titanates: Electrochemical Growth of $K_xTi_8O_{16}$, $Na_{2+x}Ti_6O_{13}$, and $Li_{2+x}Ti_3O_7$ Single Crystals with One-Dimensional Tunnel Structures

3.1. Abstract

Single crystals of lithium, sodium, and potassium titanates were grown with high-temperature constant-voltage electrolysis of TiO_2 with A_2MoO_4 (A = Li, Na, and K) as melts. Using the potassium-containing melt, needle-like crystals of hollandite-type $K_xTi_8O_{16}$ with a maximum length of ~1 mm were successfully obtained. On the other hand, needle-like crystals of $Na_{2+x}Ti_6O_{13}$ and ramsdellite-type $Li_{2+x}Ti_3O_7$ with a maximum length of ~3 mm were grown when the sodium- and lithium-containing melts were employed, respectively. This chapter demonstrates that the electrochemical crystal growth is favorable to obtain titanates with various one-dimensional tunnel structures upon varying the alkali-metal elements. The diversity in structural types of the resultant single crystals is reasonably explained in terms of the ionic size of the alkali metals incorporated.

3.2. Introduction

Titanium dioxide (TiO_2) is an important material because of its large potential for practical applications in pigments,[1] water splitting photocatalysts,[2] and dye-sensitized solar cells (DSCs).[3] TiO_2 has numerous polymorphs, such as anatase (space group $I4_1/amd$), rutile ($P4/mnm$), brookite ($Pbca$), TiO_2(B) ($C2/m$), α-PbO_2 ($Pbcn$), ramsdellite ($Pbnm$), hollandite ($I4/m$), and baddeleyite ($P2_1/c$). Among these polymorphs, rutile, anatase, brookite, and TiO_2(B) are naturally-occurring phases, but the others are synthetic ones.[4] A recent theoretical study by Buckeridge et al. indicated that the band structures of TiO_2 can be tuned largely by varying the local coordination environments of Ti and O.[5] For instance, hollandite-type TiO_2 is noteworthy because hollandite has the largest work function together with a large band gap of 3.86 eV. Such a characteristic feature makes this polymorph a potential transparent conducting oxide (TCO) applicable to photovoltaic devices as well as short-wavelength light emitting diodes.[5] Polymorph engineering of TiO_2 thus offers significant and novel functionalities. Incorporation of alkali-metal ions in the crystal lattice of TiO_2 seems to be one of the most effective routes to obtain TiO_2 polymorphs, because such cations with different ionic sizes have large impacts on the atomic configuration in the crystal lattice. Because incorporated alkali-metal ions are weakly bound to the TiO_2 framework, TiO_2 polymorphs may be obtained accordingly by means of topotactic alkali-metal extraction.

Alkali-metal titanates containing reduced Ti species also display various interesting electronic and magnetic properties originating from mixed-valent Ti^{3+}/Ti^{4+}. For instance, $LiTi_2O_4$ is known to be the only spinel-structured oxide superconductor with $T_c \sim 13.7$ K, which was first discovered by Johnston et al.[6,7] Wadsley-bronze, $Na_{0.25}TiO_2$ with a TiO_2(B)-based structure, shows a magnetic transition at T_c = 430 K, followed by a metal–insulator transition at T_p = 630 K.[8] Furthermore, magnetization measurements of hollandite-type $K_{1.46}Ti_8O_{16}$ revealed small spontaneous magnetization at room

temperature suggesting the appearance of weak ferromagnetism.[9] These oxides generally show a great deal of alkali-metal nonstoichiometry, leading to diversity in electronic/magnetic properties as a function of the alkali-metal content.

Mixed-valent alkali-metal titanates are usually accessible via reduction of TiO_2 under a H_2-containing atmosphere.[6,8–10] Meanwhile, several researchers reported the crystal growth of mixed-valent alkali-metal titanates employing high-temperature electrolysis of molten salts. Single crystals of the superconducting spinel $LiTi_2O_4$ were successfully grown by constant-current electrolysis with a mixture of $NaBO_2$, $LiBO_2$, NaF, and TiO_2 at 780 °C[11] or with a mixture of $Na_2B_4O_7$, LiF, Li_2CO_3, and TiO_2 at 1000 °C.[12] Single crystals of hollandite-type $Cs_xTi_8O_{16}$ were grown by constant-current electrolysis of a molten mixture of TiO_2 and $Cs_2Ti_2O_5$ at 925 °C[13] or TiO_2 and Cs_2MoO_4 at 900 °C.[14]

Recently, the author achieved crystal growth of $Cs_xTi_8O_{16}$ with controlled electronic properties by employing constant-voltage electrolysis of a TiO_2/Cs_2MoO_4 mixture.[15] The author anticipated that the constant-voltage mode is more advantageous than the constant-current mode to precisely control the carrier content owing to the more stable driving force of reduction for the former. Consequently, needle-like $Cs_xTi_8O_{16}$ crystals with distinct appearances, either optical transparency or metallic luster, were successfully obtained.[15] While the transparent crystals were electrical insulators, the metallic luster crystals were moderately conductive, suggesting that the carrier content in the transparent crystals would be lower than that in the metallic luster crystals. It is noteworthy that the transparent $Cs_xTi_8O_{16}$ crystals were never grown by means of any other techniques, emphasizing the advantage of the constant-voltage electrolysis.

Given the fact that hollandite $Cs_xTi_8O_{16}$ crystals with controlled electronic properties are formed with the electrolysis of the molten TiO_2/Cs_2MoO_4 mixture, crystal growth of titanates with different alkali-metal-containing melts are also intriguing to explore novel electronic functionalities. In this chapter, the electrochemical crystal growth of lithium, sodium, and potassium titanates under

constant-voltage conditions has been examined starting from a molten mixture of TiO_2 and A_2MoO_4 (A = Li, Na, and K) to discuss the influence of the ionic size of the alkali-metal elements on the crystal structure. Needle-like single crystals of $K_xTi_8O_{16}$ (hollandite-type), $Na_{2+x}Ti_6O_{13}$, and $Li_{2+x}Ti_3O_7$ (ramsdellite-type) were successfully grown. Remarkably, each crystal lattice is featured with a one-dimensional tunnel structure. The diversity in structural types is reasonably explained in terms of the ionic size of alkali metals incorporated.

3.3. Experimental Section

3.3.1. Materials

TiO_2 (anatase, 99%, Kojundo Chemical Laboratory), Li_2CO_3 (99.99%, Kojundo Chemical Laboratory), Na_2CO_3 (99.8%, FUJIFILM Wako Pure Chemical), K_2CO_3 (99.5%, FUJIFILM Wako Pure Chemical), and MoO_3 (99.98%, Kojundo Chemical Laboratory) were used as received without further purification. A_2MoO_4 (A = Li, Na, or K) was prepared by a conventional solid-state reaction technique using MoO_3 and the corresponding carbonate, Li_2CO_3, Na_2CO_3, or K_2CO_3. Stoichiometric amounts of these reagents were thoroughly ground in an agate mortar. Subsequently, the mixture was transferred into a 3 mol % yttria-stabilized zirconia (3YSZ) crucible and calcined at 600 °C for 12 h in air. After calcination, phase-pure white (colorless) A_2MoO_4 powder was obtained.

3.3.2. Electrochemical Crystal Growth

Single crystals of lithium, sodium, and potassium titanates were grown with high-temperature constant-voltage (i.e., potentiometric) electrolysis of a molten mixture of TiO_2 and A_2MoO_4 (A = Li, Na, or K), employing a method similar to that reported previously.[15] A 4.0 g powder of A_2MoO_4 was loaded into a Pt crucible (30 cm^3 in volume) or a 3YSZ crucible (20 cm^3) as a reaction vessel. To perform high-temperature electrolysis with a three-electrode configuration, three Pt wires (0.5 mm in diameter) connected to an external potentiostat (Hokuto Denko: HZ-5000) were introduced into the crucible in a box or vertical tubular furnace. The pseudoreference and working electrodes (PRE and WE, respectively) were placed near one another. A 0.10 g powder of TiO_2 was put in the vicinity of the counter electrode (CE) to prevent undissolved TiO_2 from being incorporated into grown crystals on WE.

Cyclic voltammetry (CV) was performed to determine the applied voltages for the subsequent

constant-voltage electrolysis. The voltage scan range and scan rate were $-1.2\ V \le V \le 0\ V$ (vs Pt PRE) and 100 mV s^{-1}, respectively. It should be noted that the target compounds containing reduced titanium species (Ti^{3+} ions) will form at negative voltages with respect to PRE. The electrolysis was carried out at 1050 °C for 5 h in air. For sodium titanates, the crystal growth was also performed in flowing Ar gas. The furnace was first heated to 1050 °C at a heating rate of 7 °C min^{-1} and then held for 30 min at this temperature to stabilize the melt prior to the electrolysis. Applied voltage values were set on the basis of the CV data: $V = -0.6$ V and -0.85 V for the growth of potassium titanates; $V = -0.6$, -0.7, and -0.75 V for sodium titanates; and $V = -0.4$, -0.6, -0.65, and -0.7 V for lithium titanates. At the end of each run, the applied voltage was turned off, and the Pt electrodes were immediately taken out from the furnace to be rapidly cooled to room temperature. Electrolysis for 5 h resulted in crystal growth at the surface of WE, while no crystals grew on CE. The tip part of WE was immersed in distilled water at room temperature for overnight to dissolve the solidified A_2MoO_4 residues, and thereby remove the crystals from WE. Finally, the isolated crystals were washed thoroughly with distilled water and ethanol several times.

3.3.3. Characterization

Powder X-ray Diffraction (PXRD). Phase identification of the grown crystals was conducted using a powder X-ray diffractometer (Rigaku: Ultima IV Protectus; Cu Kα radiation; $\lambda = 1.5418$ Å). The as-grown crystals were evenly spread on a "non-reflection" sample holder made of an obliquely-cut silicon crystal and analyzed in a 2θ range of 10°–90° with a step size of 0.02° (operating condition: 40 kV, 40 mA).

Chemical Analyses. The chemical composition of the crystals was analyzed with a field-emission scanning electron microscope (FE-SEM; Hitachi: SU-8010) equipped with an energy dispersive X-ray spectroscopy analyzer (EDX; Horiba: EMAX-2770). The cationic compositions were determined

by inductively coupled plasma-atomic emission spectroscopy (ICP-AES; Shimadzu: ICPE-9820). Typically, the as-grown crystals were dissolved in a hot acidic solution of H_2SO_4 and HNO_3 to prepare the sample solution.

Ultraviolet–Visible–Near Infrared (UV–Vis–NIR) Diffuse Reflectance Spectroscopy. Diffuse reflectance spectra were acquired for the lithium and sodium titanate crystals. The measurements were carried out in a wavelength window of 200–1000 nm using a UV–vis–NIR spectrophotometer (Shimadzu: UV-2600 or JASCO: V-770) equipped with an integrating sphere. The reflectance spectrum of a $BaSO_4$ powder was used as a baseline. The reflectance data were converted to absorbance data using the Kubelka–Munk function,[16] $F(R_\infty) = (1-R_\infty)^2/2R_\infty$, where R_∞ is the relative reflectance (R_{sample}/R_{BaSO_4}). Lithium- and sodium-stoichiometric titanium compounds, $Li_2Ti_3O_7$ and $Na_2Ti_6O_{13}$, were used as references. Phase-pure samples were synthesized by the solid-state reaction method; details of the syntheses and PXRD patterns are given in Figures S3.1 and S3.2 of the Supporting Information.

3.4. Results and Discussion

3.4.1. Electrochemical Measurements of Molten Salts

Figure 3.1 shows the cyclic voltammograms of the molten mixtures of (a) TiO_2 and K_2MoO_4, (b) TiO_2 and Na_2MoO_4, and (c) TiO_2 and Li_2MoO_4 at 1050 °C. In Figure 3.1a, when the applied voltage reaches approximately $V = -0.6$ V in the forward (cathodic) sweep, a small current with a negative sign arises, indicating that reduction of TiO_2 starts at −0.6 V. The negative current then increases rapidly below −0.95 V with increasing negative voltage through a small peak at about −0.84 V, and reaches −6.4 mA at −1.2 V. In the backward (anodic) sweep, the negative current steadily decreases and overshoots the horizontal axis at −0.97 V. Then, the positive current forms an oxidation peak at about −0.85 V followed by a small hump at about −0.73 V, and eventually converges to 0 mA. The wide hysteresis suggests that crystals deposited on WE in the forward sweep are electrochemically oxidized. A similar hysteresis is observed in the TiO_2/A_2MoO_4 (A = Li and Na) melts, as shown in Figure 3.1b and c. Unlike the CV result for the TiO_2/Cs_2MoO_4 melt (ref 15), oxidation peaks are clearly observed in the backward sweep in the above three experiments. This suggests that crystals grown from the TiO_2/A_2MoO_4 melts with A = Li, Na, and K have less electrochemical stability than the $Cs_xTi_8O_{16}$ crystal. With the decreasing ionic size of the alkali metals, both the reduction/oxidation peaks shift to the positive side with respect to those observed for the TiO_2/K_2MoO_4 melt. This tendency suggests that TiO_2 is reduced more easily in the melts with smaller alkali metals, and the grown crystals are less stable against electrochemical oxidation. The largest current is observed in the TiO_2/Li_2MoO_4 melt, probably originating from the high Li^+ mobility.

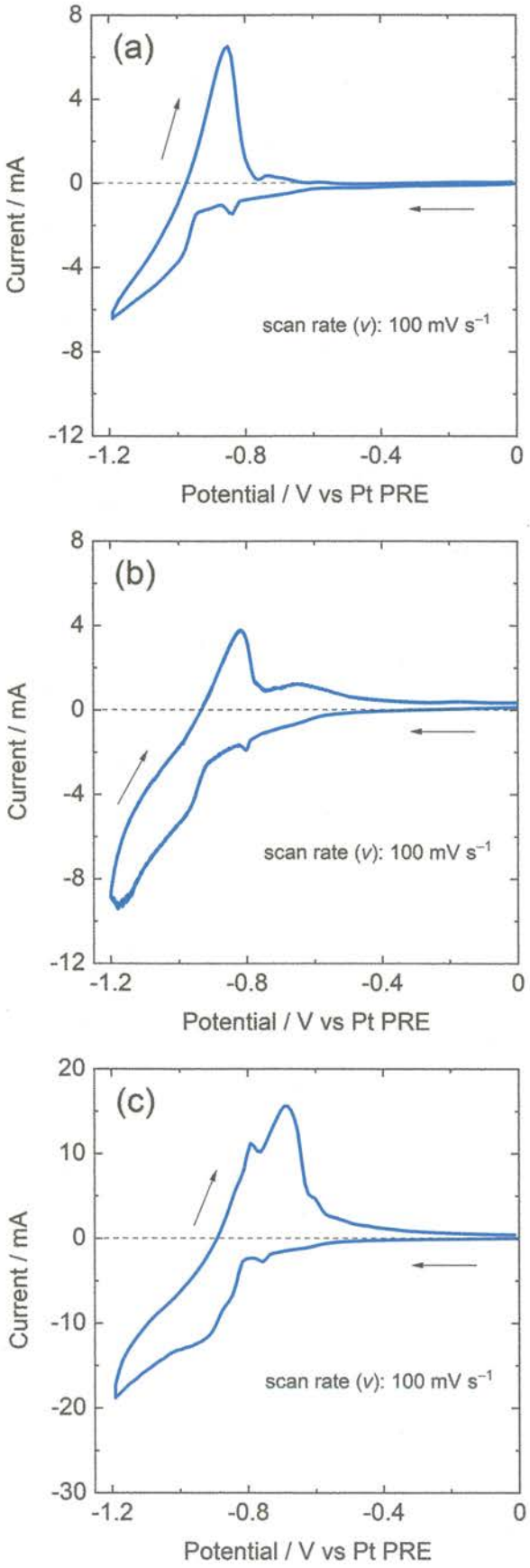

Figure 3.1. Cyclic voltammograms (scan rates: ±100 mV s^{-1}) of the molten mixtures of (a) TiO_2 and K_2MoO_4, (b) TiO_2 and Na_2MoO_4, and (c) TiO_2 and Li_2MoO_4 at 1050 °C in air. Arrows mark the potential-scan direction. The horizontal broken line is a guide of 0 mA.

3.4.2. K–Ti–O System

3.4.2.1. Crystal Growth

Electrochemical crystal growth of potassium titanates with different constant-voltage values of V = −0.6 V and −0.85 V was conducted. The shape of the resultant K–Ti–O crystals is highly anisotropic, with a maximum length of approximately 1 mm (Figure 3.2). The author has noticed that needle-like crystals always grow in a direction perpendicular to the surface of WE, indicating that the longitudinal direction of the needle-like crystals corresponds to the electric field direction. Meanwhile, attempts without applying the electric field resulted in no sizable crystals on the Pt electrodes even with the same temperature sequence. This experimental fact obviously indicates that the electric field acts as a driving force of the crystal growth. Similar to the case of Cs–Ti–O,[15] the appearance of the crystals strongly depends on the applied voltage: the crystals are brownish with optical transparency for V = −0.6 V, while they are black for V = −0.85 V. We also examined the crystal growth at V = −0.9 V and −1.0 V, but these attempts were unsuccessful, due to the breakdown of WE underneath the melt. Possible $K_xTi_8O_{16}$ formation reactions can be described with the following formulas:

$$\text{WE: } 8TiO_2 + xK^+ + xe^- \rightarrow K_xTi_8O_{16} \quad (1)$$

$$\text{CE: } x/2MoO_4^{2-} \rightarrow xe^- + x/2MoO_3 + x/4O_2 \quad (2)$$

$$\text{Overall: } 8TiO_2 + x/2K_2MoO_4 \rightarrow K_xTi_8O_{16} + x/2MoO_3 + x/4O_2 \quad (3)$$

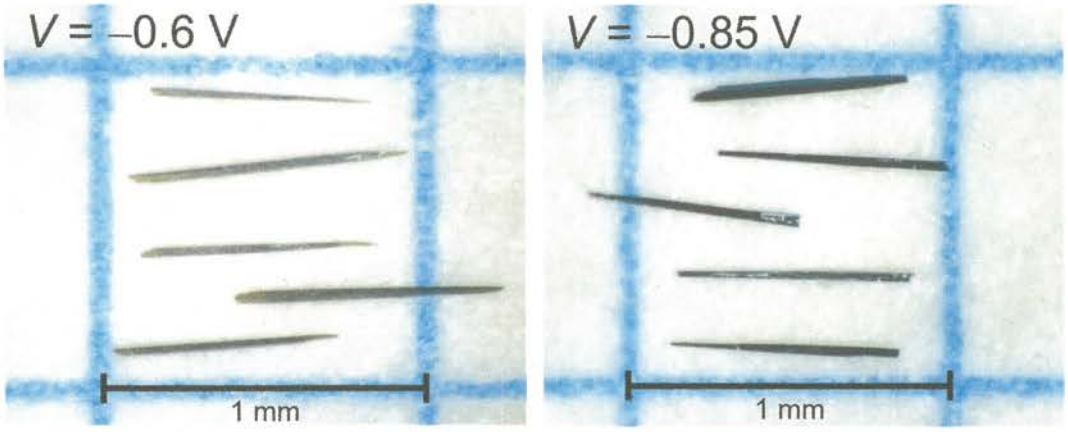

Figure 3.2. Optical micrographs of the resultant K–Ti–O crystals grown with different applied voltages $V = -0.6$ V and -0.85 V.

Also, it should be noted that transparent needle-like $K_{2+x}Ti_6O_{13}$ crystals as by-products always grew on the upper part of WE (Figure S3.3). A possible growth mechanism will be discussed in **3.4.3.1**.

The PXRD patterns of the as-grown (i.e., nonpulverized) K–Ti–O crystals are presented in Figure 3.3. Powder patterns for the K–Ti–O crystals were hardly obtained because the crystals were easily amorphized when ground intensely. Most of the reflections are indexable to a tetragonal unit cell of hollandite-type $K_xTi_8O_{16}$ belonging to the $I4/m$ space group ($K_{1.35}Ti_8O_{16}$, ICDD PDF 47-0690). The crystal of $K_xTi_8O_{16}$ is isomorphic to the Cs counterpart, consisting of double-chains of edge-shared TiO_6 octahedra that are connected by sharing the corners, forming a one-dimensional (1D) tunnel structure along the c-axis, see Figure 3.4. The $hk0$ reflections are preferentially seen in the PXRD profile; the longitudinal direction of the needle-like crystals surely corresponds to the c-axis. The a-parameters calculated from the d-spacing of the lattice plane (600) are 10.12 Å and 10.16 Å for the $V = -0.6$ V and -0.85 V crystals, respectively, being somewhat smaller than the literature values ($a =$ 10.188(2) Å and $c = 2.9661(7)$ Å (ref 18)). The a-parameter of $K_xTi_8O_{16}$ tends to increase as the K

content (x) increases.[19–22] Therefore, the $V = -0.85$ V crystal could have a larger x value than the $V = -0.6$ V crystal.

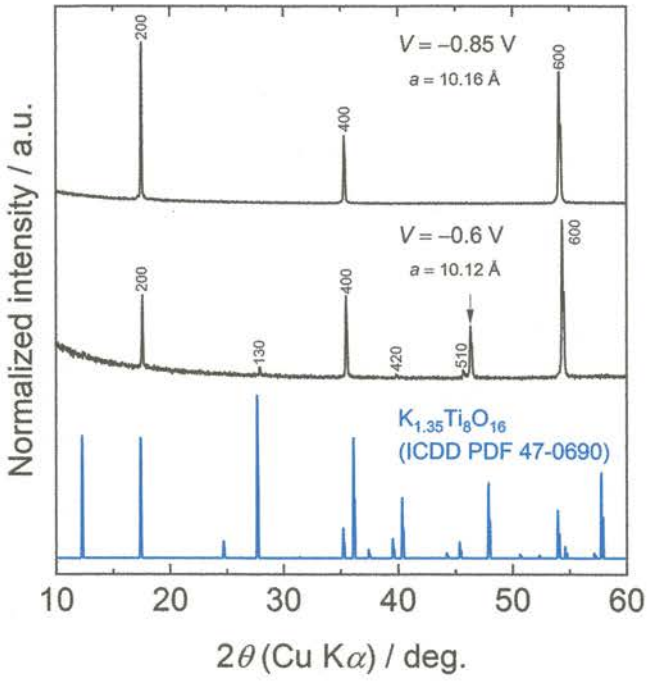

Figure 3.3. PXRD patterns for the nonpulverized $K_xTi_8O_{16}$ crystals grown with $V = -0.6$ V and -0.85 V. The simulated pattern for $K_{1.35}Ti_8O_{16}$ (ICDD PDF 47-0690) was also shown. An additional reflection is marked with arrow.

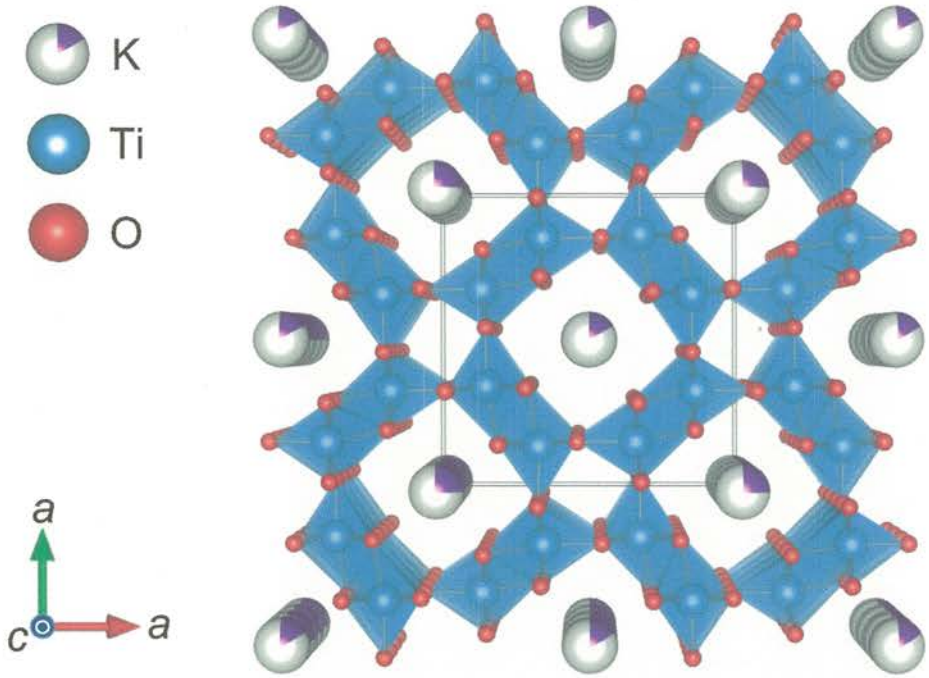

Figure 3.4. Schematic illustration of the crystal structure of hollandite-type $K_xTi_8O_{16}$ viewed along the *c*-axis. Purple, blue, and red spheres represent K, Ti, and O ions, respectively. The illustration was created with the VESTA software.[17]

For the $V = -0.6$ V crystals, an additional reflection is seen at about $2\theta = 46°$ (marked with arrow in Figure 3.3), which is not assignable to the starting materials. It is widely known that nonstoichiometric hollandite-type compounds frequently exhibit a superlattice or an incommensurately modulated structure.[23–29] For instance, Latroche et al. observed superlattice reflections at room temperature in a related hollandite $Cs_xTi_8O_{16}$ (originally represented as Cs_xTiO_2 with $x = 0.13$) and successfully refined the structure based on the tetragonal $I4_1/a$ space group.[23] Later, Fanchon et al. found a temperature-induced order ($I4_1/a$)–disorder ($I4/m$) phase transition in the electrochemically grown $Cs_xTi_8O_{16}$ ($x = 1.06$) hollandite crystal, involving a three-dimensional long-

range order of Cs cations.[24] From these aspects, the additional reflection observed in the $V = -0.6$ V crystals would be attributed to a long-range order of K cations in the crystal lattice.

The distinct appearances of the resultant crystals are likely related to the valence states of titanium through different chemical compositions. The transparent crystals are electrically insulating, and hence the K content (x) would be lower than that in the black crystals. The K/Ti ratios for the $V = -0.6$ V and -0.85 V crystals estimated from the EDX data were 0.214(2) and 0.176(4), respectively (based on the measurements for more than three points at the crystal surface; see Figure S3.4). This result is contrary to the above expectation, and would be caused by a slight amount of melt residues on the surfaces. Also, a certain amount of molybdenum was detected in the $V = -0.85$ V crystal. To validate the EDX result, the cationic ratios of the crystals were analyzed by ICP-AES. The values are summarized in Table 3.1. While no traces of possible contaminants such as Pt, Zr, and Y were detected, the $V = -0.85$ V crystal was found to contain 12.5 mol % of molybdenum. This is in contrast to the result of the Cs counterpart where Mo was never detected in the $Cs_xTi_8O_{16}$ crystals grown with $V = -0.6$ V and -1.0 V.[15] The values of K/Ti = 0.115 and 0.170 for the $V = -0.6$ V and -0.85 V crystals, respectively, are comparable to the Cs/Ti ratios for the $Cs_xTi_8O_{16}$ crystals analyzed by ICP-MS (Cs/Ti = 0.171 and 0.163 for the $V = -0.6$ V and -1.0 V crystals, respectively[15]). Further detailed characterization is highly desirable to gain deeper insight into the chemical composition and crystal structure of the resultant crystals by means of, for instance, single-crystal X-ray diffraction and electron diffraction. It is noteworthy that preliminary experiments with the use of an alumina reaction vessel resulted in a significant amount of Al incorporation (approximately 20 mol % per Ti) for the growth of $K_xTi_8O_{16}$ even with high-purity and high-density crucibles, implying that the K_2MoO_4 melt is more reactive with alumina than the Cs_2MoO_4 melt. The size of such Al-containing crystals was somewhat larger than the Al-free crystals obtained with a Pt crucible.

Table 3.1. Cationic compositions of the $K_xTi_8O_{16}$ crystals grown with V = –0.6 V and –0.85 V analyzed by ICP-AES.

applied voltage / V	K / mol %	Ti / mol %	Mo / mol %	formula[b]
–0.85	12.7	74.8	12.5	$K_{1.16}Mo_{1.15}Ti_{6.85}O_{16}$
–0.6	10.3	89.7	n.d.[a]	$K_{0.92}Ti_8O_{16}$

[a]Not detected. [b]Formula is given assuming no oxygen deficiencies in the crystals (i.e., O_{16}).

3.4.3. Na–Ti–O System

3.4.3.1. Crystal Growth

Single crystals of sodium titanates were grown with high-temperature electrolysis of the molten TiO_2/Na_2MoO_4 mixture. The applied voltages were set at onset (–0.6 V), moderate (–0.7 V), and high (–0.75 V) values on the basis of the CV data in Figure 3.1b. An optical micrograph of the resultant Na–Ti–O crystals grown with V = –0.75 V is shown in Figure 3.5. The appearance of the resultant crystals is yellowish with optical transparency. Although the electrolysis with different applied voltages resulted in crystals with a similar appearance, higher negative voltages were prone to yielding a larger amount of crystals.

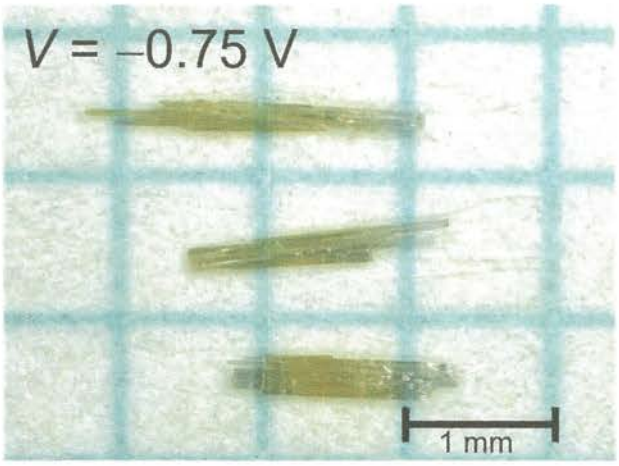

Figure 3.5. Optical micrograph of the resultant Na–Ti–O crystals grown with $V = -0.75$ V.

Shown in Figure 3.6 is the PXRD pattern of the pulverized Na–Ti–O crystals grown with $V = -0.75$ V. All the reflections are readily indexed based on a monoclinic unit cell belonging to the $C2/m$ space group ($Na_2Ti_6O_{13}$, ICSD #182965). A schematic illustration of the $Na_{2+x}Ti_6O_{13}$ structure is depicted in Figure 3.7. Three TiO_6 octahedra are edge-shared to form a single-chain, and the single-chain is connected with two identical chains at the edges, resulting in a zigzag ribbon. The ribbons are corner-shared, forming a $(Ti_6O_{13})^{2-}$ framework with (1×3) rectangular-shaped 1D tunnels along the b-axis. Sodium ions reside in the 1D tunnels, which are completely exchangeable with Li^+ and H^+.[30–32]

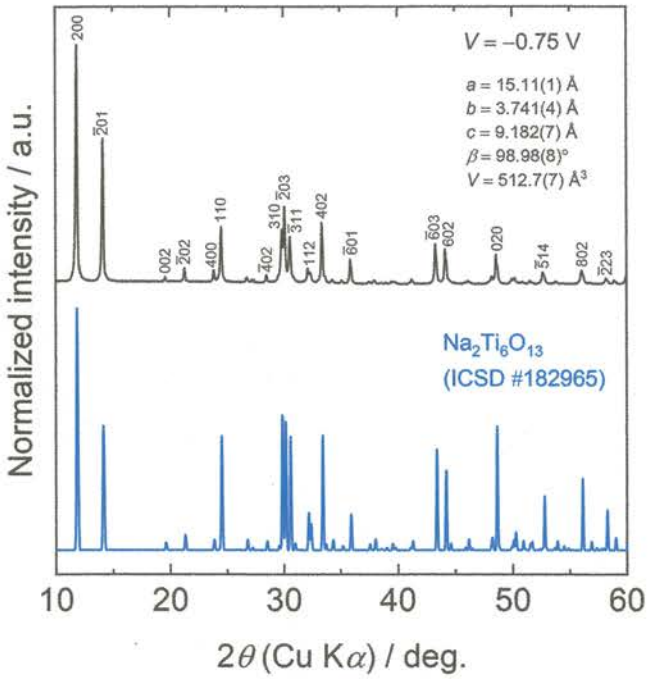

Figure 3.6. PXRD pattern for the pulverized $Na_{2+x}Ti_6O_{13}$ crystals grown with $V = -0.75$ V. The simulated pattern for sodium-stoichiometric $Na_2Ti_6O_{13}$ (ICSD #182965) was taken from the ICSD database.

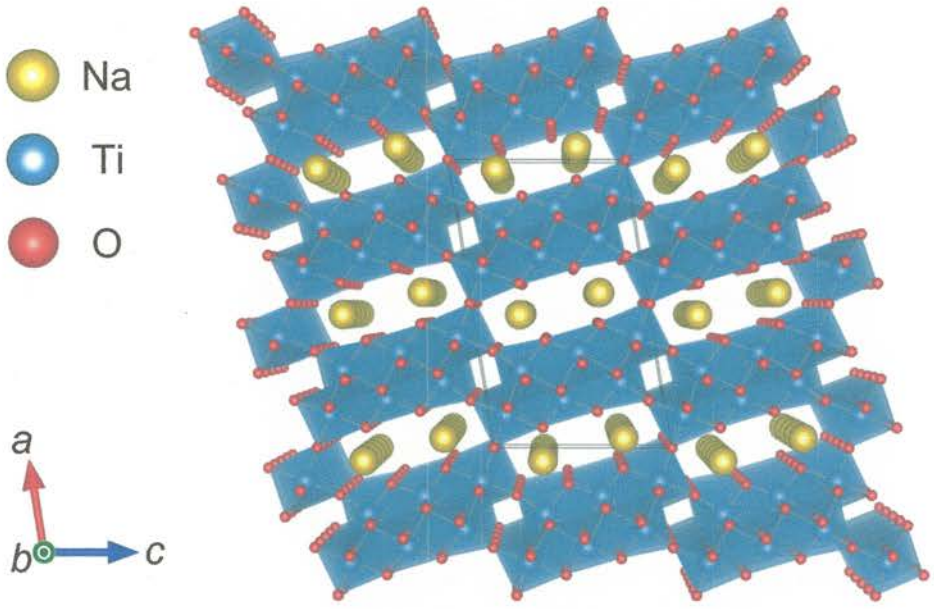

Figure 3.7. Schematic illustration of the crystal structure of $Na_{2+x}Ti_6O_{13}$ viewed along the *b*-axis. Yellow, blue, and red spheres represent Na, Ti, and O ions, respectively.

For the $V = -0.75$ V crystals, the lattice parameters refined by least-square calculations are a = 15.11(1) Å, b = 3.741(4) Å, c = 9.182(7) Å, β = 98.98(8)°, and V = 512.7(7) Å^3, being in good agreement with those previously reported for sodium-stoichiometric $Na_2Ti_6O_{13}$.[30,33,34] Upon electrochemical sodium intercalation in $Na_{2+x}Ti_6O_{13}$ (from $x = 0$ to 1), this compound exhibits a small volume expansion (1%) accompanied by significant increases both in the c-parameter and the β-angle.[35] Judging from the lattice parameters, the excess Na content (x) of the $V = -0.75$ V crystals is presumed to be small. The Na/Ti ratio estimated from the EDX data is 0.37, implying a slight sodium excess with respect to Na/Ti = 0.33 for $Na_2Ti_6O_{13}$, see Figure S3.5. The ICP-AES analysis also indicates that the crystals have a sodium excess (Na/Ti = 0.358) and are free from impurities such as Mo, Pt, Zr, and Y (Table 3.2). The mean valence number of titanium (V_{Ti}) is thus calculated to be +3.975 assuming an oxygen-stoichiometric composition of $Na_{2.15}Ti_6O_{13}$.

Table 3.2. Cationic compositions of the $Na_{2+x}Ti_6O_{13}$ crystals grown with $V = -0.75$ V analyzed by ICP-AES.

applied voltage / V	Na / mol %	Ti / mol %	formula[a]	mean V_{Ti}
–0.75	26.4	73.6	$Na_{2.15}Ti_6O_{13}$	+3.975

[a]Formula is given assuming no oxygen deficiencies in the crystals (i.e., O_{13}).

The $Na_{2+x}Ti_6O_{13}$ formation reactions may be written as:

$$\text{WE: } 6TiO_2 + 1/2O_2 + (2+x)Na^+ + (2+x)e^- \rightarrow Na_{2+x}Ti_6O_{13} \quad (4)$$

$$\text{CE: } (2+x)/2MoO_4^{2-} \rightarrow (2+x)e^- + (2+x)/2MoO_3 + (2+x)/4O_2 \quad (5)$$

$$\text{Overall: } 6TiO_2 + (2+x)/2Na_2MoO_4 \rightarrow Na_{2+x}Ti_6O_{13} + (2+x)/2MoO_3 + x/4O_2 \quad (6)$$

where O_2 molecules in eq (4) are assumed to be supplied from air. In fact, the $Na_{2+x}Ti_6O_{13}$ crystals, in analogy with $K_{2+x}Ti_6O_{13}$, always grow on the upper part of WE in contact with air. This experimental fact emphasizes the essential role of O_2 molecules in the phase formation of $Na_{2+x}Ti_6O_{13}$ and $K_{2+x}Ti_6O_{13}$. To validate this assumption, the growth of the $Na_{2+x}Ti_6O_{13}$ crystals was attempted in flowing Ar gas. In this condition, as expected, the $Na_{2+x}Ti_6O_{13}$ crystals grew on WE underneath the melt, although metallic particles (Mo and MoO_x) were obtained as by-products (Figures S3.6 and S3.7). Noticeably, the Ar-grown $Na_{2+x}Ti_6O_{13}$ crystals showed dark gray color, contrary to the air-grown crystals, suggestive of a more Na-rich composition for the former. The Na/Ti ratio of the Ar-grown crystals was estimated to be 0.59 (Figure S3.8a), which is about 1.5 times higher than that of the air-grown crystals. As shown in Figure S3.8b, the metallic particles were mainly composed of molybdenum. Clearly, crystal growth in an inert atmosphere results in more reduced phases than in air, taking into account the resultant compounds.

3.4.3.2. Optical Properties

UV–vis diffuse reflectance spectra were collected to study optical properties of the grown crystals. Figure 3.8 shows the spectra of the $Na_{2+x}Ti_6O_{13}$ ($x = 0.15$) crystals and the sodium-stoichiometric (i.e., $x = 0$) $Na_2Ti_6O_{13}$ powder prepared by the solid-state reaction (SSR) method. The $Na_2Ti_6O_{13}$ powder possesses a steep absorption edge at ~350 nm solely absorbs UV light, which reflects the white (colorless) appearance. The position of the absorption edge for the $Na_2Ti_6O_{13}$ powder is consistent with those reported previously.[30,36] By contrast, the $Na_{2+x}Ti_6O_{13}$ crystals absorb visible light at wavelengths shorter than 750 nm, with a slightly red-shifted absorption edge. This feature likely originates from doped electrons into the crystal lattice along with excess Na ions.

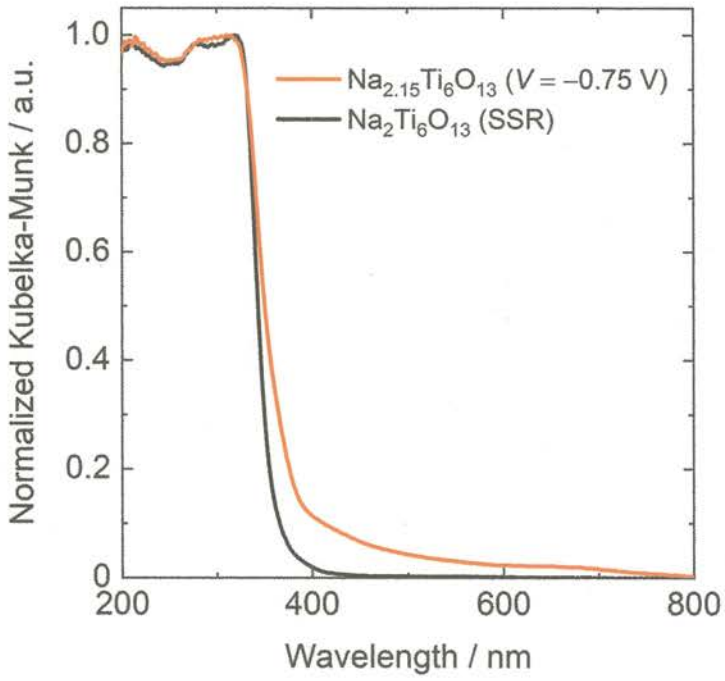

Figure 3.8. UV–vis diffuse reflectance spectra of the $Na_{2.15}Ti_6O_{13}$ crystals and $Na_2Ti_6O_{13}$ powder.

3.4.4. Li–Ti–O System

3.4.4.1. Crystal Growth

Electrochemical crystal growth of lithium titanates was conducted. Taking into account the CV data in Figure 3.1c, the applied voltages were set at onset (–0.4 V), moderate (–0.6 V), and high (–0.65 and –0.7 V) values. Shown in Figure 3.9 are the optical micrographs of the resultant Li–Ti–O crystals grown with different applied voltages. While the appearance of the needle-like crystals grown with $V = -0.4$ V is greenish with optical transparency, the electrolysis with the larger negative voltage (i.e., stronger reductive conditions) resulted in grayish transparent crystals. The $V = -0.65$ V product was found to contain a small amount of black octahedral-shaped crystals as by-products (Figure S3.9). Meanwhile, black flake-like crystals were mainly obtained instead of needle-like crystals in the electrolysis at $V = -0.7$ V (Figure S3.10).

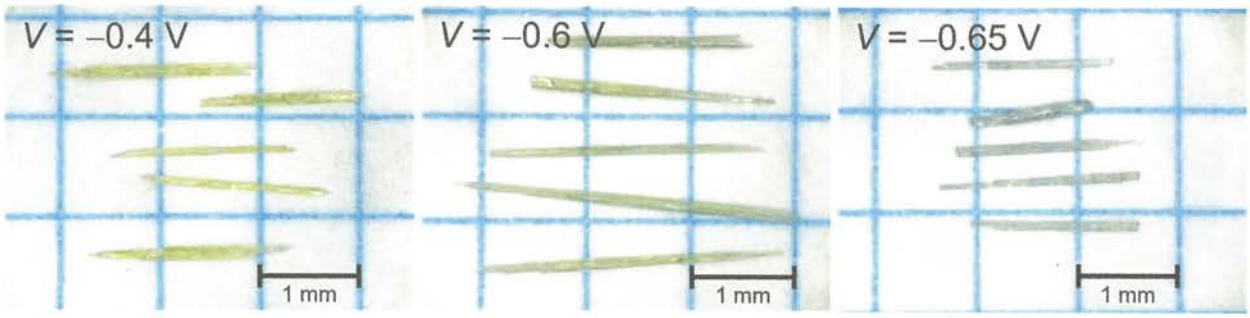

Figure 3.9. Optical micrographs of the resultant Li–Ti–O crystals grown with different applied voltages $V = -0.4$, –0.6, and –0.65 V.

Figure 3.10 shows the PXRD patterns of the as-grown Li–Ti–O crystals. All the reflections for the needle-like crystals grown with V = –0.4, –0.6, and –0.65 V are assignable to ramsdellite-type $Li_{2+x}Ti_3O_7$ belonging to the orthorhombic *Pnma* space group ($Li_2Ti_3O_7$, ICSD #202897). The formation reactions for $Li_{2+x}Ti_3O_7$ may be written as:

$$\text{WE: } 3TiO_2 + 1/2O_2 + (2 + x)Li^+ + (2 + x)e^- \rightarrow Li_{2+x}Ti_3O_7 \quad (7)$$

$$\text{CE: } (2 + x)/2MoO_4^{2-} \rightarrow (2 + x)e^- + (2 + x)/2MoO_3 + (2 + x)/4O_2 \quad (8)$$

$$\text{Overall: } 3TiO_2 + (2 + x)/2Li_2MoO_4 \rightarrow$$

$$Li_{2+x}Ti_3O_7 + (2 + x)/2MoO_3 + x/4O_2 \quad (9)$$

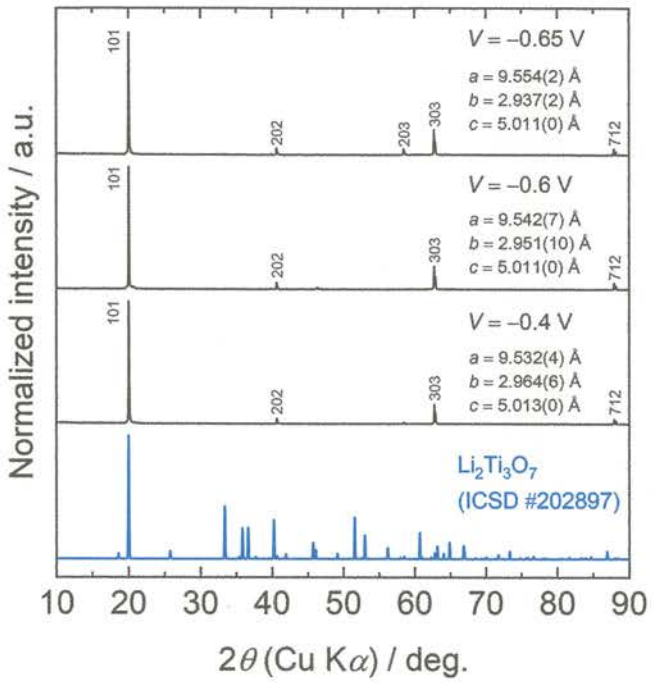

Figure 3.10. PXRD patterns for the nonpulverized $Li_{2+x}Ti_3O_7$ crystals grown with V = –0.4, –0.6, and –0.65 V. The simulated pattern for $Li_2Ti_3O_7$ (ICSD #202897) was taken from the ICSD database.

The crystal structure of $Li_{2+x}Ti_3O_7$ is schematically illustrated in Figure 3.11. The structure consists of double-chains of edge-shared $(Ti,Li)O_6$ octahedra. Each double-chain connects to one another at the corners of the octahedra to form 1D tunnels with a (1×2) rectangular-shaped cross-section along the *b*-axis. This structural model has widely been recognized, but some researchers claimed based on their neutron diffraction and $^6Li/^7Li$ MAS-NMR studies that all Li atoms reside in the 1D tunnels, and hence defective $(Ti,\square)\ O_6$ ($\square$ = vacancy) octahedra are present in the framework.[37,38] In fact, a protonated derivative ($H_2Ti_3O_7$) was successfully obtained via complete Li^+/H^+ ion exchange on $Li_2Ti_3O_7$ in an HNO_3 solution.[37–39]

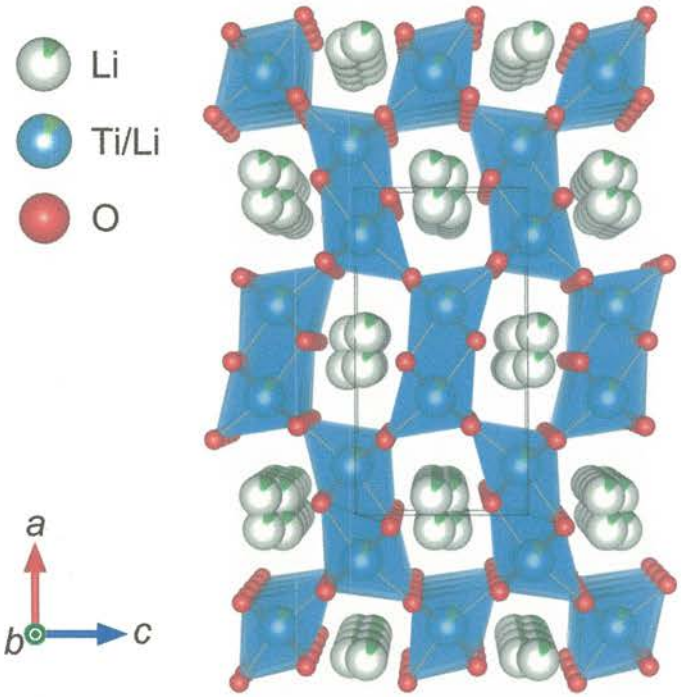

Figure 3.11. Schematic illustration of the crystal structure of $Li_{2+x}Ti_3O_7$ viewed along the *b*-axis. Green, blue, and red spheres represent Li, Ti, and O ions, respectively. The Ti ion, which lies in the center of the octahedron, is partially replaced by the Li ion, forming a $(Ti,Li)O_6$ octahedron.

The *h0l* reflections preferentially appear in the PXRD profile; therefore, the longitudinal direction of the needle-like crystals should correspond to the *b*-axis parallel to the 1D tunnels. While lattice parameter changes with varying Li contents have been reported in the literature,[40,41] a systematic trend in the lattice parameters is not observed for the sample series obtained herein, probably because of the poor accuracy of diffraction angles caused by misalignment of crystals. As shown in Figure S3.11, the octahedral-shaped crystals grown at $V = -0.65$ V are identified as spinel-type $Li_{4+x}Ti_5O_{12}$ ($Li_{5.35}Ti_5O_{12}$, ICSD #163862). Because this compound crystallizes in a face-centered cubic (fcc) lattice having well-developed {111} faces, the strongly preferred orientation seen in the PXRD profile is reasonably explained. Meanwhile, the flake-like crystals grown at $V = -0.7$ V are assigned to layered lithium molybdenum oxides such as $Li_2Mo_4O_{13}$ (ICSD #6134), $Li_{0.33}MoO_3$ (ICSD #201959), and $Li_{0.75}MoO_2$ (ICDD PDF 80-6069), see Figure S3.12. This suggests that the Li_2MoO_4 melt has a narrower potential window than the K_2MoO_4 melt.

Akimoto et al. reported crystal growth of ramsdellite-type Li_xTiO_2 ($x = 0.5$) via a direct reaction of lithium metal and TiO_2 in a sealed iron vessel.[42] Interestingly, the thus-grown crystals are black in color, suggesting that the compound is electrically conductive. They also reported that the Li content (x) in the Li_xTiO_2 crystals gradually decreases upon exposure to air over a long period, reflecting their highly reactive nature in air.[43] Also, Kuhn et al. observed color evolution from black to gray accompanied by an Li-content decrease for their polycrystalline Li_xTiO_2 sample.[44] These findings imply that the lithium titanate crystals with high Li contents are also air-sensitive, resulting in immediate re-oxidation when exposed to air at the last process of the crystal growth.

For the ramsdellite-type crystals, only titanium and oxygen are detected by EDX (lithium is undetectable; see Figure S3.13). On the other hand, the spinel-type crystals contain a large amount of molybdenum, see Figure S3.14. The Mo/Ti molar ratio is approximately 0.66 and thereby a nominal composition may be written as $Li_{4+x}Ti_3Mo_2O_{12}$. The cationic compositions of the ramsdellite-type

3.4.4.2. Optical Properties

Figure 3.12 shows UV–vis–NIR diffuse reflectance spectra of the green $Li_{2+x}Ti_3O_7$ crystals (with $x = 0.25$ grown at $V = -0.4$ V) and the lithium-stoichiometric (i.e., $x = 0$) $Li_2Ti_3O_7$ powder prepared by the solid-state reaction (SSR) method. The $Li_2Ti_3O_7$ powder solely absorbs UV light because of the steep absorption edge located at ~350 nm. Contrastingly, the absorption edge of the $Li_{2+x}Ti_3O_7$ crystals exhibits two increases near 360 and 460 nm. The short-wavelength side should correspond to absorption beyond the intrinsic optical band gap, whereas the long-wavelength side may be associated with impurity states created by oxygen vacancies, as discussed in the previous reports.[45,46] The weak absorption band centered at about 660 nm can be attributed to the d–d ($^2T_{2g} \rightarrow {}^2E_g$) electronic transition of Ti^{3+} (d^1) centers.[47] The green color of the $Li_{2+x}Ti_3O_7$ crystals surely stems from d electrons doped into the crystal lattice.

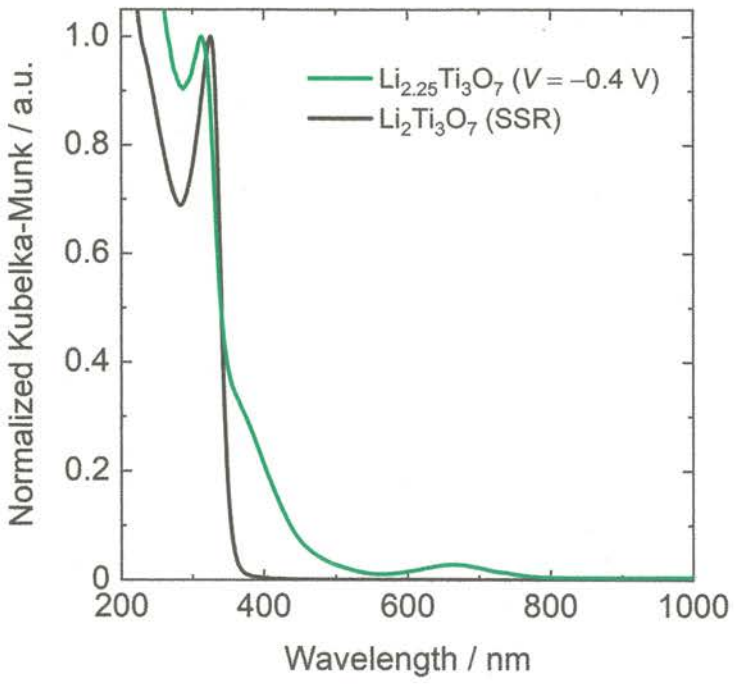

Figure 3.12. UV–vis–NIR diffuse reflectance spectra of the $Li_{2.25}Ti_3O_7$ crystals and $Li_2Ti_3O_7$ powder.

3.4.5. Structural Chemistry

The different geometries of the 1D tunnels in the three titanates ($K_xTi_8O_{16}$, $Na_{2+x}Ti_6O_{13}$, and $Li_{2+x}Ti_3O_7$) can be understood in terms of the ionic size of the alkali metals incorporated; the structures of three titanates are compared in Figure 3.13. Kesson and White proposed a modified tolerance factor (t_H) for hollandite-type $A_x(B_yC_{8-y})O_{16}$ compounds, where B cations are usually of lower valence than C cations.[48] The tolerance factor is expressed as:

$$t_H = \frac{\left[(r_A + r_O)^2 - \frac{1}{2}(r_{B,C} + r_O)^2\right]^{\frac{1}{2}}}{\sqrt{\frac{3}{2}}\,(r_{B,C} + r_O)} \qquad (10)$$

where r_A and r_O respectively represent the ionic radius of the A cation for eight-fold coordinates and the O anion for six-fold coordinates (1.40 Å (ref 49)). In addition, $r_{B,C}$ denotes the mean ionic radius of B and C cations for six-fold coordinates calculated according to the chemical formula. In the ideal hollandite-type compounds with tetragonal $I4/m$ symmetry, t_H is equal to unity. Most of the tetragonal hollandites satisfy $t_H = 0.93–1.16$.[48] The stoichiometric $K_2Ti_8O_{16}$ phase (i.e., $K_2(Ti_2^{3+},Ti_6^{4+})O_{16}$) gives $t_H = 1.02$, indicative of a stable hollandite-type structure. Given hypothetical lithium and sodium titanium hollandites ($Li_2Ti_8O_{16}$ and $Na_2Ti_8O_{16}$), the t_H values are calculated to be 0.74 and 0.87, respectively, suggesting that these cations are too small to be stabilized at the center of the (2 × 2) octahedral tunnel. Lithium and sodium titanate hollandites are obtained indirectly by topotactic Li and Na intercalation into the hollandite-type TiO_2 using a chemical or an electrochemical route.[21,50–52] However, the crystallographic sites of the intercalated Li and Na are distinct to the K position in $K_xTi_8O_{16}$, and a structural change from tetragonal ($I4/m$) to monoclinic ($I2/m$) symmetries takes place in heavily Li- and Na-intercalated compounds.[21,52] Another example is tetragonal $Na_xCr_xTi_{8-x}O_{16}$ ($x \sim 1.7$),[53] where the t_H value, 0.88, is considerably smaller than unity. This observation is partly taken

into account by unusual Na cation distribution in the 1D tunnel; in particular, some of the Na cations form a square-planar oxygen coordination.[53]

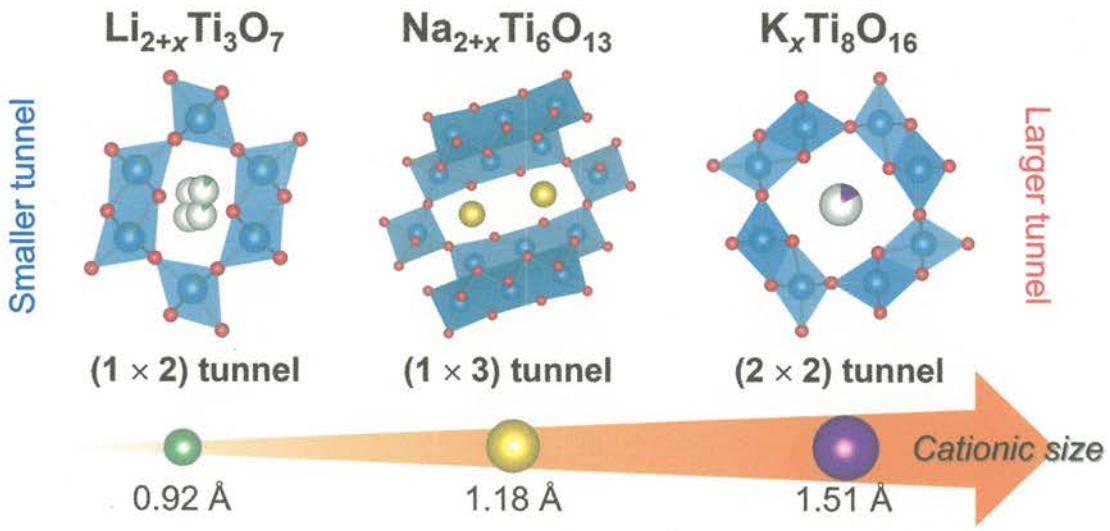

Figure 3.13. Comparison of the structures of the $K_xTi_8O_{16}$, $Na_{2+x}Ti_6O_{13}$, and $Li_{2+x}Ti_3O_7$ compounds. Larger alkali cations result in compounds with larger 1D tunnels. The tunnel size of each compound is represented based on the number of TiO_6 (or $(Ti,Li)O_6$) units forming the 1D tunnel structure.

3.5. Concluding Remarks

This chapter demonstrated the electrochemical crystal growth of $K_xTi_8O_{16}$ (hollandite-type), $Na_{2+x}Ti_6O_{13}$, and $Li_{2+x}Ti_3O_7$ (ramsdellite-type) by employing high-temperature electrolysis of a molten mixture of TiO_2 and A_2MoO_4 (A = Li, Na, and K) under constant-voltage conditions. This allowed us to know how the ionic size of incorporated alkali metals affects the crystal structure of alkali-metal titanates in the electrochemical crystal growth. Needle-like single crystals were successfully grown with different applied voltages, and remarkably, the resultant $K_xTi_8O_{16}$ and $Li_{2+x}Ti_3O_7$ crystals showed obviously distinct appearances, which suggested different chemical compositions.

The author has attempted preparation of large hollandite-type TiO_2 crystals starting from the grown $K_xTi_8O_{16}$ crystals by means of topotactic K deintercalation. Sizable hollandite-type TiO_2 crystals are noteworthy in the research field of optoelectronics. Besides, $Na^+/Li^+/H^+$ ion exchange experiments on millimeter-sized single-crystalline samples of $Na_{2+x}Ti_6O_{13}$ and $Li_{2+x}Ti_3O_7$ are of great interest. While their ion exchange capability is widely known, most of the ion-exchanged derivatives are, to the author's knowledge, in a polycrystalline form.

Rights and Permission

This chapter is based on ref 2 in the list of peer-reviewed original papers. Reproduced from *CrystEngComm*, 2019, 21, 3223–3231 with permission from the Royal Society of Chemistry.

References

(1) Braun, J. H.; Baidins, A.; Marganski, R. E. TiO_2 Pigment Technology: A Review. *Prog. Org. Coat.* **1992**, *20*, 105–138.

(2) Fujishima, A.; Honda, K. Electrochemical Photolysis of Water at a Semiconductor Electrode. *Nature* **1972**, *238*, 37–38.

(3) Bach, U.; Lupo, D.; Comte, P.; Moser, J. E.; Weissörtel, F.; Salbeck, J.; Spreitzer, H.; Grätzel, M. Solid-State Dye-Sensitized Mesoporous TiO_2 Solar Cells with High Photon-to-Electron Conversion Efficiencies. *Nature* **1998**, *395*, 583–585.

(4) Mahmood, T.; Cao, C.; Zafar, A. A.; Hussain, T.; Ahmed, M.; Saeed, M. A.; Usman, Z.; Khan, W. S. Elastic, Electronic and Optical Properties of Baddeleyite TiO_2 by First-Principles. *Mater. Sci. Semicond. Process.* **2014**, *27*, 958–965.

(5) Buckeridge, J.; Butler, K. T.; Catlow, C. R. A.; Logsdail, A. J.; Scanlon, D. O.; Shevlin, S. A.; Woodley, S. M.; Sokol, A. A.; Walsh, A. Polymorph Engineering of TiO_2: Demonstrating How Absolute Reference Potentials Are Determined by Local Coordination. *Chem. Mater.* **2015**, *27*, 3844–3851.

(6) Johnston, D. C.; Prakash, H.; Zachariasen, W. H.; Viswanathan, R. High Temperature Superconductivity in the Li–Ti–O Ternary System. *Mater. Res. Bull.* **1973**, *8*, 777–784.

(7) Johnston, D. C. Superconducting and Normal State Properties of $Li_{1+x}Ti_{2-x}O_4$ Spinel Compounds. I. Preparation, Crystallography, Superconducting Properties, Electrical Resistivity, Dielectric Behavior, and Magnetic Susceptibility. *J. Low Temp. Phys.* **1976**, *25*, 145–175.

(8) Sakurai, H.; Kato, M.; Yoshimura, K.; Tsujii, N.; Kosuge, K. Metal-Insulator Transition in Na_xTiO_2 ($x = 0.20$–0.25). *Phys. Rev. B: Condens. Matter Mater. Phys.* **2007**, *75*, 115128.

(9) Muraoka, Y.; Noami, K.; Wakita, T.; Hirai, M.; Yokoya, T.; Kayo, Y.; Muro, T; Tamenori, Y. Synthesis and Physical Properties of the Hollandite-Type Titanium Oxide $K_xTi_8O_{16}$. *Phys. Status Solidi C* **2011**, *8*, 555–557.

(10) Moetakef, P.; Larson, A. M.; Hodges, B. C.; Zavalij, P.; Gaskell, K. J.; Piccoli, P. M.; Rodriguez, E. E. Synthesis and Crystal Chemistry of Microporous Titanates $K_x(Ti,M)_8O_{16}$ where M = Sc–Ni. *J. Solid State Chem.* **2014,** *220,* 45–53.

(11) Durmeyer, O.; Kappler, J. P.; Derory, A.; Drillon, M.; Capponi, J. J. Magnetic Superconducting Properties of $LiTi_2O_4$ Single Crystal. *Solid State Commun.* **1990,** *74,* 621–624.

(12) Chen, C.; Spears, M.; Wondre, F.; Ryan, J. Crystal Growth and Superconductivity of $LiTi_2O_4$ and $Li_{1-1/3}Ti_{2-1/3}O_4$. *J. Cryst. Growth* **2003,** *250,* 139–145.

(13) Reid, A. F.; Watts, J. A. Single Crystal Syntheses by the Electrolyses of Molten Titanates, Molybdates and Vanadates. *J. Solid State Chem.* **1970,** *1,* 310–318.

(14) Abe, H.; Satoh, A.; Nishida, K.; Abe, E.; Naka, T.; Imai, M.; Kitazawa, H. Electrochemical Immobilization of Cs in Single-Crystalline SYNROC. *J. Solid State Chem.* **2006,** *179,* 1521–1524.

(15) Chiba, Y.; Saito, M.; Hagiwara, T.; Takatsu, H.; Kageyama, H.; Motohashi, T. High-Temperature Electrochemical Crystal Growth of Hollandite-Type $Cs_xTi_8O_{16}$ with Controlled Electronic Properties. *Cryst. Growth Des.* **2017,** *17,* 5691–5696.

(16) Kubelka, P.; Munk, F. Ein Beitrag zur Optik der Farbanstriche. *Z. Technol. Phys.* **1931,** *12,* 593–601.

(17) Momma, K.; Izumi, F. *VESTA 3* for Three-Dimensional Visualization of Crystal, Volumetric and Morphology Data. *J. Appl. Crystallogr.* **2011,** *44,* 1272–1276.

(18) Vogt, T.; Schweda, E.; Wüstefeld, C.; Strähle J.; Cheetham, A. K. Structural Analysis of a Potassium Hollandite $K_{1.35}Ti_8O_{16}$. *J. Solid State Chem.* **1989,** *83,* 61–68.

(19) Latroche, M.; Brohan, L.; Marchand, R.; Tournoux, M. New Hollandite Oxides: $TiO_2(H)$ and $K_{0.06}TiO_2$. *J. Solid State Chem.* **1989,** *81,* 78–82.

(20) Sasaki, T.; Watanabe, M.; Fujiki, Y. Structure of $K_{1.0}Ti_8O_{16}$ and $K_{0.0}Ti_8O_{16}$. *Acta Crystallogr., Sect. B: Struct. Sci.* **1993,** *49,* 838–841.

(21) Noailles, L. D.; Johnson, C. S.; Vaughey, J. T.; Thackeray, M. M. Lithium Insertion into Hollandite-Type TiO_2. *J. Power Sources* **1999,** *81–82,* 259–263.

(22) Sakao, M.; Kijima, N.; Akimoto, J.; Okutani, T. Synthesis, Crystal Structure, and Electrochemical Properties of Hollandite-Type $K_{0.008}TiO_2$. *Solid State Ionics* **2012,** *225,* 502–505.

(23)Latroche, M.; Brohan, L.; Marchand, R.; Tournoux, M. Cs_xTiO_2 Bronzes with Hollandite Structure: Cationic Ordering and Physical Properties. *Mater. Res. Bull.* **1990**, *25*, 139–148.

(24)Fanchon, E.; Hodeau, J. L.; Vicat, J.; Watts, J. A. Three-Dimensional/One-Dimensional Transition in the Cs^+ Sublattice of the Mixed Valence $CsTi_8O_{16}$ Hollandite: Structures at 297 and 673 K. *J. Solid State Chem.* **1991**, *92*, 88–100.

(25)Leligny, H.; Labbé, Ph.; Ledésert, M.; Raveau, B.; Valdez, C.; McCarroll, W. H. $La_{1.16}Mo_8O_{16}$: A Hollandite-Related Compound with an Incommensurate Modulated Structure. *Acta Crystallogr., Sect. B: Struct. Sci.* **1992**, *48*, 134–144.

(26)Barrier, N.; Gougeon, P.; Retoux, R. Synthesis, Crystal Structure and TEM Study of the New Hollandite-Type $Ba_{\sim 8/7}Mo_8O_{16}$. *J. Alloys Compd.* **2001**, *317–318*, 120–126

(27)Carter, M. L.; Withers, R. L. An Electron and X-ray Diffraction Study of the Compositely Modulated Barium Nickel Hollandite $Ba_x(Ni_xTi_{8-x})O_{16}$, $1.16 < x < 1.32$, Solid Solution. *Z. Kristallogr.—Cryst. Mater.* **2004**, *219*, 763–767.

(28)Carter, M. L.; Withers, R. L. A Universally Applicable Composite Modulated Structure Approach to Ordered $Ba_xM_yTi_{8-y}O_{16}$ Hollandite-Type Solid Solutions. *J. Solid State Chem.* **2005**, *178*, 1903–1914.

(29)Aubin-Chevaldonnet, V.; Deniard, P.; Evain, M.; Leinekugel-Le-Cocq-Errien, A.; Jobic, S.; Caurant, D.; Petricek, V.; Advocat, T. Incommensurate Modulations in a Hollandite Phase $Ba_x(Al,Fe)_{2x}Ti_{8-2x}O_{16}$ Intended for the Storage of Radioactive Wastes: A (3+1) Dimension Structure Determination. *Z. Kristallogr.—Cryst. Mater.* **2007**, *222*, 383–390.

(30)Kataoka, K.; Awaka, J.; Kijima, N.; Hayakawa, H.; Ohshima, K.; Akimoto, J. Ion-Exchange Synthesis, Crystal Structure, and Electrochemical Properties of $Li_2Ti_6O_{13}$. *Chem. Mater.* **2011**, *23*, 2344–2352.

(31)Pérez-Flores, J. C.; Baehtz, C.; Hoelzel, M.; Kuhn, A.; García-Alvarado, F. $H_2Ti_6O_{13}$, a New Protonated Titanate Prepared by Li^+/H^+ Ion Exchange: Synthesis, Crystal Structure and Electrochemical Li Insertion Properties. *RSC Adv.* **2012**, *2*, 3530–3540.

(32)Kataoka, K.; Kijima, N.; Akimoto, J. Structural and Electrochemical Properties of Hydrogen Titanium Oxides. *Solid State Ionics* **2013**, *252*, 109–115.

(33) Andersson, S.; Wadsley, A. D. The Structures of $Na_2Ti_6O_{13}$ and $Rb_2Ti_6O_{13}$ and the Alkali Metal Titanates. *Acta Crystallogr.* **1962**, *15*, 194–201.

(34) Torres-Martínez, L. M.; Juárez-Ramírez, I.; Ángel-Sánchez, K. D.; Garza-Tovar, L.; Cruz-López, A.; Ángel, G. D. Rietveld Refinement of Sol–Gel $Na_2Ti_6O_{13}$ and Its Photocatalytic Performance on the Degradation of Methylene Blue. *J. Sol-Gel Sci. Technol.* **2008**, *47*, 158–164.

(35) Shen, K.; Wagemaker, M. $Na_{2+x}Ti_6O_{13}$ as Potential Negative Electrode Material for Na-Ion Batteries. *Inorg. Chem.* **2014**, *53*, 8250–8256.

(36) Huerta-Flores, A. M.; Torres-Martínez, L. M.; Moctezuma, E. Overall Photocatalytic Water Splitting on $Na_2Zr_xTi_{6-x}O_{13}$ (x = 0, 1) Nanobelts Modified with Metal Oxide Nanoparticles as Cocatalysts. *Int. J. Hydrogen Energy* **2017**, *42*, 14547–14559.

(37) Le Bail, A.; Fourquet, J. L. Crystal Structure and Thermal Behaviour of $H_2Ti_3O_7$: A New Defective Ramsdellite Form from Li^+/H^+ Exchange on $Li_2Ti_3O_7$. *Mater. Res. Bull.* **1992**, *27*, 75–85.

(38) Orera, A.; Azcondo, M. T.; García-Alvarado, F.; Sanz, J.; Sobrados, I.; Rodríguez-Carvajal, J.; Amador, U. Insight into Ramsdellite $Li_2Ti_3O_7$ and Its Proton-Exchange Derivative. *Inorg. Chem.* **2009**, *48*, 7659–7666.

(39) Corcoran, D. J. D.; Tunstall, D. P.; Irvine, J. T. S. Hydrogen Titanates as Potential Proton Conducting Fuel Cell Electrolytes. *Solid State Ionics* **2000**, *136–137*, 297–303.

(40) Chen, C. J.; Greenblatt, M. Lithium Insertion into $Li_2Ti_3O_7$. *Mater. Res. Bull.* **1985**, *20*, 1347–1352.

(41) Arroyo y de Dompablo, M. E.; Várez, A.; García-Alvarado, F. Structural Study of Electrochemically Obtained $Li_{2+x}Ti_3O_7$. *J. Solid State Chem.* **2000**, *153*, 132–139.

(42) Akimoto, J.; Gotoh, Y.; Sohma, M.; Kawaguchi, K.; Oosawa, Y.; Takei, H. Synthesis and Crystal Structure of Ramsdellite-Type $Li_{0.5}TiO_2$. *J. Solid State Chem.* **1994**, *110*, 150–155.

(43) Akimoto, J.; Gotoh, Y.; Oosawa, Y.; Nonose, N.; Kumagai, T.; Aoki, K.; Takei, H. Topotactic Oxidation of Ramsdellite-Type $Li_{0.5}TiO_2$, a New Polymorph of Titanium Dioxide: TiO_2(R). *J. Solid State Chem.* **1994**, *113*, 27–36.

(44) Kuhn, A.; Amandi, R.; García-Alvarado, F. Electrochemical Lithium Insertion in TiO_2 with the Ramsdellite Structure. *J. Power Sources* **1994**, *110*, 150–155.

(45) Tsujimoto, Y.; Juillerat, C. A.; Zhang, W.; Fujii, K.; Yashima, M.; Halasyamani, P. S.; zur Loye, H.-C. Function of Tetrahedral ZnS_3O Building Blocks in the Formation of $SrZn_2S_2O$: A Phase Matchable Polar Oxysulfide with a Large Second Harmonic Generation Response. *Chem. Mater.* **2018**, *30*, 6486–6493.

(46) Yan, H.; Kuwabara, A.; Smith, M. D.; Yamaura, K.; Tsujimoto, Y.; zur Loye, H.-C. Flux Crystal Growth, Structure, and Optical Properties of the New Germanium Oxysulfide $La_4(GeS_2O_2)_3$. *Cryst. Growth Des.* **2020**, *20*, 4054–4061.

(47) Allen, G. C.; El-Sharkawy, G. A. M.; Warren, K. D. Electronic spectra of the hexafluorometalate(III) complexes of the first transition series. *Inorg. Chem.* **1971**, *10*, 2538–2546.

(48) Kesson, S. E.; White, T. J. Radius Ratio Tolerance Factors and the Stability of Hollandites. *J. Solid State Chem.* **1986**, *63*, 122–125.

(49) Shannon, R. D. Revised Effective Ionic Radii and Systematic Studies of Interatomic Distances in Halides and Chalcogenides. *Acta Crystallogr., Sect. A: Cryst. Phys., Diffr., Theor. Gen. Crystallogr.* **1976**, *32*, 751–767.

(50) Gutiérrez-Flórez, M. T.; Kuhn, A.; García-Alvarado, F. Lithium Intercalation in $K_xTi_8O_{16}$ Compounds. *Int. J. Inorg. Mater.* **1999**, *1*, 117–121.

(51) Sakao, M.; Kijima, N.; Akimoto, J.; Okutani, T. Lithium Insertion and Extraction Properties of Hollandite-Type K_xTiO_2 with Different K Content in the Tunnel Space. *Solid State Ionics* **2013**, *243*, 22–29.

(52) Pérez-Flores, J. C.; Baehtz, C.; Kuhn, A.; García-Alvarado, F. Hollandite-Type TiO_2: A New Negative Electrode Material for Sodium-Ion Batteries. *J. Mater. Chem. A* **2014**, *2*, 1825–1833.

(53) Michiue, Y.; Watanabe, M. $Na_xCr_xTi_{8-x}O_{16}$, Priderite with Sodium Ions in the Tunnel—Structural Study for Stability and Na Ion Transport. *J. Solid State Chem.* **1995**, *116*, 296–299.

Chapter 4

Electrochemical Crystal Growth of Titanium Oxyfluorides—A Strategy for Development of Electron-Doped Materials

4.1. Abstract

The author reports on the growth of single crystals of an electron-doped titanium oxyfluoride, $Li_2Ti(O,F)_3$, employing high-temperature electrolysis of TiO_2 with a eutectic Li_2MoO_4–LiF melt. Greenish octahedral-shaped crystals (~30 μm in size) with a cubic rocksalt-type structure were successfully obtained by precisely tuning the applied voltage. The temperature-dependent magnetic susceptibility data revealed a paramagnetic behavior at low temperatures, ensuring the presence of Ti^{3+} ions (mean valence number of +3.78; F/Ti ~ 0.15). The crystals exhibited clear visible-light absorption and produced H_2 from water in the presence of a sacrificial reagent under UV-light irradiation. $Li_2Ti(O,F)_3$ more efficiently produced H_2 compared with a nondoped oxyfluoride $Li_5Ti_2O_6F$, likely due to the doped electrons for the former. This chapter highlights a promising electrochemical approach toward growing electron-doped oxyfluoride crystals.

4.2. Introduction

In recent years, great efforts have been devoted to the exploration of multiple-anion-containing inorganic compounds with novel/better properties and functionalities.[1] Oxyfluorides, where O^{2-} and F^- anions coexist in a single component, have been extensively investigated for versatile applications in superconductors,[2] dielectrics,[3] proton conductors,[4] batteries,[5] phosphors,[6] scintillators,[7] photocatalysts,[8] and so on. Especially, titanium-based materials are attracting considerable attention, mostly because of their superior optical properties. For example, Mn^{4+}-activated $BaTiOF_4$ works as a red-emitting phosphor that would promise applications in LED backlighting.[9] Aurivillius-type $Bi_2TiO_4F_2$ exhibits high photocatalytic activities for degradation of Rhodamine B (RhB) and phenol under UV-light irradiation.[10] A recent discovery on excellent photocatalytic activities for water reduction/oxidation and CO_2 reduction in pyrochlore-type $Pb_2Ti_2O_{5.4}F_{1.2}$ has stimulated researchers' interest because of the unprecedented visible-light response arising from the simultaneous presence of metal–oxide (*M*–O) and metal–fluoride (*M*–F) bonds.[11,12]

To date, several synthetic approaches have been established to realize the desired oxyfluoride compounds. Polycrystalline samples of oxyfluorides are usually accessible via the following routes: (1) direct solid-state reactions between oxide and fluoride reagents, including conventional ceramic, high-temperature/pressure, and mechanochemical synthesis methods;[3,4,6,8,11–15] (2) low-temperature topochemical fluorination reactions starting from oxide precursors with fluorinating agents, such as NH_4F, MF_2 (*M* = Cu, Zn, Ni, or Ag), XeF_2, F_2 gas, NF_3 gas, poly(vinylidene fluoride) (PVDF), and polytetrafluoroethylene (PTFE);[2,16,17] (3) hydro/solvothermal reactions;[9,10,18,19] (4) oxidation of fluoride precursors using an H_2O_2 solution;[20–22] and (5) electrochemical fluoride ion intercalation into oxide precursors.[23] By contrast, growth methods to obtain sizable single crystals of oxyfluorides are limited mostly to solution processes, such as a flux[7,24–29] and a hydrothermal method[30–35] with fluoride

starting materials or an HF solution. Meanwhile, crystal growths of few oxyfluorides, such as $Ba_2Ca_5Cu_6O_{12}(O_{1-x}F_x)_2$ (ref 36) and Sr_2FeO_3F (ref 37), were achieved by utilizing a high-temperature/pressure technique. Well-formed single crystals facilitate us to investigate the intrinsic properties of the compounds. Accordingly, novel approaches toward growing sizable oxyfluoride crystals have been highly demanded.

High-temperature molten salt electrolysis has been used by Greenblatt and others to synthesize a wide variety of oxide single crystals.[38–40] This technique is also effective in growing single crystals of electron-doped titanium oxides, such as spinel-type $LiTi_2O_4$ (ref 41), pseudobrookite-type $CaTi_2O_4$ (ref 42), and hollandite-type $Cs_xTi_8O_{16}$ (ref 43). Recently, the author demonstrated the crystal growth of $Cs_xTi_8O_{16}$ with controlled electronic properties employing high-temperature constant-voltage electrolysis of TiO_2 with molten Cs_2MoO_4 (ref 44). Needle-like $Cs_xTi_8O_{16}$ crystals (maximum length of ~2 mm) with distinct properties, either electrical insulator with optical transparency or semiconductor with metallic luster, were successfully obtained upon varying the applied voltages.[44] This technique was subsequently employed for the crystal growth of lithium-, sodium-, or potassium-containing titanium oxides with A_2MoO_4 (A = Li, Na, or K) melts.[45] Consequently, needle-like crystals of $Li_{2+x}Ti_3O_7$ (ramsdellite-type), $Na_{2+x}Ti_6O_{13}$, and $K_xTi_8O_{16}$ (hollandite-type) were successfully grown.[45] These oxides unexceptionally crystallize in one-dimensional (1D) tunnel structures, and the tunnel shapes strongly depend on the ionic size of alkali metals incorporated.

On the basis of the above research background, the author anticipated that fluoride-containing melts might be applicable to the electrochemical crystal growth of electron-doped oxyfluorides. Alkali fluorides have been employed frequently as fluxes for the growth of oxide crystals because they are capable of dissolving oxide starting materials, where the fluoride works as a mineralizer.[46] In addition, alkali fluorides melt at relatively low temperatures and are soluble in water. Electron doping will significantly impact optical properties and often result in visible-light absorbing materials,

providing the possibility of applications in photocatalysts. Herein, the author presents the electrochemical crystal growth of a lithium titanium oxyfluoride by using constant-voltage electrolysis of TiO_2 with a eutectic Li_2MoO_4–LiF melt. Single crystals of rocksalt-type $Li_2Ti(O,F)_3$ were successfully grown by precisely tuning the applied voltage. Magnetic and optical studies indicate that the resultant oxyfluoride crystals are slightly electron-doped, most likely involved with O^{2-}-to-F^- replacements in the parent oxide Li_2TiO_3. The electron-doped $Li_2Ti(O,F)_3$ crystals are capable of producing H_2 from an aqueous methanol solution under UV irradiation. Noticeably, the amount of H_2 gas produced by the oxyfluoride crystals is larger than the oxide crystals ($Li_2TiO_{3-\delta}$) formed upon varying the applied voltages, emphasizing the role of multiple anions in enhancing the photocatalytic activity.

4.3. Experimental Section

4.3.1. Materials

Li_2CO_3 (99.99%), MoO_3 (99.98%), and TiO_2 (anatase, 99%) were purchased from Kojundo Chemical Laboratory. LiF (99.9%) was purchased from FUJIFILM Wako Pure Chemical. All the materials were used as received without further purification. Li_2MoO_4 was obtained by firing a stoichiometric mixture of Li_2CO_3 and MoO_3 at 600 °C for 12 h in air.

4.3.2. Electrochemical Crystal Growth

Crystals of titanium oxyfluorides were grown by means of high-temperature constant-voltage (i.e., potentiometric) electrolysis of TiO_2 with a eutectic Li_2MoO_4–LiF melt (62:38 mol %, eutectic point = 617 °C[47]), employing a method similar to that reported previously.[44,45] The Li_2MoO_4 powder was mixed homogeneously with LiF by using an agate mortar and a pestle to prepare the eutectic Li_2MoO_4–LiF mixture. This mixture (10 g) was loaded into a Pt crucible (30 cm^3 in volume) as a reaction vessel. To perform high-temperature electrolysis, three Pt wires (0.5 mm in diameter) connected to an external potentiostat (Hokuto Denko: HZ-5000) were introduced into the Pt crucible in a programmable box furnace. The working and pseudoreference electrodes (WE and PRE, respectively) were placed near one another. A 0.1 g powder of TiO_2 was put in the vicinity of the counter electrode (CE) to prevent undissolved TiO_2 from being incorporated into grown crystals on WE.

Cyclic voltammetry (CV) was performed to determine applied voltages for the subsequent constant-voltage electrolysis. The voltage range and scan rate were $-1.2\ V \leq V \leq 0\ V$ (vs Pt PRE) and 100 mV s^{-1}, respectively. It should be noted that the target compounds containing reduced titanium species (Ti^{3+} ions) will form at negative voltages with respect to PRE. The electrolysis was performed

at 1050 °C for 5 h in air. The furnace was heated to 1050 °C in 2.5 h (heating rate: 7 °C min^{-1}) and then kept at this temperature for 30 min to stabilize the melt prior to the electrolysis. Voltages applied were set at $V = -0.4$, -0.8, and -1.0 V, taking into account the onset potentials of reduction waves in the CV plot (Figure S4.1 in the Supporting Information). At the end of each run, the applied voltage was switched off, and then the Pt electrodes were immediately lifted above the melt and removed from the furnace to be rapidly cooled to room temperature. Electrolysis for 5 h resulted in crystal growth at the surface of WE (Figure S4.2), while no crystals grew on CE. Crystals deposited on WE were immersed in distilled water at room temperature overnight to dissolve the solidified residue. The crystals were mechanically isolated from WE with tweezers, washed with distilled water several times, and then allowed to dry at room temperature. Optical micrographs of the resultant crystals were taken by a digital microscope (Keyence: VHX-7000).

4.3.3. Characterization

Powder X-ray Diffraction (PXRD). Phase identification of the resultant crystals was conducted by using a powder X-ray diffractometer (Rigaku: Ultima IV Protectus; Cu Kα radiation; $\lambda = 1.5418$ Å) equipped with a silicon strip detector (Rigaku: D/teX Ultra2). As-grown crystals were evenly spread on a "non-reflection" sample holder made of an obliquely cut silicon crystal and analyzed in 0.02° increments over a 2θ range of 5°–90° at a rate of 5° min^{-1} (operating condition: 40 kV, 40 mA).

Single Crystal X-ray Diffraction (SCXRD). Structure refinement for the crystals grown with $V = -0.4$ V was performed based on SCXRD data collected at 295(2) K on a four-circle diffractometer (Rigaku: XtaLAB Pro; Mo Kα radiation; $\lambda = 0.71073$ Å). Diffraction data were processed by using the CrysAlisPro software[48] and corrected for absorption effects by means of the multiscan procedures. The structure was solved by direct methods and refined by full-matrix least-squares methods on F^2 by using SHELXL-2018.[49] Attempts were made to collect high-quality SCXRD data on the crystals

grown with $V = -0.8$ V; however, a publishable structure solution could not be obtained due to severely twinned nature of the crystals.

Chemical Analyses. Elemental analysis was performed on the single crystals by using a scanning electron microscope (SEM; Hitachi High-Tech: SU-5000) equipped with an energy-dispersive X-ray spectrometer (EDX; Bruker: XFlash Detector 630M). Selected crystal pieces were mounted on carbon tape, and analysis was performed with an accelerating voltage of 15 kV and an accumulation time of 5 min. Measurements were made for Ti, O, and F along with Mo and Pt as possible contaminants. The Li/Ti ratio was determined by inductively coupled plasma-atomic emission spectroscopy (ICP-AES; Thermo Fisher Scientific: iCAP 6500 Duo).

Magnetic Property Measurements. The magnetic susceptibilities (χ) of the crystals grown with $V = -0.8$ and -0.4 V were measured by a superconducting quantum interference device magnetometer (SQUID; Quantum Design: MPMS). Temperature vs susceptibility data were collected from 2 to 300 K under a magnetic field (H) of 10 kOe with a field-cooled (FC) condition.

Ultraviolet–Visible–Near Infrared (UV–Vis–NIR) Diffuse Reflectance Spectroscopy. Diffuse reflectance spectra were acquired for the crystals grown with $V = -0.8$ and -0.4 V. The measurements were performed in a wavelength window of 200–1000 nm by using a UV–vis–NIR spectrophotometer (JASCO: V-670) equipped with an integrating sphere. The reflectance spectrum of a $BaSO_4$ powder was used as a baseline. The reflectance data were converted to absorbance data by employing the Kubelka–Munk function,[50] $F(R_\infty) = (1-R_\infty)^2/2R_\infty$, where R_∞ is the relative reflectance (R_{sample}/R_{BaSO_4}). Some titanium compounds α-Li_2TiO_3, β-Li_2TiO_3, and $Li_5Ti_2O_6F$ were used as references. Phase-pure samples were synthesized (Figures S4.3 and S4.4) similarly to previous reports.[51–53]

Photocatalytic Activity Tests. Photocatalytic H_2 evolution reactions were conducted at room temperature by using a Pyrex test tube with a capacity of 8 mL. Approximately 1 mg of pulverized crystals was dispersed in 4 mL of an aqueous solution containing 10 vol % of methanol as a sacrificial

electron donor. A Pt cocatalyst was deposited on the crystals at 0.1 wt % through *in situ* photodeposition using H_2PtCl_6 as a precursor.[54] Prior to irradiation, the suspension was purged with Ar for 20–30 min. A 400 W high-pressure Hg lamp (SEN) without solution filter was used as a light source unless otherwise stated. The evolved H_2 was analyzed by a gas chromatograph (GL Sciences: Model GC323) with a thermal conductivity detector (TCD). To investigate the effect of electron doping on photocatalytic H_2 evolution activity, the $Li_5Ti_2O_6F$ powder as a nondoped reference was also tested in the same manner.

4.4. Results and Discussion

4.4.1. Crystal Growth

Electrochemical crystal growth was conducted at three voltages of $V = -0.4$, -0.8, and -1.0 V. The appearance of the resultant crystals is greatly dependent on the applied voltages. As seen in optical micrographs of Figure 4.1, pinkish platelike crystals (~50 μm) and greenish octahedral-shaped crystals (~30 μm) are obtained when $V = -0.8$ and -0.4 V are respectively applied. Meanwhile, crystal growth at $V = -1.0$ V led to lustrous black crystals with a platelet morphology (Figure S4.5). These crystals are distinct from the needle-like $Li_{2+x}Ti_3O_7$ crystals with an LiF-free melt,[45] revealing the significant impact of the melt compositions on the grown crystals. Attempts with zero electric field always resulted in the absence of sizable crystals on the Pt electrodes even with the same temperature sequence. This fact undoubtedly indicates that the electrical potential is important for crystal growth.

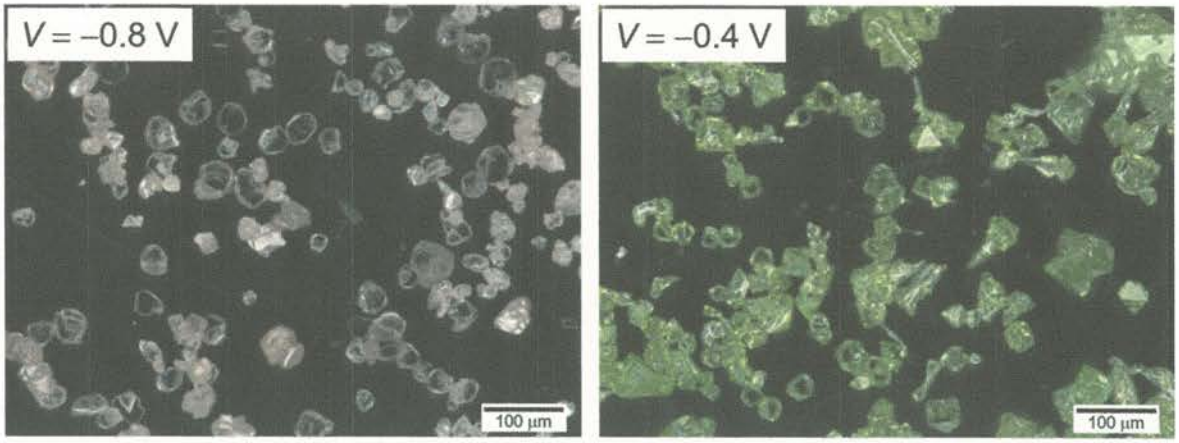

Figure 4.1. Optical micrographs of the resultant crystals grown with $V = -0.8$ V (left) and -0.4 V (right).

PXRD patterns for the as-grown (i.e., nonpulverized) crystals obtained at $V = -0.8$ and -0.4 V are presented in Figure 4.2. All the reflections of the $V = -0.8$ V crystals are indexable with monoclinic Li_2TiO_3, the so-called β-phase belonging to the $C2/c$ space group (ICSD #9058). Depicted in Figure 4.3a is the crystal structure of β-Li_2TiO_3, which adopts a cation-ordered rocksalt-type arrangement with alternating Li–O and Li–Ti–O layers along the c-axis direction.[56] Within the Li–Ti–O layer, an Li ion resides at the center of the six-membered ring of TiO_6 octahedra (see Figure 4.3a, right). The presence of the interstitial Li site in the Li–O layer was recently suggested by neutron diffraction.[57] Because the 00l reflections preferentially appear in the PXRD pattern, the well-developed faces of the platelike crystals can be indexed as {001}. The lattice parameters are $a = 5.062(1)$ Å, $b = 8.788(6)$ Å, $c = 9.750(2)$ Å, $\beta = 100.1(0)°$, and $V = 426.9(3)$ Å^3, in good agreement with the reported values.[52,57,58]

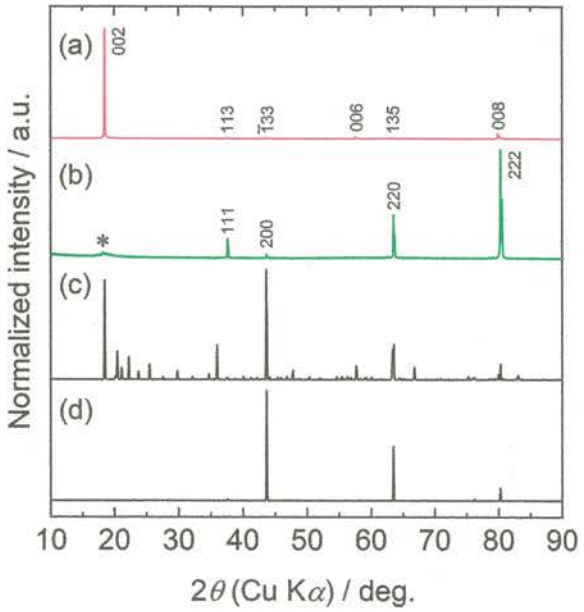

Figure 4.2. PXRD patterns for the nonpulverized crystals grown with (a) $V = -0.8$ V and (b) -0.4 V. For the $V = -0.4$ V crystals, an extra reflection assigned with 002 of β-Li_2TiO_3 is marked with asterisk (*). Simulated patterns for (c) β-Li_2TiO_3 (ICSD #9058) and (d) α-Li_2TiO_3 (ICSD #261235) were taken from the ICSD database.

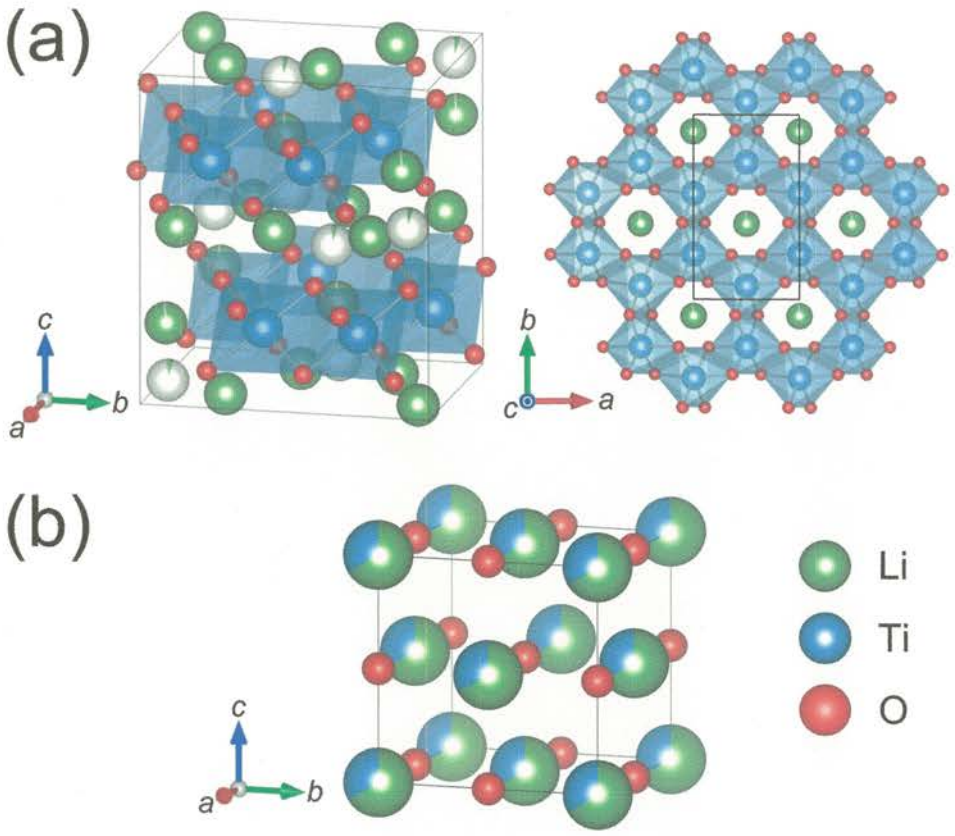

Figure 4.3. Crystal structures of (a) β-Li_2TiO_3 and (b) α/γ-Li_2TiO_3. Note: both α- and γ-Li_2TiO_3 adopt a similar cubic structure ($Fm\bar{3}m$), but the γ-phase appears only at high temperatures. The image (b) was drawn with the structural model of the α-phase. Green spheres, Li ions; blue spheres, Ti ions; red spheres, O ions. TiO_6 octahedra are shown as blue polyhedra. The right image in (a) depicts the honeycomb-like framework formed by the Ti ions as viewed down the *c*-axis (for simplicity, the Li–Ti–O layer is solely shown). The boxes indicate the unit cell of each structure. These illustrations were generated by the VESTA software.[55]

For the $V = -0.4$ V crystals, most of the reflections are assigned as cation-disordered rocksalt-type Li_2TiO_3 belonging to the $Fm\bar{3}m$ space group (ICSD #261235). An extra reflection is seen at $2\theta = 18.2°$ (marked with asterisk). The extra reflection is assignable to 002 of β-Li_2TiO_3 that formed as a byproduct even at $V = -0.4$ V. Given the strong preferred orientation of the β-Li_2TiO_3 crystals, the actual amount in the $V = -0.4$ V crystals could be negligible. Figure 4.3b shows the crystal structure of cubic α/γ-Li_2TiO_3, with a statistical distribution of Li and Ti ions at one equivalent site and O ions at another site.[59] The intensities of the 111 and 222 reflections are considerably higher than those in the simulated pattern, signifying that the dominant facet of the octahedral-shaped crystals is the {111} plane. The lattice parameters are calculated to be a = 4.138(0) Å and V = 70.84(1) Å^3, which are comparable to those reported previously.[58,59] As shown in Figure S4.6, crystals grown with $V = -1.0$ V were mainly composed of Li–Mo–O compounds such as $Li(Li_{0.313}Mo_{0.687})O_2$ (ICSD #160656) and Li_4MoO_5 (ICSD #109089), indicating that the larger negative voltage is prone to yielding Mo-containing compounds caused by deep reduction of the TiO_2/Li_2MoO_4 mixture.

4.4.2. Chemical Composition and Structural Chemistry

The distinct appearances of the resultant crystals would be associated with the oxidation numbers of titanium arising from different chemical compositions. Figure 4.4 displays the SEM-EDX images of the grown crystals. The $V = -0.8$ and -0.4 V crystals show well-developed {001} and {111} faces, respectively. Surprisingly, elemental analyses on the two crystal pieces revealed completely different anion compositions. While the $V = -0.8$ V crystal was composed of titanium and oxygen, the $V = -0.4$ V crystal contained fluorine along with those elements (lithium is undetectable by EDX). The average F/Ti ratio for the $V = -0.4$ V crystals was 0.15 based on the measurements for more than three crystals. The Li/Ti ratios determined by ICP-AES were 1.90 and 1.74 for the oxide ($V = -0.8$ V) and oxyfluoride (–0.4 V) crystals, respectively, where these values include approximately ±5%

experimental errors. The oxyfluoride crystals thus appear to be slightly Li deficient. For simplicity, the author denotes the chemical compositions as $Li_2TiO_{3-\delta}$ (oxide) and $Li_2Ti(O,F)_3$ (oxyfluoride), although some degree of Li deficiencies is suggested. The magnetic susceptibilities of the oxide and oxyfluoride crystals showed paramagnetic temperature dependencies (Figure S4.7). The averaged oxidation numbers of titanium (V_{Ti}) were estimated at +3.97 (oxide) and +3.78 (oxyfluoride) by Curie–Weiss fitting of the χ–T plots. These results indicate that both the crystals are slightly electron-doped. Details of the fitting results are listed in Table S4.1.

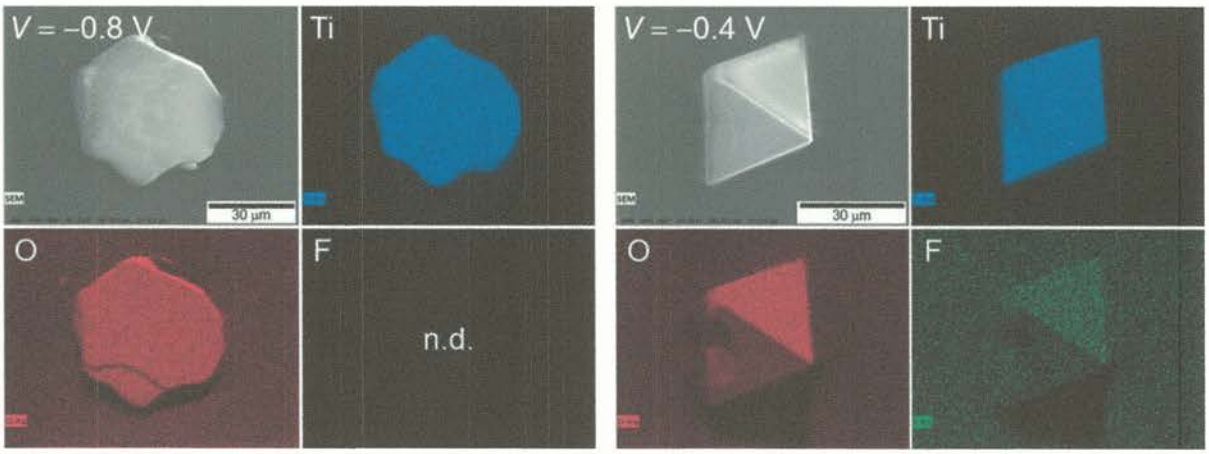

Figure 4.4. SEM-EDX images of the crystals grown with $V = -0.8$ V (left) and −0.4 V (right). Any extraneous elements, such as platinum from the electrodes and the crucible as well as molybdenum from the melt, were not detected within the detection limits of the instrument.

Li_2TiO_3 crystallizes in three types of structural modifications: α-, β-, and γ-Li_2TiO_3.[58] While the monoclinic β-phase ($C2/c$) is the most stable form at low temperatures, the compound transforms to γ-phase with a cubic rocksalt-type structure ($Fm\bar{3}m$) at about 1155 °C. The metastable α-phase, formed by low-temperature hydrothermal reactions, also adopts the cubic structure ($Fm\bar{3}m$), which transforms irreversibly to the β-phase above 300 °C. Upon heating, the α–β biphasic region is observed in a temperature window of 300–500 °C, and the β–γ region appears around 1100 °C. Of these polymorphs, the β-phase has a wide range of promising industrial applications, including a solid tritium breeder material for fusion reactors,[60] a cathode material of lithium-ion secondary batteries (LIBs),[61] a microwave dielectric,[62] and a CO_2 absorbent.[63]

It is worth noting that the growth temperature in these experiments (1050 °C) is close to the biphasic region on the high-temperature side. Given that the crystals having β- and α/γ-Li_2TiO_3 structures were grown with different applied voltages, it is reasonable to assume that the stable region of each phase is affected by not only temperature but also the chemical composition. The author tentatively suggests that fluorine-substituted compounds may be subjected to structural disorder, giving rise to the preference of the high-entropy cubic phase.

4.4.3. Structure Refinements and Description

The oxide and oxyfluoride crystals were structurally characterized by single-crystal X-ray diffraction. The oxide crystals were severely twinned, although several crystal pieces were examined, making the structure refinement unsuccessful. The oxyfluoride crystal crystallizes in the cubic space group $Fm\bar{3}m$ with a lattice parameter of a = 4.13842(14) Å. Crystallographic data and structural parameters are provided in Tables 4.1 and S4.2, respectively. The SCXRD data were readily refined assuming a cation-deficient rocksalt-type structure, $[(Li_{0.61}Ti_{0.35}\square_{0.04})(O_{0.95}F_{0.05})]$ ($\square$ = vacancy), with the atomic ratio taken from the analyzed composition and fixed during the refinement cycles.

The structure refinement was converged reasonably, with reliability factors of $R_1 = 0.0184$ and $wR_2 = 0.0492$. Figure 4.5 depicts the local coordination environment around the cation site. The cation site (Li/Ti/□) is surrounded by six O^{2-} and F^- anions, forming regular octahedral coordination geometry. The averaged Li/Ti/□–O/F interatomic distance is 2.06921(8) Å, which is somewhat shorter than the sum of Shannon's ionic radii of 6-coordinated Li^+ (0.76 Å) and O^{2-} (1.40 Å),[64] which reflects the partial occupation of the smaller Ti^{3+}/Ti^{4+} and F^- ions. No extra spots originating from long-range ordering were observed.

Table 4.1. Crystallographic data for the oxyfluoride.

formula	$Li_{0.61}Ti_{0.35}O_{0.95}F_{0.05}$
formula weight	37.27
crystal system	cubic
space group	$Fm\bar{3}m$ (no. 225)
temperature / K	295(2)
crystal size / mm^3	0.02 × 0.02 × 0.02
a / Å	4.13842(14)
V / $Å^3$	70.877(7)
Z	4
D_{calc} / g cm^{-3}	3.493
μ(Mo Kα) / mm^{-1}	3.892
F(000)	71
T_{min}, T_{max}	0.898, 1.000
θ range / deg.	8.553–36.507
no. of measured reflections	913
no. of unique reflections	18
no. of observed reflections [$I > 2\sigma(I)$]	18

Table 4.1. continued.

R_{int}	0.0337
h, k, l	$-6 \le h \le 6, -6 \le k \le 6, -6 \le l \le 6$
final *R* indices $[I > 2\sigma(I)]$[a]	$R_1 = 0.0184$, $wR_2 = 0.0492$
R indices (all data)[a]	$R_1 = 0.0184$, $wR_2 = 0.0492$
goodness-of-fit (GOF)	1.666
largest difference peak and hole / e Å^{-3}	0.273, –0.204

[a] $R_1 = \Sigma||F_o|-|F_c||/\Sigma|F_o|$, $wR_2 = [\Sigma w(F_o^2-F_c^2)^2/\Sigma w(F_o^2)^2]^{1/2}$; $w = 1/[\sigma^2(F_o^2)+0.2856P]$, where $P = (F_o^2+2F_c^2)/3$.

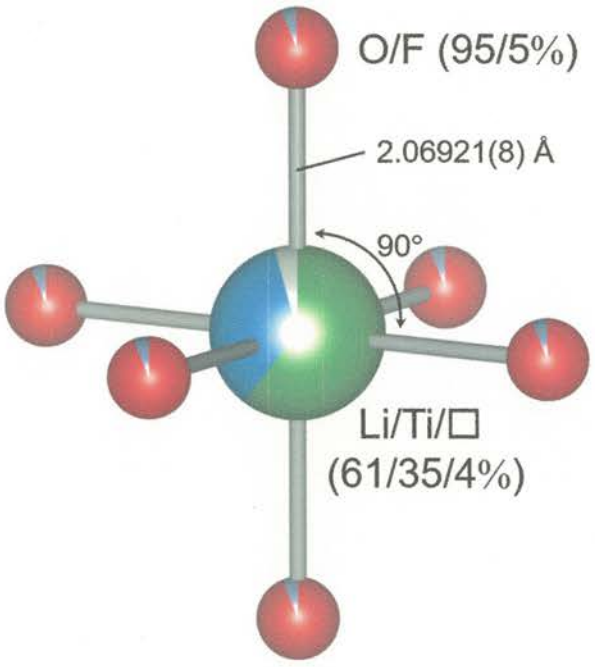

Figure 4.5. Local coordination environment around the cation site in the oxyfluoride $Li_{0.61}Ti_{0.35}O_{0.95}F_{0.05}$. Color scheme: Li in green, Ti in blue, O in red, F in gray, and vacancy in white; pie charts signify the occupancies of the sites.

4.4.4. Optical Properties

Figure 4.6 shows the UV–vis–NIR diffuse reflectance spectra for the nonpulverized oxide (pinkish) and oxyfluoride (greenish) crystals. Both of the crystals exhibit clear visible-light absorption at wavelengths longer than 400 nm, in contrast to their parent oxides (α/β-Li_2TiO_3) and oxyfluoride ($Li_5Ti_2O_6F$), where steep absorption edges appear in the UV region (Figure S4.8). Interestingly, the spectral shapes of the oxide and oxyfluoride crystals are completely different from one another. While the former possesses a broad absorption band with an edge at ~750 nm, the absorption spectrum for the latter is featured with two separated absorption bands centered at 410 and 625 nm.

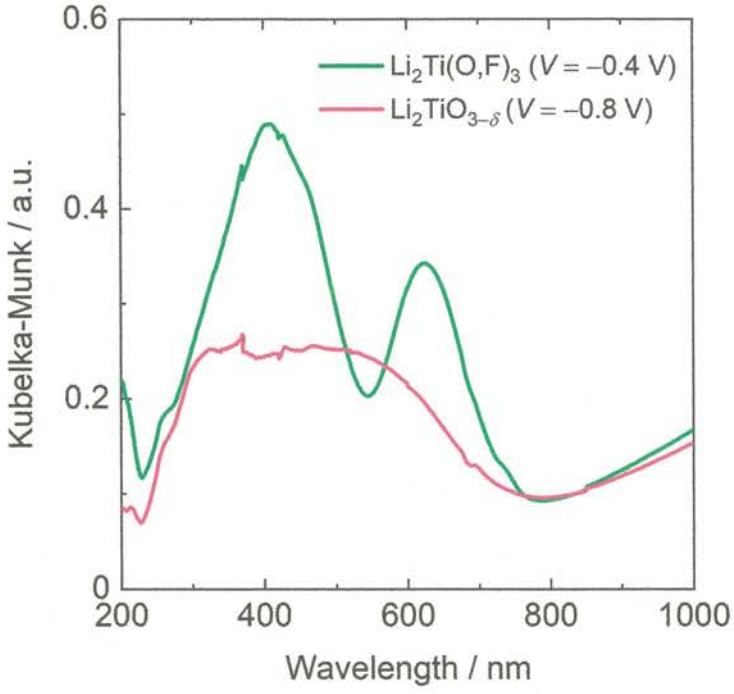

Figure 4.6. UV–vis–NIR diffuse reflectance spectra for the oxide ($V = -0.8$ V) and oxyfluoride (–0.4 V) crystals.

For the oxide crystals, the broad absorption band is likely associated with the d–d ($^2T_{2g} \rightarrow {}^2E_g$) electronic transition of Ti^{3+} (d^1) centers. A broad absorption band split into two components at 520 and 570 nm was similarly observed in $LaMgAl_{11}O_{19}:Ti^{3+}$ single crystals.[65] For the oxyfluoride crystals, the absorption band at 410 nm may be attributed to the ligand-to-metal charge transfer (LMCT).[66] Meanwhile, the absorption band at 625 nm can be ascribed to the d–d transition of Ti^{3+}, as previously observed in $K_3Ti^{3+}F_6$.[67] Most of the Ti^{3+}-containing oxides are dark blue-black in color, albeit small Ti^{3+} contents (e.g., Ti_8O_{15}; V_{Ti} = +3.75).[68] Unlike the typical Ti^{3+}-containing oxides, synthetic pyroxene ($NaTi^{3+}Si_2O_6$) (ref 69) and a mineral Ti-fassaite [$Ca(Mg,Ti^{3+},Ti^{4+},Al)(Si,Al)_2O_6$] (ref 70) display light or dark green color. Hence, the author concludes that the visible-light absorption for both the crystals most likely originates from Ti^{3+} ions in the structure.

4.4.5. Photocatalytic Activities

The visible-light absorption of the oxide and oxyfluoride crystals is fascinating for uses as photocatalysts. Table 4.2 summarizes the rates of H_2 evolution over the crystals modified with a Pt cocatalyst under UV-light irradiation along with $Li_5Ti_2O_6F$ for comparison. All the photocatalysts produce H_2 from an aqueous solution containing methanol as a sacrificial reagent. The oxyfluoride crystals show the highest H_2 evolution activity among the three.

The author suggests that the high activity of the oxyfluoride crystals results from a higher content of Ti^{3+} ions than the others. Fluorine-for-oxygen substitutions enabled the oxyfluoride crystals to be more electron-doped than the oxide crystals with oxygen deficiencies. A recent study by Nishioka et al. demonstrated that oxygen-defect-engineered strontium titanates ($SrTiO_{3-\delta}$) exhibit enhanced photocatalytic activities for the individual H_2/O_2 evolution reactions, originating from the prolonged lifetime of photogenerated electrons and the reinforced driving force for water oxidation.[71] Such an electron-doping effect on photocatalytic activities may be taken into account also in the crystals

obtained herein, and more electron doping found in the oxyfluoride crystals than in the oxide could explain its higher photocatalytic activity.

Table 4.2. Photocatalytic H_2 evolution activities (under UV light[a]) of the oxide (V = –0.8 V) and oxyfluoride (–0.4 V) crystals along with the $Li_5Ti_2O_6F$ reference.

photocatalyst	amount of evolved H_2[d] / μmol
$Li_2TiO_{3-\delta}$ (V = –0.8 V)	0.11
$Li_2Ti(O,F)_3$ (V = –0.4 V)	0.12
$Li_5Ti_2O_6F$[b]	0.04 (±0.01)
blank[c]	n.d.[e]

[a]Reaction conditions: catalyst, ~1 mg (0.1 wt % Pt photodeposited *in situ*); reactant solution, 10 vol % aqueous methanol solution (4 mL); light source, 400 W high-pressure Hg lamp without solution filter; reaction vessel, Pyrex test tube (8 mL capacity). [b]Synthesized via a solid-state reaction. [c]Only a Pt source. [d]Reaction time: 24 h. [e]Not detected.

Besides the degree of electron doping, the author assumes that the H_2 evolution activity of the catalysts tested herein is also affected by the presence of F^- ions to some extent. It has been reported that an Aurivillius-type oxyfluoride $Bi_2TiO_4F_2$ shows higher photocatalytic activities for degradation of organic compounds than a related oxide $Bi_4Ti_3O_{12}$.[10] Fluoride ions are capable of trapping photogenerated electrons and promote the separation of electron–hole pairs, thus leading to higher photocatalytic activities,[10] although excessive F^- ions are harmful because F^- ions also serve recombination centers of photogenerated carriers.[72,73] In the present case, the F/Ti ratio of the oxyfluoride crystals (F/Ti ~ 0.15) is much lower than that of $Li_5Ti_2O_6F$ (F/Ti = 0.5). The moderate

concentration of F^- ions may partly be responsible for the high activity of the oxyfluoride crystals. Unfortunately, the author was unable to measure wavelength-dependent photocatalytic activities due to an insufficient amount of the grown crystals. Hence, future works will focus on optimizing crystal growth conditions (e.g., melt compositions and electrode shapes) to obtain larger amounts of the crystals, facilitating to conduct more detailed characterizations.

4.5. Concluding Remarks

Utilizing an electrochemical technique, the author has successfully grown single crystals of an electron-doped titanium oxyfluoride $Li_2Ti(O,F)_3$ (F/Ti ~ 0.15) that adopts the cation-disordered structure. This material was obtained employing high-temperature electrolysis of TiO_2 with the eutectic Li_2MoO_4–LiF melt involving the optimized applied voltage. With the clear visible-light absorption, the $Li_2Ti(O,F)_3$ crystals exhibited much higher photocatalytic activity for sacrificial H_2 evolution than the nondoped oxyfluoride $Li_5Ti_2O_6F$ under UV light. The high activity of the former seems to be attributable to the higher content of Ti^{3+} ions than the latter. Stable electron doping into the crystals was accomplished by F^--for-O^{2-} substitutions in the parent oxide Li_2TiO_3. The author foresees that the described synthesis method based on electrochemistry becomes a promising strategy for the crystal growth of electron-doped oxyfluorides and may shed light on novel materials with intriguing electronic/magnetic properties as well as higher photocatalytic activity.

Accession Codes

CCDC 2086905 contains the supplementary crystallographic data for this chapter. These data can be obtained free of charge via www.ccdc.cam.ac.uk/data_request/cif, or by emailing data_request@ccdc.cam.ac.uk, or by contacting The Cambridge Crystallographic Data Centre, 12 Union Road, Cambridge CB2 1EZ, UK; fax: +44 1223 336033.

Rights and Permission

References

(1) Kageyama, H.; Hayashi, K.; Maeda, K.; Attfield, J. P.; Hiroi, Z.; Rondinelli, J. M.; Poeppelmeier, K. R. Expanding Frontiers in Materials Chemistry and Physics with Multiple Anions. *Nat. Commun.* **2018**, *9*, 772.

(2) Al-Mamouri, M.; Edwards, P. P.; Greaves, C.; Slaski, M. Synthesis and Superconducting Properties of the Strontium Copper Oxy-Fluoride $Sr_2CuO_2F_{2+\delta}$. *Nature* **1994**, *369*, 382–384.

(3) Oka, K.; Hojo, H.; Azuma, M.; Oh-ishi, K. Temperature-Independent, Large Dielectric Constant Induced by Vacancy and Partial Anion Order in the Oxyfluoride Pyrochlore $Pb_2Ti_2O_{6-\delta}F_{2\delta}$. *Chem. Mater.* **2016**, *28*, 5554–5559.

(4) Tarasova, N.; Animitsa, I. Protonic Transport in Oxyfluorides Ba_2InO_3F and $Ba_3In_2O_5F_2$ with Ruddlesden–Popper Structure. *Solid State Ionics* **2015**, *275*, 53–57.

(5) Kim, G.-H.; Kim, J.-H.; Myung, S.-T.; Yoon, C.; Sun, Y.-K. Improvement of High-Voltage Cycling Behavior of Surface-Modified $Li[Ni_{1/3}Co_{1/3}Mn_{1/3}]O_2$ Cathodes by Fluorine Substitution for Li-Ion Batteries. *J. Electrochem. Soc.* **2005**, *152*, A1707–A1713.

(6) Im, W. B.; George, N.; Kurzman, J.; Brinkley, S.; Mikhailovsky, A.; Hu, J.; Chmelka, B. F.; DenBaars, S. P.; Seshadri, R. Efficient and Color-Tunable Oxyfluoride Solid Solution Phosphors for Solid-State White Lighting. *Adv. Mater.* **2011**, *23*, 2300–2305.

(7) Morrison, G.; Latshaw, A. M.; Spagnuolo, N. R.; zur Loye, H.-C. Observation of Intense X-ray Scintillation in a Family of Mixed Anion Silicates, $Cs_3RESi_4O_{10}F_2$ (RE = Y, Eu–Lu), Obtained via an Enhanced Flux Crystal Growth Technique. *J. Am. Chem. Soc.* **2017**, *139*, 14743–14748.

(8) Wang, Y.; Tang, K.; Zhu, B.; Wang, D.; Hao, Q.; Wang, Y. Synthesis and Structure of a New Layered Oxyfluoride Sr_2ScO_3F with Photocatalytic Property. *Mater. Res. Bull.* **2015**, *65*, 42–46.

(9) Liang, Z.; Yang, Z.; Tang, H.; Guo, J.; Yang, Z.; Zhou, Q.; Tang, S.; Wang, Z. Synthesis, Luminescence Properties of a Novel Oxyfluoride Red Phosphor $BaTiOF_4:Mn^{4+}$ for LED Backlighting. *Opt. Mater.* **2019**, *90*, 89–94.

(10) Wang, S.; Huang, B.; Wang, Z.; Liu, Y.; Wei, W.; Qin, X.; Zhang, X.; Dai, Y. A New Photocatalyst: $Bi_2TiO_4F_2$ Nanoflakes Synthesized by a Hydrothermal Method. *Dalton Trans.*

2011, *40,* 12670–12675.

(11) Kuriki, R.; Ichibha, T.; Hongo, K.; Lu, D.; Maezono, R.; Kageyama, H.; Ishitani, O.; Oka, K.; Maeda, K. A Stable, Narrow-Gap Oxyfluoride Photocatalyst for Visible-Light Hydrogen Evolution and Carbon Dioxide Reduction. *J. Am. Chem. Soc.* **2018,** *140,* 6648–6655.

(12) Wakayama, H.; Utimula, K.; Ichibha, T.; Kuriki, R.; Hongo, K.; Maezono, R.; Oka, K.; Maeda, K. Light Absorption Properties and Electronic Band Structures of Lead Titanium Oxyfluoride Photocatalysts $Pb_2Ti_4O_9F_2$ and $Pb_2Ti_2O_{5.4}F_{1.2}$. *J. Phys. Chem. C* **2018,** *122,* 26506–26511.

(13) Chamberland, B. L. A New Oxyfluoride Perovskite, $KTiO_2F$. *Mater. Res. Bull.* **1971,** *6,* 311–315.

(14) Inaguma, Y.; Greneche, J.-M.; Crosnier-Lopez, M.-P.; Katsumata, T.; Calage, Y.; Fourquet, J.-L. Structure and Mössbauer Studies of F–O Ordering in Antiferromagnetic Perovskite $PbFeO_2F$. *Chem. Mater.* **2005,** *17,* 1386–1390.

(15) Clément, R. J.; Lun, Z.; Ceder, G. Cation-Disordered Rocksalt Transition Metal Oxides and Oxyfluorides for High Energy Lithium-Ion Cathodes. *Energy Environ. Sci.* **2020,** *13,* 345–373.

(16) Clemens, O.; Slater, P. R. Topochemical Modifications of Mixed Metal Oxide Compounds by Low-Temperature Fluorination Routes. *Rev. Inorg. Chem.* **2013,** *33,* 105–117.

(17) Slater, P.; Driscoll, L. Modification of Magnetic and Electronic Properties, in Particular Superconductivity, by Low Temperature Insertion of Fluorine into Oxides. In *Photonic and Electronic Properties of Fluoride Materials,* 1st ed.; Tressaud, A., Poppelmeier, K., Eds.; Progress in Fluorine Science Series 1; Elsevier: Amsterdam, 2016; pp 401–421.

(18) Asakura, Y.; Akahira, T.; Kobayashi, M.; Osada, M.; Yin, S. Synthesis of $NaMoO_3F$ and $Na_5W_3O_9F_5$ with Morphological Controllability in Non-Aqueous Solvents. *Inorg. Chem.* **2020,** *59,* 10707–10716.

(19) Asakura, Y.; Hasegawa, T.; Yin, S. Solvothermal Synthesis of Potassium, Rubidium, and Cesium Molybdenum Oxyfluorides. *J. Ceram. Soc. Jpn.* **2020,** *128,* 1061–1065.

(20) Ahmad, S.; Kharkwal, M.; Govind; Nagarajan, R. Application of $KZnF_3$ as a Single Source Precursor for the Synthesis of Nanocrystals of ZnO_2:F and ZnO:F; Synthesis, Characterization, Optical, and Photocatalytic Properties. *J. Phys. Chem. C* **2011,** *115,* 10131–10139.

(21) Kumar, V.; Govind, A.; Nagarajan, R. Optical and Photocatalytic Properties of Heavily F^--Doped SnO_2 Nanocrystals by a Novel Single-Source Precursor Approach. *Inorg. Chem.* **2011,** *50,* 5637–

5645.

(22) Nagarajan, R.; Ahmad, S.; Singh, P. Topochemical Oxidation of Perovskite $KCoF_3$ to a K_2PtCl_6 Structure-Type Oxyfluoride. *Inorg. Chem.* **2015**, *54*, 10105–10107.

(23) Vasala, S.; Jakob, A.; Wissel, K.; Waidha, A. I.; Alff, L.; Clemens, O. Reversible Tuning of Magnetization in a Ferromagnetic Ruddlesden–Popper-Type Manganite by Electrochemical Fluoride-Ion Intercalation. *Adv. Electron. Mater.* **2020**, *6*, 1900974.

(24) Akishige, Y. Ferroelectric and Piezoelectric Properties of Single Crystals of $Ba_{1-x}K_xTiO_{3-x}F_x$ with $x = 0.1$. *J. Phys. Soc. Jpn.* **2006**, *75*, 073704-1–073704-3.

(25) Latshaw, A. M.; Hughey, K. D.; Smith, M. D.; Yeon, J.; zur Loye, H.-C. Photoluminescent and Magnetic Properties of Lanthanide Containing Apatites: $Na_xLn_{10-x}(SiO_4)_6O_{2-y}F_y$, $Ca_xLn_{10-x}(SiO_4)_6O_{2-y}F_y$ (Ln = Eu, Gd, and Sm), $Gd_{9.34}(SiO_4)_6O_2$, and $K_{1.32}Pr_{8.68}(SiO_4)_6O_{1.36}F_{0.64}$. *Inorg. Chem.* **2015**, *54*, 876–884.

(26) Gong, P.; Luo, S.; Kang, L.; Jiang, X.; Xu, J.; Zhang, G.; Lin, Z.; Wu, Y.; Chen, C. $K_5Mo_4O_{14}F$: A Novel Fluorinated Polyoxomolybdate and Its Structural Stability. *Inorg. Chem.* **2015**, *54*, 6066–6068.

(27) Latshaw, A. M.; Wilkins, B. O.; Morrison, G.; Smith, M. D.; zur Loye, H.-C. $A_5RE_4X[TO_4]_4$ Crystal Growth: Fluoride Flux Synthesis of $Na_5Ln_4F[GeO_4]_4$ (*Ln* = Pr, Nd), the First Quaternary Germanate Oxyfluorides. *J. Solid State Chem.* **2016**, *239*, 200–203.

(28) Chen, Y.; Zhang, M.; Hu, C.; Wu, H.; Yang, Z.; Pan, S. $Li_2BaSc(BO_3)_2F$ and $LiBa_2Pb(BO_3)_2F$ with Layered Structures Featuring Special Li–O/F Configurations. *Chem. Eur. J.* **2018**, *24*, 15477–15481.

(29) Juillerat, C. A.; Kocevski, V.; Morrison, G.; Karakalos, S. G.; Patil, D.; Misture, S. T.; Besmann, T. M.; zur Loye, H.-C. Flux Crystal Growth of Uranium(V) Containing Oxyfluoride Perovskites. *Inorg. Chem. Front.* **2019**, *6*, 3203–3214.

(30) Marvel, M. R.; Lesage, J.; Baek, J.; Halasyamani, P. S.; Stern, C. L.; Poeppelmeier, K. R. Cation–Anion Interactions and Polar Structures in the Solid State. *J. Am. Chem. Soc.* **2007**, *129*, 13963–13969.

(31) Yeon, J.; Felder, J. B.; Smith, M. D.; Morrison, G.; zur Loye, H.-C. Synthetic Strategies for New Vanadium Oxyfluorides Containing Novel Building Blocks: Structures of V(IV) and V(V)

Containing $Sr_4V_3O_5F_{13}$, $Pb_7V_4O_8F_{18}$, $Pb_2VO_2F_5$, and Pb_2VOF_6. *CrystEngComm* **2015,** *17,* 8428–8440.

(32) Felder, J. B.; Yeon, J.; zur Loye, H.-C. Synthesis of Anhydrous K_2TiOF_4 via a Mild Hydrothermal Method. *Solid State Sci.* **2015,** *48,* 212–217.

(33) Sanjeewa, L. D.; McMillen, C. D.; McGuire, M. A.; Kolis, J. W. Manganese Vanadate Chemistry in Hydrothermal BaF_2 Brines: $Ba_3Mn_2(V_2O_7)_2F_2$ and $Ba_7Mn_8O_2(VO_4)_2F_{23}$. *Inorg. Chem.* **2016,** *55,* 12512–12515.

(34) You, F.; Gong, P.; Liang, F.; Jiang, X.; Tu, H.; Zhao, Y.; Hu, Z.; Lin, Z. $M_2(SeO_3)F_2$ (M = Zn, Cd): Understanding the Structure Directing Effect of $[SeO_3]^{2-}$ Groups on Constructing Ordered Oxyfluorides. *CrystEngComm* **2019,** *21,* 2485–2489.

(35) Hancock, J. C.; Nisbet, M. L.; Zhang, W.; Halasyamani, P. S.; Poeppelmeier, K. R. Periodic Tendril Perversion and Helices in the $AMoO_2F_3$ (A = K, Rb, NH_4, Tl) Family. *J. Am. Chem. Soc.* **2020,** *142,* 6375–6380.

(36) Sugimoto, A.; Ekino, T.; Gabovich, A. M.; Sekine, R.; Tanabe, K.; Tokiwa, K. Multilayered Cuprate Superconductor $Ba_2Ca_5Cu_6O_{12}(O_{1-x},F_x)_2$ Studied by Temperature-Dependent Scanning Tunneling Microscopy and Spectroscopy. *Phys. Rev. B: Condens. Matter Mater. Phys.* **2017,** *95,* 174508.

(37) Tsujimoto, Y.; Matsushita, Y.; Hayashi, N.; Yamaura, K.; Uchikoshi, T. Anion Order-to-Disorder Transition in Layered Iron Oxyfluoride Sr_2FeO_3F Single Crystals. *Cryst. Growth Des.* **2014,** *14,* 4278–4284.

(38) Strobel, P.; Greenblatt, M. Crystal Growth and Electrical Properties of Lithium, Rubidium, and Cesium Molybdenum Oxide Bronzes. *J. Solid State Chem.* **1981,** *36,* 331–338.

(39) Ramanujachary, K. V.; Greenblatt, M.; Jones, E. B.; McCarroll, W. H. Synthesis and Characterization of a New Modification of the Quasi-Low-Dimensional Compound KMo_4O_6. *J. Solid State Chem.* **1993,** *102,* 69–78.

(40) Nguyen, T. N.; zur Loye, H.-C. Electrosynthesis in Hydroxide Melts. *J. Cryst. Growth* **1997,** *172,* 183–189.

(41) Chen, C.; Spears, M.; Wondre, F.; Ryan, J. Crystal Growth and Superconductivity of $LiTi_2O_4$ and $Li_{1+1/3}Ti_{2-1/3}O_4$. *J. Cryst. Growth* **2003,** *250,* 139–145.

(42) Bright, N. F. H.; Rowland, J. F.; Wurm, J. G. The Compound $CaO.Ti_2O_3$. *Can. J. Chem.* **1958**, *36*, 492–495.

(43) Abe, H.; Satoh, A.; Nishida, K.; Abe, E.; Naka, T.; Imai, M.; Kitazawa, H. Electrochemical Immobilization of Cs in Single-Crystalline SYNROC. *J. Solid State Chem.* **2006**, *179*, 1521–1524.

(44) Chiba, Y.; Saito, M.; Hagiwara, T.; Takatsu, H.; Kageyama, H.; Motohashi, T. High-Temperature Electrochemical Crystal Growth of Hollandite-Type $Cs_xTi_8O_{16}$ with Controlled Electronic Properties. *Cryst. Growth Des.* **2017**, *17*, 5691–5696.

(45) Chiba, Y.; Koizumi, D.; Saito, M.; Motohashi, T. Structural Design of Alkali-Metal Titanates: Electrochemical Growth of $K_xTi_8O_{16}$, $Na_{2+x}Ti_6O_{13}$, and $Li_{2+x}Ti_3O_7$ Single Crystals with One-Dimensional Tunnel Structures. *CrystEngComm* **2019**, *21*, 3223–3231.

(46) Bugaris, D. E.; zur Loye, H.-C. Materials Discovery by Flux Crystal Growth: Quaternary and Higher Order Oxides. *Angew. Chem. Int. Ed.* **2012**, *51*, 3780–3811.

(47) Schmitz-Dumont, O.; Weeg, A. Über den Einfluß des Kationenradius auf die Bildungsenergie von Anlagerungsverbindungen. III. Die Systeme Alkalifluorid/Alkali-Chromat, -Molybdat, -Wolframat. *Z. Anorg. Allg. Chem.* **1951**, *265*, 139–155.

(48) *CrysAlisPro*, ver. 1.171.39.20a; Rigaku Oxford Diffraction: Tokyo, Japan, 2015.

(49) Sheldrick, G. M. Crystal Structure Refinement with *SHELXL*. *Acta Crystallogr., Sect. A: Found. Adv.* **2015**, *71*, 3–8.

(50) Kubelka, P.; Munk, F. Ein Beitrag zur Optik der Farbanstriche. *Z. Technol. Phys.* **1931**, *12*, 593–601.

(51) Liu, W.; Di, J.; Zhang, W.; Xue, L.; Yan, Y. Influence of Titanium Sources on the Microstructures and Properties of Li_2TiO_3 Ceramics Prepared by Hydrothermal Method. *Fusion Eng. Des.* **2019**, *138*, 364–371.

(52) Kataoka, K.; Takahashi, Y.; Kijima, N.; Nagai, H.; Akimoto, J.; Idemoto, Y.; Ohshima, K. Crystal Growth and Structure Refinement of Monoclinic Li_2TiO_3. *Mater. Res. Bull.* **2009**, *44*, 168–172.

(53) Zhang, Z.; Tang, Y.; Xiang, H.; Yang, A.; Wang, Y.; Yin, C.; Tian, Y.; Fang, L. $Li_5Ti_2O_6F$: A New Low-Loss Oxyfluoride Microwave Dielectric Ceramic for LTCC Applications. *J. Mater. Sci.* **2020**, *55*, 107–115.

(54)Kraeutler, B.; Bard, A. J. Heterogeneous Photocatalytic Preparation of Supported Catalysts. Photodeposition of Platinum on Titanium Dioxide Powder and Other Substrates. *J. Am. Chem. Soc.* **1978**, *100*, 4317–4318.

(55)Momma, K.; Izumi, F. *VESTA 3* for Three-Dimensional Visualization of Crystal, Volumetric and Morphology Data. *J. Appl. Crystallogr.* **2011**, *44*, 1272–1276.

(56)Azuma, K.; Dover, C.; Grinter, D. C.; Grau-Crespo, R.; Almora-Barrios, N.; Thornton, G.; Oda, T.; Tanaka, S. Scanning Tunneling Microscopy and Molecular Dynamics Study of the Li_2TiO_3(001) Surface. *J. Phys. Chem. C* **2013**, *117*, 5126–5131.

(57)Mukai, K.; Yashima, M.; Hibino, K.; Terai, T. Experimental Visualization of Interstitialcy Diffusion of Li Ion in β-Li_2TiO_3. *ACS Appl. Energy Mater.* **2019**, *2*, 5481–5489.

(58)Laumann, A.; Fehr, K. T.; Boysen, H.; Hoelzel, M.; Holzapfel, M. Temperature-Dependent Structural Transformations of Hydrothermally Synthesized Cubic Li_2TiO_3 Studied by *In-Situ* Neutron Diffraction. *Z. Kristallogr.—Cryst. Mater.* **2011**, *226*, 53–61.

(59)Laumann, A.; Ørnsbjerg Jensen, K. M.; Tyrsted, C.; Bremholm, M.; Fehr, K. T.; Holzapfel, M.; Iversen, B. B. In-Situ Synchrotron X-Ray Diffraction Study of the Formation of Cubic Li_2TiO_3 under Hydrothermal Conditions. *Eur. J. Inorg. Chem.* **2011**, *14*, 2221–2226.

(60)Gierszewski, P. Review of Properties of Lithium Metatitanate. *Fusion Eng. Des.* **1998**, *39*, 739–743.

(61)Zhang, L.; Wang, X.; Noguchi, H.; Yoshio, M.; Takada, K.; Sasaki, T. Electrochemical and Ex Situ XRD Investigations on $(1-x)LiNiO_2 \cdot xLi_2TiO_3$ ($0.05 \leq x \leq 0.5$). *Electrochim. Acta* **2004**, *49*, 3305–3311.

(62)Ma, J.; Fu, Z.; Li, Y.; Li, X. Effects of Preparation Methods on Synthesis, Microstructures and Microwave Dielectric Properties of Li_2TiO_3 Ceramics. *Ferroelectrics* **2016**, *504*, 116–122.

(63)Furuyama, Y.; Nakamura, H.; Takeda, T.; Samata, H.; Taniike, A.; Kitamura, A. Effect of Oxygen Content on CO_2 Absorption Characteristics of Li_2TiO_3. *Nucl. Mater. Energy* **2018**, *15*, 164–168.

(64)Shannon, R. D. Revised Effective Ionic Radii and Systematic Studies of Interatomic Distances in Halides and Chalcogenides. *Acta Crystallogr., Sect. A: Cryst. Phys., Diffr., Theor. Gen. Crystallogr.* **1976**, *32*, 751–767.

(65)Martinat, B.; Gourier, D.; Lejus, A. M.; Vivien, D. Optical Properties of $LaMgAl_{11}O_{19}:Ti^{3+}$, a

Potential Tunable Laser Material. *J. Solid State Chem.* **1990**, *89*, 147–154.

(66) López-Pacheco, G.; López-Juárez, R.; Villafuerte-Castrejón, M. E.; Falcony, C.; Barrera-Calva, E.; González, F. Luminescence Properties of Yb^{3+}-Doped $SrTiO_3$: The Significance of the Oxygen–Titanium Charge Transfer State on Photon Downshifting. *Dalton Trans.* **2019**, *48*, 11889–11896.

(67) Allen, G. C.; El-Sharkawy, G. A. M.; Warren, K. D. Electronic spectra of the hexafluorometalate(III) complexes of the first transition series. *Inorg. Chem.* **1971**, *10*, 2538–2546.

(68) Shen, P. K.; He, C.; Chang, S.; Huang, X.; Tian, Z. Magnéli Phase Ti_8O_{15} Nanowires as Conductive Carbon-Free Energy Materials to Enhance the Electrochemical Activity of Palladium Nanoparticles for Direct Ethanol Oxidation. *J. Mater. Chem. A* **2015**, *3*, 14416–14423.

(69) Prewitt, C. T.; Shannon, R. D.; White, W. B. Synthesis of a Pyroxene Containing Trivalent Titanium. *Contrib. Mineral. Petrol.* **1972**, *35*, 77–82.

(70) Dowty, E.; Clark, J. R. Crystal Structure Refinement and Optical Properties of a Ti^{3+} Fassaite from the Allende Meteorite. *Am. Mineral.* **1973**, *58*, 230–242.

(71) Nishioka, S.; Hyodo, J.; Vequizo, J. J. M.; Yamashita, S.; Kumagai, H.; Kimoto, K.; Yamakata, A.; Yamazaki, Y.; Maeda, K. Homogeneous Electron Doping into Nonstoichiometric Strontium Titanate Improves Its Photocatalytic Activity for Hydrogen and Oxygen Evolution. *ACS Catal.* **2018**, *8*, 7190–7200.

(72) Yu, J.; Wang, W.; Cheng, B.; Su, B.-L. Enhancement of Photocatalytic Activity of Mesporous TiO_2 Powders by Hydrothermal Surface Fluorination Treatment. *J. Phys. Chem. C* **2009**, *113*, 6743–6750.

(73) Yu, J.; Xiang, Q.; Ran, J.; Mann, S. One-Step Hydrothermal Fabrication and Photocatalytic Activity of Surface-Fluorinated TiO_2 Hollow Microspheres and Tabular Anatase Single Micro-Crystals with High-Energy Facets. *CrystEngComm* **2010**, *12*, 872–879.

Chapter 5

Na/Mo/F-Codoped $CaTiO_3$ Crystals Obtained via a High-Temperature Electrochemical Technique

5.1. Abstract

The author has succeeded in growing crystals of Na/Mo/F-codoped $CaTiO_3$ with an orthorhombic $GdFeO_3$-type perovskite structure employing high-temperature constant-voltage electrolysis of TiO_2 with an Na_2MoO_4–NaF–$CaMoO_4$ melt. This chapter will offer a possibility to grow a wide variety of titanium oxyfluorides using the electrochemical technique.

5.2. Introduction

Calcium titanate ($CaTiO_3$) is a prototype of perovskite compounds formulated as ABX_3, where A is a 12-coordinated larger cation, B is a 6-coordinated smaller cation, and X is an anion. At room temperature, $CaTiO_3$ crystallizes in a $GdFeO_3$-type structure that adopts an orthorhombically distorted perovskite lattice with lattice parameters of $a \sim \sqrt{2}a_p$, $b \sim \sqrt{2}a_p$, and $c \sim 2a_p$ (in the *Pbnm* setting),[1] where a_p denotes the cubic primitive cell, although the Sr and Ba analogs crystallize in cubic and tetragonal perovskite structures,[2,3] respectively. The crystal structure of $CaTiO_3$ is depicted in Figure 5.1[4,5] (the VESTA software[6] for visualization). The compound has a long history of research arising from its structural, dielectric, photoluminescence, and photocatalytic properties.[7–10]

Fluorine doping into titanate perovskites improves various properties. For example, K/F-codoped $BaTiO_3$ ($Ba_{1-x}K_xTiO_{3-x}F_x$) exhibits much higher piezoelectric and dielectric constants at room temperature than nondoped $BaTiO_3$ and $Pb(Zr,Ti)O_3$ (PZT).[11–13] F-doped $SrTiO_3$ is a visible-light-driven photocatalyst capable of decomposing NO and producing H_2 from aqueous methanol,[14–16] although nondoped $SrTiO_3$ is photoactive only under UV irradiation.[14,15] As far as the author knows, however, fluorine doping into the $CaTiO_3$ perovskite had not been reported.

In this chapter, the author attempted the crystal growth of F-doped $CaTiO_3$ by a high-temperature constant-voltage electrolysis method. This method has recently been proved useful for growing single crystals of electron-doped titanium oxyfluoride $Li_2Ti(O,F)_3$.[17] As a consequence, crystals of Na/Mo/F-codoped $CaTiO_3$ ($CaTiO_3$:Na,Mo,F) were successfully obtained by the electrolysis of TiO_2 with an Na_2MoO_4–NaF–$CaMoO_4$ melt. The results reveal that the electrochemical method may be applicable to the crystal growth of various titanium oxyfluorides.

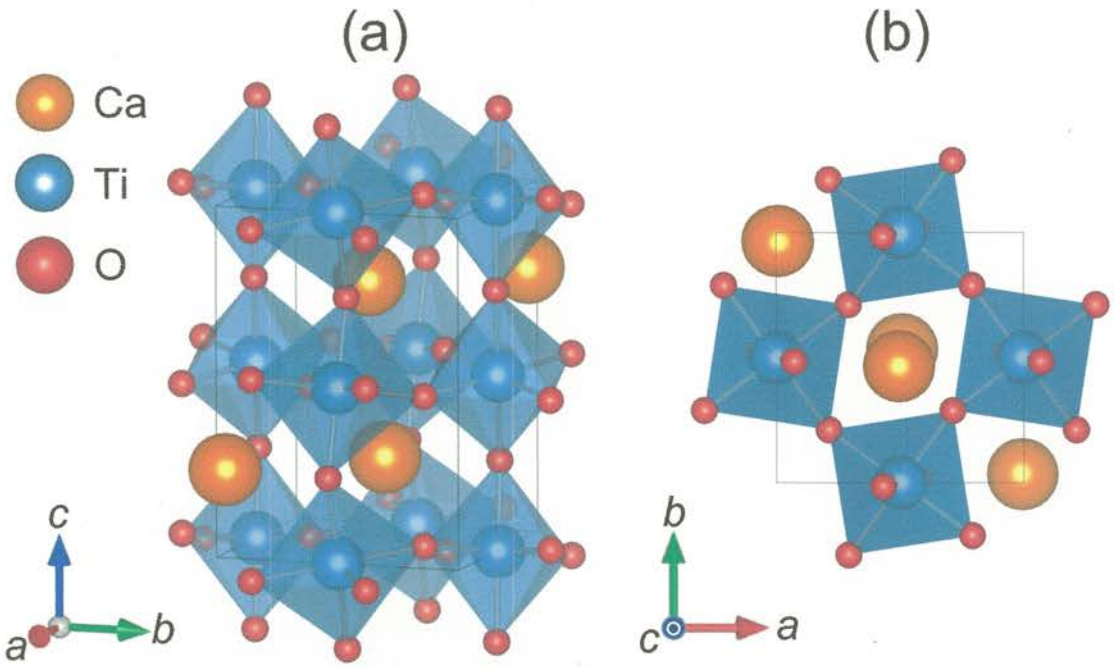

Figure 5.1. Projections of the crystal structure of $CaTiO_3$ [crystal system: orthorhombic; space group: *Pbnm* (no. 62); lattice parameters: a = 5.388(1) Å, b = 5.447(1) Å, c = 7.654(1) Å[1]], along the (a) a-axis (slightly oriented) and (b) c-axis directions. Octahedral tilting of the TiO_6 units (shown as blue polyhedra) is clearly visible; the Glazer's notation[4,5] is represented as $a^-a^-c^+$. Orange spheres, Ca ions; blue spheres, Ti ions; and red spheres, O ions. These illustrations were generated by the VESTA software.[6]

5.3. Experimental Section

5.3.1. Materials

TiO_2 (anatase, 99%), $CaCO_3$ (99.99%), and MoO_3 (99.98%) were purchased from Kojundo Chemical Laboratory. $Na_2MoO_4 \cdot 2H_2O$ (99.0%), NaF (99.0%), and K_2CO_3 (99.5%) were purchased from FUJIFILM Wako Pure Chemical. Ethylenediaminetetraacetic acid disodium salt dihydrate (EDTA-2Na; >99.5%) was purchased from Dojindo. One of the melt components, $CaMoO_4$, was prepared by firing a 1:1 molar mixture of $CaCO_3$ and MoO_3 at 800 °C for 12 h in air.

5.3.2. Electrochemical Crystal Growth

Calcium titanium oxyfluoride crystals were grown by electrolytic reduction of TiO_2 with a mixed Na_2MoO_4–NaF–$CaMoO_4$ melt having an 8:2:1 molar ratio. The 10 g mixture consisting of Na_2MoO_4 (weighed as a dihydrate form), NaF, and $CaMoO_4$ was loaded into a Pt crucible (30 cm^3 in volume) as a reaction vessel. To perform high-temperature electrolysis, three Pt wires (0.5 mm in diameter) connected to an external potentiostat (Hokuto Denko: HZ-5000) were introduced into the Pt crucible in a programmable box furnace. The working and pseudoreference electrodes (WE and PRE, respectively) were placed near one another. A 0.1 g powder of TiO_2 was put in the vicinity of the counter electrode (CE) to prevent undissolved TiO_2 from being incorporated into grown crystals on WE.

The electrolysis was carried out at 1050 °C for 5 h. The furnace was heated to 1050 °C with a heating rate of 7 °C min^{-1}, and kept for 30 min to stabilize the melt prior to the electrolysis. Voltages applied were set at $V = -0.6$, -0.8, and -1.0 V, on the basis of the onset potentials of reduction waves in the CV plot (Figure S5.1 in the Supporting Information). At the end of each run, the applied voltage was switched off, and then the Pt electrodes were immediately lifted above the melt and removed

from the furnace to be rapidly cooled to room temperature. Electrolysis for 5 h resulted in crystal growth at the surface of WE (Figure S5.2), while no crystals grew on CE. Crystals deposited on WE were immersed in an aqueous solution containing 5 wt % of K_2CO_3 and 2 wt % of EDTA-2Na at room temperature overnight to dissolve the coating solidified residue. The crystals were mechanically isolated from WE with tweezers, washed with distilled water several times, and then allowed to dry at room temperature. Optical micrographs of the resultant crystals were taken by a digital microscope (Keyence: VHX-7000).

5.3.3. Characterization

Powder X-ray Diffraction (PXRD). Phase identification of the resultant crystals was conducted by using a powder X-ray diffractometer (Rigaku: Ultima IV Protectus; Cu Kα radiation; $\lambda = 1.5418$ Å) equipped with a silicon strip detector (Rigaku: D/teX Ultra2). As-grown crystals were evenly spread on a "non-reflection" sample holder made of an obliquely cut silicon crystal and analyzed in 0.02° increments over a 2θ range of 5°–90° at a rate of 5° min^{-1} (operating condition: 40 kV, 40 mA).

Elemental Analysis. Analysis was performed on the single crystals by using a scanning electron microscope (SEM; Hitachi High-Tech: SU-5000) equipped with an energy-dispersive X-ray spectrometer (EDX; Bruker: XFlash Detector 630M). Selected crystal pieces were mounted on carbon tape and analyzed with an accelerating voltage of 15 kV and an accumulation time of 5 min.

5.4. Results and Discussion

5.4.1. Crystal Growth

Electrochemical crystal growth of calcium titanium oxyfluorides was examined by high-temperature electrolysis of TiO_2 with the Na_2MoO_4–NaF–$CaMoO_4$ melt. Optical micrographs of the crystals grown with $V = -0.6$, -0.8, and -1.0 V are shown in Figure 5.2. Most of the grown crystals are highly aggregated, and notably, the appearances strongly depend on the applied voltage values: brown for $V = -0.6$ V, dark-brown for $V = -0.8$ V, and black for $V = -1.0$ V. Crystal growth with larger negative voltages resulted in higher product yields.

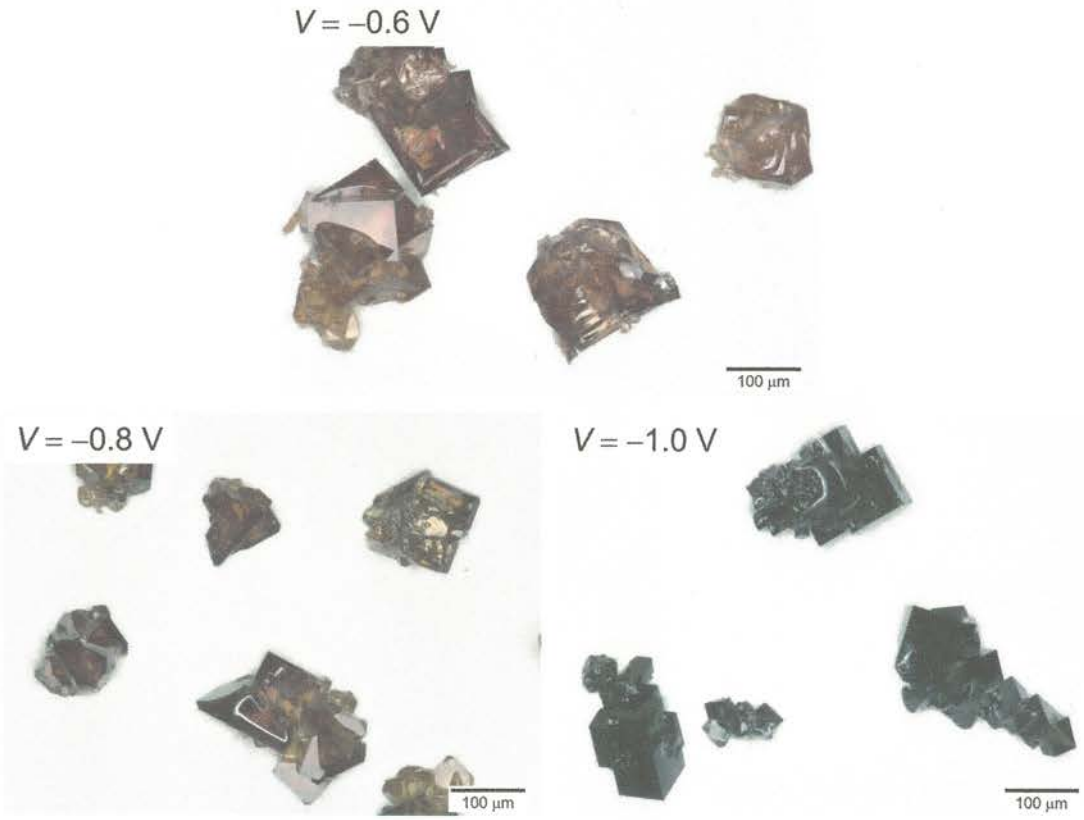

Figure 5.2. Optical micrographs of the resultant crystals grown with $V = -0.6$ (top), -0.8 (bottom left), and -1.0 V (bottom right).

PXRD patterns of the nonpulverized crystals (Figure 5.3) reveal the formation of orthorhombic perovskite-type $CaTiO_3$ (ICSD #71916) for all batches. The 220 reflection is strongly preferred; the well-developed face should be $\{hk0\}$. The lattice parameters of each crystal are the following: a = 5.391(3) Å, b = 5.452(2) Å, and c = 7.663(5) Å for V = –0.6 V; a = 5.389(2) Å, b = 5.451(1) Å, and c = 7.656(3) Å for V = –0.8 V; and a = 5.392(3) Å, b = 5.468(3) Å, and c = 7.676(8) Å for V = –1.0 V, all of which are somewhat larger than the literature values.[1] This suggests a partial reduction of Ti^{4+} to Ti^{3+} with a larger size (0.605 Å for Ti^{4+} vs 0.670 Å for Ti^{3+} in six-fold coordination[18]) and the possible incorporation of Na and/or Mo ions.

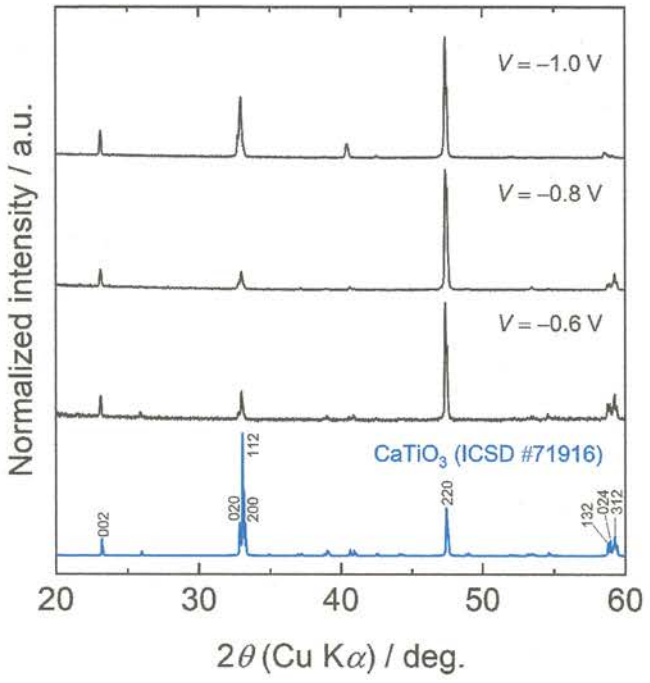

Figure 5.3. PXRD patterns for the nonpulverized crystals grown with V = –0.6, –0.8, and –1.0 V. The simulated pattern for $CaTiO_3$ (ICSD #71916) was taken from the ICSD database.

The chemical compositions of the crystals were analyzed by SEM-EDX (Figure 5.4). Electron irradiation during EDX measurements led to a slight charging effect only for the $V = -0.6$ V crystal, indicative of its low electrical conductivity. Calcium, titanium, sodium, and molybdenum were observed for all the crystals, whereas fluorine was detected for the $V = -0.6$ V and -0.8 V crystals. The Ca/Na/Mo/F/Ti ratios for the $V = -0.6$, -0.8, and -1.0 V crystals were estimated to be 1.18/0.13/0.01/0.12/1, 1.03/0.10/0.02/0.08/1, and 1.16/0.08/0.05/0.00/1 (ratios normalized by Ti), respectively, where oxygen is not shown for its poor accuracy. The calcium content looks somewhat excessive, which may be due to analytical errors of the measurements. Taking into account the ionic radii of the constituent elements,[18] the Na and Mo ions partially substitute the Ca and Ti sites, respectively. The Mo and F contents seem to relate to the applied voltages, but the Na content does not. Crystals grown with larger negative voltages tend to show higher Mo and lower F contents. The author assumes that the introduction of oxygen defects into the crystals could be promoted at larger negative voltages, which may hinder fluorine doping. Similar results have been observed in the previous study on the crystal growth of lithium titanium oxyfluorides (see also: Chapter 4).[17]

Finally, the author would like to comment on a possible application of the Na/Mo/F-codoped $CaTiO_3$ crystals as a high-performance photocatalyst. Metal doping into titanate perovskites is one of the most effective strategies to improve their photocatalytic activities. For example, Fe^{3+}- or Cu^{2+}-doped $CaTiO_3$ and La^{3+}/Cr^{3+}- or Eu^{3+}/Na^{+}-codoped $CaTiO_3$ exhibit higher activities than nondoped $CaTiO_3$ for the degradation of methylene blue (MB) and hydrogen evolution from an aqueous methanol solution.[19–23] In the case of strontium titanate perovskite $SrTiO_3$, the codoping of Na^{+} and Mo^{6+} ions has been reported to improve the hydrogen evolution activity.[24] These enhanced photocatalytic activities are mainly responsible for visible-light absorption caused by metal doping, although both nondoped $CaTiO_3$ and $SrTiO_3$ are only capable of absorbing UV light. As can be seen in Figure 5.2, the Na/Mo/F-codoped $CaTiO_3$ crystals obtained herein are obviously colored,

evidencing the visible light absorbing nature. Moreover, as mentioned in **5.2**, fluorine doping into titanate perovskites is also effective in improving their photocatalytic activities.[14–16] Fluoride ions can trap photogenerated electrons and inhibit the recombination of electron–hole pairs, which lead to higher photocatalytic activities.[25] However, excessive F^- ions have been demonstrated harmful because F^- ions also serve recombination centers of photogenerated carriers.[26,27] Investigation on photocatalytic activities of the Na/Mo/F-codoped $CaTiO_3$ crystals is thus fascinating—this theme will be pursued in future works.

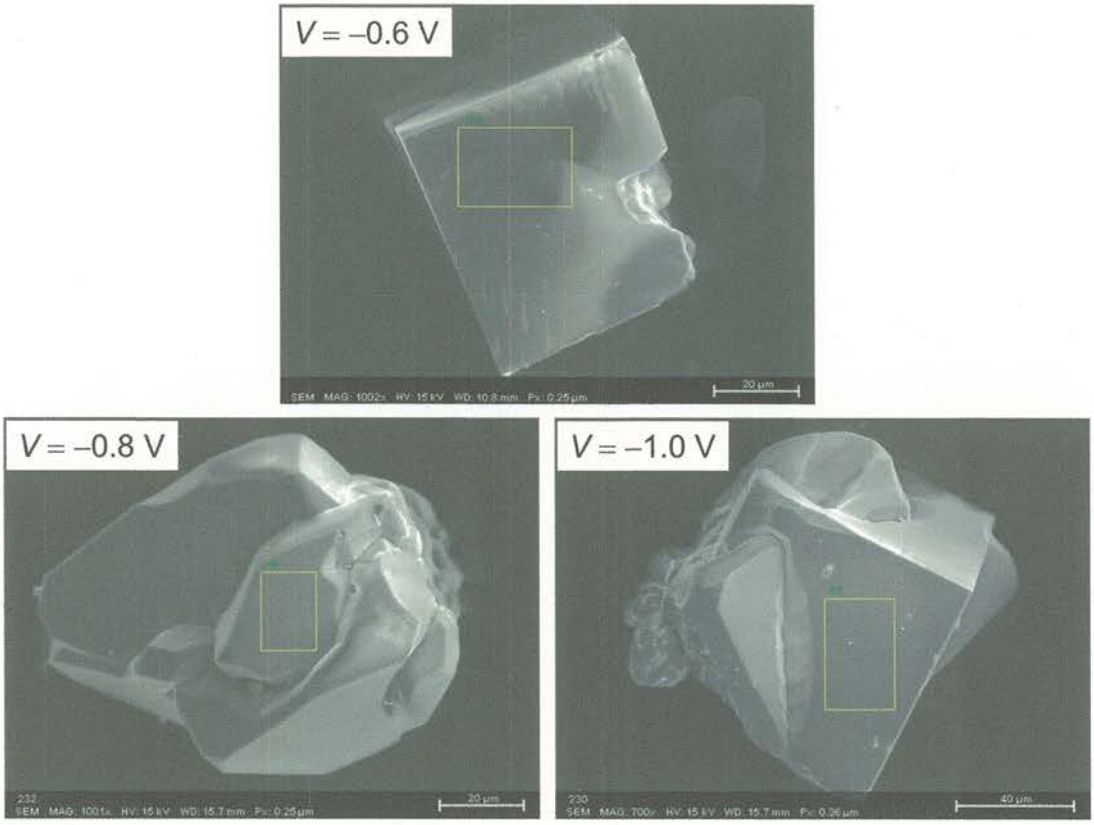

Figure 5.4. SEM images of the crystals grown with $V = -0.6$ (top), -0.8 (bottom left), and -1.0 V (bottom right). EDX analyses were performed within the yellow boxes.

5.5. Concluding Remarks

To summarize, crystals of Na/Mo/F-codoped $CaTiO_3$ with an orthorhombic perovskite-type structure were successfully grown by means of high-temperature constant-voltage electrolysis of TiO_2 with the Na_2MoO_4–NaF–$CaMoO_4$ melt. Controlling applied voltages was a key factor in growing the crystals. This chapter demonstrated that the electrochemical technique may be applicable to the crystal growth of various titanium oxyfluorides. Further investigation on the resultant crystals (e.g., photocatalytic activities) is attractive because the crystals exhibit clear visible-light absorption.

References

(1) Buttner, R. H.; Maslen, E. N. Electron Difference Density and Structural Parameters in $CaTiO_3$. *Acta Crystallogr., Sect. B: Struct. Sci.* **1992**, *48*, 644–649.

(2) Buttner, R. H.; Maslen, E. N. Electron Difference Density and Vibration Tensors in $SrTiO_3$. *Acta Crystallogr., Sect. B: Struct. Sci.* **1992**, *48*, 639–644.

(3) Buttner, R. H.; Maslen, E. N. Structural Parameters and Electron Difference Density in $BaTiO_3$. *Acta Crystallogr., Sect. B: Struct. Sci.* **1992**, *48*, 764–769.

(4) Glazer, A. M. The Classification of Tilted Octahedra in Perovskites. *Acta Crystallogr., Sect. B: Struct. Crystallogr. Cryst. Chem.* **1972**, *28*, 3384–3392.

(5) Glazer, A. M. Simple Ways of Determining Perovskite Structures. *Acta Crystallogr., Sect. A: Cryst. Phys., Diffr., Theor. Gen. Crystallogr.* **1975**, *31*, 756–762.

(6) Momma, K.; Izumi, F. *VESTA 3* for Three-Dimensional Visualization of Crystal, Volumetric and Morphology Data. *J. Appl. Crystallogr.* **2011**, *44*, 1272–1276.

(7) Yashima, M.; Ali, R. Structural Phase Transition and Octahedral Tilting in the Calcium Titanate Perovskite $CaTiO_3$. *Solid State Ionics* **2009**, *180*, 120–126.

(8) Cockayne, E.; Burton, B. P. Phonons and Static Dielectric Constant in $CaTiO_3$ from First Principles. *Phys. Rev. B: Condens. Matter Mater. Phys.* **2000**, *62*, 3735–3743.

(9) Kyômen, T.; Sakamoto, R.; Sakamoto, N.; Kunugi, S.; Itoh, M. Photoluminescence Properties of Pr-Doped (Ca,Sr,Ba)TiO_3. *Chem. Mater.* **2005**, *17*, 3200–3204.

(10) Passi, M.; Pal, B. A Review on $CaTiO_3$ Photocatalyst: Activity Enhancement Methods and Photocatalytic Applications. *Powder Technol.* **2021**, *388*, 274–304.

(11) Akishige, Y.; Michiie, T.; Tsunogae, T. Ferroelectric Curie Temperature of $BaTiO_3$ Single Crystals Grown by a Flux Method. *Ferroelectrics* **2002**, *269*, 249–254.

(12) Akishige, Y. Ferroelectric and Piezoelectric Properties of Single Crystals of $Ba_{1-x}K_xTiO_{3-x}F_x$ with $x = 0.1$. *J. Phys. Soc. Jpn.* **2006**, *75*, 073704-1–073704-3.

(13) Akishige, Y. Phase Diagram of KF-Doped $BaTiO_3$ Single Crystals. *Ferroelectrics* **2008**, *369*, 91–97.

(14) Wang, J.; Yin, S.; Zhang, Q.; Saito, F.; Sato, T. Mechanochemical Synthesis of $SrTiO_{3-x}F_x$ with High Visible Light Photocatalytic Activities for Nitrogen Monoxide Destruction. *J. Mater. Chem.* **2003**, *13*, 2348–2352.

(15) Kang, H. W.; Park, S. B. Doping of Fluorine into $SrTiO_3$ by Spray Pyrolysis for H_2 Evolution under Visible Light Irradiation. *Chem. Eng. Sci.* **2013**, *100*, 384–391.

(16) Modak, B.; Ghosh, S. K. Role of F in Improving the Photocatalytic Activity of Rh-Doped $SrTiO_3$. *J. Phys. Chem. C* **2015**, *119*, 7215–7224.

(17) Chiba, Y.; Shibata, K.; Takatsu, H.; Fujii, K.; Saito, M.; Kageyama, H.; Maeda, K.; Yashima, M.; Motohashi, T. Electrochemical Crystal Growth of Titanium Oxyfluorides—A Strategy for Development of Electron-Doped Materials. *Inorg. Chem.* **2021**, *60*, 14613–14621.

(18) Shannon, R. D. Revised Effective Ionic Radii and Systematic Studies of Interatomic Distances in Halides and Chalcogenides. *Acta Crystallogr., Sect. A: Cryst. Phys., Diffr., Theor. Gen. Crystallogr.* **1976**, *32*, 751–767.

(19) Jang, J. S.; Borse, P. H.; Lee, J. S.; Lim, K. T.; Jung, O.-S.; Jeong, E. D.; Bae, J. S.; Kim, H. G. Photocatalytic Hydrogen Production in Water-Methanol Mixture over Iron-Doped $CaTiO_3$. *Bull. Korean Chem. Soc.* **2011**, *32*, 95–99.

(20) Yang, H.; Han, C.; Xue, X. Photocatalytic Activity of Fe-Doped $CaTiO_3$ under UV–Visible Light. *J. Environ. Sci.* **2014**, *26*, 1489–1495.

(21) Zhang, H.; Chen, G.; Li, Y.; Teng, Y. Electronic Structure and Photocatalytic Properties of Copper-Doped $CaTiO_3$. *Int. J. Hydrogen Energy* **2010**, *35*, 2713–2716.

(22) Wang, R.; Ni, S.; Liu, G.; Xu, X. Hollow $CaTiO_3$ Cubes Modified by La/Cr Co-Doping for Efficient Photocatalytic Hydrogen Production. *Appl. Catal., B* **2018**, *225*, 139–147.

(23) Chen, M.; Xiong, Q.; Liu, Z.; Qiu, K.; Xiao, X. Synthesis and Photocatalytic Activity of Na^+ Co-Doped $CaTiO_3$:Eu^{3+} Photocatalysts for Methylene Blue Degradation. *Ceram. Int.* **2020**, *46*, 12111–12119.

(24) Kang, H. W.; Park, S. B.; Park, A.-H. A. Effects of Charge Balance with Na^+ on $SrTiO_3$:Mo^{6+} Prepared by Spray Pyrolysis for H_2 Evolution under Visible Light Irradiation. *Int. J. Hydrogen Energy* **2013**, *38*, 9198–9205.

(25) Wang, S.; Huang, B.; Wang, Z.; Liu, Y.; Wei, W.; Qin, X.; Zhang, X.; Dai, Y. A New

Photocatalyst: $Bi_2TiO_4F_2$ Nanoflakes Synthesized by a Hydrothermal Method. *Dalton Trans.* **2011**, *40*, 12670–12675.

(26) Yu, J.; Wang, W.; Cheng, B.; Su, B.-L. Enhancement of Photocatalytic Activity of Mesporous TiO_2 Powders by Hydrothermal Surface Fluorination Treatment. *J. Phys. Chem. C* **2009**, *113*, 6743–6750.

(27) Yu, J.; Xiang, Q.; Ran, J.; Mann, S. One-Step Hydrothermal Fabrication and Photocatalytic Activity of Surface-Fluorinated TiO_2 Hollow Microspheres and Tabular Anatase Single Micro-Crystals with High-Energy Facets. *CrystEngComm* **2010**, *12*, 872–879.

Chapter 6

General Conclusions and Suggestions for Future Works

In this dissertation, single crystals of various titanium oxides and oxyfluorides were grown employing high-temperature constant-voltage electrolysis of TiO_2 with A_2MoO_4 (A = Li, Na, K, or Cs)-based melts. Structural, electronic, magnetic, and optical properties, and photocatalytic H_2 evolution activities of the resultant crystals were extensively investigated. Clearly, the described method is highly effective in obtaining *electron-doped* titanium oxides and oxyfluorides with precisely controlled chemical compositions and crystal structures. Throughout the dissertation, the author emphasizes that crystals obtained herein are never obtained by any other techniques, and the doped d electrons significantly impact the properties of the materials. The dissertation will propagate the utility of the electrochemical technique for the research on solid-state chemistry and physics.

In Chapter 2, needle-like crystals of hollandite-type $Cs_xTi_8O_{16}$ were successfully obtained by constant-voltage electrolysis of TiO_2 with the Cs_2MoO_4 melt. The resultant crystals exhibit distinct properties, either electrical insulators with optical transparency or semiconductors with metallic luster, depending on the applied voltages. This chapter revealed that the constant-voltage mode is more advantageous than the constant-current mode, which had been widely used in previous studies, for the crystal growth of titanium oxides with different electron-doping levels.

In Chapter 3, the electrolysis method was extended to the crystal growth of lithium-, sodium-, and potassium-containing titanium oxides. With A_2MoO_4 (A = Li, Na, or K) melts, single crystals of

$Li_{2+x}Ti_3O_7$ (ramsdellite-type), $Na_{2+x}Ti_6O_{13}$, and $K_xTi_8O_{16}$ (hollandite-type) were grown. These compounds unexceptionally crystallize in one-dimensional tunnel structures built from corner- and edge-shared TiO_6 (or $(Ti,Li)O_6$ for $Li_{2+x}Ti_3O_7$) octahedra, with various tunnel shapes depending on the alkali metals incorporated. The $Li_{2+x}Ti_3O_7$ and $Na_{2+x}Ti_6O_{13}$ crystals showed clear visible-light absorption resulting from the d electrons doped along with the excess Li and Na ions, contrary to the lithium- and sodium-stoichiometric (i.e., $x = 0$) samples. This chapter further established the utility of molten salt electrolysis for the crystal growth of electron-doped titanium oxides containing various alkali metals.

In Chapter 4, electrochemical crystal growth of titanium oxyfluorides was accomplished for the first time. Using the eutectic Li_2MoO_4–LiF melt, light-green crystals of cubic rocksalt-type $Li_2Ti(O,F)_3$ were successfully obtained. The crystals exhibited much higher photocatalytic H_2 evolution activities than the $Li_5Ti_2O_6F$ (d^0) reference under UV light, possibly originating from the doped electrons for the former. The success in synthesizing the $Li_2Ti(O,F)_3$ crystals motivated the exploration of new titanium oxyfluoride phases using this technique.

In Chapter 5, the author explored F-doped $CaTiO_3$ as a second example of electrochemical crystal growth of titanium oxyfluorides. Na/Mo/F-codoped $CaTiO_3$ crystals were grown using the Na_2MoO_4–NaF–$CaMoO_4$ melt, with the necessity of controlled applied voltages. This chapter provided a possibility that crystals of various titanium oxyfluorides can be grown by the electrochemical technique.

Future perspectives for subsequent studies are as follows: (1) detailed investigation on the formation mechanism of each compound, and (2) search for other transition metal oxyfluorides. The first perspective would be indispensable because the growth mechanisms of the crystals obtained herein still remain unclear. Analysis of ionic species in molten salts may shed light on redox reactions on the electrodes. The second perspective is also significant for the exploration of novel materials

with intriguing properties and functionalities, although this work focused solely on titanium-based compounds. In the preliminary experiments, attempts to synthesize vanadium oxyfluoride crystals were unsuccessful. This is possibly due to the difficulty of controlling oxidation states of vanadium ions, which accommodate a wide range of oxidation states from +2 to +5. The use of more stable transition metals against electrochemical reductions, such as niobium and tantalum, is of great interest in achieving the above purpose. Specifically, given the successful synthesis of $Li_2Ti(O,F)_3$, crystals of electron-doped rocksalt-type lithium niobium (or tantalum) oxyfluorides might be grown because polycrystalline samples of nondoped rocksalt-type Li_4MO_4F (M = Nb, Ta) have already been synthesized.[1,2]

References

(1) Norén, L.; Withers, R. L.; Goossens, D. J.; Elcombe, M.; Kearley, G. J. Coupled Li^{1+}/Nb^{5+} and O^{2-}/F^{-} Ordering on the Na and Cl Sites of the Average NaCl Structure of Li_4NbO_4F. *J. Solid State Chem.* **2009**, *182*, 1109–1114.

(2) Agulyansky, A. *Chemistry of Tantalum and Niobium Fluoride Compounds*, 1st ed.; Elsevier: Amsterdam, 2004.

List of Tables

List of Figures

Peer-Reviewed Original Papers

(1) **Chiba, Y.**; Saito, M.; Hagiwara, T.; Takatsu, H.; Kageyama, H.; Motohashi, T. High-Temperature Electrochemical Crystal Growth of Hollandite-Type $Cs_xTi_8O_{16}$ with Controlled Electronic Properties. *Cryst. Growth Des.* **2017,** *17,* 5691–5696.

(2) **Chiba, Y.**; Koizumi, D.; Saito, M.; Motohashi, T. Structural Design of Alkali-Metal Titanates: Electrochemical Growth of $K_xTi_8O_{16}$, $Na_{2+x}Ti_6O_{13}$, and $Li_{2+x}Ti_3O_7$ Single Crystals with One-Dimensional Tunnel Structures. *CrystEngComm* **2019,** *21,* 3223–3231.

(3) **Chiba, Y.**; Shibata, K.; Takatsu, H.; Fujii, K.; Saito, M.; Kageyama, H.; Maeda, K.; Yashima, M.; Motohashi, T. Electrochemical Crystal Growth of Titanium Oxyfluorides—A Strategy for Development of Electron-Doped Materials. *Inorg. Chem.* **2021,** *60,* 14613–14621. **(Selected as Cover Art)**

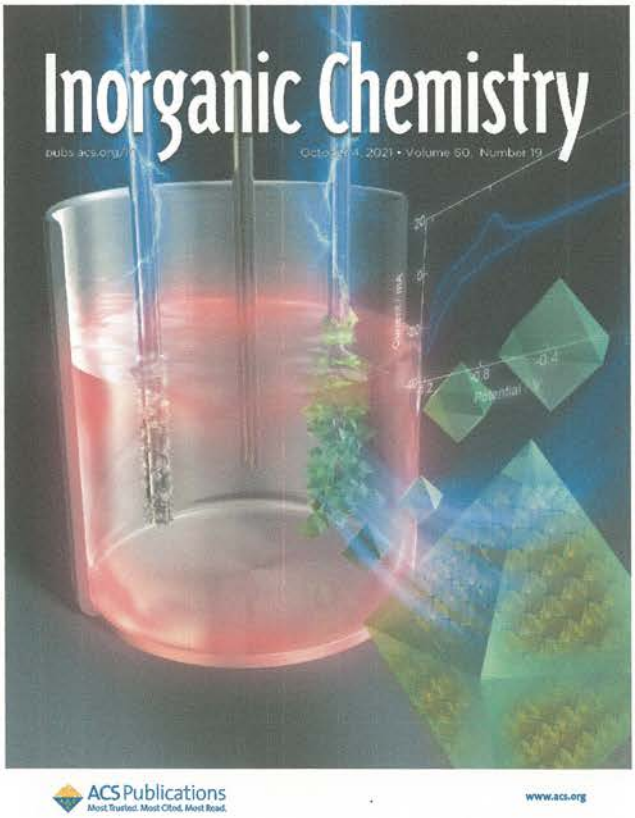

List of Presentations

Oral Presentations:

(1) **Y. Chiba,** M. Saito, T. Motohashi, "Electrolysis Synthesis and Cesium Content Control of Hollandite-Type Oxides $Cs_xTi_8O_{16}$," Annual Meeting 2016 of The Ceramic Society of Japan, Mar. 14–16, 2016, Tokyo, Japan.

(2) **Y. Chiba,** M. Saito, T. Hagiwara, H. Takatsu, H. Kageyama, T. Motohashi, "Electrolysis Synthesis and Physical Properties of Hollandite-Type Oxides $A_xTi_8O_{16}$ (A = K, Cs)," The 29th Fall Meeting of The Ceramic Society of Japan, Sep. 7–9, 2016, Hiroshima, Japan.

(3) **Y. Chiba,** M. Saito, H. Takatsu, H. Kageyama, T. Motohashi, "Electrochemical Crystal Growth and Physical Properties of the Spinel-Type Titanium Oxides," Annual Meeting 2017 of The Ceramic Society of Japan, Mar. 17–19, 2017, Tokyo, Japan.

(4) **Y. Chiba,** D. Koizumi, M. Saito, T. Hagiwara, H. Takatsu, H. Kageyama, T. Motohashi, "Single Crystal Growth of Titanium Oxides and Oxyfluorides via an Electrochemical Technique," The 58th Symposium on Basic Science of Ceramics, Jan. 9–10, 2020, Nagoya, Japan.

(5) **Y. Chiba,** K. Shibata, H. Takatsu, M. Saito, H. Kageyama, K. Maeda, T. Motohashi, "Electrochemical Crystal Growth of Lithium Titanium Oxide and Oxyfluoride," Annual Meeting 2021 of The Ceramic Society of Japan, Mar. 23–25, 2021, Online.

Poster Presentations:

(1) **Y. Chiba,** M. Saito, T. Motohashi, "Electrolysis Synthesis and Cesium Content Control of Hollandite-Type Oxides $Cs_xTi_8O_{16}$," 10th Ceramic Festa in Kanagawa, Dec. 5, 2015, Kanagawa, Japan.

(2) **Y. Chiba,** M. Saito, T. Hagiwara, H. Takatsu, H. Kageyama, T. Motohashi, "Carrier Content Control of Hollandite-Type Oxides $Cs_xTi_8O_{16}$ via Constant-Voltage Electrolysis," 6th CSJ Chemistry Festa, Nov. 14–16, 2016, Tokyo, Japan.

(3) Y. Saito, **Y. Chiba,** M. Saito, T. Motohashi, "Electrolysis Crystal Growth of Potassium Vanadium Oxides," 11th Ceramic Festa in Kanagawa, Dec. 17, 2016, Kanagawa, Japan.

(4) **Y. Chiba,** Y. Saito, M. Saito, T. Hagiwara, H. Takatsu, H. Kageyama, T. Motohashi, "Electrochemical Crystal Growths and Electronic Properties of Titanium and Vanadium Oxides with One-Dimensional Tunnel Structures," International Union of Materials Research Societies-The 15th International Conference on Advanced Materials, Aug. 27–Sep. 1, 2017, Kyoto, Japan.

(5) H. Hikobe, **Y. Chiba,** M. Saito, T. Motohashi, "Electrolysis Crystal Growth of Hollandite-Type Manganese Oxides $Ba_xMn_8O_{16}$," 12th Ceramic Festa in Kanagawa, Dec. 16, 2017, Kanagawa, Japan.

(6) D. Koizumi, **Y. Chiba,** M. Saito, T. Motohashi, "Electrochemical Crystal Growth of Sodium Titanium Oxides," The 34th Research Conference of Kanto Branch of The Ceramic Society of Japan, Sep. 26–27, 2018, Gunma, Japan. **(Poster Award)**

(7) **Y. Chiba,** M. Saito, T. Hagiwara, H. Takatsu, H. Kageyama, T. Motohashi, "High-Temperature Electrochemical Crystal Growth of Alkali-Metal Titanium Oxides with Controlled Structural and Electronic Properties," 4th E-MRS & MRS-J Bilateral Symposium on Advanced Oxides and Wide Bandgap Semiconductors, Oct. 14–19, 2018, Crete, Greece.

(8) **Y. Chiba,** D. Koizumi, M. Saito, T. Hagiwara, H. Takatsu, H. Kageyama, T. Motohashi, "High-Temperature Electrochemical Crystal Growth of Alkali-Metal Titanium Oxides and Oxyfluorides," 3rd LOBSTER School, Aug. 5–7, 2019, Ishikawa, Japan.

(9) T. Nagai, **Y. Chiba,** M. Saito, T. Motohashi, "Preparation of Oxyfluoride Single Crystals via High-Temperature Molten Salt Electrolysis," Kanagawa University Techno Festa 2019, Nov. 8, 2019, Kanagawa, Japan.

(10) **Y. Chiba,** M. Saito, H. Takatsu, H. Kageyama, T. Motohashi, "Single Crystal Growth of Lithium Titanium Oxyfluorides via High-Temperature Molten Salt Electrolysis," A School for Young Researchers, MEXT Grant-in-Aid for Scientific Research on Innovative Areas "Synthesis of Mixed Anion Compounds toward Novel Functionalities," Jan. 15, 2020, Ibaraki, Japan. **(Poster Award)**

(11) **Y. Chiba,** K. Shibata, H. Takatsu, K. Fujii, M. Saito, H. Kageyama, K. Maeda, M. Yashima, T. Motohashi, "High-Temperature Electrochemical Crystal Growth of Titanium Oxyfluorides," International Conference on Mixed-Anion Compounds, Dec. 7–10, 2021, Hyogo, Japan & Online.

Supporting Information

In this supporting information, the author presents additional experimental data for the dissertation. Please note that the first number next to "S" in captions refers to the corresponding chapter's number.

Table of Contents

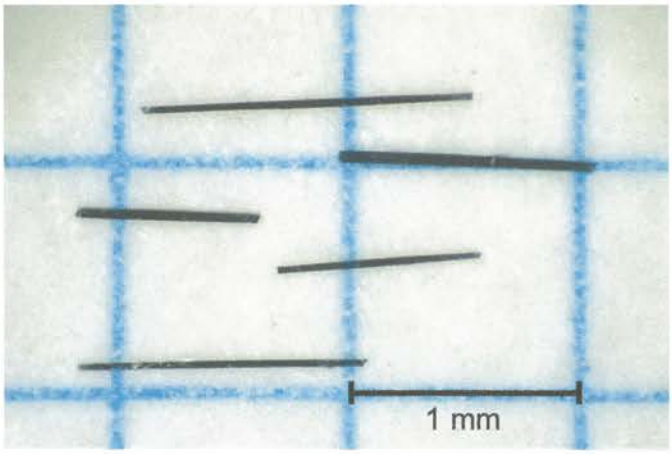

Figure S2.1. Optical micrograph of the resultant $Cs_xTi_8O_{16}$ crystals grown with constant-current conditions ($I = -1$ mA).

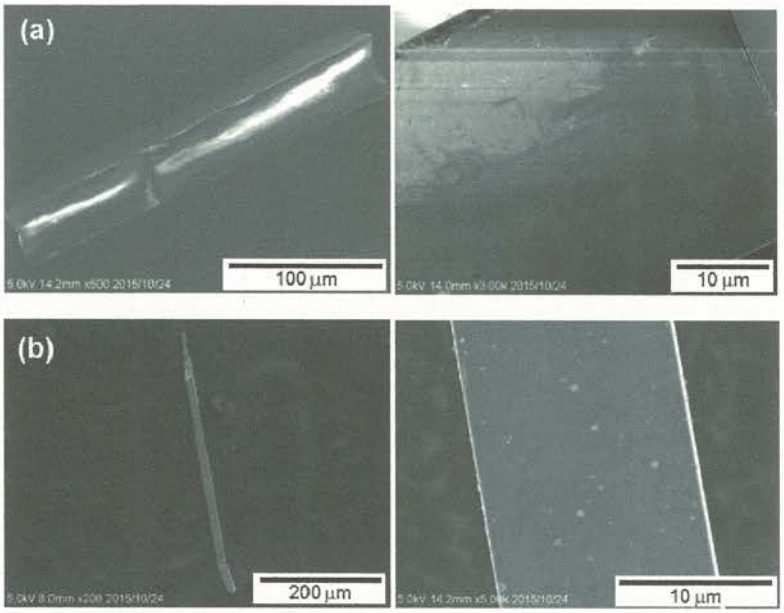

Figure S2.2. SEM images of the crystals grown with different applied voltages of (a) $V = -0.6$ V and (b) -1.0 V.

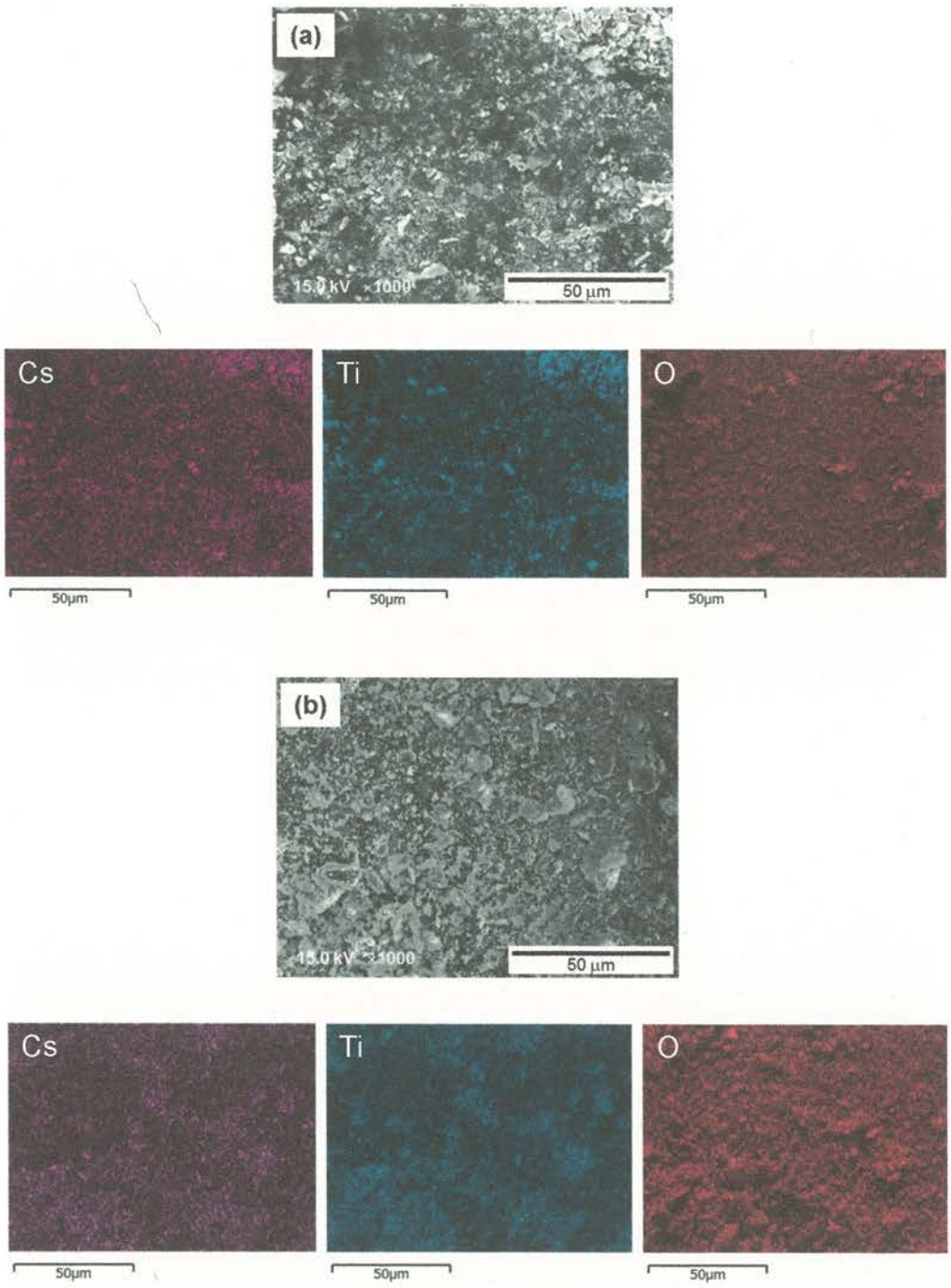

Figure S2.3. EDX mapping images of the ground crystals: (a) $V = -0.6$ V and (b) -1.0 V.

Text S2.1: ICP-MS Analysis. The Cs/Ti ratios of the crystals grown with $V = -0.6$ V and -1.0 V were analyzed by inductively coupled plasma-mass spectroscopy (ICP-MS). The $Cs_xTi_8O_{16}$ crystals were dissolved in a 3:1 mixed solution of H_2SO_4 and HNO_3 in a Teflon container. The sample quantities were 14 and 120 μg for the $V = -0.6$ V and -1.0 V crystals, respectively. The resultant solutions were made up to 50 mL, and then diluted ten times with distilled water. Data acquisition for Cs/Ti signals were repeated three times for each solution. The values of the Cs/Ti ratio are summarized in Table S2.1. These values include approximately ±5% of experimental errors such that the Cs contents (x) of the both crystals cannot be distinguished within the limited accuracy of the ICP-MS experiment.

Table S2.1. Cs/Ti ratios of the crystals grown with $V = -0.6$ V and -1.0 V analyzed by ICP-MS.

applied voltage / V	Cs/Ti ratio
−0.6	0.171
−1.0	0.163

Text S2.2: XPS Spectra of the Grown Crystals. To investigate the valence state of titanium in the grown crystals, X-ray photoelectron spectroscopy (XPS) measurements were performed. XPS spectra were collected with monochromatic Mg Kα radiation (operating condition: 400 W, 15 kV). As-grown crystals were placed on a conductive carbon tape. In Figure S2.4, Ti 2p core-level spectra of the crystals grown with $V = -0.6$, -1.0, and -1.8 V are presented, together with that of anatase-type TiO_2 as a reference material. Measurements for the $V = -1.4$ V crystal were unsuccessful, because of an insufficient amount of the crystals used for the measurement. The binding energies (E_B) of each spectrum were calibrated with the O 1s peak at 529.9 eV.[S1,S2]

The spectra of the $Cs_xTi_8O_{16}$ crystals evidence a negative chemical shift with respect to the TiO_2 reference. However, the grown crystals were subject to large contact resistance, and no special effort was made to minimize the charging effect, implying that possible extrinsic E_B shifts caused by the charging effect cannot be ruled out. According to the literature, the peak separated by 1.5 eV from Ti^{4+} state can be ascribed to the Ti^{3+} state.[S3] To examine the presence of reduced Ti species, Gaussian fits to the spectra were attempted. It appears that each of Ti $2p_{3/2}$ and $2p_{1/2}$ peaks can be fitted with two peaks, and the component at lower E_B gets enhanced as the negative voltage during the electrolysis is increased. While the evolution of the low-E_B component is consistent with a simple consideration that the larger voltage would lead to strongly reduced products, the intensity of this component is too large to be simply assigned as Ti^{3+} species.

In summary, while the negative chemical shifts as well as the low-E_B component are both consistent with the existence of reduced Ti species, the present XPS result is too preliminary to be analyzed quantitatively. Further studies will be necessary to discuss the valence state of titanium in detail.

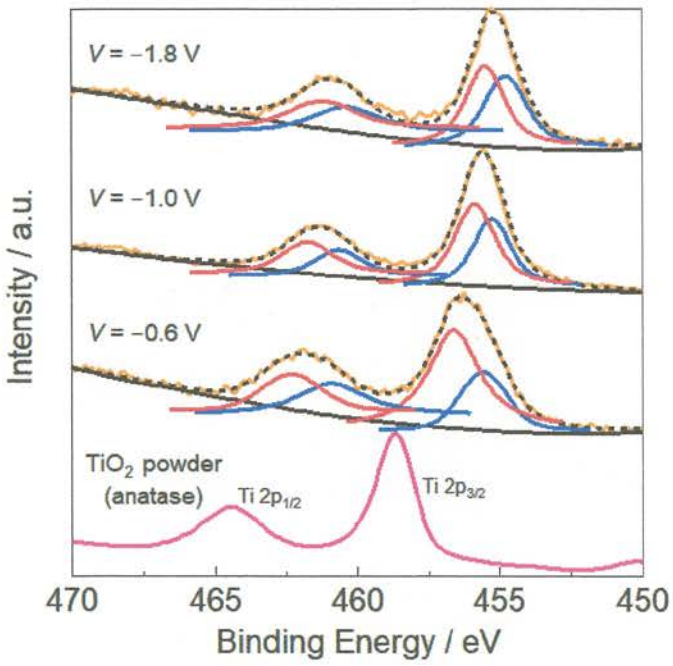

Figure S2.4. Ti 2p core-level spectra of the crystals grown with $V = -0.6$, -1.0, and -1.8 V. Solid curves represent Gaussian fits and the broken curves the resulting spectral envelopes.

Text S3.1: Syntheses of $Li_2Ti_3O_7$ and $Na_2Ti_6O_{13}$ Reference Materials.

Polycrystalline samples of $Li_2Ti_3O_7$ (ramsdellite-type) and $Na_2Ti_6O_{13}$ were synthesized via conventional solid-state reactions. $Li_2Ti_3O_7$ was prepared by firing a 1.05:3 molar mixture of Li_2CO_3 (99.99%, Kojundo Chemical Laboratory) and TiO_2 (anatase, 99%, Kojundo Chemical Laboratory). An excess amount of Li_2CO_3 (5 mol %) was added to the starting mixture to obtain a phase-pure product. The mixture was put into an alumina crucible and calcined in air at 750 °C for 12 h, followed by heating at 1050 °C for 12 h with an intermediate grinding. $Na_2Ti_6O_{13}$ was obtained by firing a mixture of Na_2CO_3 (99.8%, FUJIFILM Wako Pure Chemical) and TiO_2 (anatase, 99%, Kojundo Chemical Laboratory) with a 1:6 molar ratio at 800 °C for 50 h in air. Both of the compounds were obtained as white (colorless) powders (Figure S3.1). Phase purity of each compound was checked by PXRD (Figure S3.2).

Figure S3.1. Photoghaph of the (left) $Li_2Ti_3O_7$ and (right) $Na_2Ti_6O_{13}$ powders.

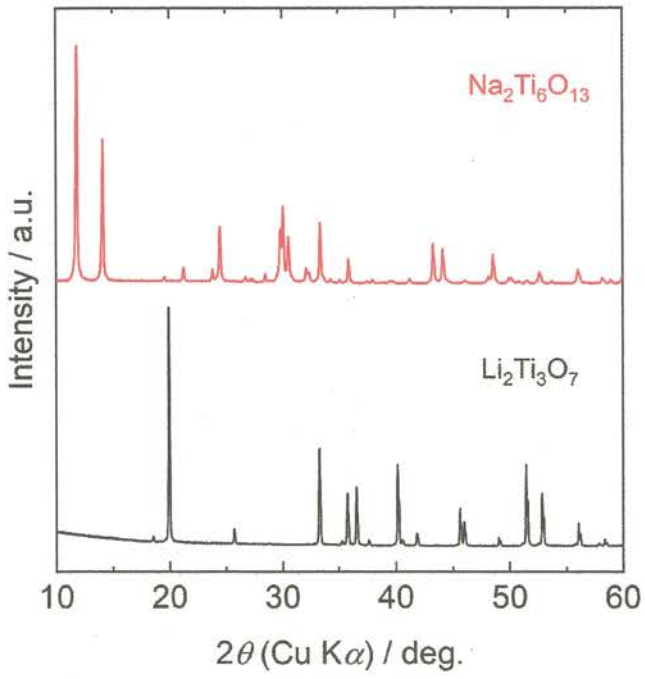

Figure S3.2. PXRD patterns for the $Li_2Ti_3O_7$ and $Na_2Ti_6O_{13}$ powders, showing the formation of phase-pure materials.

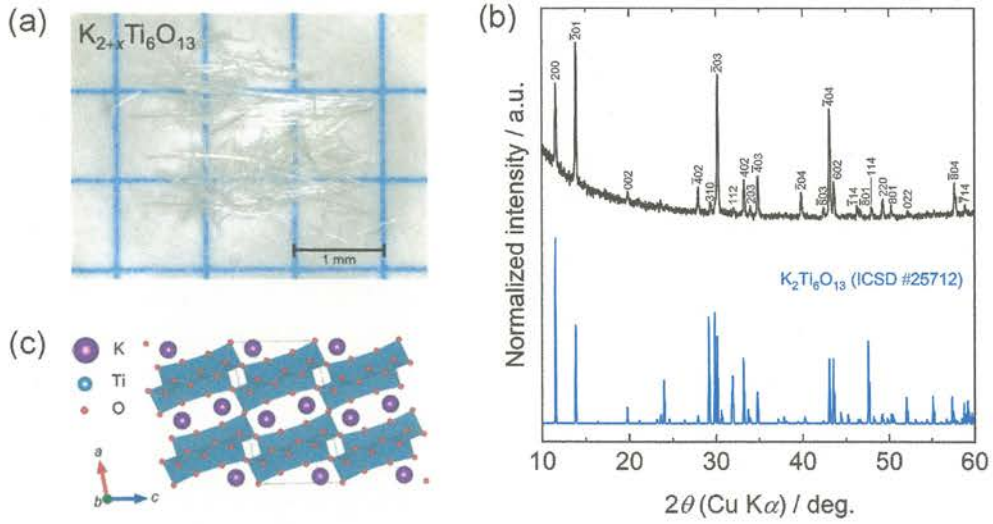

Figure S3.3. (a) Optical micrograph and (b) PXRD pattern of the nonpulverized $K_{2+x}Ti_6O_{13}$ crystals grown with $V = -0.85$ V. In (b), the simulated pattern for $K_2Ti_6O_{13}$ (ICSD #25712) is also shown. (c) Schematic illustration of the structure of $K_{2+x}Ti_6O_{13}$ viewed along the *b*-axis.

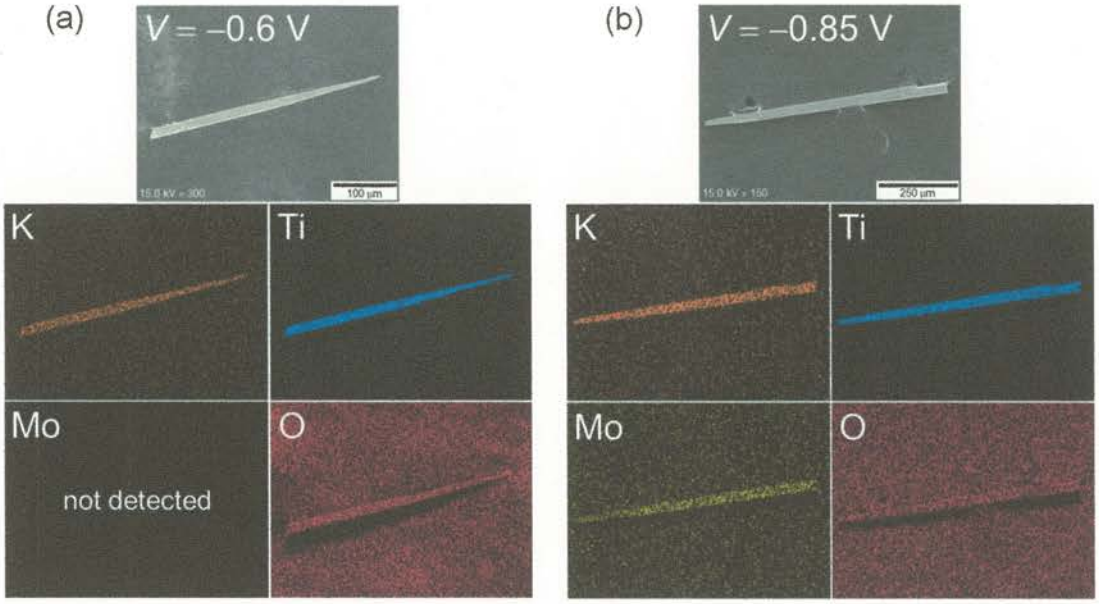

Figure S3.4. EDX mapping images of the $K_xTi_8O_{16}$ crystals grown with (a) $V = -0.6$ V and (b) –0.85 V.

Figure S3.5. EDX mapping images of the $Na_{2+x}Ti_6O_{13}$ crystal grown with $V = -0.75$ V.

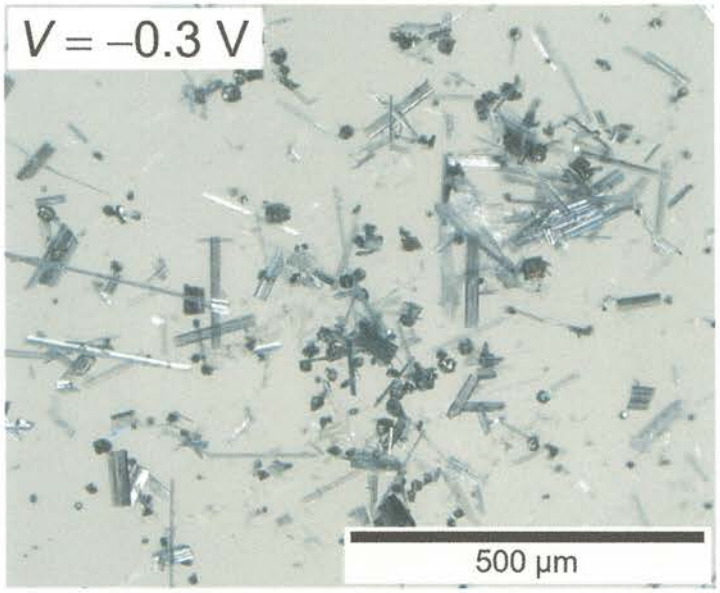

Figure S3.6. Optical micrograph of the crystals grown with $V = -0.3$ V in flowing Ar gas.

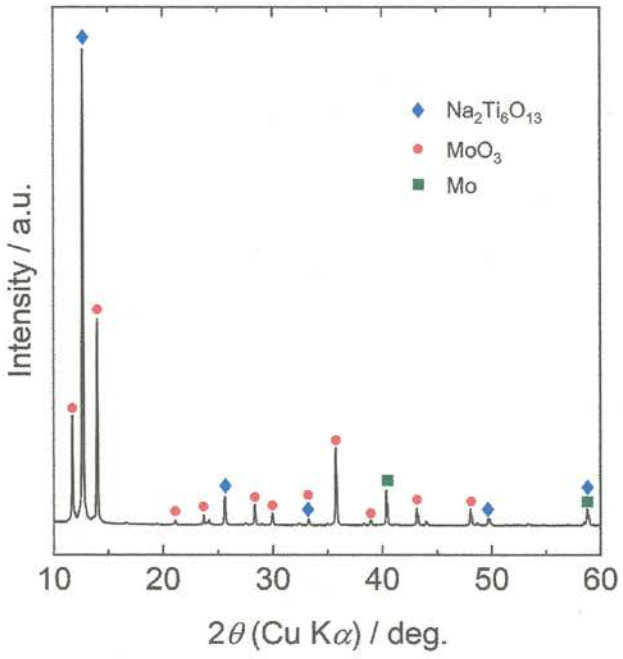

Figure S3.7. PXRD pattern for the crystals grown with $V = -0.3$ V in flowing Ar gas.

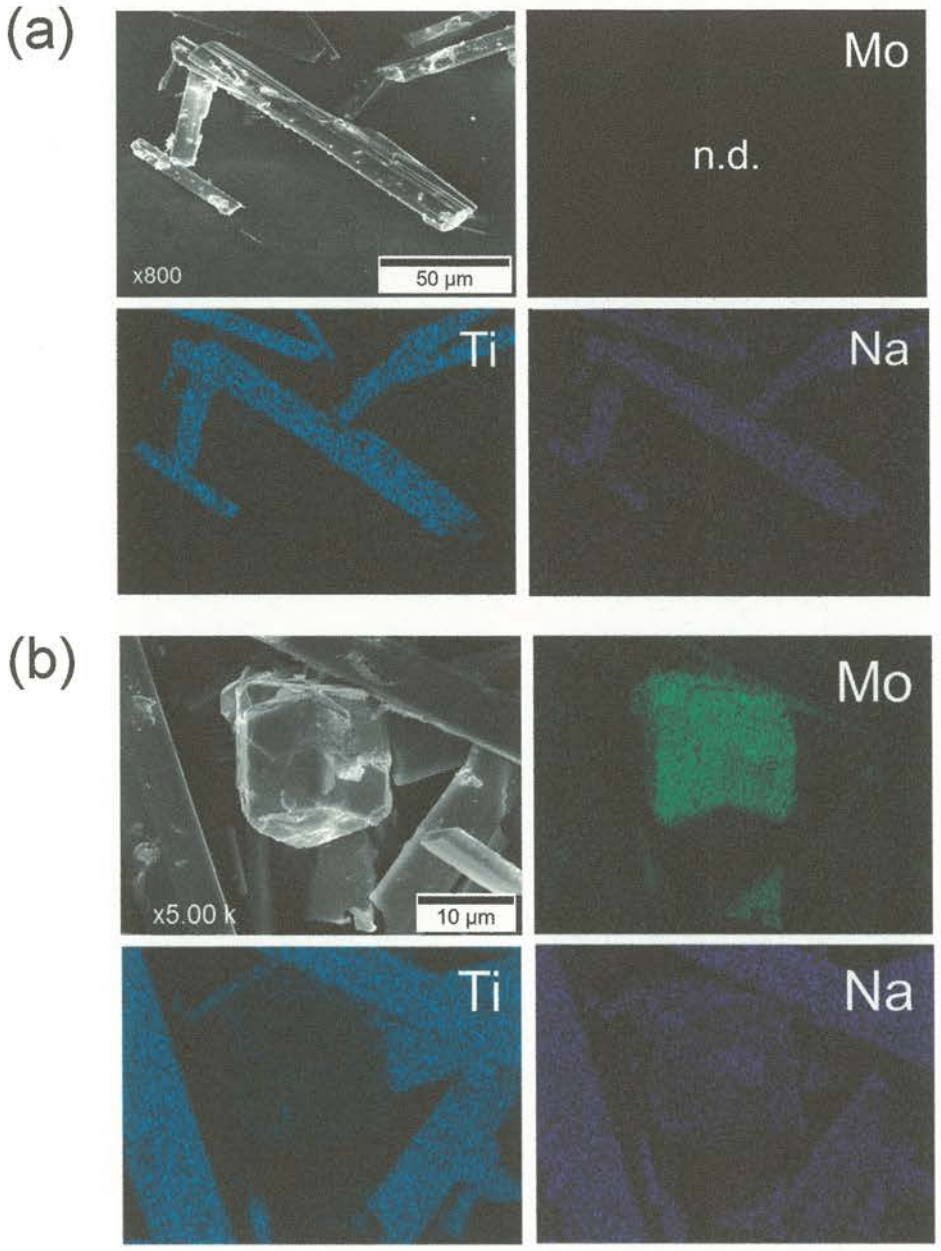

Figure S3.8. EDX mapping images of the (a) $Na_{2+x}Ti_6O_{13}$ crystal and (b) metallic particle grown with $V = -0.3$ V in flowing Ar gas.

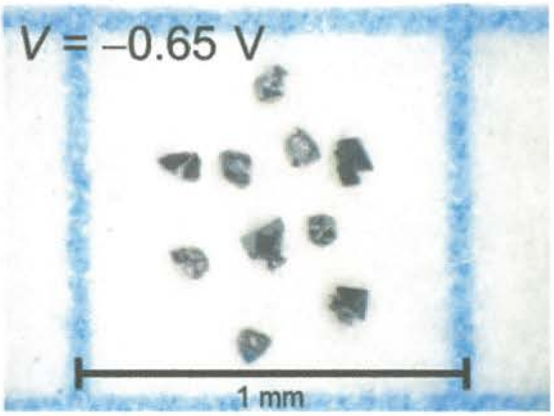

Figure S3.9. Optical micrograph of the $Li_{4+x}Ti_5O_{12}$ crystals grown with $V = -0.65$ V.

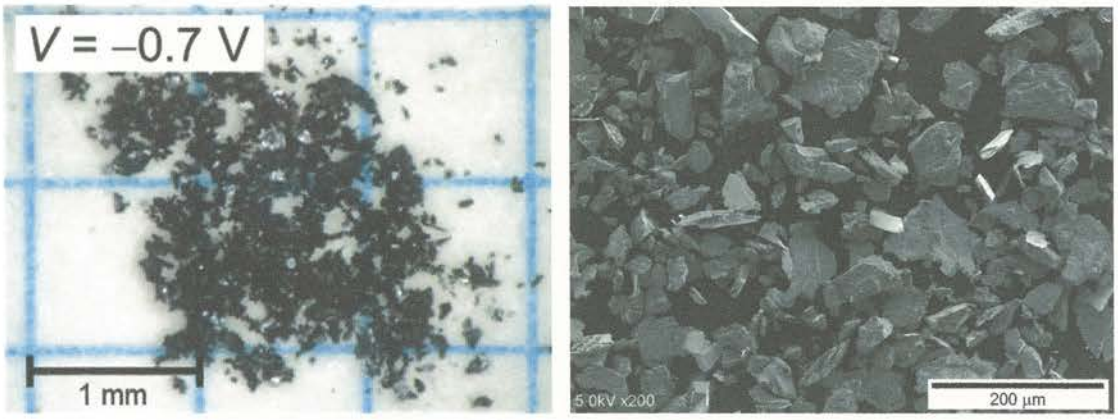

Figure S3.10. Optical micrograph (left) and SEM image (right) of the mixture mainly consisting of layered Li–Mo–O compounds grown with $V = -0.7$ V.

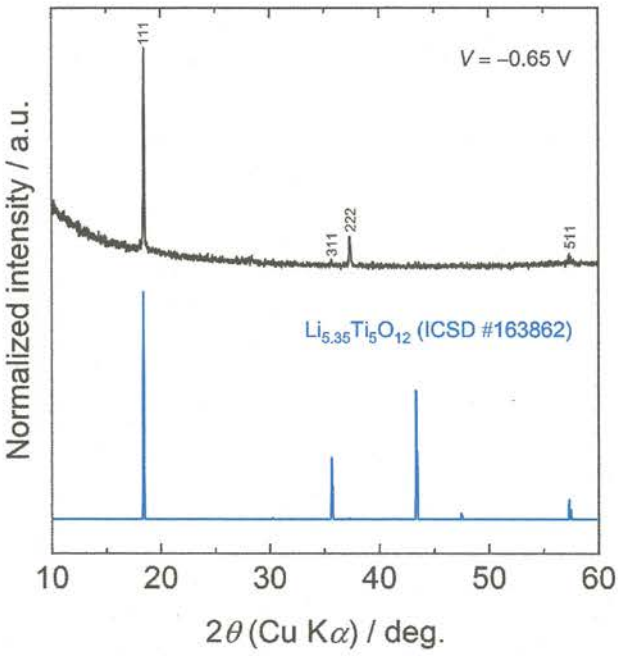

Figure S3.11. PXRD pattern for the nonpulverized $Li_{4+x}Ti_5O_{12}$ crystals grown with $V = -0.65$ V. The simulated pattern for $Li_{5.35}Ti_5O_{12}$ (ICSD #163862) is also shown.

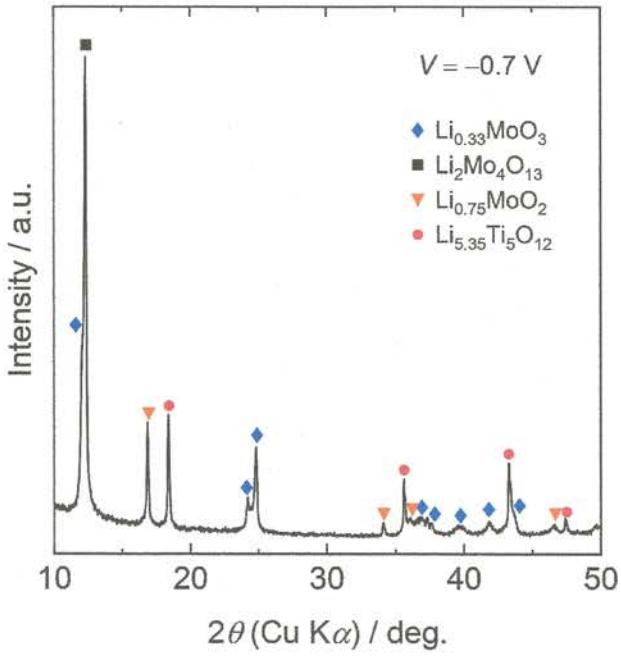

Figure S3.12. PXRD pattern for the mixture of layered Li–Mo–O compounds grown with $V = -0.7$ V.

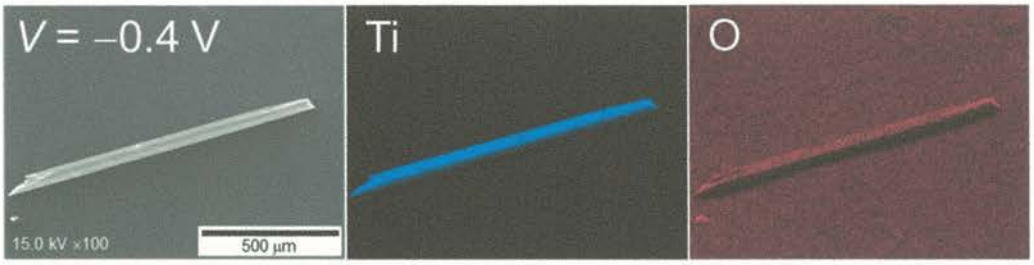

Figure S3.13. EDX mapping images of the $Li_{2+x}Ti_3O_7$ crystal grown with $V = -0.4$ V.

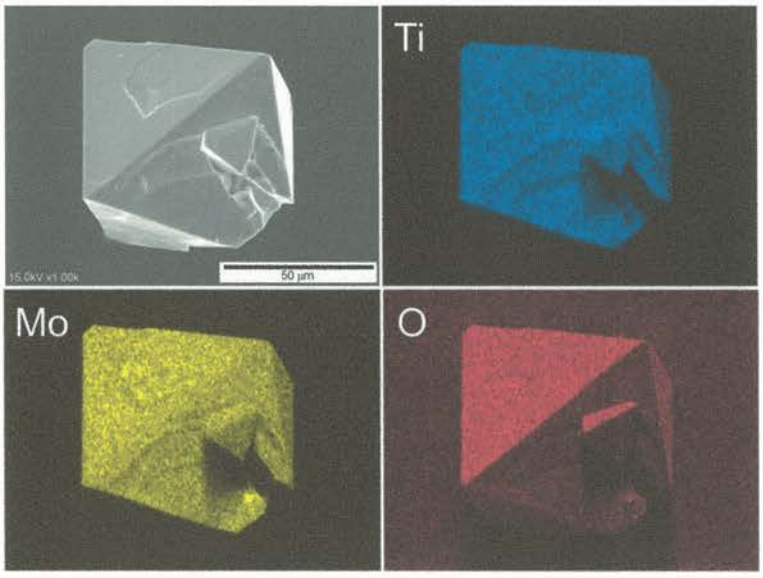

Figure S3.14. EDX mapping images of the $Li_{4+x}Ti_5O_{12}$ crystal grown with $V = -0.65$ V.

Text S4.1: Electrochemical Measurement of Molten Salt. Figure S4.1 shows a cyclic voltammogram of the molten mixture of TiO_2, Li_2MoO_4, and LiF at 1050 °C. A small current with a negative sign arises when the applied voltage reaches approximately $V = -0.4$ V in the forward (cathodic) sweep, indicating that a reduction of TiO_2 starts at –0.4 V. The negative current shows a stepwise increase at –0.60, –0.80, and –0.94 V, and finally reaches –30 mA at –1.2 V. In the backward (anodic) sweep, the negative current steadily decreases and overshoots the horizontal axis at –0.95 V. Then, the positive current forms an oxidation peak at –0.77 V, followed by small humps at –0.66 and –0.57 V, and eventually converges to 0 mA. The wide hysteresis suggests that crystals deposited on the working electrode (WE) in the forward sweep are electrochemically oxidized.

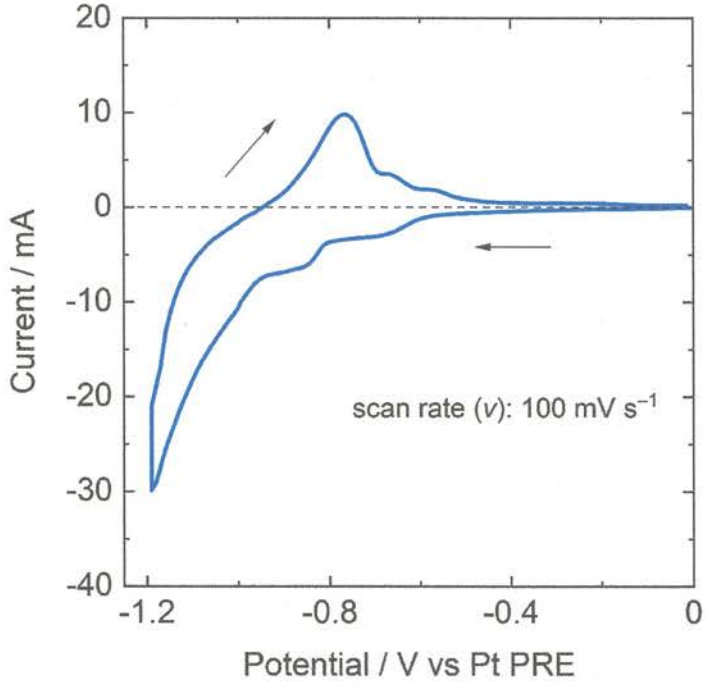

Figure S4.1. Cyclic voltammogram of the molten mixture of TiO_2, Li_2MoO_4, and LiF at 1050 °C in air. This plot was recorded at $v = 100$ mV s^{-1} with 0.5 mm-diameter Pt wire working, counter, and pseudoreference electrodes. Arrows mark the potential-scan direction. The horizontal broken line is a guide of 0 mA.

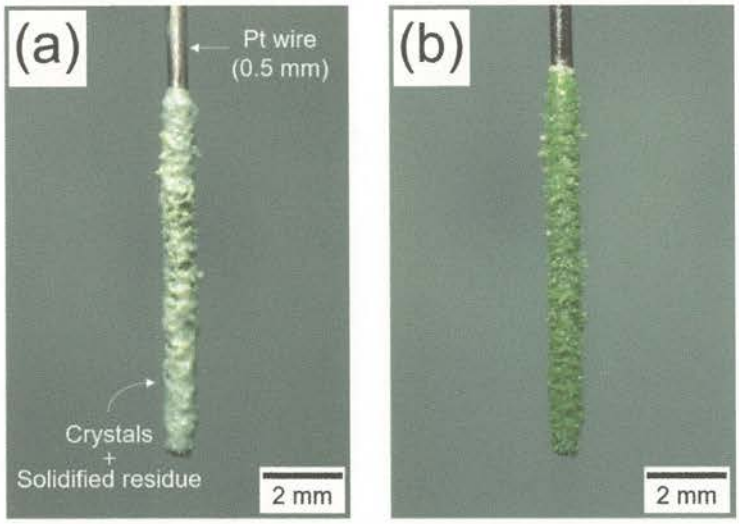

Figure S4.2. Typical photographs of the crystals deposited on WE at $V = -0.4$ V: (a) before and (b) after washing away the solidified residue with distilled water.

Text S4.2: Syntheses of α-Li_2TiO_3, β-Li_2TiO_3, and $Li_5Ti_2O_6F$ Reference Materials.

α-Li_2TiO_3 was synthesized via a hydrothermal reaction according to a procedure reported by Liu et al.[S4] To begin with, 3.3568 g (80 mmol) of $LiOH{\cdot}H_2O$ (98.0–102.0%, FUJIFILM Wako Pure Chemical) was completely dissolved in 40 mL of Milli-Q water (18 MΩ cm, Millipore) in a Teflon beaker. Then, 3.1948 g (40 mmol) of TiO_2 (anatase, average grain size ≤ 5 μm, 99.9%, FUJIFILM Wako Pure Chemical) was added into the solution under continuous magnetic stirring. After vigorous stirring at room temperature for 20 min, the slurry was transferred into a Teflon-lined stainless-steel autoclave with a capacity of 100 mL. The autoclave was sealed, directly placed in a furnace preheated at 180 °C, and held for 24 h without stirring. Once completed, the autoclave was taken out from the furnace and cooled down to room temperature. The resultant solid product was isolated by vacuum filtration, washed with Milli-Q water and ethanol several times, and finally allowed to dry at 80 °C for 15 min in an oven.

β-Li_2TiO_3 was synthesized using a conventional solid-state reaction technique as described in the previous report by Kataoka et al.[S5] A stoichiometric mixture of Li_2CO_3 (99.99%, Kojundo Chemical Laboratory) and TiO_2 (rutile, 99.9%, Kojundo Chemical Laboratory) was put into an alumina crucible and calcined at 1000 °C for 12 h in air.

$Li_5Ti_2O_6F$ was prepared according to the previously reported method by Zhang et al.,[S6] but the procedure was slightly simplified. A powder mixture of Li_2CO_3 (99.99%, Kojundo Chemical Laboratory), TiO_2 (anatase, 99%, Kojundo Chemical Laboratory), and LiF (99.9%, FUJIFILM Wako Pure Chemical) with a 2:2:1 molar ratio was put into an alumina crucible with a lid and calcined at 700 °C for 2 h in air. The calcined powder was ground and fired at 840 °C for 2 h in air.

All the targeted materials were obtained as white (colorless) powders (Figure S4.3). The formation of phase-pure materials was checked by PXRD (Figure S4.4): while β-Li_2TiO_3 crystallizes in a cation-ordered rocksalt-type structure, both α-Li_2TiO_3 and $Li_5Ti_2O_6F$ adopt a cation-disordered rocksalt-

type structure.

Figure S4.3. Photoghaph of the (left) α-Li_2TiO_3, (middle) β-Li_2TiO_3, and (right) $Li_5Ti_2O_6F$ powders.

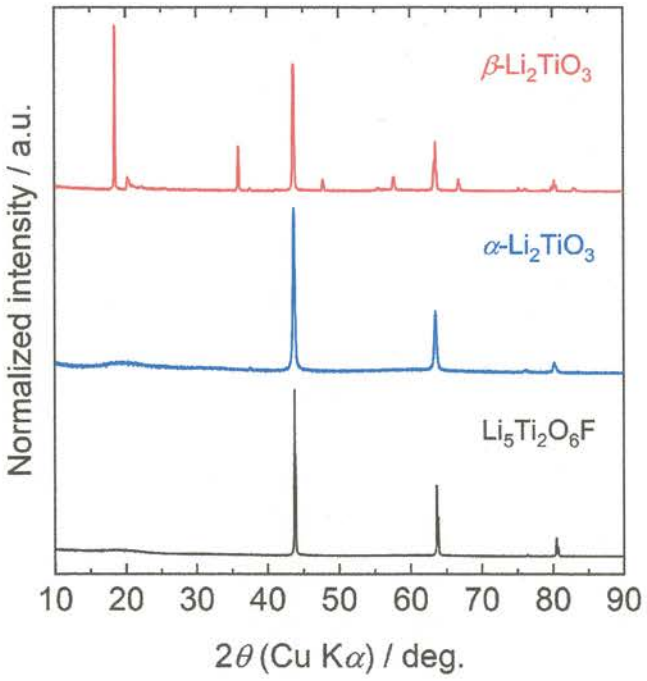

Figure S4.4. PXRD patterns for the α-Li_2TiO_3, β-Li_2TiO_3, and $Li_5Ti_2O_6F$ powders, showing the formation of phase-pure materials.

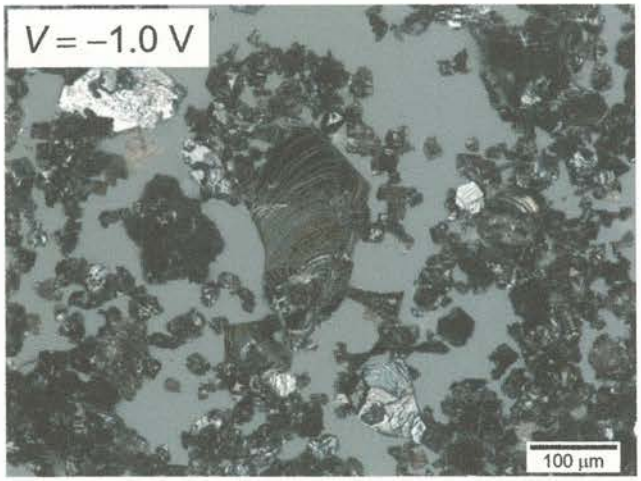

Figure S4.5. Optical micrograph of the crystals obtained at $V = -1.0$ V.

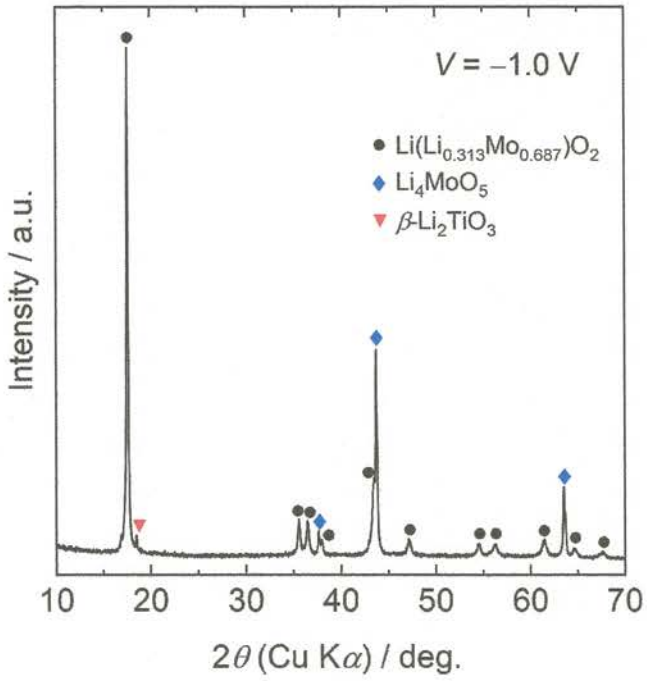

Figure S4.6. PXRD pattern for the well-pulverized $V = -1.0$ V crystals, revealing the formation of Mo-containing compounds as major products.

Text S4.3: Magnetic Properties. To study the oxidation states of titanium, the temperature dependences of the magnetic susceptibility (χ) of the oxide (V = –0.8 V) and oxyfluoride (–0.4 V) crystals were measured at 2–300 K in an applied field of 10 kOe (Figure S4.7). Both of the crystals exhibit paramagnetic behaviors in the whole temperature range measured. For the oxide crystals, χ is almost temperature-independent at 25–300 K, but exhibits a slight increase below 25 K. The upturn behavior likely originates from the localized unpaired electrons of Ti^{3+} ions, implying an oxygen-deficient composition (i.e., $Li_2TiO_{3-\delta}$). The formation of oxygen deficiencies possibly hinders F^--for-O^{2-} substitutions and hence the growth of F-free crystals.

On the other hand, the magnitude of χ for the oxyfluoride crystals is larger than the oxide crystals over the whole temperature range: notably, the χ value at 2 K is about ten times larger for the former than that for the latter. For both the crystals, no evidence of a magnetic ordering was observed down to 2 K. The χ–T plots are fitted with a modified Curie–Weiss law, $\chi = \chi_0 + C/(T - \Theta)$, where χ_0, C, and Θ denote the temperature-independent constant susceptibility, the Curie constant, and the Weiss temperature, respectively. Fitted values are summarized in Table S4.1. The small Weiss temperature values (–0.835 K and –0.716 K for the V = –0.8 V and –0.4 V crystals, respectively) suggest weak magnetic interactions in these crystals.

The C values yield effective magnetic moments (μ_{eff}) of 0.229 μ_B f.u.$^{-1}$ and 0.697 μ_B f.u.$^{-1}$ for the oxide and oxyfluoride crystals, respectively. There values lie between the theoretical spin-only values of Ti^{3+} (1.73 μ_B; S = 1/2) and Ti^{4+} (0.00 μ_B; S = 0), proving mixed-valent Ti^{3+}/Ti^{4+}. The averaged oxidation numbers of titanium (V_{Ti}) are calculated at +3.97 (oxide) and +3.78 (oxyfluoride). Taking into account the charge neutrality condition and estimated composition ratios of F/Ti and Li/Ti, the chemical compositions are readily estimated to be $Li_{1.90}TiO_{2.94}$ and $Li_{1.74}TiO_{2.69}F_{0.15}$ $[(Li_{0.61}Ti_{0.35}\square_{0.04})(O_{0.95}F_{0.05})]$, respectively. It should be noted that the V_{Ti} value for the oxide crystals is greater than that for the oxyfluoride crystals despite the larger negative voltage for the former that

is likely to lead to a stronger reductive condition. As the most plausible interpretation, the oxide crystals may be oxidized by atmospheric oxygen gas to form a less reduced phase (i.e., with a lower Ti^{3+} concentration) upon cooling to room temperature at the last process of the crystal growth. A reoxidation reaction in the oxyfluoride crystals is negligible because such a reaction is unlikely in (oxy)fluorides without anion deficiencies. Judging from the light colors and the magnetic properties of the crystals, both the crystals could be slightly electron-doped and electrically insulating.

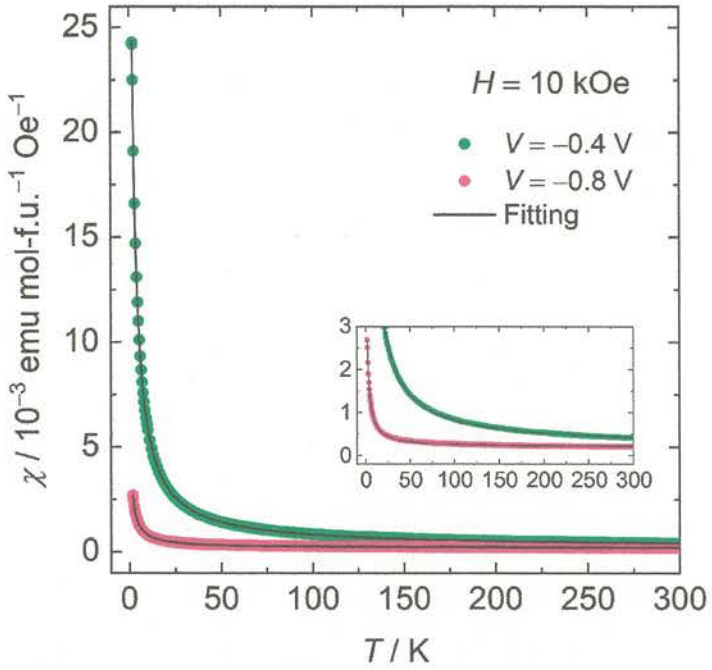

Figure S4.7. Temperature-dependent magnetic susceptibilities (χ) of the oxide (V = –0.8 V) and oxyfluoride (–0.4 V) crystals measured in an applied field (H) of 10 kOe. The green/pink circles represent the data, and solid black lines are modified Curie–Weiss fit results (see the text for details). The inset shows an enlarged plot in a lower χ region.

Table S4.1. Magnetic parameters for the oxide ($V = -0.8$ V) and oxyfluoride (−0.4 V) crystals. These values were determined based on least-square calculations for the χ–T plots (Figure S4.7).

applied voltage / V	χ_0 / emu mol^{-1} Oe^{-1}	C / emu K mol^{-1} Oe^{-1}	Θ / K
−0.8	1.93×10^{-4}	6.55×10^{-3}	-8.35×10^{-1}
−0.4	2.22×10^{-4}	6.07×10^{-2}	-7.16×10^{-1}

Table S4.2. Atomic coordinates and isotropic atomic displacement parameter (U_{iso}) for the oxyfluoride.

atom	site	g[a]	x	y	z	U_{iso} / Å^2
Li	4*a*	0.613	0	0	0	0.0112(6)
Ti	4*a*	0.352	0	0	0	0.0112(6)
O	4*b*	0.947	1/2	1/2	1/2	0.0121(8)
F	4*b*	0.053	1/2	1/2	1/2	0.0121(8)

[a]Occupancy factors, g, were fixed at the analyzed composition.

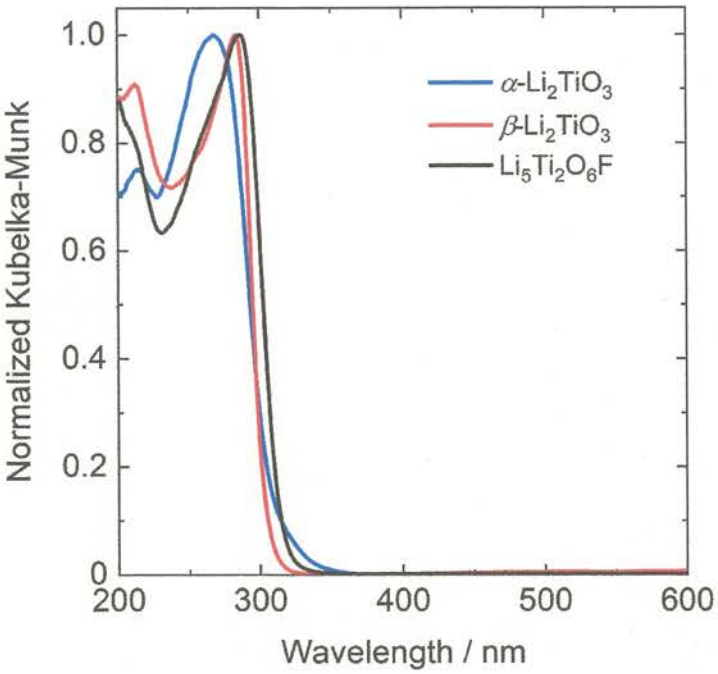

Figure S4.8. UV–vis diffuse reflectance spectra for the α-Li_2TiO_3, β-Li_2TiO_3, and $Li_5Ti_2O_6F$ powders. All the materials exhibit typical d^0 semiconducting nature.

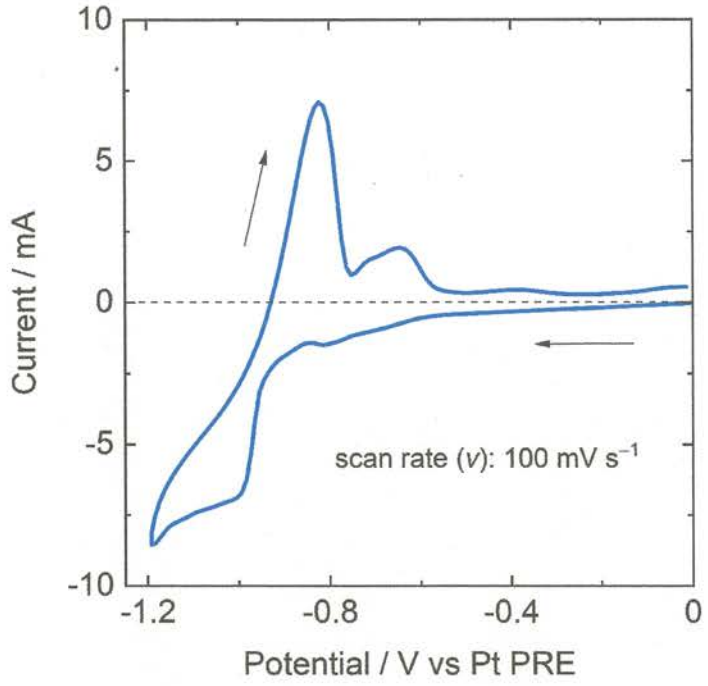

Figure S5.1. Cyclic voltammogram of the molten mixture of TiO_2, Na_2MoO_4, NaF, and $CaMoO_4$ at 1050 °C in air. This plot was recorded at v = 100 mV s^{-1} with 0.5 mm-diameter Pt wire working, counter, and pseudoreference electrodes. Arrows mark the potential-scan direction. The horizontal broken line is a guide of 0 mA.

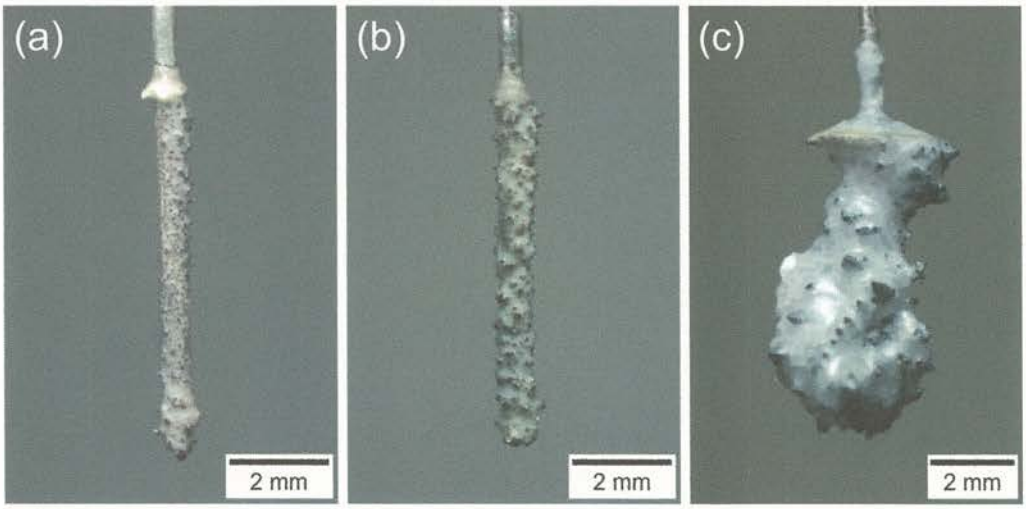

Figure S5.2. Typical photographs of the crystals deposited on WE at (a) V = –0.6, (b) –0.8, and (c) –1.0 V.

References for the Supporting Information:

(S1) Wagner, C. D.; Zatko, D. A.; Raymond, R. H. Use of the oxygen KLL Auger lines in identification of surface chemical states by electron spectroscopy for chemical analysis. *Anal. Chem.* **1980**, *52*, 1445–1451.

(S2) Hashimoto, S.; Murata, A.; Sakurada, T.; Tanaka, A. Alternation of Ti 2p XPS Spectrum for TiO_2 by Ar Ion Bombardment. *J. Surf. Anal.* **2002**, *9*, 459–462.

(S3) González-Elipe, A. R.; Munuera, G.; Espinos, J. P.; Sanz, J. M. Compositional Changes Induced by 3.5 keV Ar^+ Ion Bombardment in Ni-Ti Oxide Systems: A Comparative Study. *Surf. Sci.* **1989**, *220*, 368–380.

(S4) Liu, W.; Di, J.; Zhang, W.; Xue, L.; Yan, Y. Influence of Titanium Sources on the Microstructures and Properties of Li_2TiO_3 Ceramics Prepared by Hydrothermal Method. *Fusion Eng. Des.* **2019**, *138*, 364–371.

(S5) Kataoka, K.; Takahashi, Y.; Kijima, N.; Nagai, H.; Akimoto, J.; Idemoto, Y.; Ohshima, K. Crystal Growth and Structure Refinement of Monoclinic Li_2TiO_3. *Mater. Res. Bull.* **2009**, *44*, 168–172.

(S6) Zhang, Z.; Tang, Y.; Xiang, H.; Yang, A.; Wang, Y.; Yin, C.; Tian, Y.; Fang, L. $Li_5Ti_2O_6F$: A New Low-Loss Oxyfluoride Microwave Dielectric Ceramic for LTCC Applications. *J. Mater. Sci.* **2020**, *55*, 107–115.